

Stellar cluster ages and tests of stellar evolution - cluster member eclipsing binaries as a tool

Karsten Brogaard

Dissertation for the degree of Doctor of Philosophy

July 2010

Department of Physics and Astronomy
Aarhus University
Denmark

Abstract

Abstracts

Abstract in English:

Even though the basic principles of stellar structure and evolution are considered well known, we are still quite far from understanding and properly modeling the details. As a consequence the real error in any stellar age measurement is significantly larger than the measurement precision. Much of our current knowledge of stellar evolution comes from studying stellar clusters. However we have reached a point where most observations are not sufficient to distinguish between different physical details of current stellar models. With my work, I show here how accurate and precise measurements of masses and radii of multiple eclipsing binaries, which are members of the same stellar cluster, can improve age measurements of stellar clusters by constraining parameters of stellar models, notably the helium content, which were previously out of reach. Present and future efforts to improve this even further are then discussed. Furthermore, it is shown that cluster member eclipsing binaries are in fact quite common, and that therefore this method can and should be used for many clusters, to expose stellar models to the strongest tests ever, and result in cluster ages of unprecedented precision and accuracy. This will allow real progress to be made in our knowledge of stellar evolution and cluster ages, with implications for large areas of astrophysics.

Dansk resumé (Abstract in Danish):

På trods af at de generelle principper i stjerners struktur og udvikling anses for velkendte, er vi stadig langt fra en detaljeret forståelse. Som konsekvens heraf er den reelle fejl i enhver måling af en stjernes alder langt større end precisionen i målingen. En stor del af det nuværende kendskab til stjerneudvikling kommer fra studier af stjernehobe. Men vi har nået et punkt, hvor de fleste observationer ikke er tilstrækkelige til at skelne mellem forskellige fysiske detaljer i de seneste stjerneudviklingsmodeller. Her viser jeg, hvordan man kan forbedre aldersmålinger af stjernehobe ved at begrænse frihedsgraden af parametre i stjernemodellerne, specifikt helium indholdet, som tidligere var uden for rækkevidde, ved hjælp af nøjagtige og præcise målinger af masser og radier af multiple formørkelsesvariable dobbeltstjerner i den samme stjernebob. Jeg beskriver igangværende og fremtidige projekter til at forbedre metoden yderligere og viser at multiple formørkelsesvariable dobbeltstjerner eksisterer i en række stjernehobe. Metoden kan og bør derfor benyttes for mange stjernehobe for at opnå de strengeste tests af stjerneudviklingsmodeller nogensinde og deraf følgende mere nøjagtige aldre af stjernehobe. Det vil give anledning til reelle fremskridt i vores forståelse af stjerners udvikling og aldre, som er vigtige for mange områder af astrofysikken.

Contents

Abstracts	1
I Stellar cluster ages and tests of stellar evolution - cluster member eclipsing binaries as a tool	5
1 Introduction	7
2 Details of detached eclipsing binary measurements	13
2.1 Detached eclipsing binary measurements	13
2.2 Echelle spectroscopy	14
2.3 Extra considerations for infrared spectra	14
2.4 Observing through the atmosphere	15
2.5 Stellar spectra and radial velocity	15
2.6 Methods for radial velocity measurements	15
2.6.1 Cross correlation	16
2.6.2 Two-dimensional cross-correlation (TODCOR)	16
2.6.3 Broadening function (<i>BF</i>)	17
2.6.4 Spectral disentangling and iterative subtraction methods	19
2.6.5 Combining orders	20
2.6.6 Selecting the method(s) to use	21
2.6.7 Additional considerations for radial velocity measurements	21
2.7 Spectroscopic Binary Orbit Program (SBOP) and reliable error estimates	22
2.8 Photometry and radii determination	23
2.9 Optimising the use of telescope time	23
2.10 Exploiting all cluster member dEBs	23
3 Demonstrating the potential of cluster member dEBs	25
4 Building a stellar evolution test set	47
5 Which aspects of stellar evolution can be tested?	61
6 Conclusion	69
II Reports & Articles	77
A EFFECTS OF ASSUMED CHEMICAL COMPOSITION ON THE ACCU- RACY OF STELLAR AGES	79

B	DETECTION OF SOLAR-LIKE OSCILLATIONS FROM KEPLER PHOTOMETRY OF THE OPEN CLUSTER NGC 6819	89
C	PHOTOSPHERIC AND CHROMOSPHERIC ACTIVITY ON EY DRA	97
D	OSCILLATIONS IN PROCYON A: FIRST RESULTS FROM A MULTI-SITE CAMPAIGN	107
E	A MULTISITE CAMPAIGN TO MEASURE SOLAR-LIKE OSCILLATIONS IN PROCYON. I. OBSERVATIONS, DATA REDUCTION, AND SLOW VARIATIONS	117
F	A MULTI-SITE CAMPAIGN TO MEASURE SOLAR-LIKE OSCILLATIONS IN PROCYON. II. MODE FREQUENCIES	131

Part I

Stellar cluster ages and tests of stellar evolution - cluster member eclipsing binaries as a tool

Chapter 1

Introduction

Even though the basic principles of stellar structure and evolution are considered well known, we are still quite far from understanding and properly modeling the details. As a consequence the real error in any stellar age measurement is significantly larger than the measurement precision. Since age is an important parameter in so many aspects of astrophysics, this alone is a good reason to improve things. Moreover, with e.g. the discovery of multiple populations in some globular clusters, the recent progress in asteroseismology, and the desire to characterize exoplanet host stars, there is an increasing need to obtain physical parameters by comparing observations to stellar models. This makes it even more crucial that we understand the details of stellar evolution.

The Milky Way contains a large number of stellar clusters of different ages, from the oldest compact globular clusters to the younger and less compact open clusters. The stars in a stellar cluster are all formed from the collapse of the same gas cloud and therefore share the same age and original composition of hydrogen, helium and heavier elements (with the exception of globular clusters with multiple populations). Photometric studies of stellar clusters have been extensively used for determining their ages and testing stellar models by comparing them to the observed brightness and colors of the cluster stars. This method, isochrone fitting, has the potential to test subtle effects, but is limited due to degeneracies between the distance to the cluster, its age and composition of elements, interstellar reddening and poorly understood physics in the stellar models. An additional problem is the need to convert measured colors to effective temperatures, to compare observations properly with stellar models. Much of our current knowledge of stellar evolution comes from studying these clusters. However we have reached a point where most observations are not sufficient to distinguish between different physical details of current models. See Fig. 1.1 for an illustration of these aspects.

Accepting that the absolute ages of stars depend on physics which we presently do not understand in detail, some astronomers have resorted instead to measuring the relative ages of the globular clusters, which are supposedly easier to determine (Marín-Franch et al. 2009), since even relative ages are interesting for understanding the formation and evolution of the Milky Way. But even here there are major unresolved problems, related to the effects of the detailed abundance pattern on stellar evolution (e.g. D’Antona et al. 2009).

Another way to obtain age information from stars is through asteroseismology, the inference of stellar properties from their oscillation frequencies. This research field is evolving fast, and with the current observations from the Kepler mission (Gilliland et al. 2010), asteroseismology is now possible for stars in some stellar clusters (Stello et al. 2010, Appendix B). However the stellar parameters, including age, determined from asteroseismology, are model dependent to some extent.

A detached eclipsing binary (dEB) is a gravitationally bound system of two well separated

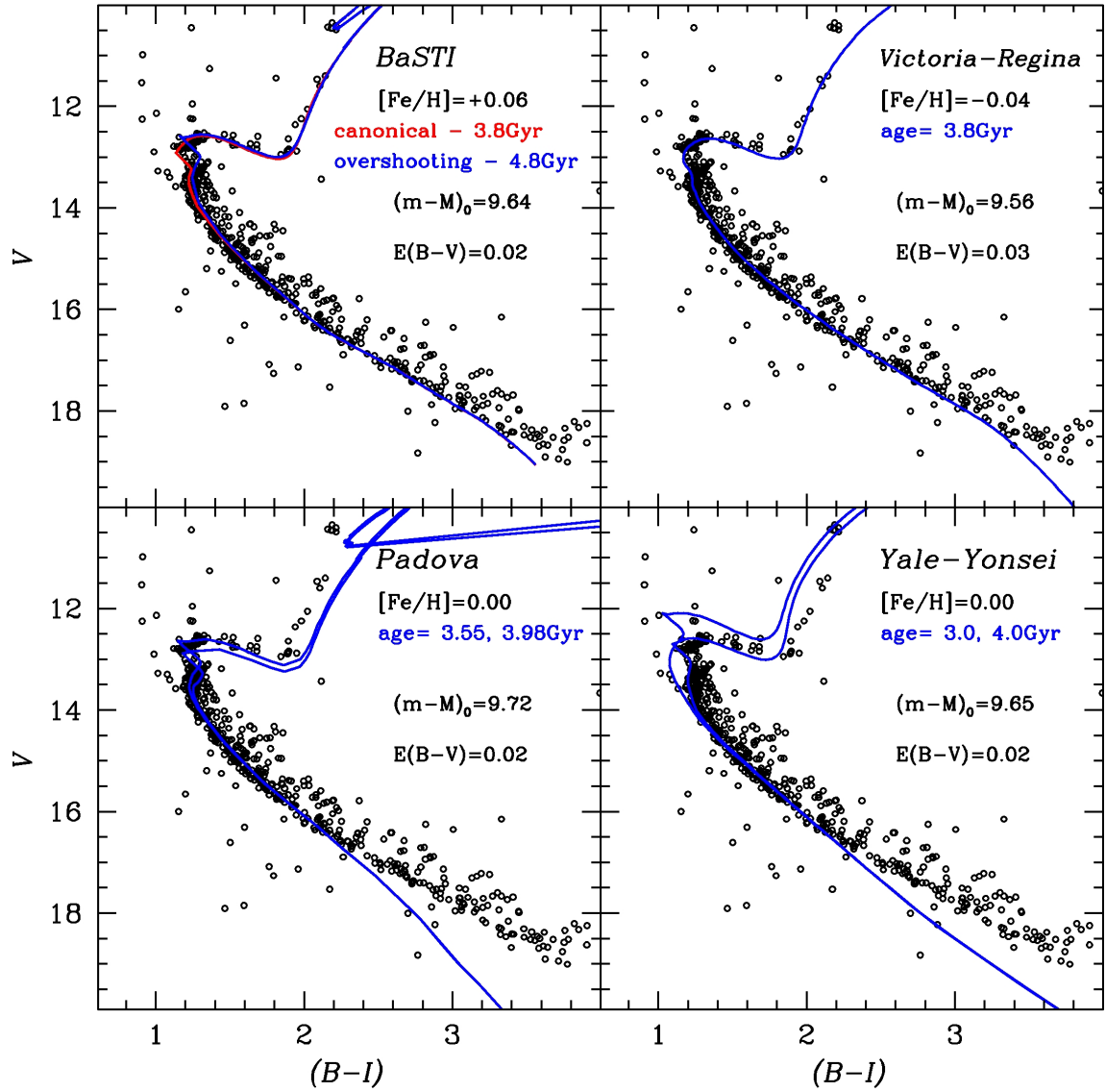


Figure 1.1: The color magnitude diagram of the open cluster M67 compared to different stellar model isochrones. Within the flexibility given by the observational uncertainties, one can not distinguish between these models. Figure taken from Yadav et al. (2008)

stars oriented such that the orbit plane intersects the line of sight. This causes eclipses when one star passes the other. The combination of spectroscopic radial velocity measurements and an observed light curve of the eclipses allow the measurement of accurate masses, radii and radiative properties of the two stars. Masses and radii determined this way are very nearly model independent. Since mass and radius can be compared directly to stellar models without the need for any uncertain conversions, dEBs are prime objects to test stellar evolution models. Danish astronomers have contributed significantly to this research field over the years (Reviews: Andersen 1991; Torres et al. 2010). However, because age is a free parameter for each dEB system of two stars, the comparison of single dEBs to stellar models only provides relatively weak stellar model constraints.

For all the observational methods mentioned two issues prevent accurate stellar age measurements: (i) limited measurement precision caused by observational uncertainties and (ii) limited measurement accuracy caused by theoretical uncertainties.

dEB members of open or globular star clusters offer stronger model constraints by allowing a combined analysis of dEBs and the single cluster stars. This reduces significantly the number and range of free parameters in model comparisons, since each method provides complementary data. This was to some extent exploited by Grundahl et al. (2008b), who analysed their measurements of masses and radii of a dEB in the open cluster NGC6791, together with literature metallicities from single cluster stars. Their procedure demonstrated that the age precision obtained is so high that the stellar model uncertainties dominate the age error, see Fig. 1.2. A small follow-up investigation (Brogaard 2008, unpublished, Appendix A, hereafter KB08) showed that the helium content is a major contributor to the model differences. Thompson et al. (2010) measured and analysed a dEB in the globular cluster 47 Tucanae, and also here the dominating error is the systematics from model uncertainties, again with the helium content as a dominant source.

If multiple dEBs can be found in the same cluster, all the component stars will have the same age, and thus the mass-radius diagram can be populated with many more points, thereby constraining the shape of the model isochrone in the mass-radius and $\log(T_{eff}) - \log(L)$ diagrams. In addition, by requiring that the same model matches also the cluster color-magnitude diagram (CMD), this pins down the isochrones in the CMD, since then the mass is known at given positions along the isochrone. The dEBs can also improve the metallicity determinations, both through measurement of metallicities from disentangled spectra of the dEB components themselves, but also by providing very accurate values of the surface gravity along the isochrone. This removes the surface gravity as a free parameter from the metallicity measurement of the single cluster stars, and allows more accurate spectroscopic temperatures to be determined. This also avoids the need for less precise photometric temperatures, which depend on interstellar reddening. In fact, the reddening can be measured by demanding that spectroscopic and photometric temperatures agree (chapter 3).

Such a combined analysis can provide very precise stellar cluster ages and tight constraints for stellar models, and allow one to progress from demonstrating model discrepancies to improving the stellar models.

While the analysis of a specific cluster with multiple dEBs should optimally address specific weaknesses in stellar models, it will of course also test the stellar models in general. In fact, due to the complex way in which stellar model uncertainties are connected because of our need to calibrate models using the sun (KB08), it is in fact unclear which physical aspects exactly are being tested by such a comparison. This of course also makes the interpretation harder. A combined analysis of many clusters with multiple dEBs, each of different age and metallicity, therefore provides stronger model constraints than any individual analysis, and the long term aim of my research career is to build a large state-of-the art stellar evolution test set of clusters

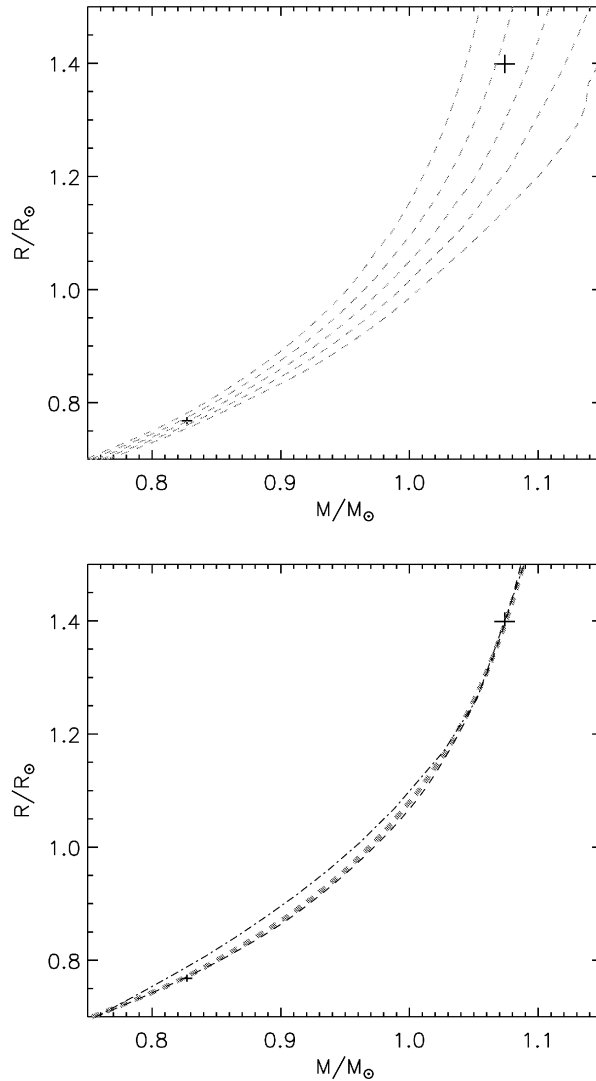


Figure 1.2: Plots from Grundahl et al. (2008b) reproduced for illustration purposes. Upper: The mass-radius diagram showing the measurements of masses and radii of the dEB V20, member of the open cluster NGC 6791. The crosses are one sigma error bars. The measurements are compared to Victoria-Regina stellar model isochrones of ages 5 to 9 Gyr in steps of 1 Gyr (radius growing with age). Comparing the size of the error bar of the primary component of V20 (the most massive) to the separation between isochrones, the inferred age precision is 0.3 Gyr.

Lower: The same measurements as in the upper panel, now compared to isochrones from three different stellar models, selected to match the primary component of V20. VRSS (7.7 Gyr, dashed thick gray), Y^2 (8.2 Gyr, dot-dashed), and BaSTI (9.0 Gyr, dashed black). The age difference between models is 1.3 Gyr corresponding to four times the precision of a single model. This demonstrates that stellar model differences are the dominant error source in the age measurement. But additional information is needed to judge which model is the better one.

with multiple dEBs.

Present and future space telescope missions will provide complementary data. Specifically the ongoing *Kepler* mission will allow asteroseismology of cluster stars (Stello et al. 2010, Appendix B), and the GAIA mission (Cacciari 2009) will soon measure accurate geometric cluster distances. Combining these with the measurements of multiple cluster member dEBs will expose stellar models to the strongest tests ever, and result in cluster ages of unprecedented precision and accuracy. This should allow real progress to be made in our knowledge of stellar evolution with implications for large areas of astrophysics.

The idea of, and methods for, measuring multiple cluster member dEBs is in fact not new, and has already been used on young open clusters (e.g. Southworth et al. 2004), but the measurements were not at a precision level where they could challenge stellar models.

In the following chapters I first describe new and improved observational and analysis techniques which make it possible to extend measurements to older and fainter clusters while improving measurement accuracy to a level where current stellar models can be challenged. Then, with the old open cluster NGC6791 as an example, it is shown how accurate measurements of multiple cluster member dEBs can improve age measurements of stellar clusters while constraining the helium content. Present and future attempts to improve this even further are then discussed. It is shown that cluster member dEBs are in fact quite common, and that this method can and should therefore be used for many clusters. Finally, ongoing projects with other clusters aimed at revealing e.g. the relation between the detailed abundance pattern and stellar evolution are discussed.

Chapter 2

Details of detached eclipsing binary measurements

The methods for measuring accurate and precise parameters (masses, radii, effective temperatures, and luminosities) of eclipsing binaries are described in great details in a number of works (e.g. "An Introduction to Close Binary Stars" by Hilditch, 2001). Here, after a very short introduction to the general subject, this section concentrates on specific details, some of which concerns specifically cluster member binaries. The reader not interested in such details can skip this chapter.

2.1 Detached eclipsing binary measurements

Two stars orbiting each other because of their mutual gravitational attraction are called a binary. As stars are in general very far away, such stars can usually not be spatially resolved even by large telescopes and are seen as one. However their binary nature is revealed in spectra, since they will contain spectral lines from both stars, lines which will be shifted relative to each other depending on the orbital radial velocities of the components at the time of observation. In some cases the orbit plane will be close to the line of sight from earth to the binary and a dimming of the light from the binary will occur when the stars eclipse each other. Such a system is called an eclipsing binary. The brightest star is usually called the primary star and the other the secondary star. For some eclipsing binaries, a separate star along the line of sight blends with the binary. Such a star is referred to as a third light.

An eclipsing binary has the unique feature, that the masses and radii of the components can be determined with high accuracy from a combined analysis of light curves of the eclipses and spectra covering the orbit. Details on such analysis is covered elsewhere (e.g. Hilditch 2001), but the basic principle is the following. From spectra the radial velocities of each star are found and compared to orbit expectations from Kepler's laws. This gives the minimum masses $M_{1,2} \sin^3(i)$ and projected separation between the stars $a \sin(i)$, where i is the inclination angle between the orbit and the plane of the sky, $M_{1,2}$ are the masses of the stars, and a is the semi major axis of the orbit. Analysis of the shape and depth of the photometric light curves during eclipses gives i and the radii in units of a . Combining all these results finally gives the masses and radii.

Once the masses and radii of the component stars have been found, their age can be found by comparison to stellar model isochrones in a mass-radius diagram. However this procedure assumes that the stars in the binary evolve as single stars, which is not always the case. In

some binaries, the stars are so close that mass is transferred between the stars or their rotation is spun up significantly. Therefore only well detached eclipsing binaries (dEBs), which can be assumed to evolve as single stars, can be used in such a procedure.

Since such a procedure is not new, and has been well described by others and applied to a number of dEBs (see Torres et al. 2010 for a recent review), I concentrate here on describing analysis and observational methods useful for faint cluster member dEBs.

2.2 Echelle spectroscopy

To determine the radial velocities of a dEB, the light variation with wavelength, a spectrum, has to be measured. In order to see details in the spectrum, high resolution is needed. High resolution spectra are recorded with an echelle spectrograph; light from the telescope goes through a slit or an optical fiber and is dispersed by a grating and then cross dispersed by another grating or a prism. To associate a wavelength with each position on the detector, a spectrum of a thorium-argon (ThAr) emission lamp, with known line positions, is also recorded. For very high precision spectrographs, the ThAr light comes through an extra fiber, allowing it to be recorded together with the light from the star. Changes in the light path caused by the spectrograph will be equal for the star light and ThAr light and will therefore not appear in the final spectrum. To get the final one dimensional wavelength calibrated spectrum, several calculations are needed. This is known as the reduction of the spectrum. Reduction steps include dark subtraction, flat fielding, tracing of orders, extraction of the 1D spectrum, and wavelength calibration. For many spectrographs a program called a pipeline, which does this automatically, is made for this purpose. This makes it easy for the inexperienced spectroscopist to get the final spectra, but one often needs to examine the raw spectra and tweak the parameters of the pipeline to be able to produce optimal results for observations at the limit of instrument capabilities.

2.3 Extra considerations for infrared spectra

Obtaining spectra in the infrared is a bit more complicated. This is because the Earth's atmosphere both emits and absorbs light at infrared wavelengths. To complicate things the spectrograph itself also emits light at infrared wavelengths. The instrument emission is minimized by cooling the instrument to a very low temperature. The method of nodding is used to correct or remove sky emission, detector dark current and glow. In a simple application of this technique a spectrum is taken with the telescope at position A, after which the telescope is moved along the direction of the slit to position B and another spectrum is taken. By subtracting the A and B images, dark and sky subtractions are performed. Since infrared detectors often have relatively many bad pixels, the method of jittering is also used. Jittering is obtained by adding a small, random offset to the telescope in addition to the nodding offset, when shifting back and forth between A and B positions.

Many prominent features in IR spectra are telluric absorption lines created by the Earth's atmosphere. Unfortunately, many telluric absorption lines are saturated and do not scale linearly with airmass. Therefore, it is necessary to observe a telluric standard star as close as possible in airmass and with the same instrument setup as that used for the science target. Furthermore, the strength of some telluric lines varies with time, so it is also necessary to observe the standard soon after or soon before the science target. Since the telluric standard star spectrum is known, the lines from this star can be removed leaving only the telluric lines. The spectrum of the science target can then be divided by the telluric spectrum to remove the telluric lines.

Since this procedure adds a lot of overhead to the observations and is often not very accurate, another strategy is to select certain spectral regions, where atmospheric absorption is known to be minimal.

The high resolution infrared spectrograph CRIRES at the VLT has the disadvantage that it is not cross dispersed. This means that it only records one spectral order, thereby limiting the wavelength range available in an observation. Furthermore this one order is spread over four detectors of which the first and last are not usable in many settings, since contaminating light from other orders is not properly removed.

2.4 Observing through the atmosphere

For a telescope on earth with a mirror diameter larger than about 40 cm, the spatial resolution is given by the Earth's atmospheric conditions rather than the diffraction limit. Therefore, the resolution at a given time on a given night is quantified by the measured full width half maximum of a star. This measure is called the seeing. As the seeing is caused by turbulent air layers giving random phase shifts to the light, techniques exist to minimize the effect. Adaptive Optics (AO) analyses the light at the telescope and (partly) corrects the phase shifts before the light reaches the detector, thereby minimizing the effects of the atmosphere. This technique works best at infrared wavelengths. In the optical, the method of Lucky Imaging can be used to improve resolution. This technique uses a very fast camera, taking images at high frequency. At a given snapshot in time, the atmosphere provides good or bad seeing. By only making use of the frames taken at good seeing, the resolution of the final image is better than the average seeing. This of course comes at the cost of having wasted the time it took to take the frames at bad seeing.

2.5 Stellar spectra and radial velocity

When the light from a star is dispersed by a prism or grating, the variation of the brightness of the light with wavelength can be seen. The form of this variation is generally a continuous change in brightness, which depends on the temperature of the object, with the superposition of sharp peaks, which may rise from the continuum or drop below the continuum, at places in the spectrum dependent on the chemical composition of the star. This allows us to derive a lot of information about a star simply by studying its spectrum. The central wavelength of an absorption line is the wavelength at which there is an increase in opacity due to the presence of many atoms or ions of one type in the stellar photosphere. The difference in velocity between the star and an observer causes the wavelength of the detected light to be different from its wavelength on leaving the Star. C. Doppler showed that, for velocities much less than the speed of light, the shift in wavelength, $\Delta\lambda$, depends on the rest wavelength, λ_0 , the relative radial velocity between the emitter and observer, v , and the speed of light, c :

$$\frac{\Delta\lambda}{\lambda_0} = \frac{v}{c} \quad (2.1)$$

Light from a star which is moving away from the observer is thus found to increase in wavelength, an effect called redshift. The opposite effect is called blueshift.

2.6 Methods for radial velocity measurements

Once spectra have been obtained, the radial velocities of the components of a dEB can be found. Several procedures exist for measuring radial velocities and some of them are described here.

2.6.1 Cross correlation

The idea of this basic method is based on the fact that the presence of a weak signal, hidden in noise, can be better revealed from overall coincidence of the whole spectrum than from some local features. The Doppler shift x of a spectrum is constant in logarithmic wavelength scale

$$x = c \ln \lambda \quad (2.2)$$

and, in the non-relativistic approximation ($v = \frac{c\Delta\lambda}{\lambda} = \Delta x$), linear in radial velocity v . The cross-correlation

$$CC(v) \equiv \int f(x)g(x-v)dx \quad (2.3)$$

of the observed spectrum $f(x)$ with a properly chosen template spectrum $g(x)$ thus measures the radial velocity shifts at which a similar pattern appears in the spectra f and g . An ideal template $g(x)$ should contain the same lines in the same ratios of their strengths as the spectrum of the star to be measured. In practice an observed spectrum of a star of similar spectral type or a synthetic spectrum from a model-atmosphere is used. Fortunately, experience shows that the cross correlation is not very sensitive to the choice of the template spectrum, at least not at optical wavelengths. Nevertheless, the template spectrum needs to be known and this can be difficult for a faint secondary star. Other shortcomings of the cross-correlation technique are the facts that the cross-correlation profile is broadened due to widths of both the observed spectrum and the template and that some side-peaks may arise in the cross-correlation from chance coincidence of mutually non-corresponding lines in the observed spectrum and the template. I used this simple method for determining the radial velocity of the magnetically active star EY Dra (Appendix C).

2.6.2 Two-dimensional cross-correlation (TODCOR)

A generalization of the cross correlation is a two-dimensional cross-correlation

$$CC2(v_1; v_2; \alpha) = \int f(x)[g_1(x-v_1) + \alpha g_2(x-v_2)]dx \quad (2.4)$$

enabling to choose templates corresponding to different spectral types for the primary and secondary star (Zucker & Mazeh 1994; Zucker et al. 1995). α is the flux ratio between the stars, which can either be set if known or solved for together with the radial velocities if unknown. This method is especially useful when the stars have very different spectral types. It can be further generalized to systems with three components

$$CC3(v_1; v_2; v_3; \alpha; \beta) = \int f(x)[g_1(x-v_1) + \alpha g_2(x-v_2) + \beta g_3(x-v_3)]dx \quad (2.5)$$

which is needed for triple systems or when light from a third star contaminates the spectra. Like before α and β are flux ratios. The result of TODCOR is a multidimensional surface, and the radial velocities of the components are determined by projections through the maximum value. Interestingly it is not mentioned anywhere in the literature that because of this, the correlation peaks are not symmetrical and therefore it is not trivial how to choose the maximal correlation value without very high velocity resolution in the correlation. A grid of different templates, g_1 , g_2 and g_3 , are tried on all observed spectra, and the ones giving the overall maximum correlation are chosen. This method was employed for the dEB s986, which has very different primary and secondary components, and includes a third light (chapter 4).

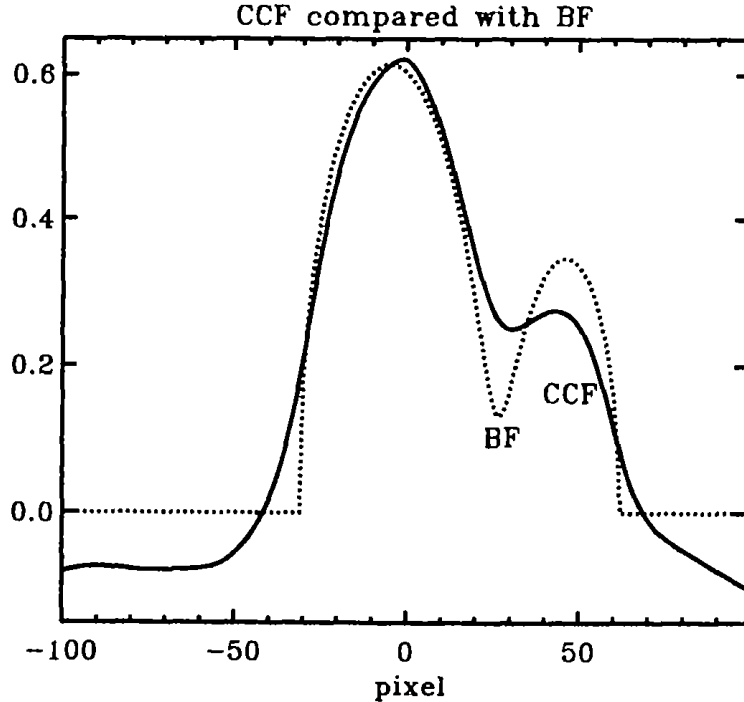


Figure 2.1: Comparison of the broadening function (BF) the the cross correlation function.

2.6.3 Broadening function (BF)

Rucinski (1992, 2002, 2004) introduced the method of broadening function to overcome some of the shortcomings of the cross correlation. In this method, the broadening function $BF(x)$ is calculated to satisfy the relation

$$f = BF * g \quad (2.6)$$

between the template spectrum g and the observed spectrum f (* denotes convolution). If the observed spectrum corresponds to a Doppler shifted template or to a superposition of them for each component, then BF is a shifted Dirac delta-function, or a sum of them. For real observations the dEB components will correspond to broadened template spectra due to instrumental and/or rotational broadening. For a given f and chosen g , equation 6 can be solved with respect to BF using the method of singular-value decomposition. The position of the peak(s) of BF gives the instantaneous Doppler-shift(s) of the observed spectrum. The width of the peak of BF , which unlike the cross correlation is not quadratic in the line profile, yields information about the broadening of lines in f . Because of the narrower peak widths compared to a cross-correlation, this method is better at determining radial velocities, than a cross correlation when the components of the dEB are close in radial velocity, see Fig. 2.1.

However, the problem of the proper choice of the template is still open in this method, though not as important as in the method of cross-correlation. Therefore this method can handle any number of components, but it is assumed that they can all be described by the same template when it comes to relative line strengths. To remove noise from the BF , Rucinski suggests to convolve the BF with a smoothing Gaussian of width corresponding to the spectrograph resolution, since features smaller than this would not be observed anyway. For fast rotating stars observed at low S/N this may still not lead to a smooth BF , and it may be advisable to select a Gaussian with larger width. However, it should be remembered that the spectrograph resolution has already made its imprint on the BF through the observed spectrum.

In a rigid body approximation of a rotating star, the theoretically expected BF is (Kaluzny et al. 2006b):

$$BF_{rot}(v) = A[(1 - \beta)\sqrt{1 - a^2} + \frac{\pi}{4}\beta(1 - a^2)] + C \quad (2.7)$$

$$a = \frac{v - v_{rad}}{v_{rot} \sin i} \quad (2.8)$$

where A is a normalization constant, β is the linear limb darkening coefficient, C is the continuum level, v_{rad} is the radial velocity of the star, v_{rot} is the linear velocity on the equator of the rotating star, and i is the inclination angle between the axis of rotation and the direction to the observer.

When using the observed BF to measure the projected rotational velocity $v \sin i$ of a star one needs to fit the BF with this equation convolved with two Gaussians, one with the width of the spectrograph resolution and one with the width of the smoothing Gaussian. Measuring the radial velocity of a BF peak can be done either by fitting a Gaussian or the above equation 7. For slowly rotating stars with $v \sin i$ below the spectrograph resolution a Gaussian gives the best result, but even faster rotating stars observed at low S/N may not show their rotational profile in the BF and such cases should also be fit with a Gaussian. Faster rotating stars which show their rotational profile in the BF should of course be fit using equation 7, not forgetting to convolve it with the two Gaussians. It should also be noted that since the width of the smoothing Gaussian can be chosen freely, one can choose the width resulting in the smallest order-to-order radial velocity scatter, if an echelle spectrograph has been used for the observations.

The BF is a measure of the mean line profile in a star. For a spectrum with two components the difference in equivalent widths between each component peak therefore measures the light ratio. Fitting the observed BF s with a rotational profile convolved with two Gaussians and integrating the area under each peak measures the ratio of equivalent widths between components. If the stars have identical spectral types this ratio measures directly the light ratio. If the spectral types are not identical, corrections are needed to take into account equivalent width differences due to different temperatures and surface gravities. This measure of light ratio can be very useful for measuring radii of eclipsing binaries with small orbital eccentricities without a total eclipse. For such systems the ratio of the radii is not well constrained by the light curve but is highly correlated with the luminosity ratio, and therefore an externally measured light ratio will improve the accuracy of the radii measurement. However, in order to use a spectroscopically measured light ratio this way, one needs to use a spectral wavelength region which corresponds to the photometric filter used for the light curve, and this is not always possible. One should also be aware that real stars are not rigid bodies and limb darkening is not too well understood, and these assumptions will limit the obtainable accuracy of a spectroscopic light ratio measurement.

A further use of the BF was introduced by myself and used for the first time for dEBs in NGC 6791 (chapter 3). It concerns the measurement of the radial velocity zero-point. Spectra are usually wavelength calibrated using a ThAr lamp spectrum. If this spectrum is not taken immediately after the stellar spectrum, changes to the instrument due to e.g. different orientation, temperature or pressure will have shifted the wavelengths in the ThAr lamp spectrum relative to the stellar spectrum and this introduces an offset. For high precision radial velocity measurements it is therefore advisable to always take the ThAr spectrum right before or after the science spectrum to avoid such an offset. However for slit spectrographs there is another problem, which one can not avoid when using a ThAr lamp for wavelength calibration. If the starlight is not **exactly** centered across the spectrograph slit, this effectively causes the

starlight to have an incident angle, which shifts the spectrum in wavelength relative to a star perfectly centered across the slit. Since the light from the ThAr lamp does not enter the spectrograph with this angle, it instead looks like the star changed its radial velocity. Note that for wavelength calibration using an iodine absorption cell, this problem does not exist, because the iodine absorption lines follow the same light path as the star light. But for faint cluster dEBs, one wants to avoid using an absorption cell, since that reduces the already low S/N in the spectrum. However, telluric absorption lines also follow the star light. My procedure to correct for the shift, caused by imperfect slit centering, using the BF , is therefore the following: Locate a spectral order which contains very strong telluric absorption lines (e.g. $\lambda = 6276 - 6299$). Measure the stellar BF profile in the adjacent orders, since it is next to identical for closeby orders. Convolve a synthetic stellar template spectrum covering the wavelength region with telluric absorption lines with the obtained BF , to produce the expected stellar spectrum in that order. Multiply this with synthetic telluric spectra which are broadened to the spectrograph resolution, shifted in radial velocity from -3 to +3 km/s in small steps of 50 m/s, and modified in line strengths. Cross-correlate the resulting set of artificial spectra of stellar+telluric lines with the observed spectra. The one giving the highest cross correlation determines the shift of the telluric lines. This shift is the radial velocity zero-point correction, since the telluric absorption lines are always at zero radial velocity (except for very small shifts due to wind in the Earth's atmosphere at the level of ≈ 10 m/s), and the observed shift can only be caused by the before mentioned imperfect slit centering or a bad wavelength calibration. Note that if the stars did not have any lines in the region of the telluric absorption lines, a simple cross-correlation with a synthetic telluric spectrum would have measured the radial velocity zero-point, but since we usually observe a combination of stellar and telluric lines, we have to follow the above procedure.

2.6.4 Spectral disentangling and iterative subtraction methods

The method of spectral disentangling produces both the radial velocities and the spectra of the individual dEB components. To understand the method let us start by looking at a much simpler method called direct subtraction. Two spectra, S_1 and S_2 of a dEB observed at different phases are used, and the radial velocities of the components at each phase are assumed known. If the spectra of the individual components are A and B , then

$$S_1(x) = A(x - v_{A1}) + B(x - v_{B1}) \quad (2.9)$$

$$S_2(x) = A(x - v_{A2}) + B(x - v_{B2}) \quad (2.10)$$

From these equations we can calculate the spectra of each component recurrently

$$A(x) = A(x - v_{A1} + v_{A2} + v_{B1} - v_{B2}) - S_1(x + v_{A2} + v_{B1} - v_{B2}) + S_2(x + v_{A2}) \quad (2.11)$$

$$B(x) = B(x - v_{A1} + v_{A2} + v_{B1} - v_{B2}) - S_2(x - v_{A1} + v_{A2} + v_{B1}) + S_1(x + v_{B1}) \quad (2.12)$$

starting from a wavelength, where the spectra of both components can be approximated by continuum, and proceeding towards groups of spectral lines. The main disadvantage of this method is the fact, that owing to the recurrent procedure of solution, the influence of random observational noise (which should be added on the right-hand sides of Eqs. (9) and (10)) is cumulative, so that after passing a group of spectral lines the solution can deflect from the correct value of the continuum. The influence of the noise can be reduced by averaging results of solutions obtained from a larger number of pairs of exposures. However, this suggests to develop a method searching for the best fit to a higher number of observed spectra, so that the solutions A and B of the corresponding system of linear equations would be overdetermined. This would also allow a solution without having to know the radial velocities in advance.

The first method enabling such a simultaneous decomposition of the spectra of binaries and simultaneous measurement of their radial velocities, or actually a direct solution of orbital parameters, was published by Simon & Sturm (1994). They called the method spectral disentangling. This method, which works in the wavelength domain, has been applied on real data in several studies. A similar method, which does the decomposition from Fourier transforms of observed spectra is implemented in the program KOREL (Hadrava 1995). This makes the solution numerically easier and enables further generalizations (e.g. Hadrava 1997, 2004). One interesting generalization is to include a component with variable line strength, which enables the (only approximate!) removal of telluric lines as part of the fitting procedure. These disentangling methods have the advantage that they do not use a template spectrum, and therefore one does not depend on knowing the stellar spectral types up front. This has been used as an argument why disentangling is superior to other methods. However when working with relatively few spectra of low S/N, which is usually the case for faint cluster member dEBs, it is questionable whether this procedure produces better results than the more simple iterative subtraction method I describe next. This method was nicely outlined by González & Levato (2006) who refers to it as spectral disentangling, though some will disagree, since this method does rely on template spectra. The idea is that the component spectra A and B can be found iteratively from the combined dEB spectra S from the equations

$$A^j = \langle S_i(x + v_{a,i}) - B^{j-1}(x - v_{b,i} + v_{a,i}) \rangle_i \quad (2.13)$$

$$B^j = \langle S_i(x + v_{b,i}) - A^j(x - v_{a,i} + v_{b,i}) \rangle_i \quad (2.14)$$

where $\langle \rangle_i$ denotes averaging over all observed spectra. Only a few iterations in j are needed to reach convergence. First estimate radial velocities are needed up front (as in ALL disentangling methods!), but new radial velocities can be measured iteratively by subtracting the calculated A and B spectra, respectively, from each observed spectrum, leaving only the other component in the spectrum. Because of this, separate template spectra can be applied for each component and therefore the method will work with components of different spectral types. Although the method is only described for two components it is easily generalised to three or even more components. One is also free to choose the method of determining the radial velocities. Since no publicly available program exist for this method, I implemented these ideas in an IDL program generalising it to three components (useful for dEBs with a third light) and using the BF for the radial velocity measurements. These disentangling methods have the disadvantage that they can not properly reconstruct features which are wider than the maximal radial velocity changes between the observed spectra, and therefore wide lines and continuum regions are not always well recovered. For low S/N spectra where the continuum normalisation is already not too good, this can give rise to rather large low frequency modulation in the separated spectra, which may also affect the precision of the radial velocity measurements. Therefore, I prefer to use the BF for precise radial velocity measurements unless the component spectra are different, and use the disentangling only to separate the spectra for further spectral analysis. This was the approach used for the NGC6791 dEBs (chapter 3).

2.6.5 Combining orders

An echelle spectrograph provides the spectrum divided into many orders. While they can often be merged into a single spectrum, this is usually not done if the purpose is to obtain radial velocities. Instead each order is treated separately and the final radial velocity is taken as some mean of the radial velocity from each order. This is to avoid the errors introduced by combining orders. Treating each order separately also allows one to estimate the error of the final radial velocity from the spread of the individual order radial velocities, and in the case of the BF to

find the best width of the smoothing Gaussian as mentioned earlier. Zucker (2003) provided an approach to optimally combine individual order cross-correlations based on maximum-likelihood analysis. He later used the same approach to combine TODCOR projections in a method called Multi-order TODCOR (Zucker et al. 2003). The method can be used to combine any type of correlation function. The *BF* is however not a correlation function so for combining *BF*s some form of averaging must be done. I have used simple averaging but one could also consider weighted averaging according to e.g. S/N.

2.6.6 Selecting the method(s) to use

While many methods exist for determining radial velocities of stars, they have different strengths and weaknesses. Selecting the best method depends on the situation. Often a combination of methods will be the optimal approach. For eclipsing binaries, spectral disentangling is optimal, since it gives both radial velocities and the spectra of the components, and no (or little) systematic errors occur because of mismatch between the observed and an artificial template spectrum. However the method requires (relatively) many spectra of high S/N from different orbital phases and it remains to be seen whether good results can be obtained when one component is much weaker than the other. Therefore it is wise to combine spectral disentangling with either TODCOR or *BF* (or even both) to get a robust error estimation. Situations can also occur where spectral disentangling cannot be used because of the need of many spectra. This is the case when a few spectra are taken first to determine feasibility, before proceeding with the observations. Examples are dEBs with a large flux ratio, where it is uncertain whether the secondary can be seen in the spectra, or for determining whether the dEB is a cluster member. For the first case TODCOR is the obvious choice, since it can handle the fact that the spectra of the individual stars will also differ. The *BF* will be a good choice when the component stars are similar and/or in cases of blending of many (and unknown number of) spectra due to e.g. observing in crowded fields.

2.6.7 Additional considerations for radial velocity measurements

Because v is the relative radial velocity between the star and observer, part of it will come from the motion of Earth around the Sun. To allow comparison of radial velocities taken at different times, a correction is applied to the observed radial velocity, to make it a barycentric radial velocity, that is the radial velocity of the star as measured from the center of mass of the solar system. When very accurate radial velocities are needed, it should also be noted that the observed radial velocity is not only due to the motion of the star. Other effects like convective blueshift and gravitational redshift give a contribution to the observed radial velocity.

Convective blueshift is the decrease in wavelength caused by convective motions on the surfaces of stars. These convective motions cause stellar surfaces to be divided into columns of rising and falling gas, visible as the granulation effect on the surface of our Sun. The rising and falling components occupy roughly equal areas of a stellar surface but the convective velocities cause spectral lines to be blueshifted from rising columns and redshifted from falling columns. As the rising material is hotter, it is brighter, so it contributes more to the stellar flux, resulting in an overall blueshift. This shift is of the order of 1 km/s or less for main sequence (MS) stars. The magnitude of the effect is greater for intrinsically brighter stars and at shorter wavelengths but not known in detail.

Gravitational redshift is the increase in wavelength of photons caused by their escape from the gravitational potential of the star which emitted them. The term also encompasses the slight blueshift due to the photons falling into the gravitational potential well of the Sun and the Earth before being detected by observers. The gravitational redshift effect is of the order

of 1 km/s or less for MS stars. The radial velocity change due to gravitational redshift is given by

$$v_{grav} = \frac{GM}{Rc} \quad (2.15)$$

where G is the gravitational constant, M is the mass of the star, R is the radius of the star and c is the speed of light.

When determining the orbit of a dEB, these contributions to the radial velocity are unimportant for single-lined solutions (meaning that one component is dealt with at a time), since they result only in a shift of all the radial velocities. But for double-lined solutions they can become non-negligible since the shifts may not be of the same size for each component, and this will shift the velocities of the components relative to each other.

2.7 Spectroscopic Binary Orbit Program (SBOP) and reliable error estimates

Once the radial velocities have been obtained, the orbital elements including their errors can be found by fitting theoretical orbits to the observed radial velocities. One program for this, SBOP, written by P. B. Etzel, does this using one of several optimisation schemes based on differential corrections. It is known that internal errors from such procedures are sometimes too optimistic. In order to check the error estimates given by SBOP I developed a Monte Carlo based IDL wrapper program for SBOP for alternative error estimates. In one mode, this program calculates errors according to given input errors for the radial velocities. Based on my finding that, for slit spectrographs, a radial velocity zero-point error could be dominant (chapter 3), one can input both a zero-point error common to both components, and a random error different for each component. A potential problem with this approach is that one needs to know realistic values for these error contributions. My approach for finding these estimates is the following: I assume that the total radial velocity error for each measurement is a combination of a random error and a zero-point error. To separate the two I compare the radial velocity ($O - C$) rms error from SBOP single-lined solutions to the radial velocity rms error found from order-to-order measurement scatter. For each component I subtract the order-to-order error from the ($O - C$) error in quadrature and assume that the remaining error is the zero-point error. Finding a good agreement between components gives confidence that this is a good assumption. To be conservative I choose the largest of the two error measurements (one for each component) to be the zero-point error. With these error estimates I then run SBOP a larger number of times, every time adding to each original radial velocity measurement a Gaussian error contribution according to the order-to-order measurement scatter different for each component, and a Gaussian zero-point error contribution common to both components. From all these solutions, the rms is calculated to give the final error estimate. For the dEBs in NGC6791 (chapter 3) I found that, after my zero-point correction, these error estimates are in very good agreement with the internal errors given by SBOP indicating that the SBOP errors are trustworthy, except when large epoch-to-epoch zero-point offsets are present. Other alternative error estimates from the IDL program are so called jack knife estimates. Two different jack knife estimates are calculated. Here SBOP solutions are calculated for all possible combinations of leaving out one or two epochs of observations. The jack knife estimate is then again the rms of the solutions. This error estimate was found to be much smaller than both the SBOP error estimate and the above Monte Carlo error estimate, and therefore not reliable. This is in fact not surprising, since the different solutions found this way are not independent. Others have noted this, but never the less some people still use such unreliable jack knife errors (see Mantegazza et al. 2010 for one example) thus underestimating the true errors on the

spectroscopic elements. I therefore included another jack knife error estimate, which is instead one half times the maximum minus the minimum value of all the jack knife solutions. This error estimate will of course be dependent on the total number of radial velocity measurements, and should in fact be calibrated on artificial data, which I intend to do in the future. However I found that for the NGC 6791 dEBs, this estimate gave only slightly larger error estimates than the SBOP program, which again signals that SBOP gives realistic error estimates.

2.8 Photometry and radii determination

The variation of the apparent brightness of the eclipses of a dEB depends on the geometry of the system including the direction from which it is viewed, the variation of effective temperatures over the surfaces of the stars, and the characteristics of the mutual orbit of the two stars. Additional complications can arise from contaminating light, coming from a third star orbiting the dEB or possibly due to an entirely unrelated foreground or background star along the line of sight.

The light curve of the eclipses is produced by the method of differential photometry: Images are taken continuously during the eclipses and the difference between the light from the dEB and light from one or more reference stars is calculated for each image. Once the light curve has been produced, a light curve analysis program, e.g. EBOP (Eclipsing Binary Orbit Program), is used to retrieve the inclination i and the radii in units of a .

2.9 Optimising the use of telescope time

Quite a large amount of telescope time is needed for measuring accurate parameters of a dEB. Therefore a lot of telescope time can be saved when multiple dEBs can be observed at the same time. This is the case when multiple cluster member dEBs have been located. Photometry to be used for light curves can be scheduled on nights where more than one dEB shows eclipses, and even the ones not showing eclipses will have useful measurements, since it is important to know whether the out-of-eclipse light curve is flat or shows signs of magnetic activity or other variability. Such an optimal observing strategy is of course only possible if the observatory allows scheduled observing. Luckily this is the case for some telescopes, like the Nordic Optical Telescope. This strategy was followed for the observations of the dEBs in NGC6791 (chapter 3). Spectroscopy to be used for radial velocity measurements can also be done for multiple dEBs at a time using a multi-object spectrograph, e.g. FLAMES at the Very Large Telescope. FLAMES has an integral field unit (IFU) mode, where 15 IFUs covering about $2'' \times 3''$ can be placed in a field of view of $25'$ diameter. This means that up to 15 dEBs can be observed at the same time, and since each IFU is rather large this can even be done in poor seeing conditions. I introduced this approach for determining membership, periods and minimum masses for all known cluster member dEB candidates in the open clusters NGC2243 and NGC2506 (with preliminary results in chapter 4).

2.10 Exploiting all cluster member dEBs

Although it will be shown that cluster member dEBs are quite common, every system is valuable and should be exploited. This can be a challenge in some cases. Sometimes a so-called third light from an additional star appears in the light curve and spectra of the dEB. Although this could be a third member of a triple system, it is usually just a single star close to the line of sight. This will be the case more often for cluster member dEBs than for field star dEBs because

of the increased crowding in the cluster field. Since the amount of contaminating third light can not be determined from the analysis of the dEB light curve (Southworth 2010), other methods must be used to measure it. High resolution imaging with the Hubble Space Telescope or Lucky Imaging from the ground can separate the third light from the dEB in some cases when they are not too close. This was the case for V20 in NGC6791 (chapter 3). For cluster member dEBs one can also try to exploit the CMD by seeking a solution where the total light from the dEB and third light is constrained to be shared among three stars on the cluster fiducial. This was done by Grundahl et al. (2008b) for V20 in NGC6791, but unfortunately they underestimated the error (chapter 3), which shows that one has to be very careful using such a procedure.

Another potential problem is that sometimes the secondary star is so much fainter than the primary that the spectral lines of the secondary are not seen in the dEB spectra. Without radial velocity measurements for both components, the masses can not be measured. In some cases the difference in magnitude between components is so large that nothing can be done to circumvent this problem. But since for main sequence stars the fainter component is also the reddest one, the light ratio will be less extreme in the infrared. By observing in the infrared the secondary may therefore be visible. This is the approach followed for the dEB s986 in M67 (chapter 4).

Chapter 3

Demonstrating the potential of cluster member dEBs

This chapter demonstrates the potential of using multiple cluster member detached eclipsing binaries for new insights into stellar clusters and stellar evolution. This is done in the article: "Age and helium content of the open cluster NGC 6791 from multiple cluster member eclipsing binaries. I. Measurements, methods and first results." - submitted to A&A.

Age and helium content of the open cluster NGC 6791 from multiple eclipsing binary members ★ ★★

I. Measurements, methods, and first results.

K. Brogaard¹, H. Bruntt¹, F. Grundahl¹, J.V. Clausen², S. Frandsen¹, D. A. Vandenberg³, and L. R. Bedin⁴

¹ Department of Physics and Astronomy, Aarhus University, Ny Munkegade, DK-8000 Aarhus C, Denmark

² Niels Bohr Institute, Copenhagen University, Juliane Maries Vej 30, DK-2100 Copenhagen Ø, Denmark

³ Department of Physics and Astronomy, University of Victoria, P.O. Box 3055, Victoria, B.C., V8W 3P6, Canada

⁴ Space Telescope Science Institute, 3700 San Martin Drive, Baltimore, MD 21218, USA

Received xx XX 2010 / Accepted xx XX 2010, version 04.03.2010

ABSTRACT

Context. Models of stellar structure and evolution can be constrained by measuring accurate parameters of detached eclipsing binaries in open clusters. Multiple binary stars provide the means to determine helium abundances in these old stellar systems, and in turn, improved age estimates.

Aims. Grundahl et al. (2008) measured masses and radii of the detached eclipsing binary V20 in the open cluster NGC 6791, accurately enough to demonstrate that there are significant differences between current stellar models. Here we improve on those results and add measurements of two additional detached eclipsing binaries, the cluster members V18 and V80. The enlarged sample sets much tighter constraints on the properties of stellar models than has hitherto been possible, and therefore leads to an improvement in both the accuracy and precision of the cluster age.

Methods. We employ high-resolution UVES spectroscopy of V18, V20 and V80 to determine their spectroscopic effective temperatures, [Fe/H] values, and spectroscopic orbital elements, and time-series photometry from the Nordic Optical Telescope to obtain the photometric elements.

Results. The masses and radii of the V18 and V20 components are found to high accuracy, with errors on the masses in the range 0.27 – –0.36%, and errors on the radii in the range 0.61 – –0.92%. V80 is found to be magnetically active, and more observations are needed to determine its parameters accurately. The metallicity of NGC 6791 is measured from disentangled spectra of the binaries and a few single stars to be [Fe/H] = +0.29 ± 0.03 (random) ± 0.07 (systematic). The cluster reddening and apparent distance modulus are found to be $E(B - V) = 0.160 \pm 0.025$ and $(m - M)_V = 13.51 \pm 0.06$. A first model comparison shows that we can constrain the helium content of the NGC 6791 stars, and thus reach a more accurate age than previously possible. It may be possible to constrain additional parameters, in particular the C, N and O abundances. This will be investigated in paper II.

Conclusions. Using multiple detached eclipsing binaries for determination of stellar cluster ages, it is now possible to constrain parameters of stellar models, notably the helium content, which were previously out of reach. By observing a suitable number of detached eclipsing binaries in several open clusters it will be possible to calibrate the age–scale and the helium enrichment parameter $\Delta Y/\Delta Z$, and provide firm constraints which stellar models must reproduce.

Key words. Open clusters: individual NGC 6791 – Stars: evolution – Stars: binaries: spectroscopic – Stars: binaries: eclipsing – Techniques: spectroscopy – Techniques: photometry

1. Introduction

The open cluster NGC 6791 is interesting for several reasons. The main scientific motivation for studying this cluster is that it is one of the oldest and, at the same time, one of the most metal-rich open clusters known (Origlia et al. 2006; Carretta et al. 2007; Anthony-Twarog et al. 2007), and thus it is of great importance for our understanding of chemical evolution. In addition, it is a particularly populous open cluster, with stars in all stages of evolution from the main sequence to the white dwarfs

(King et al. 2005; Bedin et al. 2005, 2008) as well as containing numerous variable stars (Bruntt et al. 2003; Mochejska et al. 2002; de Marchi et al. 2007).

Despite a number of studies that have presented well-calibrated photometry and high-precision color-magnitude diagrams (CMDs) (King et al. 2005; Stetson et al. 2003, hereafter SBG03), the age of NGC 6791 has until recently remained very uncertain because of correlated uncertainties in distance, reddening, color-temperature transformations, and metallicity.

It is widely appreciated that detached eclipsing binaries offer the possibility to determine accurate (and precise) masses and radii for the system components, nearly independent of model assumptions (Andersen 1991; Torres et al. 2010). If the binary resides in a star cluster, and one or both of its components are close to the turn-off, it is possible to put tight constraints on the age of the system through a comparison of the position of the primary and secondary in a mass–radius (MR) diagram to theo-

Send offprint requests to: K. Brogaard, e-mail: kfb@phys.au.dk

* Based on observations carried out at the Nordic Optical Telescope at La Palma and ESO's VLT/UVES ESO, Paranal, Chile (75.D-0206A, 77.D-0827A, 081.D-0091).

** Tables 11–22 are only available in electronic form at the CDS via anonymous ftp to cdsarc.u-strasbg.fr (130.79.128.5) or via <http://cdsweb.u-strasbg.fr/cgi-bin/qcat?J/A+A/>

Table 1. Names and coordinates for the eclipsing binaries.

Name	Alternative name	RA(2000.0)	DEC(2000.0)
V18	v565 Lyr	19 : 20 : 49.38	+37 : 46 : 09.3
V20	v568 Lyr	19 : 20 : 54.30	+37 : 45 : 34.7
V80	–	19 : 21 : 06.48	+37 : 47 : 27.8

retical isochrones. For stellar clusters, such an analysis has some significant advantages: the determination of the masses and radii is independent of the usual uncertainties such as reddening and distance. Furthermore, since the comparison to models is carried out in the MR diagram, one avoids the difficult process of transforming the effective temperatures and luminosities of the models to observed colors and magnitudes. Thus, a determination of cluster ages in the MR diagram allows a direct confrontation between observations and theory.

Grundahl et al. (2008; hereafter GCH08) showed that using this method, with their measurements of the cluster member eclipsing binary V20, they could determine a precise cluster age with an error of only ± 0.3 Gyr for a given stellar model. However, despite this they were unable to determine which of the models (if any) to trust, because the difference in predicted age due to the specific stellar model adopted was about four times larger than their measurement precision.

Here we undertake an analysis of three detached eclipsing binary systems, V18, V20 and V80, in NGC 6791, and determine accurate masses and radii for the components of two of the systems. We also measure spectroscopic T_{eff} and $[\text{Fe}/\text{H}]$ values from disentangled spectra of the binary stars. This is used, together with the cluster CMD, to demonstrate how multiple cluster member eclipsing binary measurements constrain stellar models and cluster parameters, like age and helium content, better than previously possible.

2. Targets

The detached eclipsing binaries analysed here are V18, V20 and V80, with names, alternative identifications, and coordinates given in Table 1, along with finding charts in appendix A. These systems were first identified as eclipsing binaries by Rucinski et al. (1996) (V18 and V20) and Bruntt et al. (2003) (V80). Their locations in the $(B - V)$, V CMD are shown in Fig. 1.

3. Photometry

The photometric data for V18 and V80 consists of V (Johnson) and R (Cousins) CCD observations from the 2.56m Nordic Optical Telescope (NOT) and its ALFOSC instrument. In order to reduce the readout time, while still including both V18 and V80 in each frame, we limited the readout section of the CCD to half its full size, thus covering a field-of-view of $6'28'' \times 3'12''$. We refer to the telescope homepage for further information about the ALFOSC instrument¹.

Observations were carried out on 9 nights between May and August 2009. Most observations were obtained on nights when both systems showed eclipses, in order to make efficient use of telescope time, resulting in a total of 580 and 538 exposures in V and R , respectively. For all observations we employed an exposure time of 240s in V and 180s in R . The photometric data

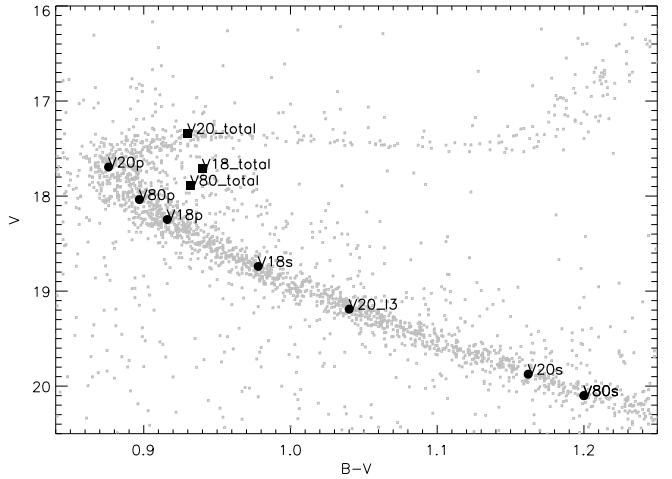


Fig. 1. The eclipsing binaries V18, V20 and V80 in the CMD of NGC 6791. Squares are the total system light, for V20 including a third light (l_3). Circles are the individual components as determined in this paper. p , s , and l_3 indicate primary, secondary, and third light components, respectively.

for V20 used in this paper are the same as those by GCH08. We note that this data set also contained an egress of the primary eclipse of V18, which was missed during the 2009 campaign, thereby allowing us to obtain complete coverage of both eclipses and better out-of-eclipse coverage in the V light curve for this object.

The bias frames and flat fields, used in the data reduction, were obtained during evening twilight on each observing night. All photometry was carried out with DAOPHOT/ALLSTAR/ALLFRAME (Stetson 1987, 1994) and transformed to a common coordinate system using MATCH and MASTER (P. Stetson, private comm.). Each frame was processed using a point-spread function (PSF) calculated from about 200 of the brightest stars in the field.

3.1. Light curves and standard indices

With the instrumental photometry in hand, we proceeded to transform the observations to the V and R standard system using the same methodology as in GCH08. SBG03 put a large effort into the transformation of BVI magnitudes onto the standard system, and we have used the available V photometry from this source as internal standard stars. For each frame, a linear transformation from instrumental magnitudes to standard magnitudes was calculated, using $(B - I)$ (available from SBG03 for all stars in the field) as the color term. Subsequently we averaged the coefficient for the color term for all frames (for a given filter) and used this for the final determination of the zeropoint for each frame. The BVI photometry listed in Table 2 is therefore on the same system as SBG03. The accuracy of the photometric zeropoint is in the range $0^{\text{m}}01$ to $0^{\text{m}}02$ as mentioned in SBG03. Our source for R standard magnitudes was the photometry by Mochejska et al. (2005), as downloaded from the PISCES homepage². Apart from the different source of standard magnitudes, the procedure followed was identical to that for V . We note that Mochejska et al. (2005) reports an offset in their V photometry of 0.047 relative to SBG03, and therefore the $(V - R)$ colors in Table 2 may not be very accurate.

¹ <http://www.not.iac.es>

² <http://users.camk.edu.pl/mochejsk/PISCES/data.html>

The V and R light curves of V18 and V80 are listed in Tables 11–14. A few obvious outliers and systematically deviating measurements at dusk and dawn have been removed. V light curves of V18, V20 and V80 are shown in Fig. 2–4 with phases calculated from the ephemerides given in Eqs. 1–3 (Sect. 3.4). For V20 we reuse the light curves from GCH08. In the top panels, all systems are shown on the same scale for easy comparison.

Throughout the paper, the component eclipsed at the deeper eclipse at phase 0.0 is referred to as the primary (p), and the other as the secondary (s) component.

V18 and V20 are seen to be well detached with a practically constant light level outside eclipses, while V80 shows signs of magnetic activity, most likely due to its shorter orbital period. For V20 and V80 the secondary eclipse occurs at phase 0.50, and the eclipses are of equal duration, indicating that their orbits are circular. V18 has a slightly eccentric orbit, as seen by the offset from phase 0.5 of the secondary eclipse.

3.2. A new measurement of the third light component of V20

For V20, a very close companion is included in the light curves, meaning that a significant amount of third light is present. GCH08 estimated the amount of third light by finding a solution where the total light of the system is shared among three stars constrained to lie on the cluster main sequence. However, they also mention that high-resolution imaging would allow a direct determination of the contribution to the total light from the third star. We therefore identified V20 in ACS images from the Hubble Space Telescope (*HST*), measured the magnitudes of the light emitted by the third star, which is well separated from the binary, and transformed the resultant magnitudes in the *HST* filters to V and I . To accomplish the latter, we selected stars bearing the closest similarity to the third light that we could find; specifically, stars within 0.003 mag in the ($m606 - m814$) color index and within 0.05 mag in $m606$. The four twins to the third light that were identified this way, in our *HST* photometry, were located in the ground-based observations of SBG03, from which their B , V , and I magnitudes were determined.

The mean and rms spread of these four stars is our measurement of the third light magnitudes in these bands. We find $B = 20.23 \pm 0.01$, $V = 19.19 \pm 0.01$ and $I = 18.12 \pm 0.01$. Since we only have four stars these error estimates could be underestimated and we therefore conservatively adopt an error of ± 0.02 for all bands. From these and the magnitudes of the combined light of V20 we calculated the third light contribution to V20, $l_3 = \frac{L_3}{L_p + L_s + L_3}$, which is 0.164 ± 0.004 in B , 0.182 ± 0.004 in V and 0.197 ± 0.004 in I . Note that these values are significantly higher and much more accurate than 0.146 ± 0.022 in V and 0.168 ± 0.025 in I as found indirectly by GCH08.

3.3. Standard photometry of the binary components

Standard, out-of-eclipse, B , V , R , I photometry for the binaries is listed in Table 2 together with calculated individual photometry for the stars from their light curve solutions and, in addition for $B - V$, the assumption that all stars of each system are located on the cluster CMD fiducial (as done for V20 in GCH08). For V80 the colors are calculated using only this assumption, which results in $L_s/L_p = 0.15 \pm 0.05$ in V , since the light curve does not constrain the light ratio of this system.

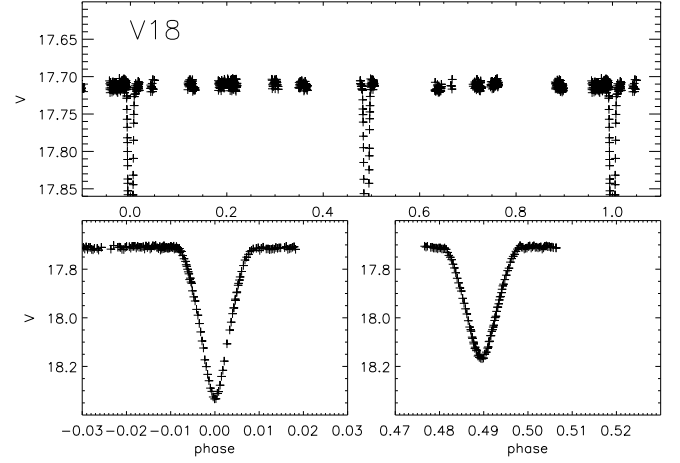


Fig. 2. Phased V light curve for V18. The secondary eclipse is shifted away from phase 0.5, showing that the orbit is eccentric.

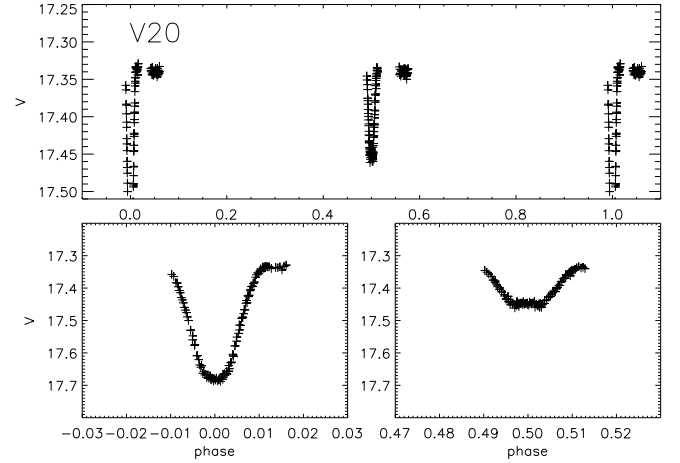


Fig. 3. Phased V light curve for V20 from GCH08. The secondary eclipse is at phase 0.5 indicating that the orbit is circular. The secondary eclipse is total.

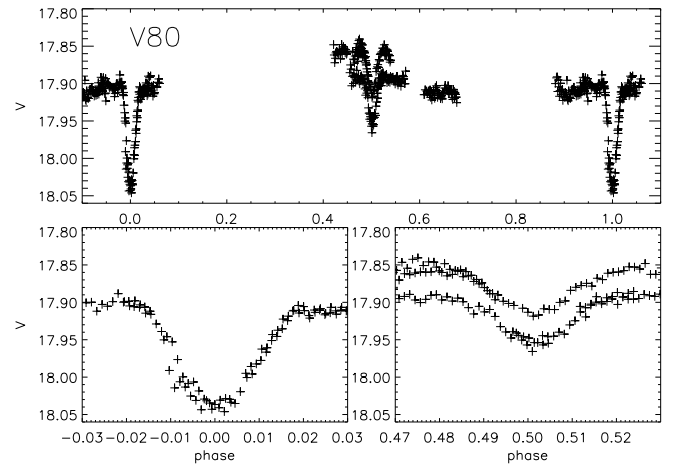


Fig. 4. Phased V light curve for V80. The secondary eclipse is at phase 0.5, indicating that the orbit is circular. Variations in the overall magnitude level indicate magnetic activity.

Table 2. Standard photometry for the eclipsing binaries and their components.

Name	V	$B - V$	$V - R$	$V - I$
$V18_{total}$	17.713	0.940	0.505	0.990
$V18_{primary}$	18.247	0.916	0.478	-
$V18_{secondary}$	18.740	0.978	0.546	-
$V20_{total}$	17.340	0.930	-	0.985
$V20_{primary}$	17.695	0.876	-	0.923
$V20_{secondary}$	19.874	1.162	-	1.246
$V20_{l_3}$	19.190	1.040	-	1.070
$V80_{total}$	17.886	0.932	-	1.015
$V80_{primary}$	18.037	0.897	-	-
$V80_{secondary}$	20.100	1.200	-	-

NOTE 1: The reason some color indices are missing is that we do not have light curves and light ratios for all systems in all colors. For $(B - V)$ we have calculated the color indices by finding solutions where all components are constrained to the main sequence. This is done to be able to put all systems on the same CMD (Fig. 1).

3.4. Periods and ephemerides

For V20 we adopted the ephemeris of GCH08. For V18 and V80 we produced phased diagrams adding small shifts to the spectroscopic periods in order to determine the best initial estimates for the periods and ephemerides. We used these initial estimates to determine both the epoch and the period from analysis of our V and R light curves (see Sect. 3.5). For each system the periods obtained from the two light curves agree well and are very close to the initial estimates.

We adopt the following linear ephemerides for all analysis in this paper:

$$\text{Min I (V18)} = 2454651.4506 \pm 1 + 18^{\text{d}}798638 \pm 10 \times E \quad (1)$$

$$\text{Min I (V20)} = 2453151.6061 \pm 9 + 14^{\text{d}}469918 \pm 25 \times E \quad (2)$$

$$\text{Min I (V80)} = 2454652.3045 \pm 13 + 4^{\text{d}}88594 \pm 16 \times E \quad (3)$$

3.5. Photometric elements

V18 and V20 are well detached systems with no signs of out-of-eclipse variability. Furthermore, the components of each system are small relative to their separation. Thus, they are well suited for accurate measurements. The light curves of V80 show signs of magnetic activity (Fig. 4), and more observations are needed before we can hope to obtain precise and accurate photometric elements for this system. However, since we can already get a good measurement of $\log g$, which is useful for the further spectroscopic study, we include preliminary dimensions of this system as well.

We adopted the simple Nelson-Davis-Etzel model (Nelson & Davis 1972; Etzel 1981) for the light curve analysis. It represents the deformed stars as biaxial ellipsoids and applies a simple bolometric reflection model. We have used the corresponding JKTEBOP³ code, which is a revised and extended version of the original EBOP code (Etzel 1981). The Levenberg-Marquardt minimization algorithm (MRQMIN; Press et al. 1992) is used for

the least-squares optimization of the parameters, and the code has been extended to include non-linear limb darkening and adjustment of epoch and orbital period. We made use of important new features in the latest version, namely the possibility to fit the light curve simultaneously with an externally determined light ratio (Southworth et al. 2007), a third light ratio (Southworth 2010), and $e \sin \omega$ and $e \cos \omega$ (Southworth et al. 2009), including their errors. In some of its modes, JKTEBOP performs Monte Carlo simulations (Southworth et al. 2004a, 2004b) and residual shift analysis (Southworth 2008), which we used to assign realistic errors to the photometric elements.

The magnitude at quadrature was always included as a free parameter, and the phase of primary eclipse was allowed to shift from 0.0. In initial JKTEBOP analysis, the epoch and orbital period were included as free parameters and then fixed at the values given in Eqs. 1–3. A circular orbit was assumed for V20 and V80. The mass ratios, q , between the components were kept at the spectroscopic values (Table 6). Gravity darkening coefficients corresponding to convective atmospheres were applied, and the simple bolometric reflection model built into JKTEBOP was used. Tests showed that these assumptions have negligible effect on the derived photometric elements.

The procedure we followed in order to minimize the errors related to limb darkening deserves some attention. It is well known that the linear limb-darkening law is a poor fit to both the observed limb darkening of the Sun and that predicted by theoretical model atmospheres. We therefore adopted a non-linear limb-darkening law, more precisely the square root law, since according to Van Hamme (1993) this gives the best fit to stellar atmospheres in the temperature range of these binary stars. Theoretical coefficients to be used with the square root law for a given star have been calculated by several authors using 1D stellar atmospheres (e.g. van Hamme 1993; Claret 2000). They all depend on the T_{eff} , $\log g$, and $[\text{Fe}/\text{H}]$. Furthermore, they depend on the stellar atmosphere model used for the calculation. To make things more complicated it has been shown that 1D stellar atmospheres do not reproduce the limb darkening of the Sun (Sing et al. 2008), and therefore theoretical limb-darkening coefficients will be inaccurate in any case. In order to minimize the errors related to these facts, the optimal approach would be to fit the coefficients as part of the light curve solutions, instead of fixing them at theoretical values. But most light curves, including ours, are not of sufficient quality to fit for both a linear and non-linear coefficient for both stars. Instead we exploit a fact demonstrated by Southworth et al. (2007) that for the square root law, the linear and non-linear coefficients are highly correlated. Therefore, by fixing one coefficient and fitting for the other, errors will tend to compensate for one another. This is the approach we adopted, since it allowed us to use a non-linear law while minimizing dependence on the model and the exact stellar parameters.

In the text and tables with photometric solutions we use the following symbols: i orbital inclination; $r_p = R_p/a$; relative radius of primary; r_s relative radius of secondary; $k = r_s/r_p$; J central surface brightness ratio; L luminosity; l_3 third light fraction; e eccentricity; ω longitude of periastron.

3.5.1. V18 photometric elements

Our first photometric solutions for V18 showed that k is not well constrained by the light curve without additional external constraints. This is typical for a system with a slightly eccentric orbit without a total eclipse. We therefore found solutions for the V band light curve which simultaneously fit the light curve

³ <http://www.astro.keele.ac.uk/~jkt/>

Table 3. Photometric solution for V18 from the JKTEBOP code.

Parameter	Value
Spectroscopic constraints	
$L_s/L_p(V)$	0.636 ± 0.020
$e \sin \omega$	0.09987 ± 0.00110
Measured parameters	
i (°)	89.3768 ± 0.0215
$r_p + r_s$	0.0560 ± 0.0002
$k = r_s/r_p$	0.8817 ± 0.0113
r_p	0.02975 ± 0.00018
r_s	0.02623 ± 0.00024
e	0.0193 ± 0.0006
ω	149.13 ± 2.77
$J_s/J_p(V)$	0.817 ± 0.018
$J_s/J_p(R)$	0.791 ± 0.074
$L_s/L_p(V)$	0.635 ± 0.016
$L_s/L_p(R)$	0.674 ± 0.042
σ (V-mmag.)	4.36

and spectroscopic values of $e \sin \omega$ and the light ratio (Sect. 4.1 and 4.2), including their errors. We could not repeat this procedure for the R band, since we have no spectroscopic measurement of the light ratio corresponding to this band. Therefore we adopt the V band solution for our final measurements. To get the R band surface-brightness ratio and luminosity ratio, we fit the R band light curve with the other parameters fixed from the V band solution. Table 3 shows our adopted photometric elements. Errors are determined using JKTEBOP Monte Carlo simulations, since residual shift errors indicated that correlated errors are not present at a significant level in the observed light curves. Square root limb-darkening coefficients from Claret (2000) for our spectroscopically measured metallicity and effective temperatures were used as a starting point. We followed the previously mentioned strategy of fixing either the linear or non-linear coefficient and solving for the other. The resulting elements remained identical to well below 0.01% whether we solved for the linear or non-linear coefficient. Further tests showed that fixing both the linear and non-linear limb-darkening coefficients instead of employing the spectroscopic $e \sin \omega$ constraint changes the relative radii by only 0.13% and 0.04% for the primary and secondary component respectively. This seems to suggest that at least in this case the theoretical limb-darkening coefficients are reliable. As seen in Table 3, the relative radii of V18 have been measured with errors of 0.6% and 0.9% for the primary and secondary components respectively.

3.5.2. V20 photometric elements

V20 was analysed by GCH08. However, we measured more directly and accurately the third light and found it to be outside their error estimate. We therefore performed a new analysis using their light curve. Table 4 shows our measured photometric elements for each band and our adopted solution. From the JKTEBOP Monte Carlo and residual shift solutions we found that significant correlated errors are present in the observed light curves, and we chose to adopt the larger residual shift errors as our error estimates. For the final parameters we adopted an er-

Table 4. Photometric solutions for V20 from the JKTEBOP code.

Parameter	V	I	adopted
i (°)	89.99 $+0.01$ -0.15	89.99 $+0.01$ -0.18	89.99 $+0.01$ -0.15
$r_p + r_s$	0.0700 ± 0.0005	0.0710 ± 0.0010	0.0702 ± 0.0005
k	0.559 ± 0.005	0.559 ± 0.008	0.560 ± 0.005
r_p	0.04491 ± 0.00040	0.04551 ± 0.00078	0.04501 ± 0.00040
r_s	0.02513 ± 0.00017	0.02546 ± 0.00026	0.02519 ± 0.00017
$J_s/J_p(V)$	0.414 ± 0.043		0.410 ± 0.043
$J_s/J_p(I)$		0.591 ± 0.074	0.590 ± 0.074
$L_s/L_p(V)$	0.134 ± 0.003		0.134 ± 0.003
$L_s/L_p(I)$		0.181 ± 0.005	0.181 ± 0.005
$l_3(V)$	0.182		0.182
$l_3(I)$		0.197	0.196
σ (mmag.)	4.6	6.8	

ror weighted mean of the light curve solutions from each band. Due to the systematics present, we do not allow the error of the adopted solution to be reduced by averaging the solutions from the two bands, but adopt the error from the V band as our final estimate. As seen in Table 4, relative radii of V20 have been measured with errors of 0.9% and 0.7% for the primary and secondary components respectively. Our measurement of $r_s = 0.02519 \pm 0.00017$ is two sigma larger than $r_s = 0.0248 \pm 0.0002$ found by GCH08. Although we also use a different limb darkening law than GCH08, this has minor effects on the solution. Our new measurement of the third light is the main reason we find a larger radius for the secondary.

3.5.3. V80 photometric elements

As mentioned earlier, V80 shows signs of magnetic activity in the light curve and more observations are needed for very accurate measurements. In any case, to obtain a measurement of $\log g$ to be used for T_{eff} and $[\text{Fe}/\text{H}]$ measurements, we did a preliminary light curve analysis for V80. To be specific, we first rectified the light curves. In Fig. 4 both primary and secondary eclipses are covered by observations from two different nights. As seen the overall magnitude level remained identical for the nights covering the primary eclipse while it changed between the two nights covering the secondary eclipse. However, the depth of the secondary eclipse did not change between nights. The rectification we employed was therefore to shift the one secondary eclipse coverage which was offset relative to the rest, so that all eclipse observations were aligned in magnitude. Then deviating out-of-eclipse observations were also shifted to match this magnitude level. We then found JKTEBOP solutions employing the V band light ratio determined from the CMD in Sect. 3.3. The results for the relative radii and inclination are shown in Table 5. Errors are based on solutions of the V band light curve varying the light ratio within the errors given by the external constraint

Table 5. Photometric solution for V80 from the JKTEBOP code.

Parameter	Value
Constraints from CMD	
L_s/L_p (V)	0.15 ± 0.05
Measured parameters	
i ($^\circ$)	84 ± 1
r_p	0.0900 ± 0.0054
r_s	0.0605 ± 0.0123

and on the level of consistency between V and R band solutions. As expected, the errors are much larger than for the other systems, in the range of 6-20%.

4. Spectroscopy

The spectroscopic observations were carried out in service mode with UVES at the ESO VLT during allocation periods 75+77 (V20) and 81 (V18 and V80). Since NGC 6791 is at declination $+37^\circ$, it can be observed at Paranal only at an airmass larger than 2.1. Therefore all observations were carried out during the short observing window of a few hours around meridian passage. Due to the faintness of the stars, and in order to minimize slit losses, a slit of $1''.20$ width, corresponding to a resolution of approximately 37 000, was used. For the observations of V18 and V20, the slit was aligned along the parallactic angle (ELEV mode), and the atmospheric dispersion corrector (ADC) was not inserted in the beam, since it causes a slight loss of flux. The procedure for V80 was different, since a fixed slit position allowed us to put an additional star on the slit together with V80, to be used for a metallicity measurement. The UVES standard 580nm setup, and on-chip binning of 2×2 pixels, was used for all observations. The corresponding wavelength ranges covered by the two CCD detectors employed in UVES are approximately 4775–5750Å and 5875–6830Å, respectively. The typical S/N per pixel for the red chip was between 15 and 25. A total of 13, 15, and 10 usable epochs were obtained for V18, V20 and V80, respectively, each followed by a ThAr exposure for wavelength calibration.

We used the UVES pipeline to reduce the spectra of all three binaries, with a few changes relative to the standard pipeline settings: We reduced the threshold to discard deviating pixels from 10 sigma to 3 sigma, and we used the semi-automatic flux-weighted wavelength calibration. For the observations with more than one star on the slit, we applied offsets and reduced the extraction slit length, to extract the spectrum of each star separately. We did not merge orders, since the regions of overlap have low S/N and could introduce unwanted noise in the later analysis.

V20 was previously analysed by GCH08 using the UVES pipeline reduced spectra as supplied by ESO. However, inspecting the raw spectra of V20 revealed that the choice of the ELEV mode had the unfortunate effect of allowing light from a close-by star (in addition to the third light) to reach the slit for some observations. This affects the radial velocity zero-point determination significantly, regardless of whether this is done using the third light component as in GCH08 or with our present method as we describe below. Therefore, these spectra were re-reduced with offsets and reduced slit length, to mask out the unwanted star.

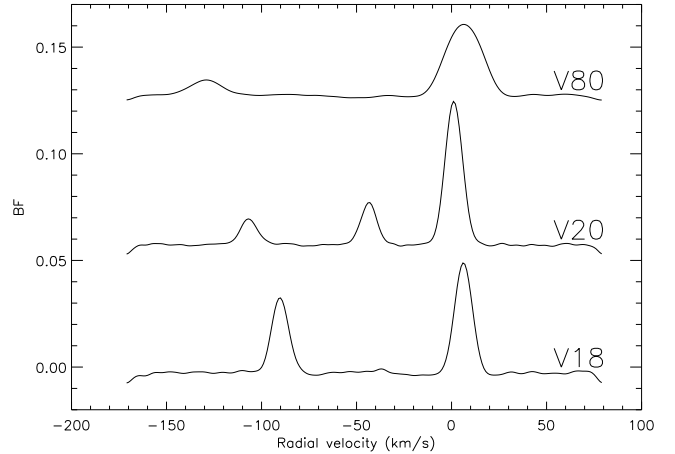


Fig. 5. Averaged broadening functions for the three binaries using the optimal templates and Gaussian smoothing, showing the characteristics of each system. V80, V20, and V18 BFs are shown from top to bottom with offsets of 0.13, 0.06, and 0.00 for clarity. V18 and V20 are seen to be slowly rotating systems, while V80 rotates faster. V20 contains a third light component.

The orbital periods of V18 and V80 were not well known prior to the spectroscopic observations. Therefore, we retrieved the data from the ESO Archive the day after each new observation, reduced the spectrum, made an orbital solution to find a better period estimate, and then rescheduled the remaining observations to optimal epochs.

4.1. Radial velocities and spectroscopic elements

For the radial velocity measurements we employed the broadening function (BF) formalism (Rucinski 1999, 2002, 2004). The BF method assumes that all components in the observed spectrum can be well described by the same synthetic template spectrum with respect to the relative strengths of spectral lines. This assumption holds as long as the spectral types of the components do not differ too much. We used synthetic spectra from the grid of Coelho et al. (2005) and repeated the procedure with templates covering a reasonable range in $\log g$, T_{eff} and $[\text{Fe}/\text{H}]$ and found that the effect of the adopted template is much smaller than the final adopted error estimates. We also confirmed the similarity of the spectral types of the components by separating the spectra (see Sect. 4.3).

In our implementation BFs are calculated for each order and averaged to give the final BF profile. This profile is smoothed by convolution with a Gaussian. The width of this smoothing Gaussian was chosen to minimize the order-to-order scatter of radial velocities measured from single-order BFs. Fig. 5 shows example BFs for each system.

The final BFs were then fitted with a Gaussian around each peak to measure the radial velocities. We found that this procedure gives a lower order-to-order radial velocity scatter than fitting a rotational profile, when applied to the individual orders. We did not use all spectral orders, since in the bluest region, the S/N was too low to obtain a decent BF, and some orders contain wide lines or telluric lines, and are therefore not well-suited for radial velocity measurements. We ended up using ten orders from each chip.

Spectroscopic elements were derived from the measured radial velocities using the method of Lehman-Filhés implemented

in the SBOP program (Etzet 2004). The orbital periods were fixed at their photometrically determined values.

Our first solutions had ($O - C$) errors of up to 1 km/s in a systematic pattern identical for the primary and secondary components. This indicated that the radial velocity errors were dominated by radial velocity zero-point offsets between epochs. Since our spectra are calibrated with ThAr spectra taken immediately after the stellar spectra, these offsets cannot be attributed to wavelength calibration errors. Instead they occur because the starlight is not exactly centered across the rather wide spectrograph slit, effectively causing an incident angle, which shifts the spectrum in wavelength relative to a star perfectly centered across the slit. To correct for this shift, we did the following: We identified a spectral order with very strong telluric absorption lines ($\lambda = 6276 - 6299 \text{ \AA}$). In the adjacent orders we measured the BF profile, which is nearly identical for close-by orders. We then convolved our synthetic stellar template spectrum, covering the wavelength region with telluric absorption lines, with the obtained BF, to produce the expected stellar spectrum in that order. This spectrum was then multiplied with synthetic telluric spectra which were broadened to the spectrograph resolution, shifted in radial velocity from -3 to $+3$ km/s in small steps of 50 m/s, and multiplied with factors between 0.5 and 1.5 in steps of 0.1. The resulting set of artificial spectra of stellar+telluric lines were all cross-correlated with the observed spectra, and the one giving the highest cross correlation determined the shift of the telluric lines. This shift is our radial velocity zero-point correction, since the telluric absorption lines are always at zero radial velocity (except for small shifts due to winds in the Earth's atmosphere), and the observed shift can only be caused by the aforementioned imperfect slit centering.

Applying the zero-point radial velocity shifts reduced the errors on the orbital parameters very significantly. It also changed the orbital parameters to just outside their original one-sigma error bars, indicating that these were underestimated because the zero-point shifts had not been taken into account.

In order to check that the errors on the spectroscopic elements given by the SBOP program for our zero-point corrected radial velocities can be trusted we developed a Monte Carlo routine for alternative error calculations. We assumed that the radial velocity errors have two Gaussian components, one of which represents any remaining radial velocity zero-point error and is identical for both components. We subtracted in quadrature the standard deviation radial velocity errors found from order-to-order scatter from the SBOP ($O - C$) standard errors in order to estimate the magnitude of the radial velocity zero-point error. We found this error contribution to be ~ 150 m/s. We then ran SBOP a large number of times adding to each radial velocity two Gaussian errors with standard deviations of 150 m/s and the order-to-order standard deviations, respectively. From the output solutions we calculated the one-sigma error. We found that this approach gives errors consistent with the errors from SBOP, and concluded that these errors can be trusted. Adopting a conservative approach we have anyway chosen to adopt the Monte Carlo errors, which are slightly (1-10%) larger than the SBOP errors. For more details on the error estimates we refer to Brogaard (2010).

We derived orbital parameters for the three binaries from both single- and double-lined solutions (meaning that a solution was found both by fitting one component at a time, and by fitting the two components in a combined solution). For the double-lined solutions, the radial velocities of the secondary were adjusted to account for the difference in gravitational redshift between components. These adjustments were calculated

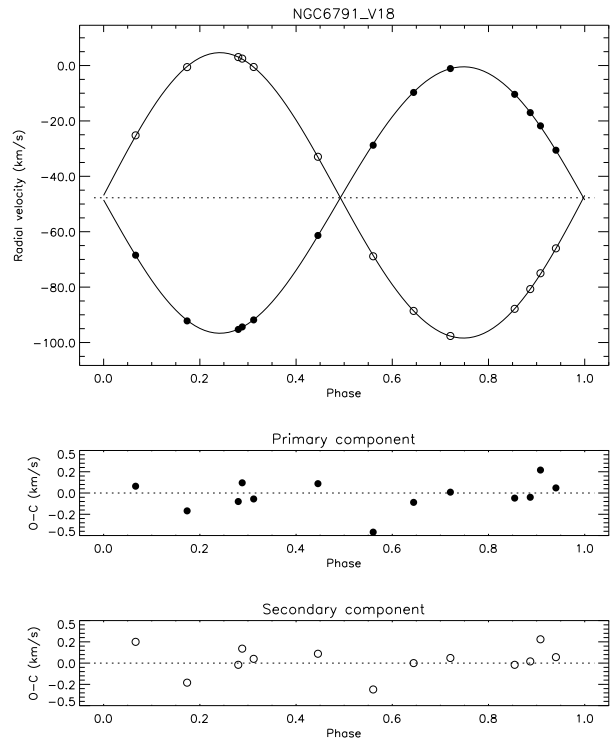


Fig. 6. Spectroscopic double-lined orbital solution for V18. Phase 0.0 corresponds to central primary eclipse. The horizontal dotted line (upper panel) represents the center-of-mass velocity.

iteratively from the obtained absolute masses and radii and are -35 m/s for V18, -180 m/s for V20 and -150 m/s for V80. Furthermore, the relative radial velocity weights between components were set according to the difference in ($O - C$) errors between components from single-lined solutions. For V18 the orbit is slightly eccentric, so to obtain a consistent set of semi-amplitudes corresponding to the same e and ω we adopted the double-lined solution. For this system, a measurement of $e \sin \omega$, including its error, was desirable for constraining the light curve solution, where this quantity is poorly determined. However, since e and ω are correlated parameters, one cannot obtain the error on $e \sin \omega$ from the errors on e and ω . We therefore ran SBOP using Sterne's method, which fits for $e \sin \omega$ and $e \cos \omega$ directly. Sterne's method only works for one component, so we did a solution for both the primary and secondary component. This resulted in values for e and ω on either side of the adopted solution. We therefore calculated the value of $e \sin \omega$ from the adopted e and ω while we obtained the error on $e \sin \omega$ from the SBOP solutions using Sterne's method. This result is $e \sin \omega = 0.009987 \pm 0.00110$.

For V20 we cannot rule out a small eccentricity of ~ 0.002 from the spectra alone, but both V and I light curves prefer an orientation of 90 degrees when any eccentricity is forced upon them, indicating a strong preference for a circular orbit, which is what we adopt. Furthermore, we adopt the single-lined solutions since they correspond to a consistent set for a circular orbit, and this avoids any speculations about differences in observed system velocity between components due to exact differences in gravitational redshift, convective blueshifts and any template mismatch. Note that for V18 such differences must be very small

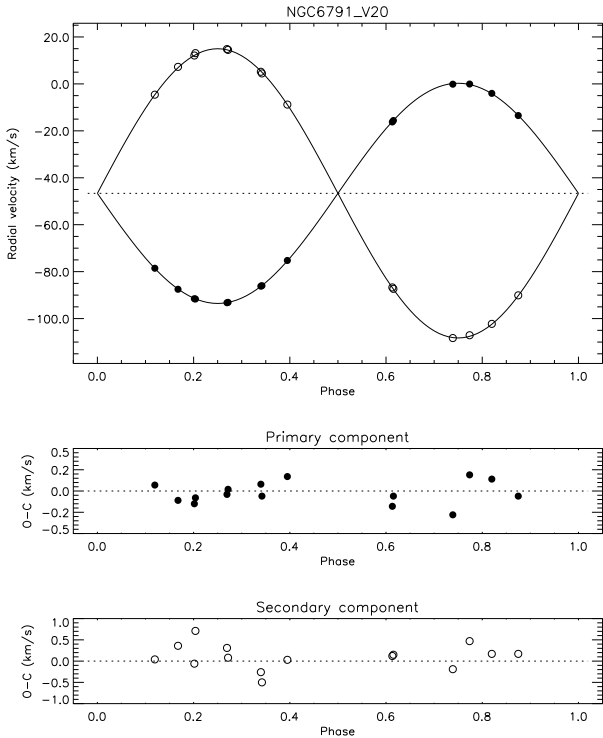


Fig. 7. Spectroscopic double-lined orbital solution for V20. Phase 0.0 corresponds to central primary eclipse. The horizontal dotted line (upper panel) represents the center-of-mass velocity. Note the different scales in the ($O - C$) panels.

because the stars are of very similar masses, radii and spectral types, and therefore negligible errors are introduced by adopting the double-lined solution for this system. For V80 rotational broadening reduces the accuracy of both radial velocities and zero-point measurements, but because of the larger radial velocity amplitudes caused by the shorter orbital period, the minimum masses are still determined to an accuracy better than 1%.

We list the final spectroscopic elements for the systems in Table 6 and show double-lined solutions in Figs. 6–8. Tables 15–17 containing radial velocities and ($O - C$) errors can be found on CDS. As seen, minimum masses accurate to well below 1% have been obtained for all systems. For V20, the errors on both the semi-amplitudes and individual measurements are about half of those found by GCH08. Perhaps the most convincing evidence, which indicate that our measurements are more accurate, is to compare our Fig. 7 to their Fig. 8; note in particular the sets of measurements close to phases 0.2, 0.25, 0.35, and 0.6, which were taken immediately after each other and are therefore expected to give identical results.

As also seen from Table 6, the systemic velocities, γ , of the systems are in excellent agreement with the value of $-47.1 \pm 0.8 \text{ km s}^{-1}$ as determined from 15 cluster members by Carraro et al. (2006), who also found the dispersion in the radial velocities of the 15 stars to be $2.2 \pm 0.4 \text{ km s}^{-1}$. This provides a strong argument that all systems are cluster members. V18 and V80 are in addition proper-motion members (96% and 86% probability according to Dr. Kyle Cudworth as stated by Rucinski et al. 1996 and de Marchi et al. 2007, respectively). Given also the similarity

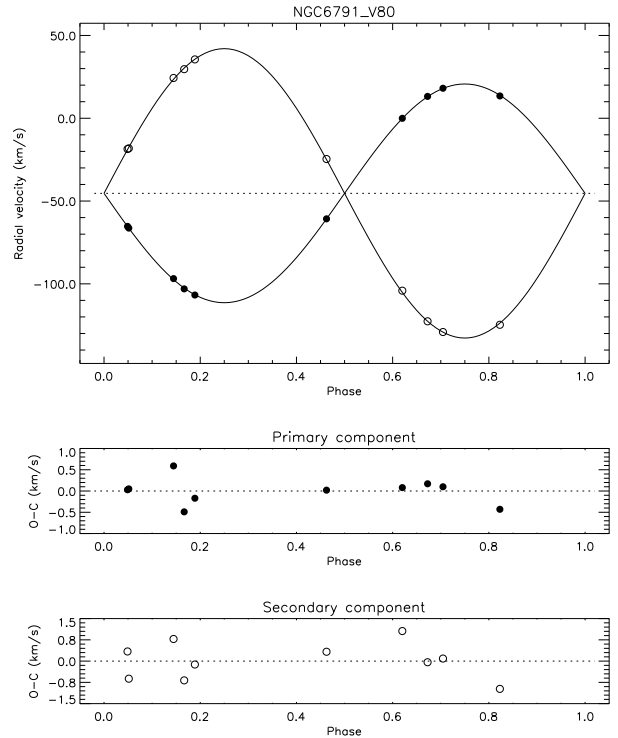


Fig. 8. Spectroscopic double-lined orbital solution for the V80. Phase 0.0 corresponds to central primary eclipse. The horizontal dotted line (upper panel) represents the center-of-mass velocity. Note the different scales in the ($O - C$) panels.

in the metallicities that we derive (Sect. 4.3) there should be no doubt that these stars are cluster members.

4.2. Spectroscopic light ratio of V18

For V18 we found that a spectroscopic light ratio could improve the photometric elements (cf. Sect. 3.5.1). For this system we therefore found an additional use for our calculated broadening functions, since the BF is a proxy for the mean line profiles in the stars. The difference in equivalent widths between each component peak therefore measures the light ratio. We selected BFs from 10 orders for which the mean luminosity ratio corresponds very closely to the luminosity ratio in the V band according to tests with both Planck functions and synthetic spectra of Coelho et al. (2005). For each epoch of observations we fitted these BFs with a rotational profile convolved with a Gaussian and integrated the area under each peak to measure the ratio of equivalent widths between components. If the stars had identical spectral types this ratio measures directly the light ratio in the V band. Since the light curve solutions suggest an effective temperature difference of about 200 K, a very small correction of -0.06 was applied to the measured light ratio. We found $L_s/L_p = 0.636 \pm 0.020$ where the error is a sum of the epoch-to-epoch measurement scatter (± 0.005), a contribution due to possible differences between light ratio in the V band and the spectral region measured (± 0.005), an estimated uncertainty in the correction due to different spectral types (± 0.005), and a contribution to account for the exact continuum placement in the measurement and the fact that real stars may not be accurately

Table 6. Spectroscopic orbital solutions. T is the time of central primary eclipse.

Parameter	V18	V20	V80
Fixed parameters:			
T (HJD–2 400 000)	54651.4506	53151.6061	54652.3045
P (days)	18.798638	14.469918	4.88594
Free parameters:			
K_p (km s ⁻¹)	48.0940 ± 0.0750	46.8998 ± 0.0500	66.0507 ± 0.1560
K_s (km s ⁻¹)	51.5233 ± 0.0760	61.5880 ± 0.1000	87.3838 ± 0.2560
γ (km s ⁻¹)	-47.7433 ± 0.0378	-46.6385 ± 0.0350	-45.3546 ± 0.0984
e	0.0196 ± 0.0012	0.00(fixed)	0.00(fixed)
ω (°)	149.3654 ± 3.1138	90.00(fixed)	90.00(fixed)
Derived parameters:			
$M_p \sin^3 i$ (M _⊙)	0.9953 ± 0.0033	1.0868 ± 0.0039	1.0415 ± 0.0069
$M_s \sin^3 i$ (M _⊙)	0.9291 ± 0.0032	0.8276 ± 0.0022	0.7872 ± 0.0043
q	0.9334 ± 0.0020	0.7615 ± 0.0015	0.7559 ± 0.0028
$a \sin i$ (R _⊙)	37.0096 ± 0.0397	31.0301 ± 0.0320	14.8186 ± 0.0290
Other quantities:			
σ_p (km s ⁻¹)	0.241	0.140	0.326
σ_s (km s ⁻¹)	0.226	0.308	0.689
N_{obs}	13	15	10
Time span (days)	88	377	92

described by a rotational profile (± 0.005). We chose all these error contributions conservatively and add them directly (not in quadrature) because they have a systematic character with exception of the measurement scatter. We were unable to repeat this procedure for the R band, since we found no combination of orders for which the light ratio corresponds to the R band light ratio.

4.3. Spectroscopic analysis: T_{eff} and $[\text{Fe}/\text{H}]$

To determine effective temperatures and metallicities of the binary stars, we first separated their spectra. This was done following the description of González & Levato (2006), which we expanded to handle systems with three components (needed for V20). When separating spectra of binary stars the light contribution from each component to the continuum level cannot be determined from the spectra themselves (except when the spectral types are almost identical, where one can follow the procedure we used for V18 in the previous section). We therefore employed our photometric light ratios from Tables 3–5 to correct each component spectrum for the continuum contribution from the other component. Since these light ratios are measured in the Johnson V band, we used Planck functions to calculate the corresponding light ratio in each spectral order from initial photometric temperature estimates. This procedure was iterated with the derived temperatures, with negligible differences. We checked that the Planck approximation was adequate, e.g. using MARCS models instead produced identical results. The binary target V80 was observed with an additional star on the slit on some epochs. After acquiring the spectra, a more careful inspection revealed that this was in fact two very close stars, which we also analyse below. For simplicity we shall refer to this composite spectrum as the subgiant (SG) star spectrum.

We made a detailed spectral analysis of four of the separated binary spectra, the primary and secondary of V18 (abbreviated V18p and V18s), V20p, V80p, and SG. We did not analyse V20s and V80s, since the signal-to-noise (S/N) was very low, and therefore the placement of the continuum introduced

very large systematic errors. The continuum was normalized using a synthetic template spectrum with the assumed atmospheric parameters of the star. This was done by identifying continuum windows with the `rainbow` software as described in Bruntt et al. (2010b).

In Fig. 9 we show a small section of the spectra, which shows their range of quality. The full-length one-dimensional spectra can be found in Tables 18–22 on CDS. The S/N in the continuum ranges from 30 (V18s) to 60 (V20p). In Fig. 9 we also overplot a high resolution ($R=110000$) high S/N spectrum of α Cen A as observed with HARPS. This star has parameters very similar to the observed stars in NGC 6791: Bruntt et al. (2010a) used the HARPS spectrum to determine $v \sin i = 1.9 \pm 0.6$ km/s, $T_{\text{eff}} = 5745 \pm 80$ K, $\log g = 4.31 \pm 0.08$, and $[\text{Fe}/\text{H}] = +0.22 \pm 0.07$.

We used the semi-automatic software package VWA (Bruntt et al. 2010a; Clausen et al. 2008) to analyse the spectra. The program interpolates in a grid of MARCS model atmospheres (Gustafsson et al. 2008) and uses atomic line data from VALD (Kupka et al. 1999). The spectral lines are fitted iteratively by calculating synthetic profiles using SYNTH (Valenti & Piskunov 1996). Oscillator strengths are corrected using a solar spectrum. The software is described more thoroughly in Bruntt et al. (2010a,b), and we will mention here only differences to the standard approach. Most importantly, we made the analysis by fixing the $\log g$ values as constrained by the accurate measurements of the eclipsing binaries (Table 10). This breaks the degeneracy between $\log g$ and T_{eff} , which is usually a problem when analysing spectra at this S/N level, and allows a reliable T_{eff} determination.

As discussed above, the SG spectrum is a composite of the spectra of two stars with nearly identical radial velocity. We identified them to be stars 1621 and 1627 in the photometry of SBG03 (finding chart in Fig. A.3), but their measured magnitudes are wrong due to their small separation. We therefore transformed their magnitudes from our *HST* photometry into B and V magnitudes from which we measured their V light ratio and extrapolated along an isochrone to obtain their $\log g$ values (Table 7). Since they are very close to the binaries in the CMD, this should give $\log g$ values with errors of less than 0.05

dex. The spectrum of SG was then analysed using the approach for composite spectra described in Clausen et al. (2008). As for the binaries our prior knowledge of $\log g$ of the two components made it possible to constrain their temperatures.

We adjusted the $\nu \sin i$ of the synthetic spectra to provide the best fit to the observations. The values of $\nu \sin i$ are listed in Table 7. We used the calibration from Bruntt et al. (2010a) to fix the macroturbulence at 2.0 km/s for all stars. The microturbulence could only be determined with rather large errors. However, the values found are consistent with the calibration for solar-type stars from Bruntt et al. (2010a).

For all the analysed spectra, we adjusted the T_{eff} of the atmosphere model to make the mean abundances of Fe I and Fe II lines agree. We evaluated the internal error on T_{eff} by changing its value until the Fe I and Fe II deviated by one sigma.

To confirm the method, Bruntt et al. (2010a) compared the T_{eff} s from VWA with results for 10 nearby stars where interferometric methods can be used, and found very good agreement. They claimed a systematic offset of $T_{\text{eff;VWA}} - T_{\text{eff;Interf.}} = 40 \pm 20$ K should be applied to the spectroscopic effective temperatures. However comparing the $(b - y)$ temperature calibration of Casagrande et al. (2010) for 17 stars in common with the spectroscopic analysis of Bruntt et al. (2010a), we find that the situation is more complicated. The derived temperature offset is sensitive to the absolute magnitude of Vega, which is difficult to determine (see Casagrande et al. 2010 for a discussion). Equally importantly, there are indications that one cannot interpret the T_{eff} difference between VWA and other methods as a simple offset, since differences may depend on both T_{eff} and $[\text{Fe}/\text{H}]$. Unfortunately, we do not have enough stars measured to reach a firm conclusion. Due to these complications, any attempt to apply an offset to the T_{eff} derived using VWA may introduce more systematic error. Therefore, we adopt the T_{eff} values as determined from VWA analysis without any correction and add in quadrature a systematic error of 70 K to the internal VWA errors.

In Table 7 we list the adopted $\log g$, the determined T_{eff} , $\nu \sin i$, microturbulent velocity, and $[\text{Fe}/\text{H}]$ for all stars analysed. The errors for $[\text{Fe}/\text{H}]$ are determined by changing the T_{eff} and microturbulent velocity by one sigma in the analysis. The quoted errors in this table are internal errors.

With the final atmospheric parameters determined, we computed the abundances of all elements with at least four unblended lines available. In Table 8 we list the mean abundances and number of lines used for each spectrum. We only used relatively weak lines with equivalent widths between 10 and 100 mÅ. The quoted errors are the rms of the abundances for each element in a given ionization stage. All elements are consistent within 0.1 dex, except for vanadium, which has a higher mean abundance in all stars.

We tested the effect of the assumed helium content, following the prescription of Strömgren et al. (1982). They argue that a change in the helium content is effectively the same as a change in the pressure, and hence $\log g$, in the atmosphere. Using their prescription, we find that even a large change in Y from solar to 0.33 (high value for NGC 6791) is accommodated by a change in $\log g$ of only 0.03 which leads to a change in $[\text{Fe}/\text{H}]$ of 0.01 or less. At the same time, helium diffusion would tend to lower the helium content in stellar atmospheres with time. Thus, for the old stars in NGC 6791 more helium will have left the atmospheres due to diffusion compared to the Sun, and therefore the correction due to a different helium abundance should be even smaller and effectively negligible. Finally, we repeated the analysis of the stars when changing the light ratio by two sigma, and found negligible changes to the determined T_{eff} and metallicity.

For our final estimate of $[\text{Fe}/\text{H}]$ for NGC 6791 we calculated the weighted mean of the six stars $[\text{Fe}/\text{H}]$ in Table 7, resulting in $[\text{Fe}/\text{H}]_{\text{NGC 6791}} = +0.29 \pm 0.03 \pm 0.07$, where the quoted uncertainties are the weighted mean error and the adopted systematic error.

There are several spectroscopic measurements of the metallicity of NGC 6791 in the literature, with results spanning a rather wide range in $[\text{Fe}/\text{H}]$ from +0.30 to +0.47. Nearly all are all based on giant stars (Friel & Janes 1993; Peterson & Green 1998; Gratton et al. 2006; Origlia et al. 2006; Carraro et al. 2006). These analyses of giant stars are complicated by the presence of molecules and blending of lines, especially since they are based on low-to-medium resolution spectra (all have $R < 30\,000$). In such cases, blending makes the placement of the continuum difficult (cf. Fig. 2 in Gratton et al. 2006 and Fig. 2 in Carraro et al. 2006). Boesgaard et al. (2009) analysed two sub-giant stars at higher resolution ($R = 45\,000$), but they adopted a $\log g$ which is 0.3 dex higher than inferred from our binary measurements. Interestingly, their different $\log g$ and T_{eff} parameters conspire to give $[\text{Fe}/\text{H}] = +0.30 \pm 0.08$ (Boesgaard et al. 2009), in agreement with our result, despite their different atmospheric parameters.

We believe that the metallicity determined from our sample of stars is reliable, since the parameters of the stars are close to the Sun, and therefore less prone to systematic effects coming from the adopted model atmospheres. Furthermore, our use of accurate $\log g$ values from the binary measurements has strongly constrained one free parameter in the spectroscopic analysis. We note also that the $[\text{Fe}/\text{H}]$ measurements of the two single stars in the SG spectrum give results in excellent agreement with the binary stars. This is clear evidence that the spectral separation of the binary stars has not affected the metallicity measurements.

5. Absolute dimensions and distance

5.1. The reddening of NGC 6791

The reddening, $E(B - V)$, is needed to obtain the true distance of the cluster, and to constrain isochrones in the CMD. Using V18p, V18s, and V20p, we restricted the acceptable range of $E(B - V)$ by requiring our spectroscopic values of T_{eff} to agree with the temperatures obtained from a photometric color-temperature calibration. We used the calibrations from Casagrande et al. (2010) and from MARCS model atmospheres (calculated for use in Vandenberg et al. 2010). For a range of $E(B - V)$ we found the de-reddened colors of the binary components, and from those the photometric temperatures, assuming $[\text{Fe}/\text{H}] = +0.3$. The two calibrations give very consistent T_{eff} s with the largest deviation being 40 K. We set the one-sigma limits on $E(B - V)$ where differences between the spectroscopic and the photometric T_{eff} s become larger than 200 K for one of the stars, or larger than 100 K for all three stars. This one sigma range in $E(B - V)$ is 0.135–0.185 with the best match at 0.16. Repeating the procedure for an assumed $[\text{Fe}/\text{H}]$ of +0.2 and +0.4 showed that the result is only slightly dependent on $[\text{Fe}/\text{H}]$ and thus the acceptable range in $E(B - V)$ is independent of $[\text{Fe}/\text{H}]$ within ± 0.1 dex of our $[\text{Fe}/\text{H}]$ measurement. We thus find from this method that $E(B - V) = 0.160 \pm 0.025$ in excellent agreement with other recent results (Vandenberg et al. 2010; and references therein), and out other measurement, which we now describe.

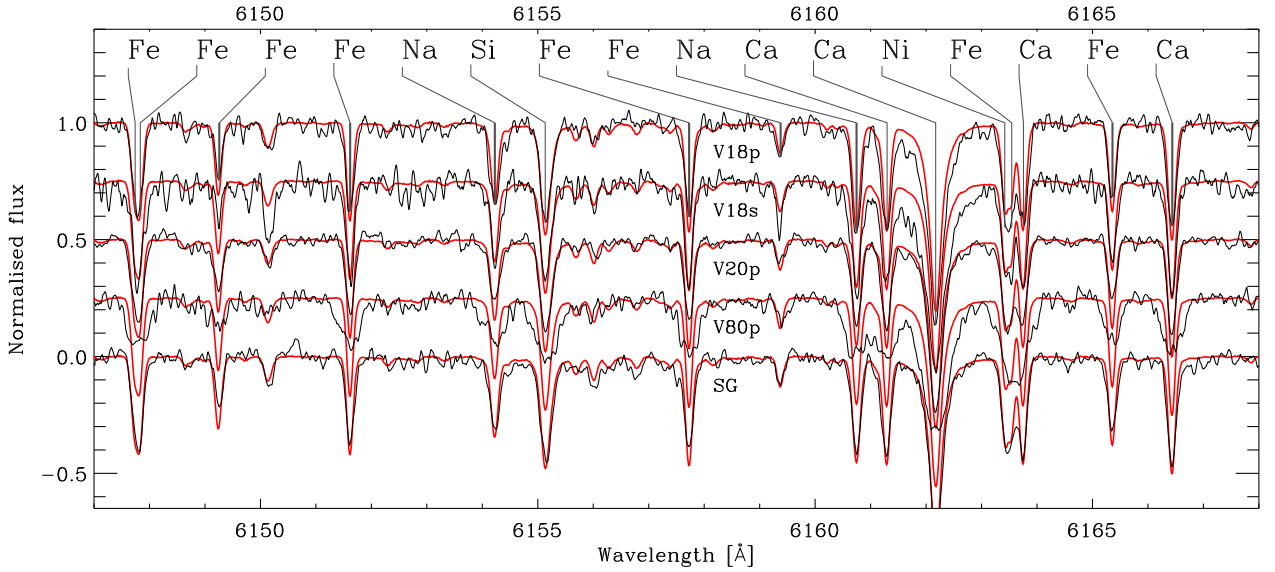
For an additional measure of the interstellar reddening, we used the calibration of Munari & Zwitter (1997) for the relationship between the equivalent width (W) of interstellar NaI D lines and $E(B - V)$. We first combined all our binary spectra

Table 7. Parameters determined from the spectral analysis (log g values were fixed). The uncertainties are internal errors.

	V18p	V18s	V20p	V80p	SGp	SGs
T_{eff} [K]	5600 ± 50	5430 ± 95	5645 ± 50	5600 ± 95	5540 ± 60	5570 ± 75
log g	4.35	4.43	4.18	4.21	4.04	4.19
$v \sin i$	4.00 ± 1.00	3.50 ± 1.00	4.50 ± 1.00	14.00 ± 2.00	4.00 ± 1.00	4.00 ± 1.00
v_{micro}	1.00 ± 0.12	0.95 ± 0.10	0.90 ± 0.10	1.10 ± 0.10	1.20 ± 0.12	1.25 ± 0.14
[Fe/H]	$+0.31 \pm 0.06$	$+0.22 \pm 0.10$	$+0.26 \pm 0.06$	$+0.34 \pm 0.10$	$+0.32 \pm 0.07$	$+0.30 \pm 0.08$

Table 8. Abundances and number of lines used in the spectral analysis. The uncertainties are the standard deviation of the mean.

	V18p		V18s		V20p		V80p		SGp		SGs	
Si I	$+0.35 \pm 0.05$	9	$+0.46 \pm 0.06$	4	$+0.23 \pm 0.03$	10	$+0.32 \pm 0.04$	6				
Ti I	$+0.26 \pm 0.04$	11	$+0.28 \pm 0.05$	6	$+0.27 \pm 0.06$	7			$+0.17 \pm 0.04$	8	$+0.11 \pm 0.07$	8
V I	$+0.48 \pm 0.07$	7	$+0.58 \pm 0.05$	8	$+0.35 \pm 0.03$	8	$+0.57 \pm 0.07$	5				
Cr I	$+0.11 \pm 0.05$	4										
Fe I	$+0.31 \pm 0.01$	63	$+0.22 \pm 0.03$	50	$+0.26 \pm 0.01$	76	$+0.34 \pm 0.03$	30	$+0.32 \pm 0.02$	56	$+0.30 \pm 0.02$	56
Fe II	$+0.31 \pm 0.04$	5	$+0.21 \pm 0.04$	5	$+0.26 \pm 0.08$	6	$+0.34 \pm 0.05$	5	$+0.31 \pm 0.02$	6	$+0.31 \pm 0.03$	6
Ni I	$+0.38 \pm 0.03$	17	$+0.35 \pm 0.05$	18	$+0.31 \pm 0.02$	18	$+0.42 \pm 0.06$	10	$+0.42 \pm 0.05$	10	$+0.34 \pm 0.04$	10

**Fig. 9.** The five spectra analysed with VWA are compared. The continuum level of the spectra is offset in steps of 0.25 for clarity. Each spectrum is compared with the HARPS spectrum of α Cen A (thin red line).

at their barycentric velocity in order to average out the spectral signal from the stars. In the combined spectrum the continuum has been suppressed to the left of the interstellar lines because of the NaI D lines from the binary stars, which are at different wavelengths in each spectrum, because the stars orbit each other. We assumed that the continuum suppression above a line across the interstellar NaI D line removes the stellar contribution to the interstellar line depth. Removing first this contribution, we measured the equivalent widths of the interstellar NaI D lines. We repeated the procedure for different selections of spectra, first all binary spectra, then selecting only spectra where deep lines are as far from the interstellar line as possible, and then this same procedure using only spectra from one star.

Following Munari & Zwitter (1997) we note that $W(D1)/W(D2) \geq 1.1$ enabling a minimum estimate of $W(D1)$ from $W(D2)$. Since in our case this minimum estimate is slightly higher than the direct measurement, we use the mean of the two measurements as our final measurement. Results are shown in Table 9 from which we adopt 0.354 ± 0.010 as the measured W of the NaI D1 line giving most weight to the measurement us-

ing many binary spectra while avoiding strong stellar contamination. Using this value with Table 2 of Munari & Zwitter (1997) we find $E(B - V) = 0.153 \pm 0.010$. Munari & Zwitter state that for $E(B - V)$ below 0.5 the reddening uncertainty is ~ 0.05 , but from their Fig. 5 it is clear that for $E(B - V)$ below 0.2, the uncertainty is even smaller. Despite this we conservatively adopt $E(B - V) = 0.153 \pm 0.050$ as our measurement from this method, which is admittedly not very precise but in excellent agreement with the above result.

We adopt the most accurate of our two measurements to be used in the following: $E(B - V) = 0.160 \pm 0.025$.

5.2. Absolute dimensions and distance of V18, V20 and V80

Absolute dimensions for V18, V20, and V80 are calculated from the elements given in Tables 3–6, and listed in Table 10. As seen, masses and radii have been obtained to an accuracy well below 1% for both V18 and V20. Errors on the masses are in the range 0.27–0.36%, while errors on the radii are in the range 0.61–0.92%. These measurements are therefore of an accuracy

Table 9. Equivalent width measurements of the interstellar Na I D lines.

Spectra used	W(D1)	W(D2)	W(D1) min. from W(D2)	W(D1) from W(D1)+W(D2)
V18+V80+V20	0.3406	0.3200	0.3520	0.346
(V18+V80+V20)selected	0.3544	0.3222	0.3544	0.354
V80selected	0.3309	0.3558	0.3913	0.361

NOTE 1: W(D1) and W(D2) are direct measurements of the Na I lines. W(D1) min. from W(D2) is a minimum value of W(D1) calculated from $W(D1)/W(D2) \geq 1.1$. W(D1) from $W(D1)+W(D2)$ is the mean value of the two estimates of W(D1).

comparable to, or better than, that of field star eclipsing binaries (Torres et al. 2010). The masses of V80 are also measured with errors below 1%, but as expected the radii are not very precise. However, the error in $\log g$ for the primary component is still only ± 0.05 , which was useful for the $[\text{Fe}/\text{H}]$ measurement. Note that our measurements of the radius of the V20 secondary and the mass of the V20 primary are outside the 1σ error estimates of GCH08. These differences are due to our improved measurements of the third light and radial velocity zero-points.

As also seen in Table 10, our measurements of the rotational velocities are in agreement with the theoretical synchronous rotational velocities. V18 has an eccentric orbit, but the difference between theoretical synchronous and pseudo-synchronous velocities is only 0.1 km/s and has been included in the theoretical values by increasing the error of the theoretical prediction.

From our measured radii and spectroscopic T_{eff} values, we calculated the luminosities of V18p, V18s and V20p, which together with a bolometric correction (B.C.) gave M_V of the stars. From these, and our measured V and $E(B - V)$, we calculated the distance moduli and true distance, which we also tabulate in Table 10. As seen the distance moduli of the three components agree very well, with the error in the T_{eff} values being the dominant error contribution. We used B.C. from MARCS stellar atmospheres, which are in agreement with empirical B.C.s from Flower (1996) within 0.02. The true distance moduli were found using our measurement of $E(B - V) = 0.160 \pm 0.025$ and $A_V = 3.09 \times E(B - V)$ (McCall 2004). From the individual distance moduli of V18p, V18s, and V20p, we calculated the apparent and true distance moduli of NGC 6791 to be $(m - M)_V = 13.51 \pm 0.06$ and $(V_0 - M_V) = 13.01 \pm 0.08$. The distance is then $d(\text{NGC 6791}) = 4.01 \pm 0.14$ kpc.

6. A first comparison with theoretical models

GCH08 used their measurements of V20 to show that the difference in its predicted age due to the specific stellar models that were employed was about four times larger than their measurement precision. However, they were unable to determine which of the models (if any) were the most trustworthy ones. The present study has significantly improved the measured properties of the binaries — including $[\text{Fe}/\text{H}]$, T_{eff} , and $E(B - V)$; consequently, even tighter constraints may be placed on the models. Of particular importance is the fact that, given our accurate mass and radius measurements for both V18 and V20, we can define four points (and their uncertainties) on the mass-radius diagram and therefore constrain the curvature of the isochrone that best reproduces the observations.

Although we could repeat the analysis carried out by GCH08, an examination of the models that they used revealed that the different assumed helium mass-fraction, Y , of NGC 6791, is the primary reason for the differences in the ages that they derived (Brogaard 2010). Since most of the currently available isochrones do not contain variations in Y at fixed

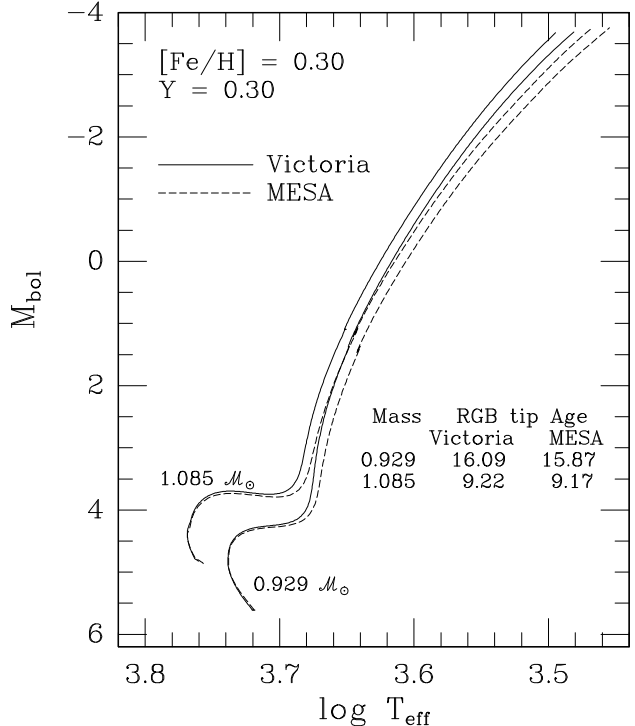


Fig. 10. Comparison between Victoria and MESA stellar evolutionary tracks for masses and chemical abundances (as indicated) that are relevant to an investigation of NGC 6791 and the binary stars V18 and V20.

$[\text{Fe}/\text{H}]$ values, a meaningful comparison of the models produced by different workers cannot be made. Moreover, there have been a number of recent revisions to nuclear reaction rates and other physics ingredients (see the next section), which further limits the usefulness of comparisons with most published models because they are not based on the most up-to-date stellar physics. In this paper, we have therefore chosen to make some initial comparisons with isochrones for a range in $[\text{Fe}/\text{H}]$ and Y , based on the tracks computed using just one stellar evolutionary code that has incorporated recent advances in nuclear reactions, opacity, etc.

6.1. Stellar models

The stellar models that are used in the present and forthcoming analysis of the binary stars V18 and V20 in NGC 6791, together with the cluster CMD, were generated using a significantly up-

Table 10. Astrophysical data for V18, V20 and V80.

	V18		V20		V80	
	Primary	Secondary	Primary	Secondary	Primary	Secondary
Absolute dimensions:						
M/M_{\odot}	0.9955 ± 0.0033	0.9293 ± 0.0032	1.0868 ± 0.0039	0.8276 ± 0.0022	1.0588 ± 0.0091	0.8003 ± 0.0062
R/R_{\odot}	1.1011 ± 0.0068	0.9708 ± 0.0089	1.3967 ± 0.0125	0.7813 ± 0.0053	1.3410 ± 0.0805	0.9015 ± 0.1833
$\log g$ (cgs)	4.3524 ± 0.0053	4.4319 ± 0.0080	4.1840 ± 0.0078	4.5698 ± 0.0059	4.2079 ± 0.0522	4.4314 ± 0.1791
T_{eff} (K)	5600 ± 95	5430 ± 125	5645 ± 95	4824 ± 140	5600 ± 95	
v_{rot} (km s ⁻¹)	4.0 ± 1.0	3.5 ± 1.0	4.50 ± 1.00		14.1 ± 2.0	
v_{sync} (km s ⁻¹)	2.96 ± 0.14	2.61 ± 0.13	4.88 ± 0.04	2.73 ± 0.02	13.88 ± 0.83	9.33 ± 1.9
V	18.247 ± 0.020	18.740 ± 0.020	17.695 ± 0.020	19.874 ± 0.020		
M_V	4.76 ± 0.10	5.22 ± 0.10	4.194 ± 0.10	6.44 ± 0.18		
$(V - M_V)$	13.49 ± 0.10	13.52 ± 0.10	13.50 ± 0.10	13.44 ± 0.18		
$(V_0 - M_V)$	13.00 ± 0.13	13.03 ± 0.13	13.01 ± 0.13	12.95 ± 0.20		
distance (kpc)	3.98 ± 0.25	4.04 ± 0.25	4.00 ± 0.25	3.89 ± 0.34		

NOTE 1: T_{eff} values are our spectroscopic measurements, except for T_{eff} of V20s, which is calculated as T_{eff} of V20p minus the difference in photometrically predicted temperatures between V20p and V20s assuming $E(B - V)=0.16$.

NOTE 2: v_{rot} is the observed equatorial rotational velocities calculated by combining $v \sin i$ and $\sin i$ measurements. v_{sync} is the theoretical equatorial velocity for synchronous rotation.

NOTE 3: Absolute magnitudes and distance moduli have not been calculated for V80 because these are very uncertain due to uncertain V magnitudes and radii (and T_{eff} for V80s) caused by the magnetic activity.

dated version of the University of Victoria evolutionary code (last described by Vandenberg, Bergbusch, & Dowler 2006; and references provided therein). The most important improvement that has since been made to it is the incorporation of the treatment of the gravitational settling of helium presented by Proffitt & Michaud (1991). A simple prescription for turbulent mixing has also been implemented, given that additional mixing below envelope convection zones must be assumed in order for theoretical models to reproduce the observed variations of the surface metal abundances of stars between the main sequence and the giant branch in old stellar systems (e.g., see the study of NGC 6397 by Korn et al. 2007). The free parameter in the adopted formulation of turbulence is set by monitoring the settling and nucleosynthesis of lithium and requiring that a Standard Solar Model yield the observed Li abundance of the Sun. In fact, it turns out that, with such a normalization, models for very metal-poor stars predict variations of the surface helium abundance with evolutionary state that are quite similar to those reported by Korn et al. For a much more detailed description of these results and the adopted treatment of diffusion and turbulence, we refer to a forthcoming study which examines the impact of varying the abundances of individual heavy elements (D. Vandenberg et al., in preparation.) Note that the settling of heavy elements is not considered. However, as discussed below, this omission is expected to have only minor consequences for the derived age of NGC 6791.

Since 2006, there have been a number of improvements to the rates of several reactions in the pp -chain and the CNO-cycle (for a convenient summary, see Weiss 2008) — including, in particular, the rate of the “bottle-neck” $^{14}\text{N}(p, \gamma)^{15}\text{O}$ reaction (Marta et al. 2008). The current version of the Victoria code has been revised to take these advances into account, as well as the improved conductive opacities published by Cassisi et al. (2007). In addition, particular care has been taken concerning the surface boundary conditions that are needed to solve the stellar structure equations (see, e.g., Vandenberg 1992), because the predicted T_{eff} scale depends so sensitively on them. As demon-

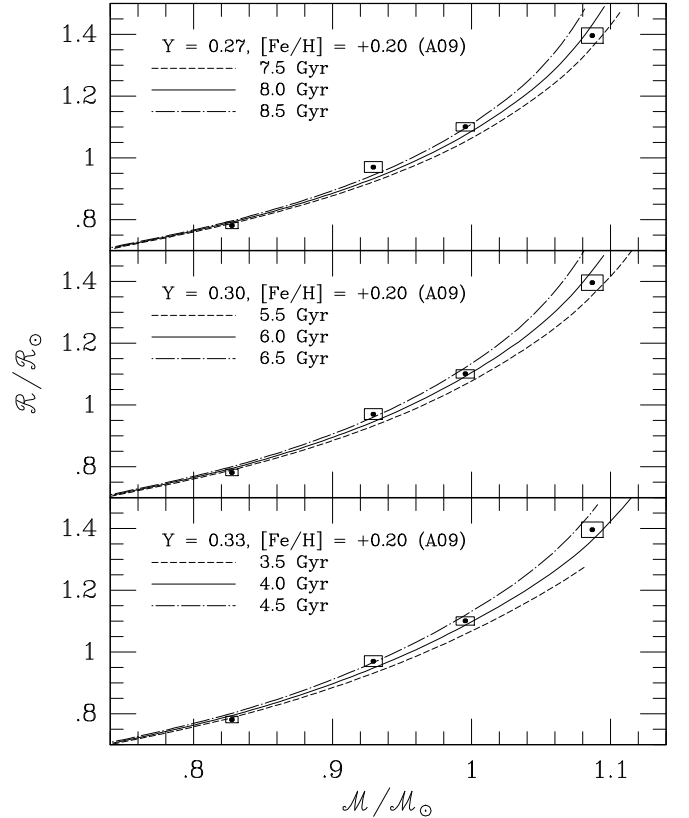


Fig. 11. The measured masses and radii of the components of V18 and V20 compared to best matching isochrones for $[\text{Fe}/\text{H}] = +0.20$ and helium contents of $Y = 0.27, 0.30,$ and 0.33 . From left to right the stars are V20s, V18s, V18p, and V20p. Error boxes are two-sigma.

strated by Vandenberg et al. (2008), simple model atmospheres that are obtained by integrating the hydrostatic equation in con-

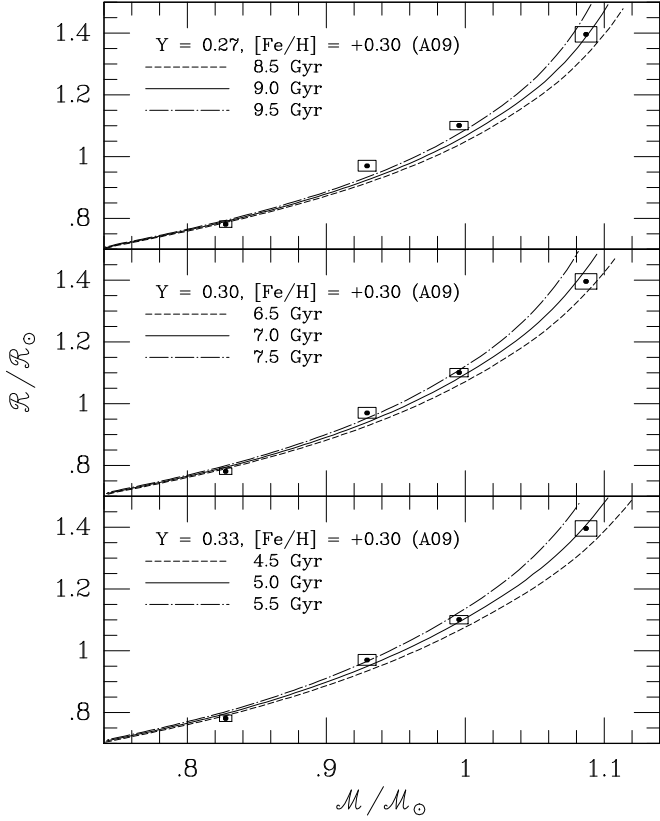


Fig. 12. As Fig. 11 but for isochrones with $[\text{Fe}/\text{H}] = +0.30$

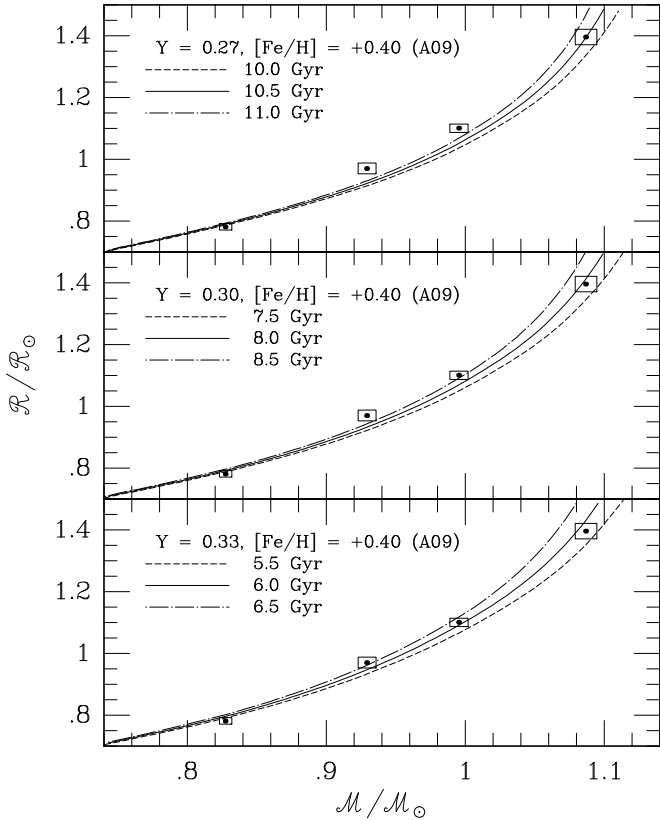


Fig. 13. As Fig. 11 but for isochrones with $[\text{Fe}/\text{H}] = +0.40$

junction with the scaled empirical Holweger & Mueller (1974) $T-\tau$ relation yield pressures at $T = T_{\text{eff}}$ that are in very good agreement with the values obtained from scaled, differentially corrected MARCS model atmospheres over wide ranges in T_{eff} , $\log g$, and metallicity. That is, the former approach provides a good approximation to the use of modern, blanketed model atmospheres as boundary conditions; hence, we have opted to determine the boundary pressures in this way, using the fit to the Holweger-Müller $T-\tau$ data given by Vandenberg & Poll (1989). In support of this choice, Vandenberg, Casagrande, & Stetson (2010) have shown that the resultant temperatures predicted by stellar models for field subdwarfs are in excellent agreement with those determined for them using the infra-red flux method.

Fig. 10 shows that the Victoria code produces evolutionary tracks for super-metal-rich (SMR) stars that agree quite well with those computed for the same masses and initial helium content using the completely independent MESA code (B. Paxton et al., in preparation; also see <http://mesa.sourceforge.net>). Except for the fact that the MESA code takes the gravitational settling of the metals into account (i.e., as well as helium) using the Thoul, Bahcall, & Loeb (1994) formalism, the physics incorporated in the two codes is quite similar. The MESA computations assume an initial mass-fraction abundance of the metals, Z , that is about 20% higher than the predicted surface metallicity at an age of ~ 7 Gyr, when the corresponding $[\text{Fe}/\text{H}]$ value is $\approx +0.30$. The surface values of Z and $[\text{Fe}/\text{H}]$ in the Victoria models do not vary with time. Encouragingly, the tracks superimpose one another nearly exactly between the zero-age main sequence and the lower red-giant branch (RGB), and they predict the same ages at the tip of the RGB to within 1.4%, despite the noted differences in the treatment of diffusion. Thus, models computed using either code can be expected to predict very similar temperatures and ages for the NGC 6791 binaries considered in this study, which are all in their core H-burning phases. Although the settling of the metals reduces the minimum mass that retains a convective core throughout its main-sequence phase (see Michaud et al. 2004), NGC 6791 appears to be old enough (see below) that this is unlikely to be a concern for the interpretation of the observations. Indeed, as pointed out by Christensen-Dalsgaard (2009), the $\sim 50\%$ reduction in the rate of the $^{14}\text{N}(p, \gamma)^{15}\text{O}$ reaction (Marta et al. 2008) has the important consequence of increasing the mass of the lowest mass star that retains a convective core throughout its main-sequence phase, thereby decreasing the age of the oldest isochrone that predicts a gap near the turnoff. The main reason for the difference in the predicted location of the RGB is that the MESA code requires a smaller value of the mixing-length parameter ($\alpha_{\text{MLT}} \approx 1.8$) than the Victoria code (≈ 2.0) to satisfy the solar constraint.

For this initial analysis of NGC 6791 and its binaries, we have adopted the relative abundances of the heavy elements recently derived for the Sun by Asplund et al. (2009).

6.2. Mass-Radius diagrams

The best starting point for an analysis of binary stars is arguably the mass-radius (MR) diagram because it provides the most direct comparison between theory and observations that can be made, being independent of uncertainties in distance, reddening, and color-temperature transformations. Since the measured $[\text{Fe}/\text{H}]$ value is very close to +0.3 (with a systematic error that is difficult to determine), we will compare our observations with models that have $[\text{Fe}/\text{H}] = +0.2, +0.3,$ and $+0.4$, with $Y = 0.27, 0.30,$ and 0.33 at each $[\text{Fe}/\text{H}]$. In Figs. 11–13 the measured masses and radii of the components of V18 and V20 are com-

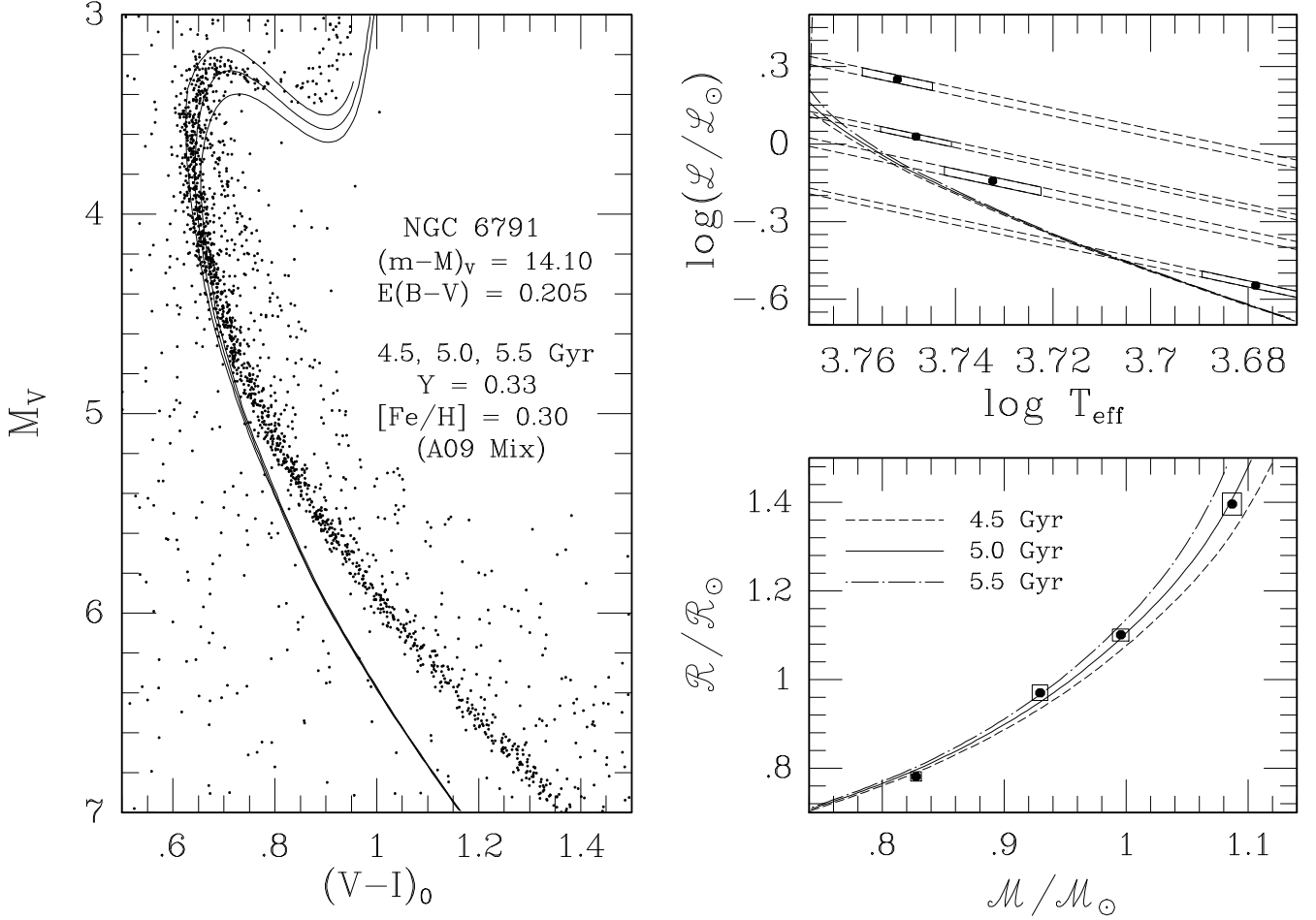


Fig. 14. Measurements of the detached eclipsing binaries V18 and V20 and the cluster $(V - I)_0, V$ CMD compared to isochrones with $[\text{Fe}/\text{H}] = +0.30$ and $Y = 0.33$. The observations in the CMD are from a 2010 re-reduction of the SBG03 data set by P. Stetson (see Vandenberg et al. 2010). Only the stars with the highest precision VI photometry have been plotted.

pared with isochrones for these chemical abundances (as noted) and for the indicated ages, which span the range needed to match the most massive, and thus most highly evolved, star in the sample (which is the primary of V20). It is worth reiterating the fact that having four measurements in the MR diagram allows us to constrain the shape of the isochrone on this plane.

Note that the error boxes correspond to two sigma uncertainties. We have chosen to do this because, with an increasing number of measurements in the mass-radius diagram, the likelihood of fitting all of the observations to within one sigma decreases. On the other hand, simple statistics cannot be used to predict the probability of fitting all of the observations to within 1σ (or 2σ) given that errors in the masses and radii can compensate for one another to a extent that depends on the slope of the isochrone in the vicinity of each of the observed points. For more rigorous results, we intend to use Monte Carlo simulations to quantify how well we should expect to fit our observations (Brogaard et al. 2010, in prep.; hereafter Paper II).

Figs. 11–13 show quite clearly that the morphology of an isochrone over the range in mass encompassed by the binaries depends quite sensitively on the assumed helium abundance (and only weakly on $[\text{Fe}/\text{H}]$). Indeed, it is only because we have measurements of multiple eclipsing binaries that we are able to use the shape of an isochrone on the MR plane to constrain the value of Y . This would obviously not have been possible if only V18

(the two middle measurements) or only V20 (the highest and lowest points) were used in the comparisons with theory — as a change in Y would then be indistinguishable from a change in age. With four stars, this degeneracy is now broken. As seen from the three figures, isochrones for $Y = 0.27$ are unacceptable for all choices of $[\text{Fe}/\text{H}]$, because the isochrones miss one star by more than two sigma, and only touches the others at or near the corners of their 2σ error boxes. Isochrones for $Y = 0.30$ match the observations somewhat better, though they also tend to pass through the corners of the 2σ error boxes: the least acceptable of the $Y = 0.30$ isochrones is that for $[\text{Fe}/\text{H}] = +0.40$. In fact, the shallow curvature suggested by the measured masses and radii indicates a preference for the highest helium abundance that we have considered ($Y = 0.33$), independently of the assumed $[\text{Fe}/\text{H}]$ value. However, such a high value of Y requires rather young ages, which turn out to be problematic, as we will now demonstrate.

6.3. T_{eff} –luminosity and color-magnitude diagrams

The isochrones plotted in the various MR diagrams that we have considered may, of course, also be compared with observations of the components of V18 and V20 on the $\log(T_{\text{eff}})$ – $\log(L/L_{\odot})$ (TL) diagram, using luminosities for the latter which can be readily calculated from their measured radii and the values of

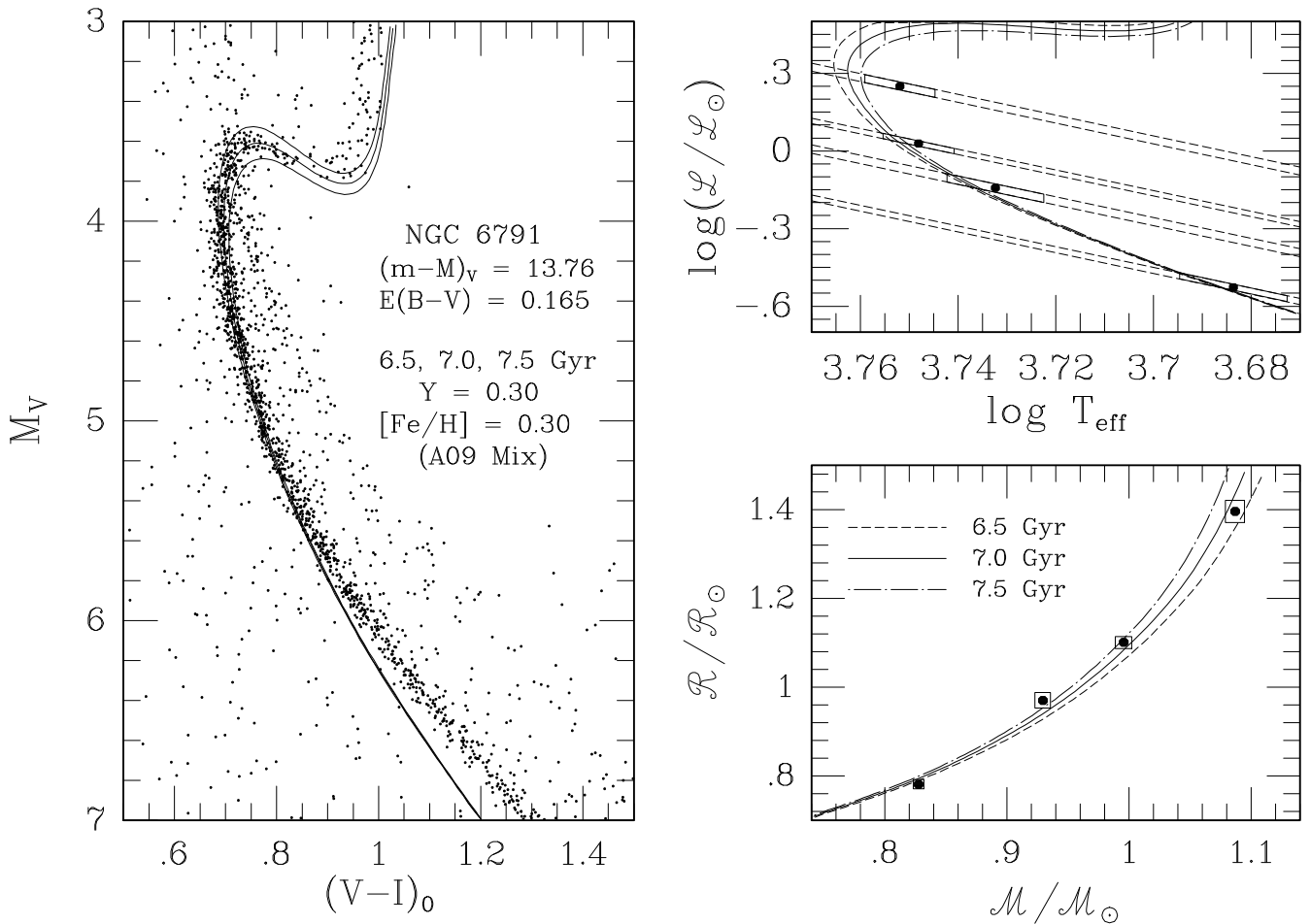


Fig. 15. As Fig. 14 but for isochrones with $[Fe/H] = +0.30$ and $Y = 0.30$

T_{eff} that were derived in our spectroscopic analysis. In addition, the same isochrones may be fitted to the CMD of NGC 6791 to determine the apparent distance modulus that corresponds to a given age. The value of $(m - M)_V$ derived in this way should agree with the modulus found from the binary stars themselves (13.51 ± 0.06 , see Table 10). An acceptable model must therefore be able to fit the MR and TL diagrams, as well as the observed CMD, simultaneously.

Fig. 14 provides an example, for the case of $[Fe/H] = +0.30$ and $Y = 0.33$, that can be ruled out because it is not possible for the models to match the observations on these three planes in a fully consistent way. Clearly both the predicted effective temperatures and the apparent distance modulus are way too high. For the same reasons, the other $Y = 0.33$ cases (as well as the possibility of even higher helium contents) can be excluded. Because our examination of the MR diagram has already precluded $Y \leq 0.27$ as viable possibilities, we are then left to consider the models having $Y = 0.30$. If $[Fe/H] = +0.20$, an isochrone for the age that does the best job of reproducing the MR diagram will fit the turnoff of the cluster CMD only if the apparent distance modulus is ~ 13.95 (not shown), which is unacceptably high. As already noted, models for $[Fe/H] = +0.40$ provide an unsatisfactory fit to the mass-radius data, leaving us with only the $Y = 0.30$, $[Fe/H] = +0.30$ case. As illustrated in Fig. 15, these parameter choices result in a level of agreement between theory and observations that can be considered satisfactory. The failure of the isochrones to reproduce the lower main-

sequence of NGC 6791 on the CMD could well be due mostly to problems with the adopted color- T_{eff} relations. The discrepancies would be significantly smaller had we used the empirical color transformations given by Casagrande et al. 2010; see Vandenberg et al. 2010. For stars brighter than $M_V \sim 6$ the MARCS and the Casagrande et al. transformations are in good agreement.

While we could explore the impact of small changes in Y and $[Fe/H]$ close to this solution, we believe that we should first expand our comparisons with theoretical models to those which assume different chemical abundance patterns. For instance, we have noticed that models which assume the older Grevesse & Sauval (1998) metals mixture, which are also favored from helioseismological studies (e.g., Bahcall et al. 2005), are able to reproduce the properties of the secondary of V20 much better than those that assume the Asplund et al. (2009) mix of heavy elements. (Whether better agreement can also be found for the other binary components remains to be seen.) In addition, it is worthwhile to examine the effects of varying the CNO abundances, given that they have been found to be under-abundant in NGC 6791 by 0.2–0.3 dex relative to scaled solar (see Carretta et al. 2007). It is well known that the CNO elements have important consequences for stars in their core H-burning phases through both nucleosynthesis and opacity effects. In Paper II we will present a thorough investigation of these and other issues, in the hope that we will obtain much more satisfactory fits of stellar models to both the CMD of NGC 6791 and the cluster binaries

than those reported here. Thus, our best estimates of the age and helium abundance of NGC 6791 will be reported in Paper II.

7. Summary and conclusions

In this paper we have presented extensive photometric and spectroscopic observations of the eclipsing binaries V18, V20 and V80, which are members of the old open cluster NGC 6791, and determined accurate masses and radii for the components of two of these systems. Additionally we exploited the eclipsing binaries for reliable measurements of spectroscopic T_{eff} s, and the metallicity and reddening of NGC 6791.

By performing a combined stellar model comparison with *multiple* eclipsing binaries in MR and TL diagrams and the cluster CMD we showed that we can constrain stellar models better than ever before. This allowed us to constrain the helium content, and thereby obtain a more precise (and hopefully accurate) age of the cluster, although in a model-dependent way. It turned out that in order for models to match both the MR and TL diagram and the CMD, only an age close to 7 Gyr is allowed by the observations, even though models are selected with a range of ± 0.1 dex in $[\text{Fe}/\text{H}]$ and a large range in Y . Our best current estimate of the cluster age and helium content is 7.0 Gyr and $Y=0.30$. This solution indicates that the helium enrichment law is $\Delta Y/\Delta Z \sim 2$, assuming that such a relation exist and applies to NGC 6791. However, these conclusions may depend on the details of the stellar models and the detailed abundance pattern of NGC 6791, which will be investigated in the forthcoming paper II.

We note that NGC 6791 contains a large number of additional detached eclipsing binaries (Rucinski et al. 1996; de Marchi et al. 2007; Mochejska et al. 2005). Accurate measurements of these, which we have shown to be possible, would allow even tighter model constraints in the MR diagram by extending the mass range over which the observed mass–radius relation must be reproduced. This has the potential to strengthen tests of other physical aspects of stellar models. This is so because incorrect model physics may be concealed in the models due to the flexibility offered by the uncertain helium content, but only up to a certain level. Furthermore, NGC 6791 is in the Field-Of-View of the NASA *Kepler* mission (Borucki et al. 2010), which will not only allow many more detached eclipsing binaries to be found, and their periods determined, but also complementary model constraints from asteroseismology of the giant stars in the cluster.

Multiple detached eclipsing binaries have also been confirmed in a number of other old open clusters (Brogaard 2010; Talamantes et al. 2010). Extending this kind of analysis to these clusters will allow more reliable cluster ages to be determined and more aspects of stellar models to be tested, when stellar models have to reproduce observations in clusters with a wide range in age and metallicity. By extending studies also to the globular clusters, detached eclipsing binaries could ultimately provide the strongest constraints on their ages and helium contents.

Acknowledgements. We thank the staff at the Nordic Optical Telescope and at ESO for allowing very flexible scheduling of observations, which resulted in optimal data and a faster completion of this project than would otherwise have been possible. We thank J. Southworth for access to JKTEBOP and P. Stetson for sharing his excellent photometry software with us and for permission to use his latest photometry of NGC6791. We are also grateful to Aaron Dotter for computing the MESA evolutionary tracks in Fig. 10. The project "Stars: Central engines of the evolution of the Universe", carried out at University of Aarhus and Copenhagen University, is supported by the Danish National Science Research Council. FG acknowledges financial support from the Carlsberg Foundation, the Danish

AsteroSeismology Centre at the University of Aarhus, and Instrumentcenter for Dansk Astronomi. The following internet-based resources were used in research for this paper: the NASA Astrophysics Data System; the SIMBAD database and the ViziR service operated by CDS, Strasbourg, France; the arXiv scientific paper preprint service operated by Cornell University.

References

- Andersen, J. 1991, *A&A Rev.*, 3, 91
 Anthony-Twarog, B. J., Twarog, B. A., & Mayer, L. 2007, *AJ*, 133, 1585
 Asplund, M., Grevesse, N., Sauval, A. J., & Scott, P. 2009, *ARA&A*, 47, 481
 Bahcall, J. N., Basu, S., Pinsonneault, M., & Serenelli, A. M. 2005, *ApJ*, 618, 1049
 Bedin, L. R., King, I. R., Anderson, J., et al. 2008, *ApJ*, 678, 1279
 Bedin, L. R., Salaris, M., Piotto, G., et al. 2005, *ApJ*, 624, L45
 Boesgaard, A. M., Jensen, E. E. C., & Deliyannis, C. P. 2009, *AJ*, 137, 4949
 Borucki, W. J., Koch, D., Basri, G., et al. 2010, *Science*, 327, 977
 Brogaard, K. 2010, PhD Thesis, Aarhus University, submitted
 Bruntt, H., Bedding, T. R., Quirion, P., et al. 2010a, *MNRAS*, 405, 1907
 Bruntt, H., Deleuil, M., Fridlund, M., et al. 2010b, *ArXiv e-prints*
 Bruntt, H., Grundahl, F., Tingley, B., et al. 2003, *A&A*, 410, 323
 Carraro, G., Villanova, S., Demarque, P., et al. 2006, *ApJ*, 643, 1151
 Carretta, E., Bragaglia, A., & Gratton, R. G. 2007, *A&A*, 473, 129
 Casagrande, L., Ramírez, I., Meléndez, J., Bessell, M., & Asplund, M. 2010, *A&A*, 512, A54
 Cassisi, S., Potekhin, A. Y., Pietrinferni, A., Catelan, M., & Salaris, M. 2007, *ApJ*, 661, 1094
 Christensen-Dalsgaard, J. 2009, *ArXiv:0912.1405*
 Claret, A. 2000, *A&A*, 363, 1081
 Clausen, J. V., Torres, G., Bruntt, H., et al. 2008, *A&A*, 487, 1095
 Coelho, P., Barbuy, B., Meléndez, J., Schiavon, R. P., & Castilho, B. V. 2005, *A&A*, 443, 735
 de Marchi, F., Poretti, E., Montalto, M., et al. 2007, *A&A*, 471, 515
 Etzel, P. B. 1981, in *Photometric and Spectroscopic Binary Systems*, ed. E. B. Carling & Z. Kopal, 111
 Etzel, P. B. 2004, *SBOP: Spectroscopic Binary Orbit Program* (San Diego State University), ed. Etzel, P. B.
 Friel, E. D. & Janes, K. A. 1993, *A&A*, 267, 75
 González, J. F. & Levato, H. 2006, *A&A*, 448, 283
 Gratton, R., Bragaglia, A., Carretta, E., & Tosi, M. 2006, *ApJ*, 642, 462
 Grevesse, N. & Sauval, A. J. 1998, *Space Science Reviews*, 85, 161
 Grundahl, F., Clausen, J. V., Hardis, S., & Frandsen, S. 2008, *A&A*, 492, 171
 Gustafsson, B., Edvardsson, B., Eriksson, K., et al. 2008, *A&A*, 486, 951
 Holwegger, H. & Mueller, E. A. 1974, *Sol. Phys.*, 39, 19
 King, I. R., Bedin, L. R., Piotto, G., Cassisi, S., & Anderson, J. 2005, *AJ*, 130, 626
 Korn, A. J., Grundahl, F., Richard, O., et al. 2007, *ApJ*, 671, 402
 Kupka, F., Piskunov, N., Ryabchikova, T. A., Stempels, H. C., & Weiss, W. W. 1999, *A&AS*, 138, 119
 Marta, M., Formicola, A., Gyürky, G., et al. 2008, *Phys. Rev. C*, 78, 022802
 McCall, M. L. 2004, *AJ*, 128, 2144
 Michaud, G., Richard, O., Richer, J., & Vandenberg, D. A. 2004, *ApJ*, 606, 452
 Mochejska, B. J., Stanek, K. Z., Sasselov, D. D., & Szentgyorgyi, A. H. 2002, *AJ*, 123, 3460
 Mochejska, B. J., Stanek, K. Z., Sasselov, D. D., et al. 2005, *AJ*, 129, 2856
 Nelson, B. & Davis, W. D. 1972, *ApJ*, 174, 617
 Origlia, L., Valenti, E., Rich, R. M., & Ferraro, F. R. 2006, *ApJ*, 646, 499
 Peterson, R. C. & Green, E. M. 1998, *ApJ*, 502, L39
 Press, W. H., Teukolsky, S. A., Vetterling, W. T., & Flannery, B. P. 1992, *Numerical recipes in FORTRAN. The art of scientific computing*, ed. Press, W. H., Teukolsky, S. A., Vetterling, W. T., & Flannery, B. P.
 Proffitt, C. R. & Michaud, G. 1991, *ApJ*, 371, 584
 Rucinski, S. 1999, in *Astronomical Society of the Pacific Conference Series*, Vol. 185, *IAU Colloq. 170: Precise Stellar Radial Velocities*, ed. J. B. Hearnshaw & C. D. Scarfe, 82
 Rucinski, S. M. 2002, *AJ*, 124, 1746
 Rucinski, S. M. 2004, in *IAU Symposium*, Vol. 215, *Stellar Rotation*, ed. A. Maeder & P. Eenens, 17
 Rucinski, S. M., Kaluzny, J., & Hilditch, R. W. 1996, *MNRAS*, 282, 705
 Sing, D. K., Vidal-Madjar, A., Désert, J., Lecavelier des Etangs, A., & Ballester, G. 2008, *ApJ*, 686, 658
 Southworth, J. 2008, *MNRAS*, 386, 1644
 Southworth, J. 2010, *ArXiv:1006.4443*
 Southworth, J., Bruntt, H., & Buzasi, D. L. 2007, *A&A*, 467, 1215
 Southworth, J., Hinse, T. C., Dominik, M., et al. 2009, *ApJ*, 707, 167
 Stetson, P. B. 1987, *PASP*, 99, 191
 Stetson, P. B. 1994, *PASP*, 106, 250

- Stetson, P. B., Bruntt, H., & Grundahl, F. 2003, *PASP*, 115, 413
- Strömgren, B., Gustafsson, B., & Olsen, E. H. 1982, *PASP*, 94, 5
- Talamantes, A., Sandquist, E. L., & Clem, J. L. Robb, R. M. 2010, submitted
- Thoul, A. A., Bahcall, J. N., & Loeb, A. 1994, *ApJ*, 421, 828
- Torres, G., Andersen, J., & Giménez, A. 2010, *A&A Rev.*, 18, 67
- Valenti, J. A. & Piskunov, N. 1996, *A&AS*, 118, 595
- van Hamme, W. 1993, *AJ*, 106, 2096
- Vandenberg, D. A. 1992, *ApJ*, 391, 685
- VandenBerg, D. A., Bergbusch, P. A., & Dowler, P. D. 2006, *ApJS*, 162, 375
- Vandenberg, D. A., Casagrande, L., & Stetson, P. B. 2010, *AJ*, submitted
- VandenBerg, D. A., Edvardsson, B., Eriksson, K., & Gustafsson, B. 2008, *ApJ*, 675, 746
- Weiss, A. 2008, *Physica Scripta Volume T*, 133, 014025

Appendix A: Finding charts

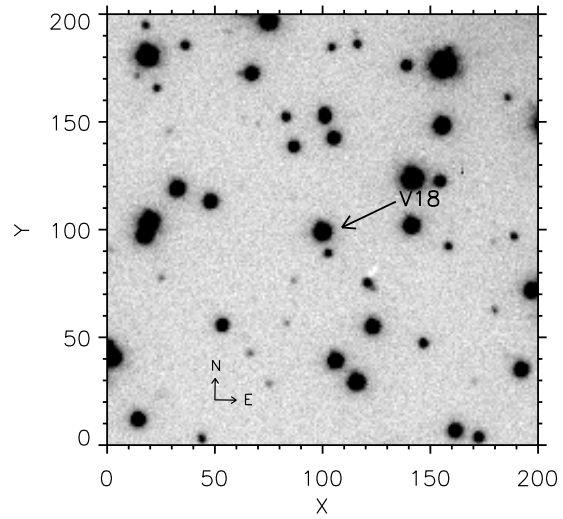


Fig. A.1. Finding chart for V18. Plate scale is $0.19''$ per pixel. Image from ALFOSC at the Nordic Optical Telescope.

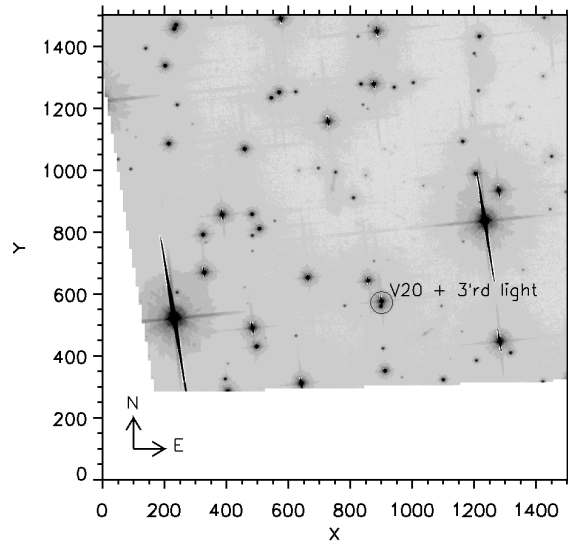


Fig. A.2. Finding chart for V20. Plate scale is $0.05''$ per pixel. Image from ACS on *HST*

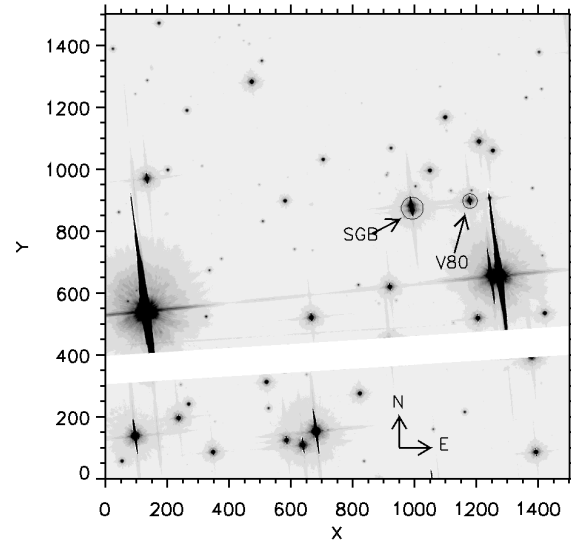


Fig. A.3. Finding chart for V80 and SG. Plate scale is $0.05''$ per pixel. Image from ACS on *HST*

Chapter 4

Building a stellar evolution test set

Generalising the ideas of the previous chapter to many clusters requires that multiple cluster member detached eclipsing binaries exist in a number of stellar clusters. In this chapter, this is proven to be true. Methods for detecting and measuring these and many more systems are detailed.

In order for the multiple cluster member dEB method to be more than just something which can be used in rare cases, multiple cluster member dEBs in a number of stellar clusters need to be located, and have their parameters measured accurately. Since eclipses only occur in binary systems with a very favourable orientation, one may think that stellar clusters with more than one usable dEB are very rare, and that this will never be possible. But another point of view is that they could just be hard to find.

Finding cluster member dEBs takes a lot of effort and observing time. They are usually searched for along with other variable stars in photometric observing campaigns where the same stellar cluster is monitored continuously during several nights. But single telescope observations are interrupted by daytime, during which eclipses will be missed. Bad weather may decrease the detection rate even further. Rucinski et al. (1996) made a rough simulation of how many eclipsing binaries are missed during a single site observing campaign of 14 nights. Even under favorable assumptions they find that for progressively longer orbital periods starting at around 8 days, as many as one third of all systems will go undetected. This number is further increased for periods close to a multiple of one day. Although not commented upon by Rucinski et al., most systems with periods longer than the observing campaign will also go undetected. And for many systems which are detected, only one eclipse is seen. Systems which are detected then need to have cluster membership confirmed through radial velocity measurements, which also establish the periods and ephemeris and a first mass estimate.

The open clusters NGC2243 and NGC2506 have both been targeted by photometric campaigns to look for variable stars including dEBs. NGC2243 was monitored by Kaluzny et al. (1996, 2006a) who identified a number of cluster member dEB candidates, but they only targeted one of these systems with a full analysis (Kaluzny et al. 2006b). NGC2506 was monitored by Arentoft et al. (2007) who identified a number of dEB candidates worthy of follow-up. For each of these two clusters we obtained 15 epochs of spectra of the cluster member dEB candidates using FLAMES at the VLT in the IFU mode. Results of a preliminary analysis are shown in table 4.1, and confirm the existence of multiple cluster member dEBs in both clusters. Furthermore the observed period distribution strongly indicates in addition a detection bias in favour of short periods in line with the results of Rucinski et al., indicating that many more systems could, and most likely do, exist in these and other clusters. Very recent results from the *Kepler* mission show that for dEBs in the field, there is only a slow drop in the number of

Table 4.1: Preliminary orbital periods and cluster membership information on known dEBs in the fields of the open clusters NGC2243 and NGC2506. *Published P* are the periods of the systems where a photometric period has been published. *Spectroscopic P* are the new periods determined from FLAMES spectra using the broadening function formalism. As seen, multiple cluster member dEBs are confirmed in both clusters, since they are radial velocity members (an exception is V5 in NGC2243 which is a radial velocity member, but its mass reveals that it is not a real cluster member.) As seen, all orbital periods determined are below 4.6 days, with a single exception. This suggests that many more dEBs, with longer periods, exist in the clusters, but have just not been identified yet.

Variable name	Published P	Spectroscopic P	RV (km/s)	Member	Note
NGC2506:					
V4	2.868	2.868	83.74	Y	SB2
V5	10.078	3.3593	84.58	Y	SB2, <i>l3</i> ?
V9	0.9392	0.9392		Y	
V26	-	4.589	60.36	N	$M_{1,2} \sim 0.5M_{sun}$
V27	-	4.053	76.92	?	SB1
NGC2243:					
V1	1.18851590	1.18851590		Y	
V7	1.382703	1.382703		Y	
V9	-	3.257	58.16	Y	SB2, <i>l3</i> !
V14	-	1.0777	57.97	Y	SB2, detached?
V4	-			N	SB2
V5	-	25.6	57.52	N	$M_{1,2} \sim 3.6M_{sun}$
V8	-				SB1
V11	-			?	most likely not dEB

dEBs with increasing orbital period (Prsa et al. 2010, Fig. 4.1). Assuming that cluster member dEBs have the same period distribution as field dEBs, this is a further indication that more dEBs exist in clusters. If the period distribution is different in clusters relative to field stars, then that is interesting to determine.

The next step for these clusters is to gather the remaining data needed for a full analysis of the cluster member dEBs along the lines of Brogaard et al. (2010) in chapter 3. Some of the systems contain a third light, and therefore we are planning to observe them using Lucky Imaging to separate the third light and measure its contribution. Additional photometry for some systems is needed as well.

The open cluster NGC188 has been monitored for variable stars several times, latest by Mochejska et al. (2008) with observations spread over 45 nights. Despite this, only one dEB was identified from photometry. This was V12, first discovered by Zhang et al. (2002), followed by measurements of masses and radii by Meibom et al. (2009). But when Geller et al. (2009) published their radial velocity survey of the cluster, they noticed that another star V11, which they find to be a cluster member spectroscopic binary with an orbital period of 35.178 days, was actually classified as an eclipsing binary by Kaluzny (1990) based on the dimming of the star by almost 0.4 magnitudes (but measured from only 1 data point!). Since, if true, that would put the most massive component on the giant branch and the other at the cluster turnoff, two rapid phases of evolution, such a system would be very useful for cluster age measurement and stellar evolution tests, especially when combined with the measurements of V12. Only two detached eclipsing binaries with a giant component have so far been found and measured (TZ For and

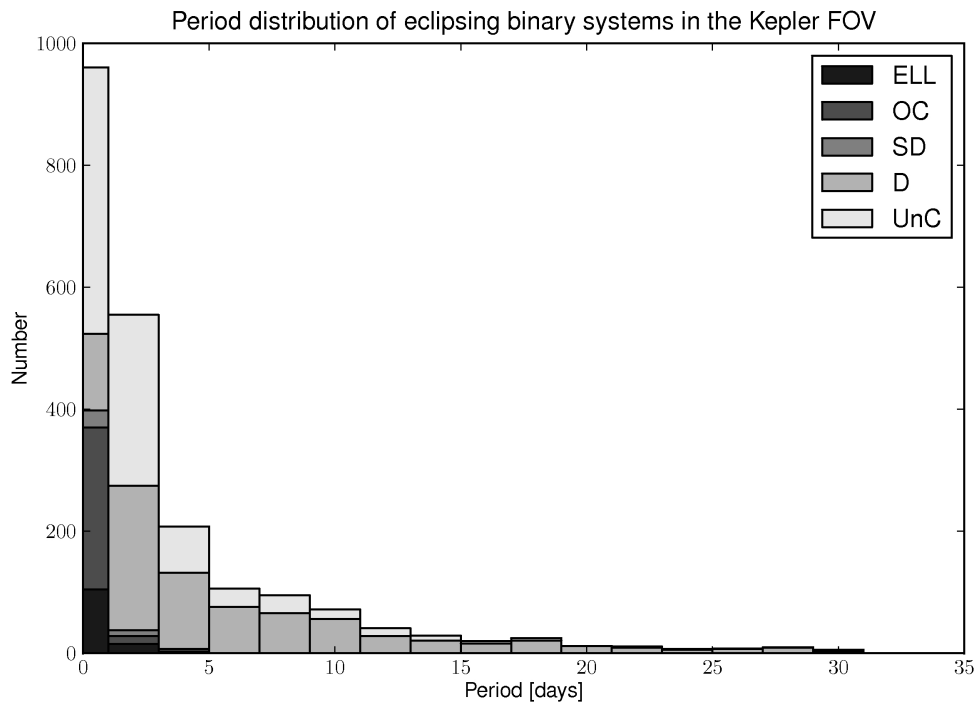


Figure 4.1: Period distribution for the eclipsing binaries in the Kepler FOV from Prsa et al. (2010). *D* is detached eclipsing binaries.

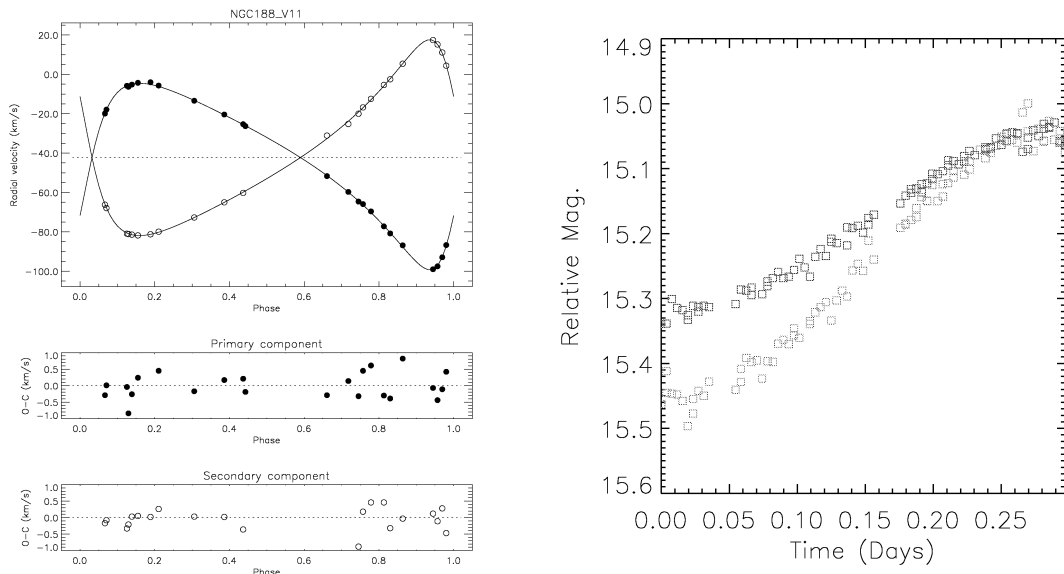


Figure 4.2: Radial velocity and light curve measurements of the dEB V11. Radial velocity measurements are those of Geller et al. (2009) supplemented by additional measurements from FIES spectra from the Nordic Optical Telescope. The light curve measurements are those of Arto Oksanen from his own observatory. Shown are V and I band measurements (the eclipse is deepest in V).

AI Phe) and none of those are stellar cluster members, for which additional information can be added to the analysis. We therefore obtained spectra of V11 using the FIES spectrograph at the Nordic Optical Telescope and measured more radial velocities, which we combined with the radial velocities of Geller et al. (2009), in order to improve the period and ephemeris of the system. We then confirmed a dimming of V11 by about 0.3 magnitudes in V and I and about 0.4 in B on nights of expected eclipse from a few observations taken at the Nordic Optical Telescope with the kind assistance of several people who happened to be observing on those nights (thanks!). With our instructions, amateur astronomer Arto Oksanen then managed to observe part of an eclipse from his own observatory. Data gathered so far for V11 is presented in figure 4.2, and its CMD position along with that of the other dEB, V12, is shown in figure 4.3. One should note that three additional spectroscopic binaries in the survey of Geller et al. (2009) could potentially be eclipsing systems (IDs 3344, 4411 and 4986), but with their long periods (>30 days) and presently not very precise ephemerides it will take some effort to confirm or reject them.

M67 has also been the target for a number variable star searches. Sandquist & Shetrone (2003) found a cluster member dEB at the turnoff, s986, which they partially analysed, but they were unable to measure the component masses and radii because the secondary component is so faint that it was not visible in their (optical) spectra. Sandquist (2006) found additional cluster member dEB candidates, which seem questionable members from their CMD positions, but should be investigated further. Stello et al. (2006) had a multi-site observing campaign on M67, but their dataset was never investigated for the presence of dEBs (D. Stello, private communication). For this cluster we have so far concentrated on attempting to measure the

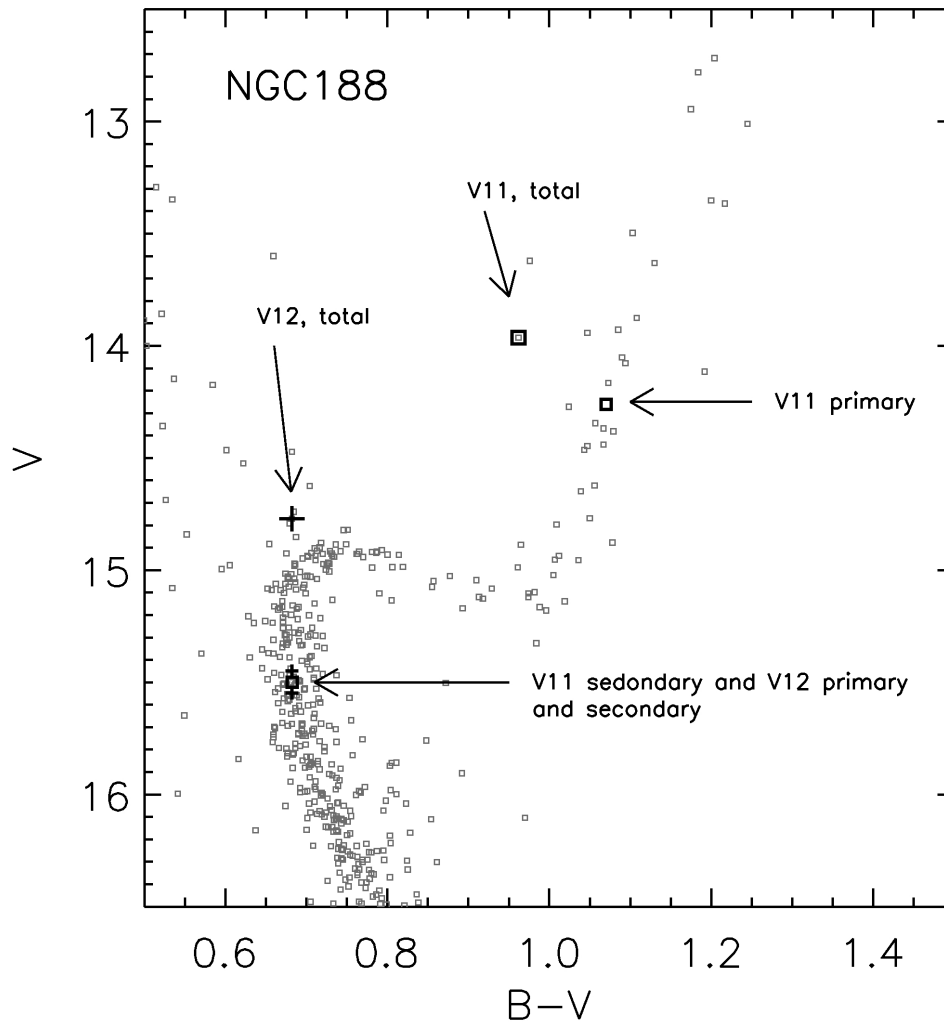


Figure 4.3: The dEBs V11 and V12 in the CMD of then open cluster NGC188.

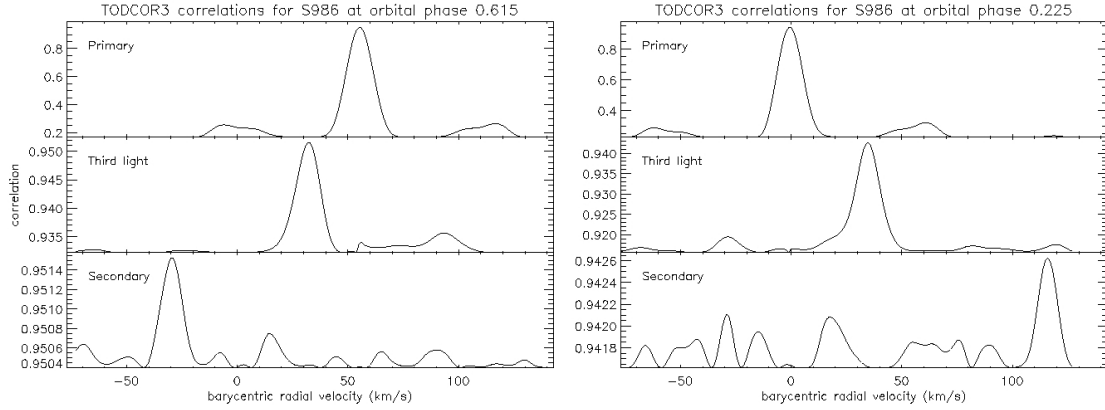


Figure 4.4: S986 TODCOR3 cross correlation projections for radial velocity measurements of the components.

masses and radii of the known dEB s986 because its position in the cluster CMD suggests that it may provide additional model constraints on top of the usual masses and radii (chapter 5). We managed to measure the radial velocity of the secondary component in infrared spectra using the CRIRES instrument at the VLT. Unfortunately CRIRES has had (and still has) several technical problems, both concerning its operations and its pipeline, which has delayed this project severely. Therefore, at this point we have only measured the radial velocity of the secondary component in two spectra. 7 additional infrared spectra have been obtained but are not reduced and analysed yet. High quality light curves of the eclipses in R and I bands have been obtained from 6 nights of observations at the Nordic Optical Telescope. These were reduced and analysed by BSc student Jens Jessen-Hansen under my co-supervision. Relative radii with an accuracy better than 1% have been obtained. With future analysis of the infrared spectra we will be able to measure the masses and radii of this very interesting dEB. But presently it is unclear how many additional spectra will be needed in order to reach an accuracy of 1%, which is needed to make interesting conclusions. Figures 4.4 and 4.5 show radial velocity measurements and light curves of s986.

The open cluster NGC6791 has been targeted by numerous photometric campaigns, many of which were looking for planets in the cluster. Mochejska et al. (2005) and de Marchi et al. (2007) identified a very large number of dEBs in the field of NGC6791. While we already confirmed 3 dEB cluster members, V18, V20 and V80 (chapter 3), there are many additional cluster member candidates. I went through these works, and selected interesting cluster member candidates based on their position in the CMD and any available proper motion membership. I selected only dEBs which show no out-of-eclipse variability, indicating that the components are well detached. Only systems with a total V magnitude brighter than 20 was selected, since experience from V20 and V80 shows that we can measure accurate masses at least down to this limit. Light curves for these systems, with CMD positions shown in Fig. 4.6, will be observed by the *Kepler* mission (chapter 4), and a proposal for spectroscopy using FLAMES at the VLT will be submitted at the next proposal deadline. Since this cluster is very rich in stars and dEBs, this is also an obvious place to look for dEBs with a component which has evolved off the main sequence and therefore has very age sensitive parameters. We identified among the dEBs in Mochejska et al. (2005) two such candidate systems, for which we obtained Directors Discretionary Time with UVES at the ESO VLT to determine cluster membership. Unfortunately, in this case they both turned out to be non-members, both by radial velocity

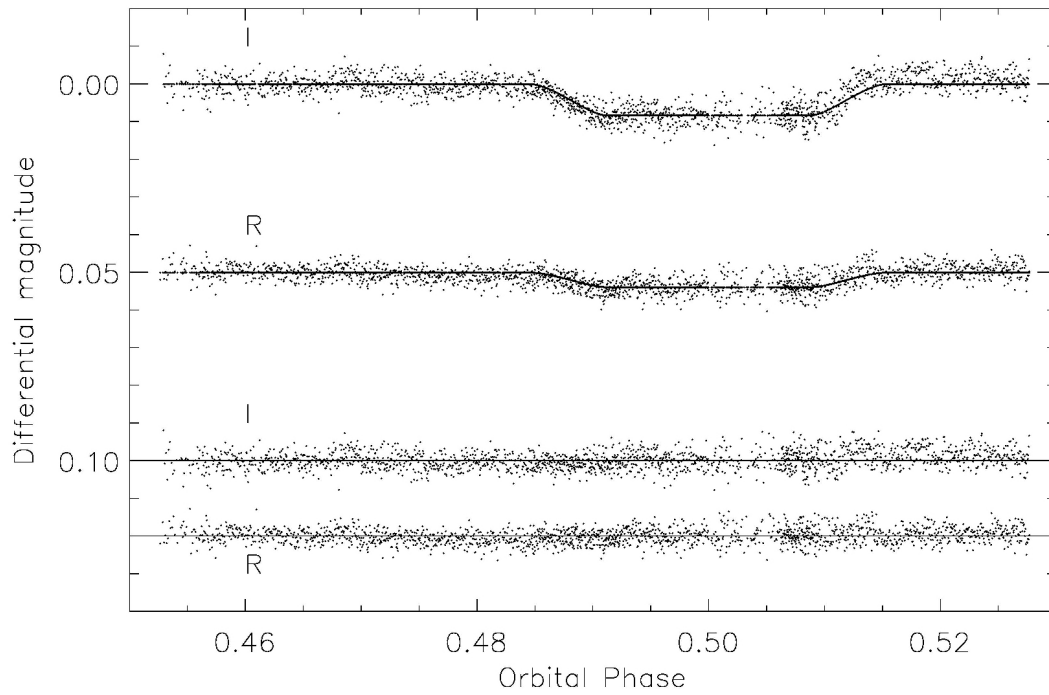
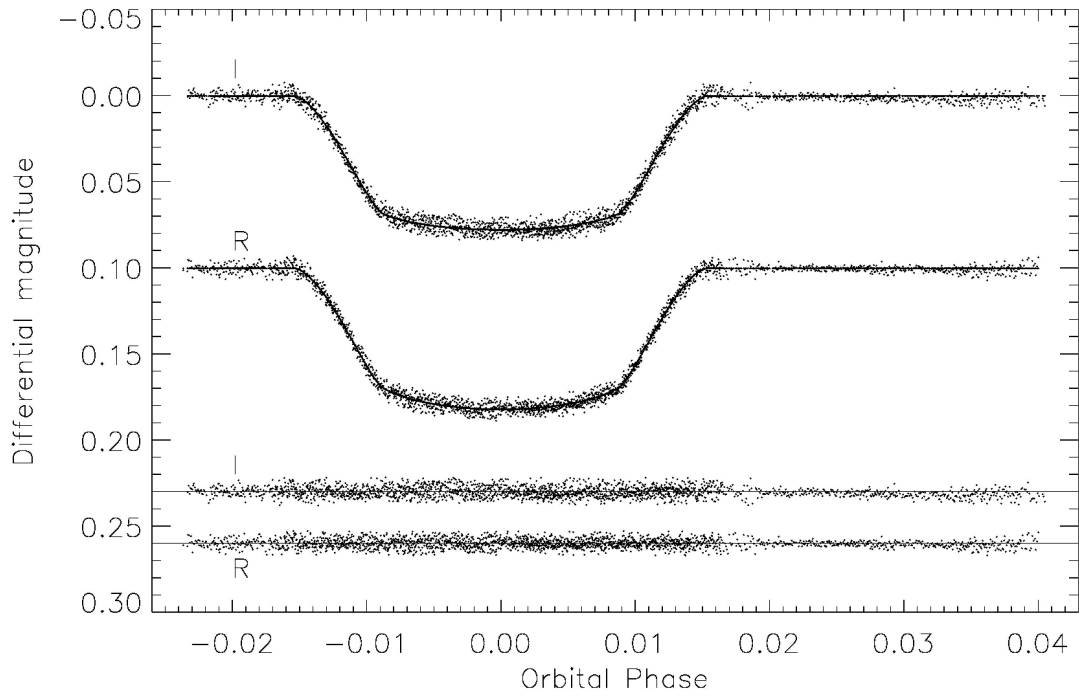


Figure 4.5: S986 light curves as reduced by Jens-Jessen-Hansen. The lightcurve is overplotted with the best-fitting model from the light curve analysis program JKTEBOP.

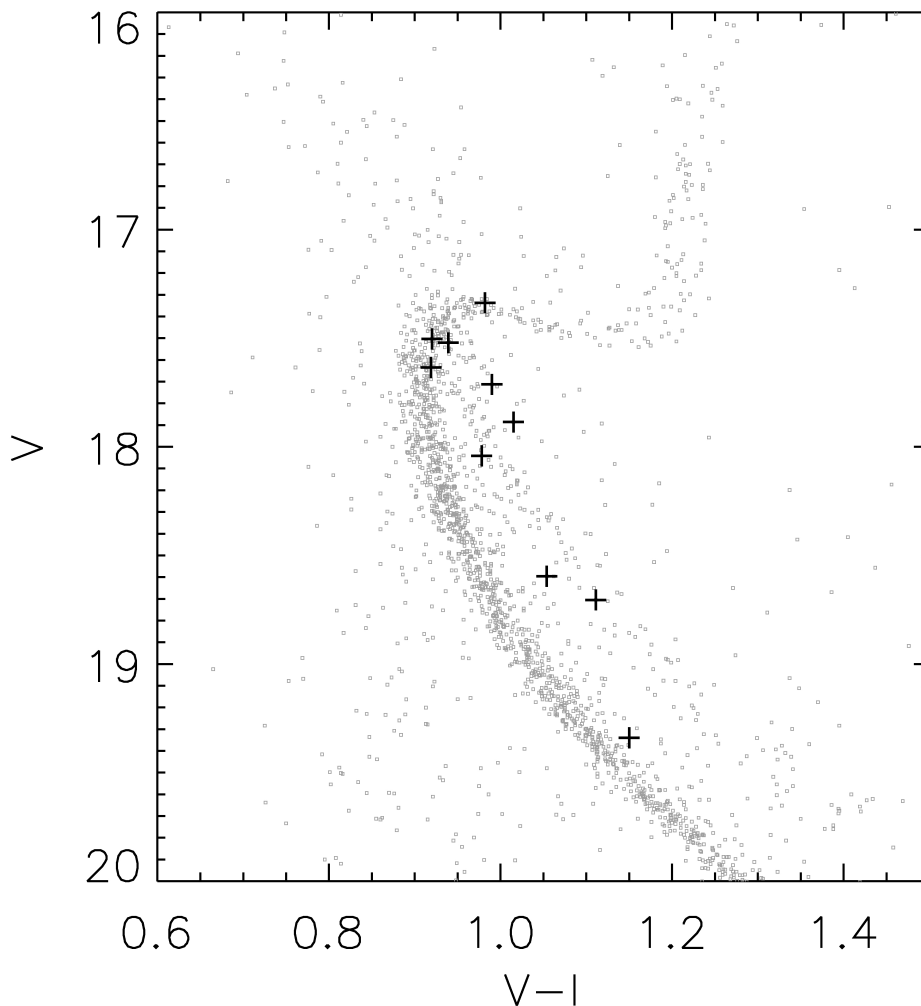


Figure 4.6: NGC6791 detached eclipsing binary cluster member candidates with $V \leq 20$.

and by mass (Fig. 4.7 and Table 4.2).

So far our work has only adressed open clusters, and not the older globular clusters. However there is no reason why multiple dEBs should not exist in globular clusters as well. There does seem to be a smaller fraction of binary stars in the globular clusters than in the open clusters, but again the problem of detection could be the main reason why so few dEBs have been found in the globular clusters so far. Thompson et al. (2010) measured accurate parameters of a dEB in the globular cluster 47 Tucanae. Actually we also attempted to measure parameters of a dEB in 47 Tucanae, WF4-04, identified by Albrow et al. (2001). However, I found that the field was too crowded for the observations using UVES at the VLT with a $0.8''$ slit to be useful. Since then other options have become available and with this being potentially the second dEB in 47 Tucanae, with prospects for much better model constraints, I am considering observing this dEB again. To reduce crowding issues it could be observed with either the new VLT instrument X-shooter, which can observe with a narrow slit of $0.4''$, or with FLAMES in the IFU mode,

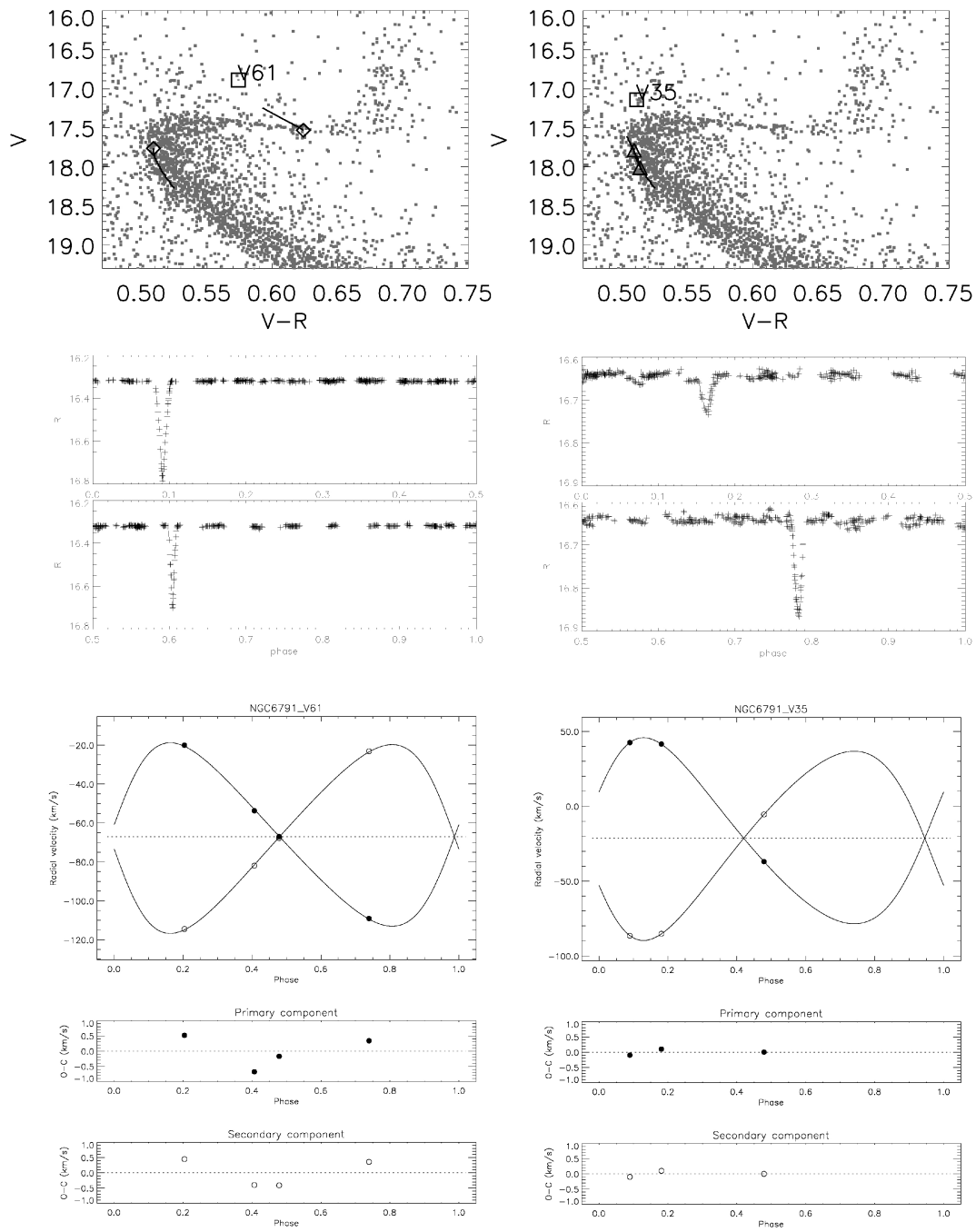


Figure 4.7: Data on V35 and V61.

Table 4.2: Summary information on the dEBs V35 and V61 shown in Fig. 4.7. These systems were found to be possible cluster members based on their position in the CMD, see Fig. 4.7 top panels. I redetermined the orbital periods from the photometry of Mochejska et al. (2005), finding that their period for V35 was a factor of four too low, while the period of V61 was found in good agreement with their determination. Fig. 4.7 middle panels show the R band light curves of Mochejska et al. (2005) phased with my period measurements. No attempts have been made to shift primary eclipse to phase 0. From the phase difference between primary and secondary eclipses and the difference in duration between eclipses, I measured the eccentricity of the systems. These measurements of period and eccentricity were used as input for SBOP orbital solutions of radial velocity measurements from UVES spectra, see Fig. 4.7 lower panels. Results (in this table) show that the dEBs are unfortunately not cluster members - their radial velocities are not near the radial velocity of the cluster ($\gamma_{\text{NGC6791}} \sim -47$ km/s) and their minimum masses are not consistent with the masses of the known dEB cluster members V18, V20 and V80 (chapter 3).

	V61	V35
P (days)	19.3838	12.875
e	0.23	0.193
γ	-67.05 ± 0.260	-21.35 ± 0.110
$M_p \sin^3(i)/M_{\text{sun}}$	0.822 ± 0.016	1.254 ± 0.008
$M_s \sin^3(i)/M_{\text{sun}}$	0.799 ± 0.015	1.232 ± 0.008

which effectively is many small slits of 0.5" width.

NGC6362 will be an important target in going to the globular clusters. This globular cluster hosts 8 cluster member dEB candidates (6 found by Mazur et al. 1999, and 2 additional found by Lars Glowienka as part of his master thesis at Aarhus University) and is thus the presently best candidate to exploit FLAMES in the IFU mode, to observe the 8 candidates simultaneously and determine their cluster membership.

For finding practically ALL cluster member dEBs in any cluster in a time efficient way, I have suggested to use the world-wide telescope network of the Stellar Observations Network Group (SONG, Grundahl et al. 2008a) which is currently being built. Since such a network can observe 24 hours a day (or rather night!), there is no daytime interruptions during which eclipses can be lost. And since eclipses last around 6-9 hours in most cases, one observation every 3-4 hours will be enough to be sure not to miss a single eclipse of any dEB present in the cluster field. Continuing this procedure for some months on a given cluster will detect all interesting dEBs. Further advantages of using SONG is that they will use Lucky Imaging cameras, which will help detect and measure any third light components right from the beginning. And because all the telescopes are identical, data reduction will be as easy as for a single telescope. The only small problem is that the currently planned field-of-view is quite small, and therefore one may need a couple of exposures instead of one, every 3-4 hours, in order to cover the cluster. But with the promise of this procedure to find ALL interesting cluster member dEBs, it should still be considered.

Even without such dedicated efforts more cluster member dEBs will be found in the future as bi-products of other observational efforts like Pan-STARRS (Panoramic Survey And Rapid Response System, Burgett & Kaiser 2009) which will survey the sky with the primary aim of detecting near-Earth objects that threaten to cause impact events. A few open clusters, including NGC 6791, are located in the field-of-view of the *Kepler* satellite, which is continuously

observing the same section of the sky for a period of several years with the primary aim of detecting planets around stars. Due to a limited transmission capacity data will not be recorded for every star in the field, but luckily large areas centered on the two open clusters NGC6791 and NGC6819 are being monitored for other purposes, and this data will be publicly available at some point to be searched for cluster member dEBs. In addition, a *Kepler* Guest Observer program by Ruth Peterson et al. (Fig. 4.8) will search for bright dEBs in the outer regions of NGC6791. Such efforts promise to find practically all dEBs in these clusters, though some additional observations will be needed for exact identification, since each *Kepler* pixel is about 4" x 4" and will therefore often contain more than one star. This will not be a problem for the *Kepler* Guest Observer program by Sandquist et al. (Fig. 4.8) which targets only known dEBs in the clusters. The large pixel size and the long integration time (29.44 minutes) in the so-called long cadence mode which is being used will make it challenging for these programs to use the *Kepler* light curves of the dEBs for accurate radii measurements. The long integration time will blur the fine details of the eclipses. As already mentioned several stars can be present in each pixel due to the large pixel size, and all additional stars will combine to a third light contribution, which will be difficult to measure. But it may still be possible with the proper use of image subtraction methods and the use of prior knowledge from higher resolution imaging. The fact that *Kepler* rotates once every three months may be a help in the deblending of starlight, since the stars will then be positioned differently at the subpixel level, and this will aid in determining the origin of each light contribution.

As an example of the promises and challenges awaiting, let us look at the *Kepler* long cadence light curve of the NGC6791 cluster member dEB V20 (Fig. 4.9 and 4.10), which was publicly released on June 15 2010, along with light curves of all other dEBs found in the *Kepler* field-of-view (excluding the open clusters for unknown reason), except V20 (again for unknown reason). The light curve shows the eclipses nicely and the rms scatter is at millimag per measurement level, indicating that dEBs present in NGC6791 can quite easily be found and have their periods and ephemerides measured. However the light curve of V20 also shows an out-of-eclipse variability with an amplitude of about 1%. This variability could originate from V20, but it could also come from any other star fully or partially present in the same pixel as V20. This cannot be determined at present, because only the pipeline reduced light curve is available, and not the pixel level data, which will be needed to attempt to solve such problems. Similarly it is presently not possible to determine the amount of third light due to contamination from nearby stars.

ECLIPSING BINARIES IN THE OLD OPEN CLUSTER NGC 6791

Ruth Peterson
Astrophysical Advances

We propose 73 photometrically-selected targets with $V < 16.6$ within $12'$ of the center of the old, metal-rich open cluster NGC 6791 for Kepler 30-min sequence observations. The goal is to detect eclipsing binaries suitable for determining the masses of the components, through future observations of radial velocities with large ground-based telescopes, and possibly of orbits with SIM. Our targets are giants and subgiants, not main-sequence stars, in order to reduce confusion in the Kepler field and to provide feasible targets for spectroscopy. Towards the center of the cluster, the high stellar densities dramatically increase crowding and cause binaries to be more readily perturbed. Consequently we are including many targets in the outer regions of the cluster, those which fall on the cluster color-magnitude and color-color diagrams defined by the inner members. We need a large target sample to isolate favorable binaries, as some stars will be non-members, only half of the members will be in binaries, many of these will have merged, and only a few of those remaining are useful. Suitable binary systems must not be triple, and should include a giant and a main-sequence turnoff star so that both components can be detected spectroscopically. The components must not have previously exchanged or lost mass. Binary periods must be nearly a year to a few years, so the orientation must be nearly edge-on and the eccentricity will be finite. We expect the proposed observations to yield at least two non-interacting binaries from which both component masses can be obtained. For such binaries, eclipse depths of 10% over a day or more are expected, and are readily apparent from applying standard filters to the pipeline light curves. Radial-velocity curves will be based on echelle spectroscopy analyzed with IRAF, as we have done in our decade-long survey of the brightest NGC 6791 giants with the Lick Hamilton echelle. The effective temperature, gravity, and metallicity of each of the stellar components will be found from theoretical spectral calculations, which now match such strong-lined stars reasonably well thanks to an updated list of line parameters. This work should stringently constrain comparisons of observed color-magnitude diagrams to produce meaningful cluster parameters. Such constraints would have major significance for the validation or refinement of stellar evolutionary tracks at high metallicity, and the derivation of age and metallicity from broadband colors of both individual stars and integrated spectra of old elliptical galaxies, for which NGC 6791 is a critical template.

AGE-SENSITIVE DETACHED ECLIPSING BINARIES IN OPEN STAR CLUSTERS NGC 6791 AND NGC 6819

Eric Sandquist
San Diego State University

Age is difficult to measure extremely precisely for stars other than the Sun. In the field being observed by Kepler, the stars of the open clusters NGC 6791 and NGC 6819 are the ones that can be most precisely age-dated. However, different methods provide ages that differ significantly. We propose an effort to bring methods of stellar age determination into agreement through the use of Kepler data for these star clusters. Here we focus on the use of masses and sizes measured from weakly-interacting eclipsing binary star systems in the clusters. Massive stars run out of hydrogen fuel at their centers before less massive ones, and start to change rapidly in size - for such rapidly evolving stars, measurements of both mass and radius that are precise to 1% can lead to ages precise to 10% and better. Further, mass and radius measurements are conceptually simple to derive from observations, and avoid complicating effects like uncertainties in distance and reddening. High precision age measurements from this and other methods will make these star clusters important testbeds for models of stars and stellar populations in galaxies.

Figure 4.8: *Kepler* Guest Observer programs on cluster member detached eclipsing binaries.
(<http://keplergo.arc.nasa.gov/Programs.shtml>)

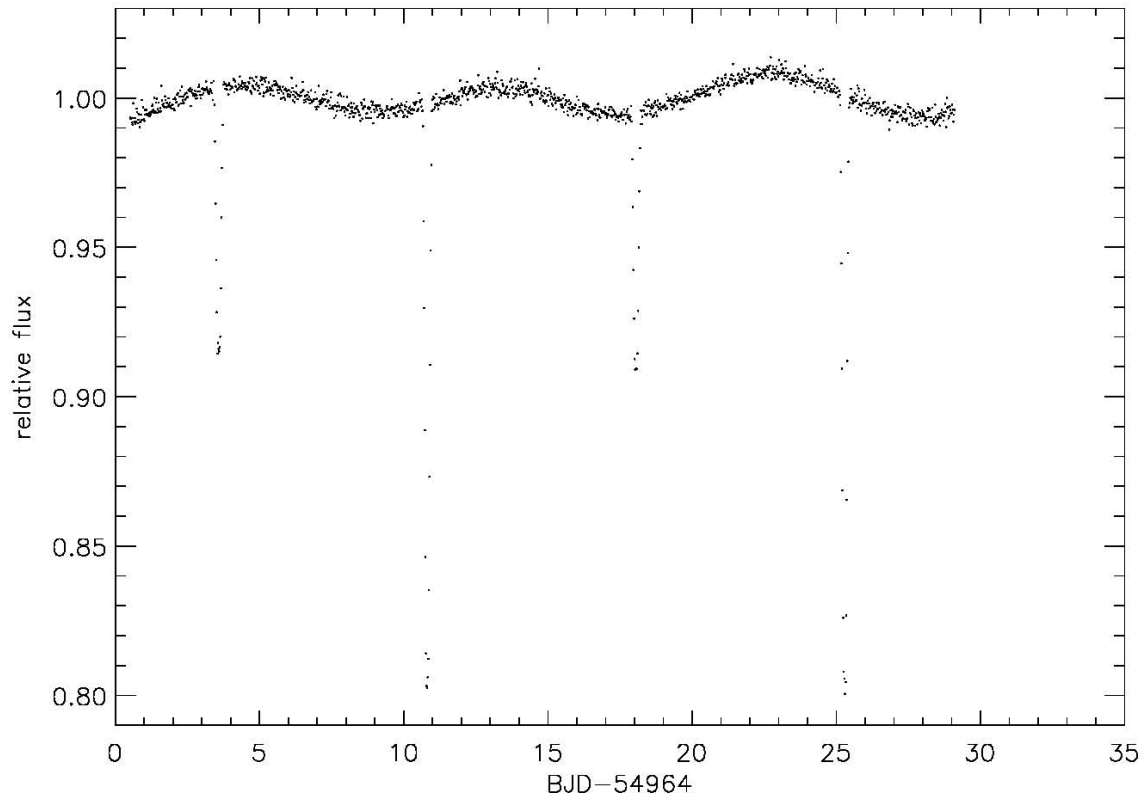


Figure 4.9: Light curve of V20 observed by it Kepler.

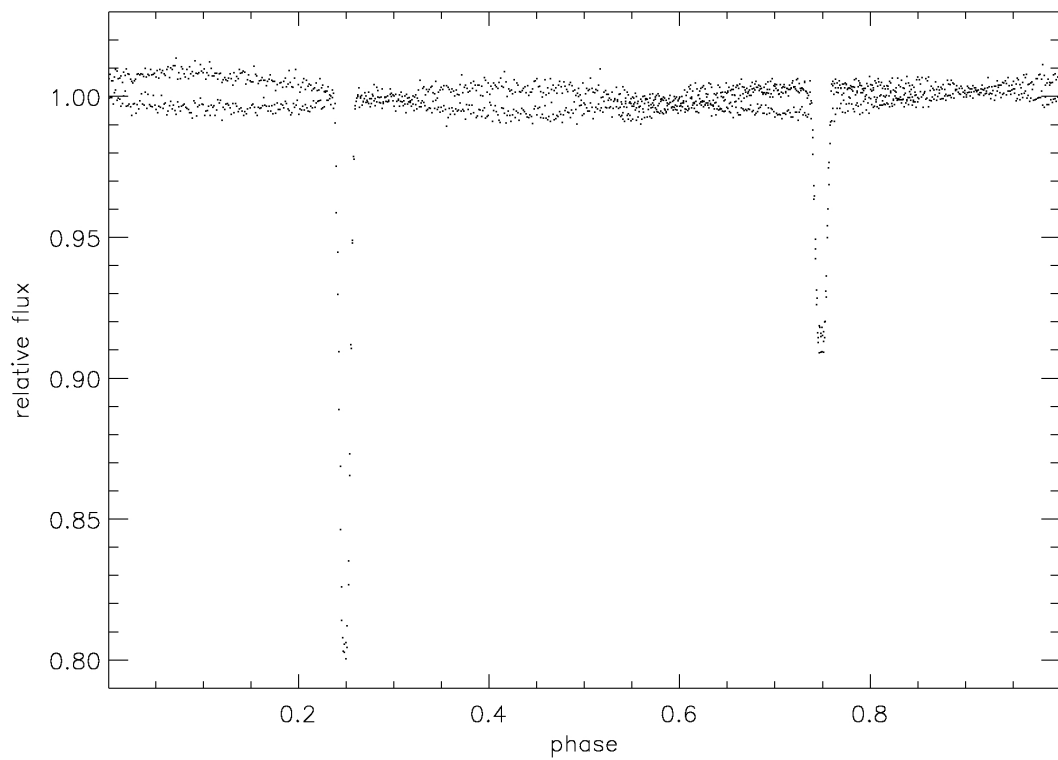


Figure 4.10: Light curve of V20 observed by *Kepler*, phased with the period determined by Grundahl et al. (2008b).

Chapter 5

Which aspects of stellar evolution can be tested?

Here we look into some details on stellar evolution tests using multiple cluster member eclipsing binaries, to see which aspects are tested. It turns out that, while it is clear that the method does provide new insights, it is very difficult to predict what they are.

The idea behind using multiple cluster member dEBs for cluster age measurements and tests of stellar evolution is actually very simple. It all comes down to gathering as many complementary constraints as possible. Unfortunately, even when doing this, it can be quite difficult to interpret results (KB08, and chapter 3). To see this, let us first look at a specific project aimed at understanding the effects of the detailed abundance pattern on stellar evolution. Fig. 5.1 shows a mass-radius diagram with preliminary measurements of the dEB V1 in the open cluster NGC2243. Measurements are compared to stellar model isochrones, chosen to match the measurements of the primary dEB component. One can see that measurable differences exist between different stellar model sets, but also between models where the only difference is the detailed abundance pattern, in this case the abundance of the α elements.

The potential of obtaining measurements of multiple dEBs of different masses in the same cluster should be clear: the shape of the isochrone in the mass-radius diagram can be constrained. Stars with masses close to or after the turn-off are mostly sensitive to age. Going to lower mass stars, they will be less sensitive to age while increasingly sensitive to the chemical composition, including helium content and the detailed heavy element abundance pattern. Therefore, by measuring stars with masses near the turn-off, mostly sensitive to age AND stars of lower mass, mostly sensitive to composition, it is the hope that the two can be disentangled, leading to a more accurate age measurement. Adding also information from the cluster CMD should aid this, since the hook at the turn-off in the CMD of NGC2243 appears to be also very sensitive to the abundance pattern (F. Grundahl, private communication). This is the basic reasoning behind our ongoing project to measure parameters of multiple dEBs in NGC2243 and NGC2506 (chapter 4). However this simple reasoning only holds true if the details of stellar evolution are correct. One may expect to be able to discard models with wrong assumptions based on their inability to match such measurements, but this is still difficult because age is a free parameter and the model helium content is flexible due to our inability to measure directly the helium content of stars. In fact, due to the need for a mixing length theory of convection, and a corresponding model calibration on the sun, a wrong model may turn out to match measurements better than one employing the correct physics because of assumptions in the mixing length theory which may turn out to be incorrect. Efforts are on the way to improve this situation by implementing the results of new hydrodynamical convection simulations into stellar

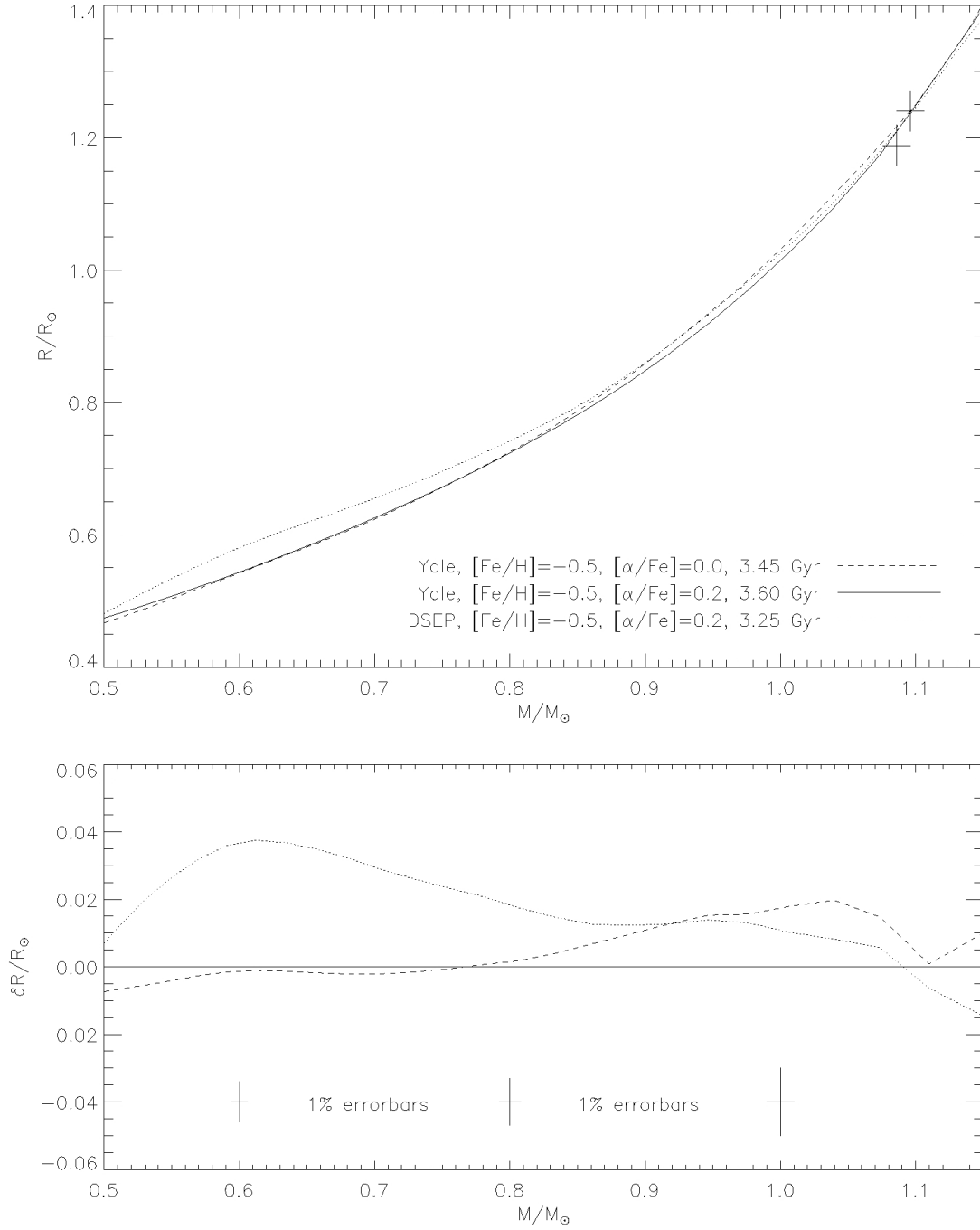


Figure 5.1: Preliminary measurements of the dEB V1 in NGC2243 compared to model isochrones. Top: Isochrones from two stellar evolution codes, Yale and Dartmouth, and two different abundance patterns, compared to masses and radii of the cluster member dEB V1. Bottom: Model differences illustrated by showing the isochrones relative to each other. The 1% error bars indicate expected errors on dEB measurements. It is seen that measuring more dEBs in this mass range will allow to distinguish between the models shown.

models, thus avoiding the need to calibrate convection on the sun (Arnett et al. 2010). Early results indicate that the present assumption of a mixing length theory with identical convective efficiency for all stars is not valid. This will complicate the situation when trying to interpret measurements of multiple cluster member dEBs as described above. On the other hand, this may be the only way to confirm or reject the validity of such new stellar models.

Another current issue for stellar models is the dispute on the absolute values of the solar abundances. Briefly, new solar abundances have been derived using highly sophisticated non-LTE 3D model atmospheres (Asplund et al. 2006, and references therein). The difference from earlier results is particularly in the C, N and O abundances, which are now predicted to be as much as 0.15-0.20 dex lower than previously thought. However results from helioseismology (Christensen-Dalsgaard 2002, and Turck-Chièze et al. 2004) strongly favor the old set of solar abundances (by Grevesse & Sauval 1998, hereafter GS98). Caffau et al. (2008, 2009) recently found abundances for O and N in between these values, but they did not argue why their results should be trusted more than the ones by Asplund, although they claim to have identified the reason for the different results. Asplund et al. (2009) then published a set of further revised abundances, which were not as extreme in their differences from the GS98 values, but still significantly different. The case remains unsettled and, since it has wide implications for many branches of astrophysics, it is highly desirable to obtain further and stronger constraints on this problem. Interestingly, the information needed to make progress may be found in the open cluster M67. This is due to a fortuitous combination of features of this cluster: (i) it has virtually the same abundances as the Sun (Randich et al. 2006, Pace et al. 2008) and (ii) the turn-off stars have convective cores. This second feature creates a hook and a gap at the turn-off of the cluster color-magnitude diagram (CMD), because stars with convective cores undergo a fast contraction phase just after depletion of hydrogen in the core. Stars with radiative cores do not undergo this phase, and thus no hook and gap will be present in the CMD of a cluster, if the turn-off stars have radiative cores. The mass at which there is a transition between radiative and convective core, at the end of hydrogen burning, is called the transition mass. If the transition mass is higher than the turn-off mass, the turn-off stars will have radiative cores and no hook and gap will be present in the CMD. If the transition mass is lower than the turn-off mass, the turn-off stars will have convective cores and the CMD will show hook and gap features. The transition mass depends strongly on abundances, particularly the CNO abundances, because the transition to convective cores happens when the CNO-cycle burning process becomes dominant. More CNO means faster CNO-cycle burning, producing a convective core at lower mass. Therefore, if the cluster transition mass is close to the turn-off mass, which is the case for M67, the assumed CNO abundances will make the difference of whether or not a stellar model isochrone will display hook and gap features. Vandenberg et al. (2007) used these facts to show that with the new (low Z) abundances it was impossible to find an isochrone of any age, which matches the hook at the turn-off, whereas a nicely fitting isochrone was found using the old (high Z) abundances, see Fig. 5.2. This might be taken as an indication that the old (high Z) solar abundances are correct and that the recent downward revisions are in error. However, as also mentioned by these authors, one should not ignore the possibility that the effects of diffusion of helium and metals in the M67 stars have lowered the transition mass (Michaud et al. 2004).

Very recently, the issue of using M67 for constraints on the solar abundances was revisited by (Magic et al. 2010). They first reproduce the results of Vandenberg et al. (2007), and then move on to show that when including element diffusion, the results are too dependent on other uncertain factors, particularly overshooting, for any conclusions to be made about the solar abundances based on the CMD of M67. Neither Vandenberg et al. (2007) nor Magic et al. (2010) mention that maybe something could be said by adding more information into the

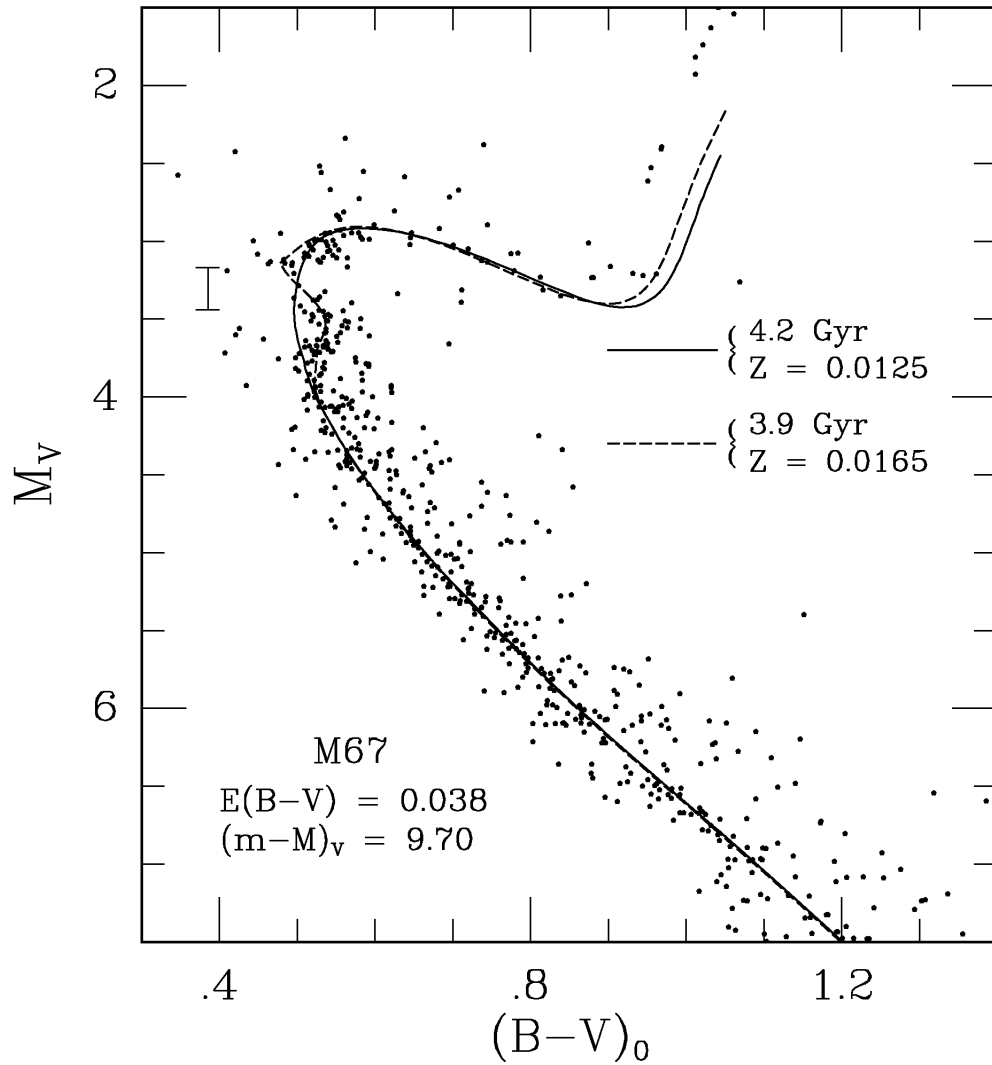


Figure 5.2: M67 CMD from VandenBerg et al. (2007). The solid line is an isochrone calculated assuming the Asplund et al. (2006) abundances. The dashed line is an isochrone calculated assuming Grevesse & Sauval (1998) solar abundances. As seen, only the latter reproduces the observed hook at the cluster turn-off.

analysis. More specifically we aim to add measurements of masses and radii for the presently only known dEB in M67, s986 (Sandquist et al. 2003). It is well suited, as it has a component just above the cluster turn-off (see Fig. 5.3), and moreover the components have very different masses and radii. Furthermore, because the dEB primary component is located in the hook region of the CMD, its mass must be just above the transition mass. Measuring accurate masses and radii of the components of this dEB will therefore allow us to discriminate between at least some of the model physics, by requiring that the correct model isochrone matches the observations, in both the mass-radius diagram and the CMD, and has a transition mass smaller than the dEB primary component. Employing these additional constraints may therefore lead to a conclusion regarding both the solar abundances and diffusion as well as an accurate age determination of M67. This will be attempted once our mass and radius measurements are completed. Additional clusters which may also provide additional information on this problem in the future is NGC188, NGC7789, and NGC6819, which all have very close to solar metallicity and hosts multiple dEBs, some of which we are the process of measuring.

From the above it should be clear that in order to make real progress in our knowledge of stellar evolution, we need to gather as many and as strong model constraints as possible. A combined analysis of many clusters with multiple dEBs, each of different age and metallicity (or as in the above example of different age but the same metallicity), will provide stronger model constraints than any individual analysis. But for each cluster, one should also focus on adding as many constraints as possible.

For some open clusters it will now be possible to do asteroseismology on the single stars. This is the case for NGC2506, where a number of γ Doradus variable stars have been located in the turn-off region (Arentoft et al. 2007). As part of our project on this cluster we measured the radial velocities of the γ Doradus stars, and confirmed the vast majority to be cluster members (the few which are not directly radial velocity members are most likely binaries). They are thus usable for an analysis combining the cluster member dEBs, the cluster CMD and asteroseismology of the γ Doradus stars. Grigahcene et al. (2010) already analysed one of these stars demonstrating the potential of combining asteroseismology with cluster parameters. Such analysis will be further strengthened once including all the γ Doradus stars, and even more, when adding the accurate dEB measurements we will obtain once finishing our analysis of this cluster.

Perhaps the most promising candidates for enhancing our knowledge of stellar evolution are the open clusters NGC6791 and NGC6819, due to their position in the FOV of the *Kepler* mission. Ensemble asteroseismology will be performed on stars in these clusters showing solar-like oscillations, which on its own should provide a better insight into these clusters. Due to the faintness of the clusters, results can only be expected for giant stars in NGC6791 and for stars at or brighter than the turn-off in NGC6819. First asteroseismic results have already been published for stars in NGC6819 (Stello et al. 2010, Appendix B) where we also hint at the prospects of combining the asteroseismology with cluster member dEB measurements. Here I will elaborate on this. First, since asteroseismology will be done for stars brighter than the turn-off and the known dEBs in these clusters are located from the turn-off and down, a combined analysis will address a larger range of stars in the clusters. For the same chemical composition, helium content and age, we can demand that a model gives consistent results for the dEBs and asteroseismology, thus that they are consistent from the main sequence to the red giant branch. Second, because the dEBs reveal the mass at the cluster turn-off, where it is not very different from the mass at the red giant branch (model dependent difference, but below 1.5%), due to the very fast evolution after the turn-off, this measures the mass of the giant stars better than it can be measured from asteroseismology. Therefore, the mass of the giant stars can be measured by the dEBs and used as input for the asteroseismology rather than something which is measured.

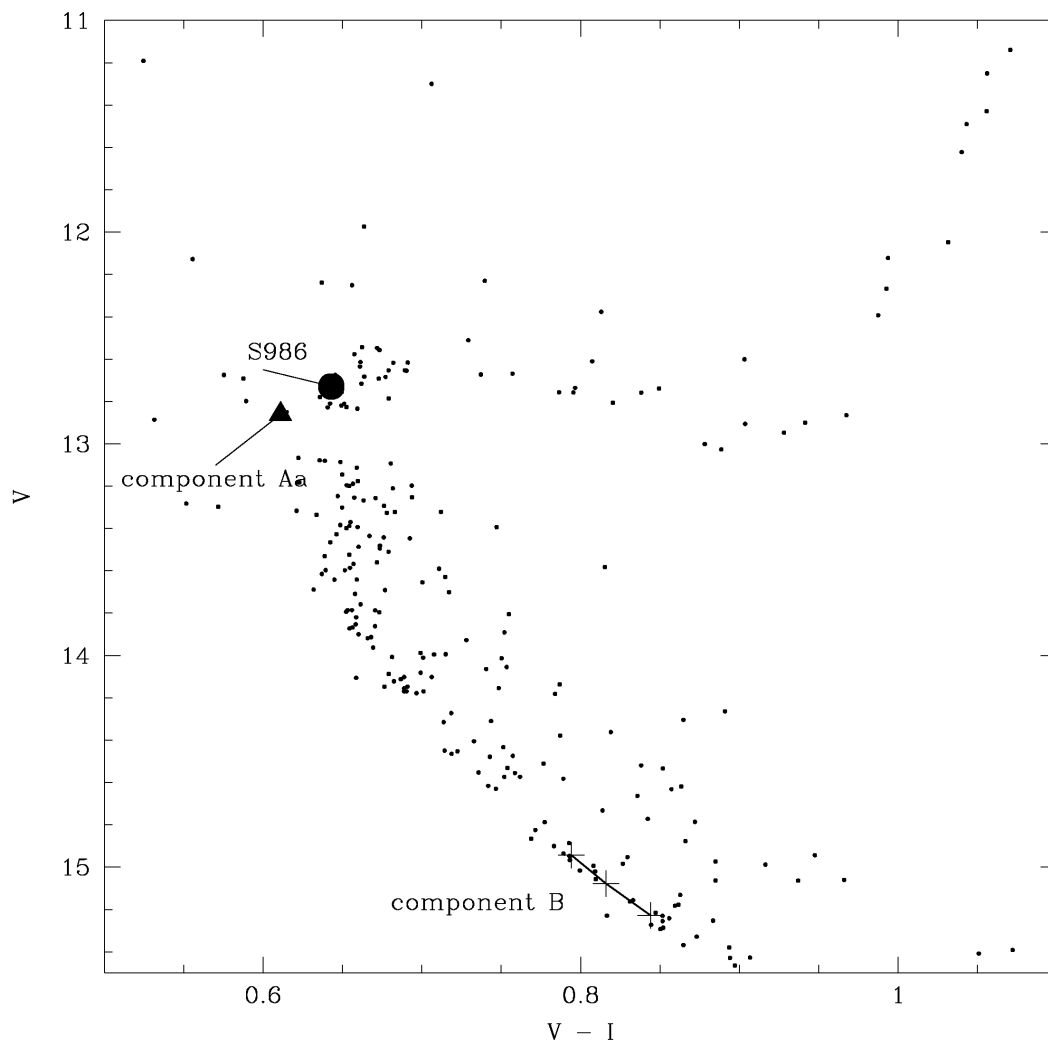


Figure 5.3: M67 CMD from Sandquist et al. (2003), showing the position of the dEB s986. Aa is the primary component and B is the third light.

Since no one has ever done such analysis before it is still not clear how to best exploit such a combined analysis and what to expect from it, but it is clear that this will be a very promising testbed for stellar evolution theory.

Chapter 6

Conclusion

With the present work, it has been demonstrated that measurements of the parameters (masses, radii, effective temperatures, luminosities) of multiple cluster member dEBs can lead to improved knowledge of stellar evolution and more accurate stellar cluster ages. It has been shown that, with currently existing instruments, accurate parameters can be measured for dEBs at least as faint as magnitude 20 in the V band. Multiple cluster member dEBs have been shown to exist in a number of old open clusters, with statistics, and a large number of additional identified candidates, suggesting that many more dEBs exist, also in the globular clusters. New methods for efficiently detecting and measuring parameters of these systems have been demonstrated or proposed. Systems with third light components and very faint secondary stars have been shown to be measurable, expanding the useable fraction of dEBs.

J. Kaluzny tried to promote the use of cluster member dEBs during the discussion after a presentation of "Relative and absolute ages of Galactic globular clusters" at the IAU meeting on "The ages of Stars" in 2008. The reply was:...I have not covered this method in my talk because I decided to discuss methods that have been applied to many clusters, in a survey approach, so as to derive the global properties of the Milky Way clusters as they pertain to their ages. This suggests that dEBs are not being taken into account simply because they can not be used for a larger sample of clusters. It is my hope that this thesis will make people aware that it no longer has to be that way. The dEBs are there, we have the tools for exploiting them, and with multiple cluster member dEBs we can obtain a better understanding of stellar evolution and more accurate stellar cluster ages. Now is the time to do this ...

Bibliography

- Albrow, M. D., Gilliland, R. L., Brown, T. M., et al. 2001, *ApJ*, 559, 1060
- Andersen, J. 1991, *A&A Rev.*, 3, 91
- Arentoft, T., De Ridder, J., Grundahl, F., et al. 2007, *A&A*, 465, 965
- Arnett, D., Meakin, C., & Young, P. A. 2010, *ApJ*, 710, 1619
- Asplund, M., Grevesse, N., & Jacques Sauval, A. 2006, *Nuclear Physics A*, 777, 1
- Asplund, M., Grevesse, N., Sauval, A. J., & Scott, P. 2009, *ARA&A*, 47, 481
- Burgett, W. & Kaiser, N. 2009, in *Advanced Maui Optical and Space Surveillance Technologies Conference*,
- Cacciari, C. 2009, *Memorie della Societa Astronomica Italiana*, 80, 97
- Caffau, E., Ludwig, H., Steffen, M., et al. 2008, *A&A*, 488, 1031
- Caffau, E., Maiorca, E., Bonifacio, P., et al. 2009, *A&A*, 498, 877
- Christensen-Dalsgaard, J. 2002, *Reviews of Modern Physics*, 74, 1073
- D'Antona, F., Stetson, P. B., Ventura, P., et al. 2009, *MNRAS*, 399, L151
- de Marchi, F., Poretti, E., Montalto, M., et al. 2007, *A&A*, 471, 515
- Geller, A. M., Mathieu, R. D., Harris, H. C., & McClure, R. D. 2009, *AJ*, 137, 3743
- Gilliland, R. L., Brown, T. M., Christensen-Dalsgaard, J., et al. 2010, *PASP*, 122, 131
- González, J. F. & Levato, H. 2006, *A&A*, 448, 283
- Grevesse, N. & Sauval, A. J. 1998, *Space Science Reviews*, 85, 161
- Grigahcene, A., Moya, A., Suarez, J., & Martin-Ruiz, S. 2010, *ArXiv:1004.1976*
- Grundahl, F., Christensen-Dalsgaard, J., Arentoft, T., et al. 2008a, *Communications in Asteroseismology*, 157, 273
- Grundahl, F., Clausen, J. V., Hardis, S., & Frandsen, S. 2008b, *A&A*, 492, 171
- Hadrava, P. 1995, *A&AS*, 114, 393
- Hadrava, P. 1997, *A&AS*, 122, 581

- Hadrava, P. 2004, in *Astronomical Society of the Pacific Conference Series*, Vol. 318, *Spectroscopically and Spatially Resolving the Components of the Close Binary Stars*, ed. R. W. Hilditch, H. Hensberge, & K. Pavlovski, 86–94
- Hilditch, R. W. 2001, *An Introduction to Close Binary Stars*, ed. Hilditch, R. W.
- Kaluzny, J., Krzeminski, W., & Mazur, B. 1996, *A&AS*, 118, 303
- Kaluzny, J., Krzeminski, W., Thompson, I. B., & Stachowski, G. 2006a, *Acta Astronomica*, 56, 51
- Kaluzny, J., Pych, W., Rucinski, S. M., & Thompson, I. B. 2006b, *Acta Astronomica*, 56, 237
- Magic, Z., Serenelli, A., Weiss, A., & Chaboyer, B. 2010, *ApJ*, 718, 1378
- Mantegazza, L., Rainer, M., & Antonello, E. 2010, *A&A*, 512, A42
- Marín-Franch, A., Aparicio, A., Piotto, G., et al. 2009, *ApJ*, 694, 1498
- Mazur, B., Kaluzny, J., & Krzemiński, W. 1999, *MNRAS*, 306, 727
- Meibom, S., Grundahl, F., Clausen, J. V., et al. 2009, *AJ*, 137, 5086
- Michaud, G., Richard, O., Richer, J., & Vandenberg, D. A. 2004, *ApJ*, 606, 452
- Mochejska, B. J., Stanek, K. Z., Sasselov, D. D., et al. 2005, *AJ*, 129, 2856
- Mochejska, B. J., Stanek, K. Z., Sasselov, D. D., et al. 2008, *Acta Astronomica*, 58, 263
- Pace, G., Pasquini, L., & François, P. 2008, *A&A*, 489, 403
- Prsa, A., Batalha, N. M., Slawson, R. W., et al. 2010, *ArXiv:1006.2815*
- Randich, S., Sestito, P., Primas, F., Pallavicini, R., & Pasquini, L. 2006, *A&A*, 450, 557
- Rucinski, S. M. 1992, *AJ*, 104, 1968
- Rucinski, S. M. 2002, *AJ*, 124, 1746
- Rucinski, S. M. 2004, in *IAU Symposium*, Vol. 215, *Stellar Rotation*, ed. A. Maeder & P. Eenens, 17
- Rucinski, S. M., Kaluzny, J., & Hilditch, R. W. 1996, *MNRAS*, 282, 705
- Sandquist, E. L. 2006, *Information Bulletin on Variable Stars*, 5679, 1
- Sandquist, E. L. & Shetrone, M. D. 2003, *AJ*, 126, 2954
- Simon, K. P. & Sturm, E. 1994, *A&A*, 281, 286
- Southworth, J. 2010, *ArXiv:1006.4443*
- Southworth, J., Maxted, P. F. L., & Smalley, B. 2004, *MNRAS*, 349, 547
- Stello, D., Arentoft, T., Bedding, T. R., et al. 2006, *MNRAS*, 373, 1141
- Stello, D., Basu, S., Bruntt, H., et al. 2010, *ApJ*, 713, L182
- Thompson, I. B., Kaluzny, J., Rucinski, S. M., et al. 2010, *AJ*, 139, 329

- Torres, G., Andersen, J., & Giménez, A. 2010, *A&A Rev.*, 18, 67
- Turck-Chièze, S., Couvidat, S., Piau, L., et al. 2004, *Physical Review Letters*, 93, 211102
- VandenBerg, D. A., Gustafsson, B., Edvardsson, B., Eriksson, K., & Ferguson, J. 2007, *ApJ*, 666, L105
- Yadav, R. K. S., Bedin, L. R., Piotto, G., et al. 2008, *A&A*, 484, 609
- Zhang, X. B., Deng, L., Tian, B., & Zhou, X. 2002, *AJ*, 123, 1548
- Zucker, S. 2003, *MNRAS*, 342, 1291
- Zucker, S. & Mazeh, T. 1994, *ApJ*, 420, 806
- Zucker, S., Torres, G., & Mazeh, T. 1995, *ApJ*, 452, 863

Acknowledgements

First of all I thank my wife for supporting me in my choice to become an astronomer. After that, there are so many people which I would like to thank that the Acknowledgments section could become longer than the rest of the present work, if I was to mention each and every one of them. Therefore I instead express my thanks to all the people who assisted, inspired or in any other way helped me during my 8 years of study. Special thanks goes to my supervisor Søren Frandsen, and well as co-supervisors (official or not) Frank Grundahl and Jens Viggo Clausen for introducing me to this exciting field of research, for which we now share a common interest and appreciation. I would also like to thank all employees and students of the astronomy group at Aarhus University for being so helpful and inspiring, making the past 8 years some of the best of my life. I want to thank ESO for proving me not only with the possibility to stay for a year at the ESO headquarters in Garching but also for supplying part of the financial support which was needed for a student without straight A's, but other qualities, to be accepted as a PhD student. In this regard, I also want to thank the Instrument centre for Danish Astrophysics (IDA) for their financial support (will alone gets you far, but money talks!). Last, but not least I want to thank all my international collaborators who are involved in the various projects described in the present work. As special thanks among those goes to Professor Don VandenBerg, who from the beginning has appreciated my field of research and my eagerness to push forward. Your kindness and overwhelming work effort is highly appreciated!

Part II

Reports & Articles

Appendix A

EFFECTS OF ASSUMED CHEMICAL COMPOSITION ON THE ACCURACY OF STELLAR AGES

Unpublished report by K. Brogaard (2008)

Effects of assumed chemical composition on the accuracy of stellar ages

by Karsten Brogaard

Introduction

Traditionally ages of stellar clusters have been measured using the technique of isochrone fitting to the cluster color-magnitude diagram. However this approach suffers from many observational uncertainties, such as distance, reddening and color-temperature transformations. Using instead cluster member detached eclipsing binaries, for which the masses and radii can be measured with an accuracy better than 1%, one avoids these problems. As recently shown by Grundahl et al. 2008 the remaining uncertainties, due to adopting different stellar models, are larger than the measurement precision. Furthermore I noticed by studying their table 10, which is reproced here for convenience, that the age of the primary star responds differently to the assumed metallicity in the BaSTI model compared to the other two models. Using the BaSTI model, the age increases with increasing assumed metallicity. Using the other models the age decreases with increasing assumed metallicity. Identifying the reason for this difference in behaviour between the models motivated a small investigation of stellar model differences. This let not only to the answer, but also some unpleasant consequences of assumed chemical composition on the accuracy stellar ages.

The stellar model isochrones

In figure 12 and table 10, reproduced from Grundahl et al. 2008, the accurate dimensions obtained for the detached eclipsing binary V20, in the open cluster NGC 6791, are compared with properties of the VRSS (scaled-solar mixture) Victoria-Regina stellar model isochrones (VandenBerg et al., 2006), the YY (Yonsei-Yale) grids (Demarque et al. 2004), and the extensive material available from the BaSTI database (Pietrinferni et al. 2004). These three recent models are all based on up-to-date input physics but differ somewhat with respect to e.g. core overshoot and diffusion (if included) treatment, He enrichment law, adopted solar mixture, and envelope convection calibration. Further details can be found in Clausen et al. (2008), as well as in the original papers. Grids of isochrones spanning a wide range in Z and age are available on the internet and form the basis of the comparisons.

Model differences in different metallicity regimes

Figure 1 shows comparisons between the VRSS and BaSTI sets of isochrones in the mass-radius diagram at an age of 8 Gyr in different metallicity regimes, sub-solar (low metallicity), solar, and supersolar (high metallicity). It is seen that while there is rough agreement at solar metallicity, the BaSTI isochrone has to be younger than the VRSS isochrone in order for them to match at low metallicity. Further tests show that the age shift, needed to keep the BaSTI and VR isochrones match, is constant over a large range in Z at low metallicity.

At high metallicity the effect is different. Here the BaSTI isochrone has to be older than the VRSS isochrone in order for them to agree, and the needed age difference is larger than at low metallicity. And here the age shift needed to keep the different isochrones in agreement changes with Z . As shown in figure 2, with increasing Z the top end of the VRSS isochrone first moves to the right, then stalls and finally moves back left. The same thing is seen for the YY isochrones, but here the stalling effect and direction change is more moderate. The BaSTI isochrone does not show the effect at all, it just keeps moving right. It should be noted here, that the BaSTI grid ends at $Z=0.04$ and therefore one can not rule out that the effect is present at $Z=0.05$ or higher (I have requested a $Z=0.05$ isochrone from the BaSTI team, but so far no reply).

In order to identify the reason for these effects, we now turn to some details of the models as described in the papers accompanying them.

Calibration issues and helium enrichment laws

Due to our inability to measure the helium content of stars and our limited knowledge of convection, stellar models are calibrated on the sun, requiring the 1 solar mass model to match the solar luminosity and radius at the solar age and the assumed content of metals induced from spectra of the solar photosphere. This calibration gives the value of the mixing length parameter and the solar helium content. From this value of the helium content and an assumed primordial helium content, the helium enrichment law is set up. But the calibration is not done consistently between models, and this introduces model differences which can be quite large.

The solar calibration of the BaSTI isochrones is done including diffusion of both helium and metals, since diffusion is known from helioseismology to be important in the sun. But after the calibration, diffusion is removed from the models. This is done arguing a lack of evidence of diffusion in old stellar clusters. We note here that evidence of diffusion in globular clusters has been found by Korn et al. 2007, and this makes the approach questionable. In any case it is thus assumed that the model stars without diffusion have the same mixing length parameter as they would have if diffusion was present. Furthermore it is assumed that the helium enrichment law is the same as it would have been if diffusion was included. And last but not least the 'solar' model isochrone has $[Fe/H]=0.06$ because this is the initial metallicity needed to have $[Fe/H]=0.0$ at the solar age when diffusion is included. Note that this way of calibrating is so unintuitive that it remained unnoticed by Clausen et al. 2008 when giving a short summary of the BaSTI model ingredients. They instead wrongly state that only the solar model includes diffusion.

The YY models include diffusion, but only of helium. However they are at least consistent and include diffusion both in the models and in the calibration. The VR models do not include diffusion at all, not in the models and not in the calibration.

As a consequence varying input physics and the different ways of calibrating on the sun, the different models obtain different values of the mixing length parameter and the helium content at solar metallicity. This difference in the helium content at solar metallicity together with a different assumed primordial Z results in different helium enrichment laws for the different models, shown in the below table.

Helium enrichment laws in the different models			
	YY	VRSS	BaSTI
$Y(Z)$	$0.23 + 2Z$	$0.23544 + 2.2Z$	$\sim 0.245 + 1.4Z$
Y_{sun}	0.267	0.2768	0.2734

Assuming that diffusion of both metals and helium do occur in all stars, none of the models would be correctly calibrated and one never compares the observation to a model with the correct value of the mixing length and helium content, even if everything else in those models is 100% correct! And unfortunately this problem is not easily solved, as a change in model age can often compensate the error in the calibration. It should also be noted here, that if the debated solar abundances by Asplund et al. 2006 turn out to be correct, the assumed mix of metals in the solar calibration would also be wrong and make this problem even worse.

High Z effects

The isochrone differences at high Z are nicely explained by examining the details of Mowlavi et al. 1998. Briefly described there are two competing effects at high Z . First with increasing Z the opacity increase decreases the energy flux resulting in a decrease in luminosity and through that a longer main sequence lifetime. This is what Mowlavi calls the κ -effect. But at high Z one can also get high Y depending on the adopted helium enrichment law. Higher Y gives a higher mean molecular weight μ . Let us follow Mowlavi and "imagine a *thought experiment* in which μ is

arbitrarily increased over the whole star, all other quantities being unaltered (though keeping, of course, their density and temperature dependences). The reduction in the gas pressure leads to an overall contraction (and heating) until hydrostatic equilibrium is re-established. As a result, the stellar radius decreases and the surface effective temperature increases. The surface luminosity L , on the other hand, increases with μ since $L(r)$ is proportional to $T^3 dT/dr$ [in the case of radiative transfer, with $L(r)$ and T being the luminosity and temperature at radius r , respectively]. In summary, *an increase in μ tends to increase both L and T_{eff}* and therefore shorten the main sequence lifetime. This is what Mowlavi calls the μ -effect. At high Z (and Y) the κ -effect and the μ -effect competes and at some point the μ -effect becomes dominant. This is exactly what is seen in figure 2 for the VRSS and YY isochrones: Going from $Z \sim 0.02$ to $Z = 0.03$ the κ -effect is dominant leading to longer main sequence lifetimes and thus the mass-radius isochrone moves to the right. From $Z = 0.03$ to $Z = 0.04$ the two effects are more or less in balance and the isochrones barely change. From $Z = 0.04$ to $Z = 0.05$ the μ -effect is dominant and the resulting shorter main sequence lifetime moves the isochrone left.

But the Z at which the two effects comes into balance depends strongly on the adopted helium enrichment law. The models used by Mowlavi et al. 1998 has about the same steepness in their helium enrichment law as the VRSS and YY models. Therefore it is not surprising to see the effect in these models. It is also not surprising that the effect is stronger in the VR models than the YY models, since this can be inferred directly from the different steepness in helium enrichment laws. The BaSTI models have a very flat helium enrichment compared to the other models, and therefore the κ -effect keeps dominating and the isochrone keeps moving right in the whole supersolar region.

A word on isochrone wiggles

To complicate things there is actually a third metallicity effect supplementing the κ - and μ -effects in determining the stellar properties as a function of Z . As it is far less dominant, it could be left out in the above explanation, but it nevertheless deserves attention, as it might introduce finestructure in the isochrones. It is the reaction of the nuclear energy production to metallicity changes, known as the ϵ -effect in Mowlavi et al. 1998: “The nuclear energy production ϵ sustains the stellar luminosity. If ϵ is arbitrarily increased, the central regions of the star expand, leading to a decrease in the temperatures and densities, and to an increase in the stellar radius. Thus, *an increase in ϵ tends to decrease both L and T_{eff}* The way ϵ depends on metallicity is closely related to the mode of nuclear burning. When the CNO cycles are the main mode of H burning, ϵ increases with Z . In contrast, when the main mode of burning is the pp chain, ϵ is related to X . It is thus about independent of Z at $Z < \sim 0.02$, and decreases with increasing Z at $Z > \sim 0.02$.” In the super-solar metallicity regimes the ϵ -effect therefore increases the radius of stars dominated by the CNO cycle while decreasing the radius of stars dominated by the pp chain. In the regime where both CNO and pp energy production is important, the radii will meet. This introduces a wiggle in the mass-radius isochrone. Unfortunately it will be very difficult to use this as an observational constraint, as usually one only has two points to compare with. In the color-magnitude diagram, the wiggle will be placed fairly close below the location where one sometimes observes a hook, related to convective cores in stars at the end of their main sequence life. If the cluster is a little older, the hook features will be gone, but then the wiggle will be positioned at the turn off and can therefore be misinterpreted as a small hook feature. Actually such a wiggle might be what is present in a very precise color-magnitude diagram of NGC 6791 by Grundahl et al. (private communication) where it has caused confusion since the turn-off stars are not expected to have convective cores.

Consequences for absolute and relative ages

Let us now recall table 10, showing the age of the detached eclipsing binary V20 in NGC6791 as a function of assumed metallicity. We can now understand the reason for the different age dependence on metallicity, for the primary star, in different stellar models as a consequence of the different

helium enrichment laws adopted. The VRSS and YY models have quite steep helium enrichment laws and are thus in the regime dominated by the μ -effect. The μ -effect moves the top of the isochrone left with increasing metallicity, which is the same direction as age. Therefore the age of a given turn-off star decreases when increasing the assumed metallicity. The BaSTI model has a relatively flat helium enrichment law and is therefore in the regime dominated by the κ -effect. The κ -effect moves the top of the isochrone right with increasing metallicity, which is the opposite direction of age. Therefore the age of a given turn-off star increases when increasing the assumed metallicity.

For the secondary star, table 10 shows a different age dependence on adopted metallicity. Here the solution might be sought in the way the size of main sequence stars responds to the competition of the κ -, ε - and μ -effects. We note that diffusion of helium (and metals) will change this balance, and this is probably the reason why the YY isochrone (which includes helium diffusion) has a different curvature than the others (which do not) e.g. in figure 12.

Since the models are in rough age agreement at solar metallicity (fig. 1 middle panel and fig. 2 upper left), but not at high Z (fig. 12), we seem to have also identified the helium enrichment law as the main limiting factor on the accuracy of the age of V20 and NGC6791. In fact, looking at figure 1 with the different helium enrichment laws in mind, one notices that the age differences follows the helium differences. At low Z the VRSS model has lower Y and evolves slower than the BaSTI model. At high Z the VRSS model has higher Y and evolves faster. At solar Z where Y is more or less identical in the two models, the models are in rough agreement. This strongly suggests that also at low Z is the helium enrichment law responsible for the largest model to model age discrepancies.

In the low metallicity regime it was found that, at a given age, a constant age shift between the BaSTI and VRSS isochrones kept them in agreement over a large range in Z . This means that relative ages across metallicity are identical using either of these two sets of isochrones. This points towards a meaningful use of relative ages, as in the work of Marin-Franch et al. (ApJ submitted), which shows that the globular clusters of the Milky Way separated into two groups – one which are all of more or less the same age, and one in which $[Fe/H]$ drops with increasing age, see figure 3. But one should keep in mind that such *relative age comparisons can not be extended to super-solar metallicities*. Here it is impossible to get even relative ages across metallicity until the true helium enrichment law is known, because of the strong dependence of the μ -effect on the helium content.

Conclusions and outlook

Based on a comparison between stellar model isochrones in the mass-radius diagram we draw the following conclusion: One of the dominating differences between current stellar models is their differing helium enrichment laws. These differences translate into large errors in the absolute age accuracy one can obtain from detached eclipsing binaries and cluster isochrone fitting in general, and it also makes relative age estimates across metallicity very uncertain, if not impossible, at super-solar metallicity.

In order to improve the situation one should concentrate on observations which can provide strong constraints on the helium content and the stellar models in general. This can be done by observations of several detached eclipsing binaries in the same open or globular cluster as this would also constrain the curvature of the mass-radius isochrone since more than two points would then have to be matched. It should be noted here, that present isochrone sets are interpolated from model tracks with a spacing of 0.1 solar masses or more, which is way too much to conserve the fine details in the mass-radius isochrone, which such observations can reveal. The spacing in metallicity is likewise too high. Therefore, in order to gain full advantage of accurate observations of multiple detached eclipsing binaries in the same cluster, dedicated model calculations using the measured masses and metallicity are needed.

To strengthen further such an approach, one should focus on clusters with many stars and with

either hook and gap features at the turn-off or a well populated horizontal branch, since then the color-magnitude diagram can be used for simultaneous constraints despite the many observational errors. One should also concentrate on the open clusters in the field of view of KEPLER, since then combined constraints from detached eclipsing binaries, the cluster color-magnitude diagram and asteroseismology can be combined in a synergy of strong constraints for stellar models.

References

- Asplund et al. 2006, *Commun. Asteroseis.*, 147, 76
Clausen et al. 2008, *A&A*, 487, 1095
Demarque et al. 2004, *ApJS*, 155, 667
Grundahl et al. 2008, *A&A* accepted, arxiv:0810.2407
Korn et al. 2007, *ApJ*, 671, 402
Marin-Franch et al., *ApJ* submitted
Mowlavi et al. 1998, *A&A*, 335, 573
Pietrinferni et al. 2004, *ApJ*, 612, 168
VandenBerg et al. 2006, *ApJS*, 162, 375

Table 10. Ages for the components of V20 as determined from $M - R$ isochrones calculated for different models and chemical compositions. For each model, the first line represent the available models closest to the observed $[\text{Fe}/\text{H}]$. All models include core overshoot; BaSTI standard and core overshoot models yield nearly identical results. Uncertainties due to mass and radius errors are about 0.3 Gyr (primary) and 0.9 Gyr (secondary).

Model	$[\text{Fe}/\text{H}]$	Primary	Secondary
VRSS	0.37	7.7	7.2
	0.23	7.8	7.0
	0.49	7.3	6.8
Y^2	0.40	8.2	6.2
	0.30	8.3	6.2
	0.50	7.8	6.2
BaSTI	0.395	9.0	8.6
	0.254	8.5	7.6

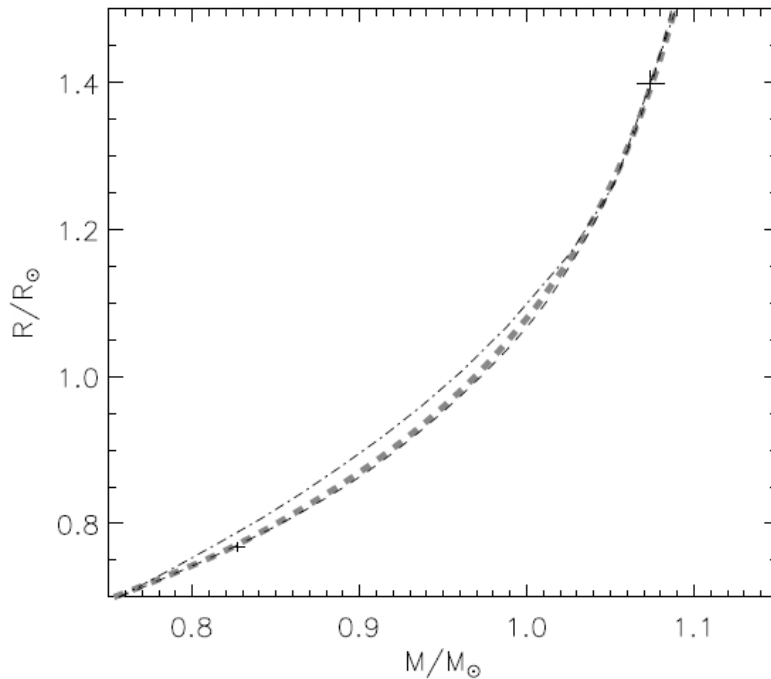


Fig. 12.

V20 compared to the VRSS (7.7 Gyr, dashed thick gray), Y^2 (8.2 Gyr, dashed-dot black), and BaSTI (9.0 Gyr, dashed black) isochrones which fit the primary component at the observed $[\text{Fe}/\text{H}]$; see Table 10.

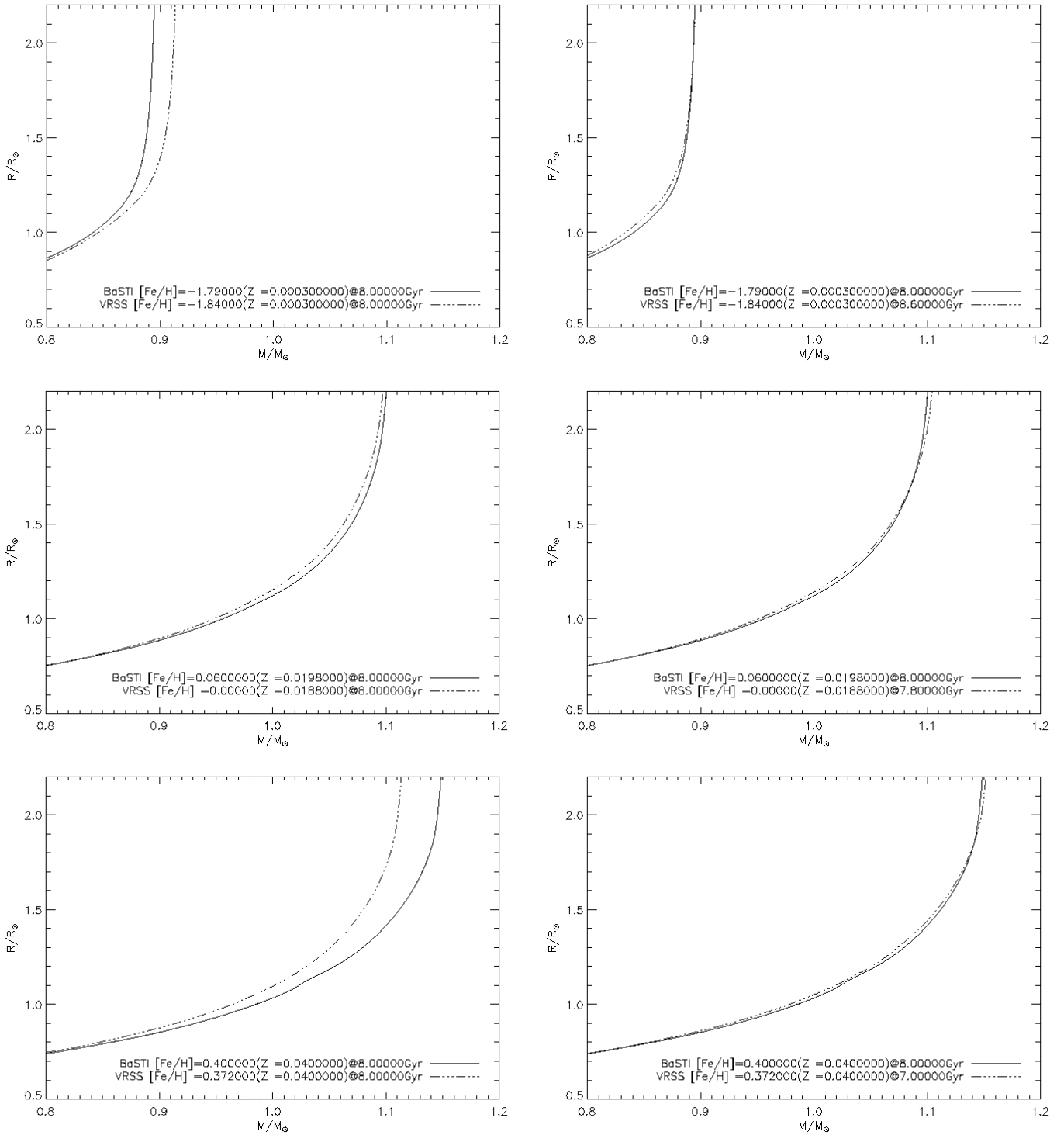


Figure 1: Mass-radius isochrone comparisons between the VRSS and BaSTI models in different metallicity regimes at 8 Gyr. Left side shows models at 8 Gyr. Right side shows VRSS model shifted in age to match BaSTI.

Top: sub-solar metallicity. VRSS has to be ~ 0.6 Gyr older than BaSTI in order for them to be in rough agreement.

Middle: solar metallicity. The models are in rough agreement. A shift of at most 0.2 Gyr is needed in order for the two models to match.

Bottom: super-solar metallicity. VRSS has to be ~ 1 Gyr younger than BaSTI in order for them to be in rough agreement.

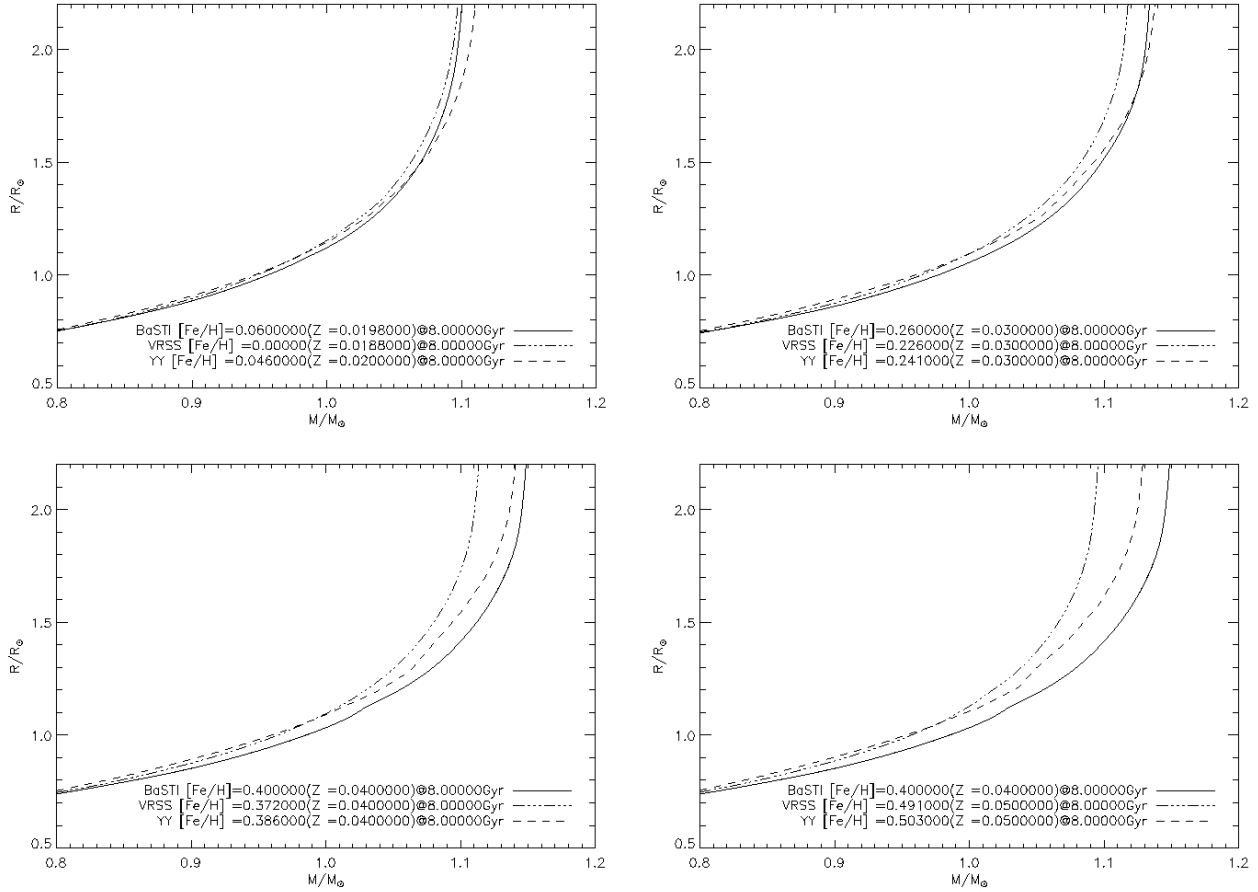


Figure 2: Isochrones at 8 Gyr as a function of Z at super-solar metallicities. Z increases from top left to bottom right. The top of the VRSS and YY isochrones first moves right from $Z \sim 0.02$ to $Z = 0.03$, barely changes from $Z = 0.03$ to 0.04 and moves back left from $Z = 0.04$ to 0.05 . The effect is strongest for the VRSS isochrone. The top of the BaSTI isochrone moves right through the whole Z range (note though that the BaSTI grid ends at $Z = 0.04$ and therefore the bottom right panel has $Z = 0.04$ for the BaSTI isochrone and it can not be excluded that the BaSTI model shows the same evolution as the others at higher Z).

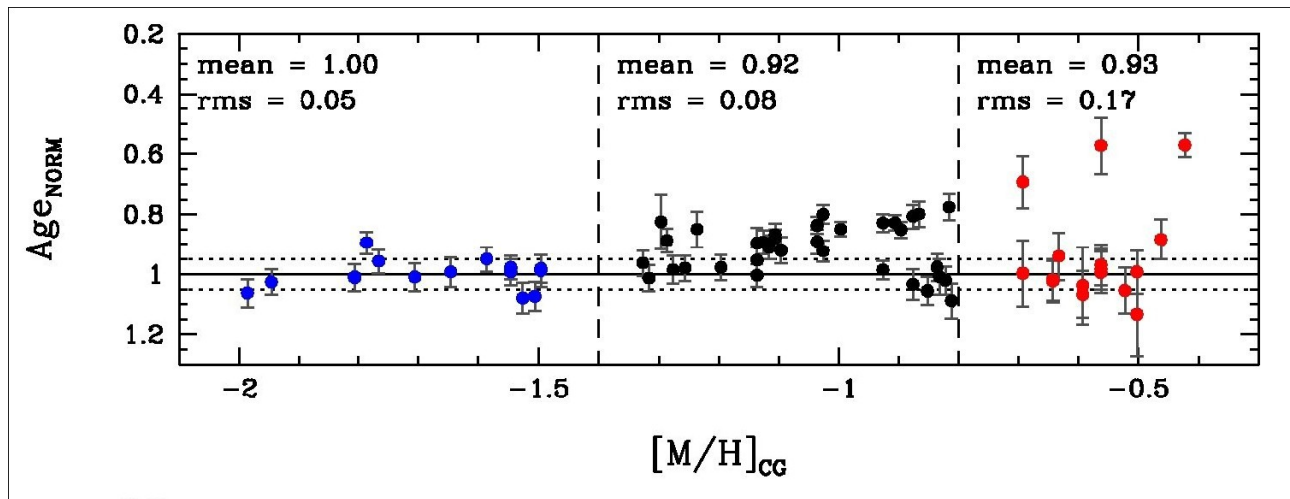


Figure 3: The relative age of Milky Way Globular clusters by Marin-Franch et al., ApJ submitted

Appendix B

DETECTION OF SOLAR-LIKE OSCILLATIONS FROM KEPLER PHOTOMETRY OF THE OPEN CLUSTER NGC 6819

DETECTION OF SOLAR-LIKE OSCILLATIONS FROM *KEPLER* PHOTOMETRY OF THE OPEN CLUSTER NGC 6819

DENNIS STELLO¹, SARBANI BASU², HANS BRUNTT³, BENOÎT MOSSER³, IAN R. STEVENS⁴, TIMOTHY M. BROWN⁵, JØRGEN CHRISTENSEN-DALSGAARD⁶, RONALD L. GILLILAND⁷, HANS KJELDSSEN⁶, TORBEN ARENTOFT⁶, JÉRÔME BALLOT⁸, CAROLINE BARBAN³, TIMOTHY R. BEDDING¹, WILLIAM J. CHAPLIN⁴, YVONNE P. ELSWORTH⁴, RAFAEL A. GARCÍA⁹, MARIE-JO GOUPIL³, SASKIA HEKKER⁴, DANIEL HUBER¹, SAVITA MATHUR¹⁰, SØREN MEIBOM¹¹, VINOOTHINI SANGARALINGAM⁴, CHARLES S. BALDNER², KEVIN BELKACEM¹², KATIA BIAZZO¹³, KARSTEN BROGAARD⁶, JUAN CARLOS SUÁREZ¹⁴, FRANCESCA D'ANTONA¹⁵, PIERRE DEMARQUE², LISA ESCH², NING GAI^{2,16}, FRANK GRUNDAHL⁶, YVELINE LEBRETON¹⁷, BIWEI JIANG¹⁶, NADA JEVTIC¹⁸, CHRISTOFFER KAROFF⁴, ANDREA MIGLIO¹², JOANNA MOLENDAN-ZAKOWICZ¹⁹, JOSEFINA MONTALBÁN¹², ARLETTE NOELS¹², TEODORO ROCA CORTÉS^{20,21}, IAN W. ROXBURGH²², ALDO M. SERENELLI²³, VICTOR SILVA AGUIRRE²³, CHRISTIAAN STERKEN²⁴, PETER STINE¹⁸, ROBERT SZABÓ²⁵, ACHIM WEISS²³, WILLIAM J. BORUCKI²⁶, DAVID KOCH²⁶, AND JON M. JENKINS²⁷

¹ Sydney Institute for Astronomy (SfA), School of Physics, University of Sydney, NSW 2006, Australia

² Department of Astronomy, Yale University, P.O. Box 208101, New Haven, CT 06520-8101, USA

³ LESIA, CNRS, Université Pierre et Marie Curie, Université Denis Diderot, Observatoire de Paris, 92195 Meudon, France

⁴ School of Physics and Astronomy, University of Birmingham, Edgbaston, Birmingham B15 2TT, UK

⁵ Las Cumbres Observatory Global Telescope, Goleta, CA 93117, USA

⁶ Department of Physics and Astronomy, Aarhus University, 8000 Aarhus C, Denmark

⁷ Space Telescope Science Institute, 3700 San Martin Drive, Baltimore, MD 21218, USA

⁸ Laboratoire d'Astrophysique de Toulouse-Tarbes, Université de Toulouse, CNRS, 14 av E. Belin, 31400 Toulouse, France

⁹ Laboratoire AIM, CEA/DSM-CNRS, Université Paris 7 Diderot, IRFU/SAP, Centre de Saclay, 91191 Gif-sur-Yvette, France

¹⁰ Indian Institute of Astrophysics, Koramangala, Bangalore 560 034, India

¹¹ Harvard-Smithsonian Center for Astrophysics, 60 Garden Street, Cambridge, MA 02138, USA

¹² Institut d'Astrophysique et de Géophysique de l'Université de Liège, 17 Allée du 6 Août, B-4000 Liège, Belgium

¹³ Arcetri Astrophysical Observatory, Largo E. Fermi 5, 50125 Firenze, Italy

¹⁴ Instituto de Astrofísica de Andalucía (CSIC), Dept. Stellar Physics, C.P. 3004, Granada, Spain

¹⁵ INAF-Osservatorio di Roma, via di Frascati 33, I-00040 Monteporzio, Italy

¹⁶ Department of Astronomy, Beijing Normal University, Beijing 100875, China

¹⁷ GEPI, Observatoire de Paris, CNRS, Université Paris Diderot, 5 Place Jules Janssen, 92195 Meudon, France

¹⁸ Department of Physics & Engineering Technology, Bloomsburg University, 400 East Second Street, Bloomsburg, PA 17815, USA

¹⁹ Astronomical Institute, University of Wrocław, ul. Kopernika 11, 51-622 Wrocław, Poland

²⁰ Departamento de Astrofísica, Universidad de La Laguna, 38207 La Laguna, Tenerife, Spain

²¹ Instituto de Astrofísica de Canarias, 38205 La Laguna, Tenerife, Spain

²² Queen Mary University of London, Mile End Road, London E1 4NS, UK

²³ Max Planck Institute for Astrophysics, Karl Schwarzschild Str. 1, Garching bei München D-85741, Germany

²⁴ Vrije Universiteit Brussel, Pleinlaan 2, B-1050 Brussels, Belgium

²⁵ Konkoly Observatory, P.O. Box 67, H-1525 Budapest, Hungary

²⁶ NASA Ames Research Center, MS 244-30, Moffat Field, CA 94035, USA

²⁷ SETI Institute/NASA Ames Research Center, MS 244-30, Moffat Field, CA 94035, USA

Received 2009 November 13; accepted 2009 December 16; published 2010 March 31

ABSTRACT

Asteroseismology of stars in clusters has been a long-sought goal because the assumption of a common age, distance, and initial chemical composition allows strong tests of the theory of stellar evolution. We report results from the first 34 days of science data from the *Kepler Mission* for the open cluster NGC 6819—one of the four clusters in the field of view. We obtain the first clear detections of solar-like oscillations in the cluster red giants and are able to measure the large frequency separation, $\Delta\nu$, and the frequency of maximum oscillation power, ν_{\max} . We find that the asteroseismic parameters allow us to test cluster membership of the stars, and even with the limited seismic data in hand, we can already identify four possible non-members despite their having a better than 80% membership probability from radial velocity measurements. We are also able to determine the oscillation amplitudes for stars that span about 2 orders of magnitude in luminosity and find good agreement with the prediction that oscillation amplitudes scale as the luminosity to the power of 0.7. These early results demonstrate the unique potential of asteroseismology of the stellar clusters observed by *Kepler*.

Key words: open clusters and associations: individual (NGC 6819) – stars: fundamental parameters – stars: interiors – stars: oscillations – techniques: photometric

1. INTRODUCTION

Open clusters provide unique opportunities in astrophysics. Stars in open clusters are believed to be formed from the same cloud of gas at roughly the same time. The fewer free parameters available to model cluster stars make them interesting targets to analyze as a uniform ensemble, especially for asteroseismic studies.

Asteroseismology is an elegant tool based on the simple principle that the frequency of a standing acoustic wave inside a star depends on the sound speed, which in turn depends on the physical properties of the interior. This technique applied to the Sun (helioseismology) has provided extremely detailed knowledge about the physics that governs the solar interior (e.g., Christensen-Dalsgaard 2002). All cool stars are expected to exhibit solar-like oscillations of standing acoustic waves—called

p modes—that are stochastically driven by surface convection. Using asteroseismology to probe the interiors of cool stars in clusters, therefore, holds promise of rewarding scientific return (Gough & Novotny 1993; Brown & Gilliland 1994). This potential has resulted in several attempts to detect solar-like oscillations in clusters using time-series photometry. These attempts were often aimed at red giants, since their oscillation amplitudes are expected to be larger than those of main-sequence or sub-giant stars due to more vigorous surface convection. Despite these attempts, only marginal detections have been attained so far, limited either by the length of the time series usually achievable through observations with the *Hubble Space Telescope* (Edmonds & Gilliland 1996; Stello & Gilliland 2009) or by the difficulty in attaining high precision from ground-based campaigns (e.g., Gilliland et al. 1993; Stello et al. 2007; Frandsen et al. 2007).

In this Letter, we report clear detections of solar-like oscillations in red-giant stars in the open cluster NGC 6819 using photometry from NASA’s *Kepler Mission* (Borucki et al. 2009). This cluster, one of four in the *Kepler* field, is about 2.5 Gyr old. It is at a distance of 2.3 kpc, and has a metallicity of $[Fe/H] \sim -0.05$ (see Hole et al. 2009, and references therein).

2. OBSERVATIONS AND DATA REDUCTION

The data were obtained between 2009 May 12 and June 14, i.e., the first 34 days of continuous science observations by *Kepler* (Q1 phase). The spacecraft’s long-cadence mode ($\Delta t \simeq 30$ minutes) used in this investigation provided a total of 1639 data points in the time series of each observed star. For this Letter, we selected 47 stars in the field of the open cluster NGC 6819 with membership probability $P_{RV} > 80\%$ from radial velocity measurements (Hole et al. 2009). Figure 1 shows the color–magnitude diagram (CMD) of the cluster with the selected stars indicated by green symbols. The 11 annotated stars form a representative subset, which we will use to illustrate our analyses in Sections 3 and 4. We selected the stars in this subset to cover the same brightness range as our full sample, while giving high weight to stars that appear to be photometric non-members (i.e., stars located far from the isochrone in the CMD). Data for each target were checked carefully to ensure that the time-series photometry was not contaminated significantly by other stars in the field, which could otherwise complicate the interpretation of the oscillation signal.

Fourteen data points affected by the momentum dumping of the spacecraft were removed from the time series of each star. In addition, we removed points that showed a point-to-point deviation greater than 4σ , where σ is the local rms of the point-to-point scatter within a 24 hr window. This process removed on average one data-point per time series. Finally, we removed a linear trend from each time series and then calculated the discrete Fourier transform. The Fourier spectra at high frequency have mean levels below 5 parts per million (ppm) in amplitude, allowing us to search for low-amplitude solar-like oscillations.

3. EXTRACTION OF ASTEROSEISMIC PARAMETERS

Figure 2 shows the Fourier spectra (in power) of nine stars from our subset. These range from the lower red-giant branch to the tip of the branch (see Figure 1). The stars are sorted by apparent magnitude, which for a cluster is indicative of luminosity, with brightest at the top. Note that the red giants in NGC 6819 are significantly fainter ($12 \lesssim V \lesssim 14$) than the sample of *Kepler* field red giants ($8 \lesssim V \lesssim 12$) studied by

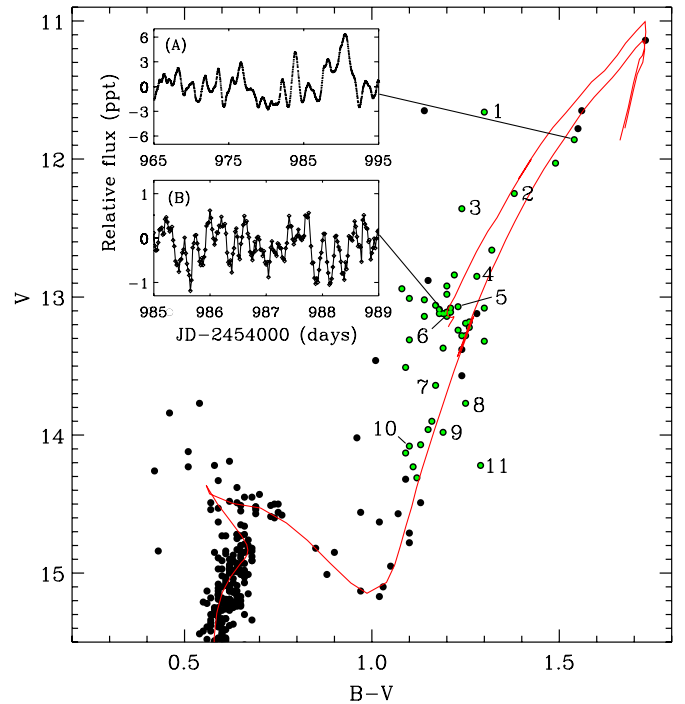


Figure 1. CMD of NGC 6819. Plotted stars have membership probability $P_{RV} > 80\%$ as determined by Hole et al. (2009). Photometric indices are from the same source. The isochrone is from Marigo et al. (2008) (age = 2.4 Gyr, $Z = 0.019$, modified for the adopted reddening of 0.1 mag). Color-coded stars have been analyzed, and the annotated numbers refer to the legend in panels of Figure 2 and star numbers in Figure 3 (see also Table 1). Insets show light curves in parts per thousand of two red giants oscillating on different timescales. The variations of the light curves in Panels A and B are dominated by the stellar oscillations with periods of a few days and of about six hours, respectively.

Bedding et al. (2010). Nevertheless, it is clear from Figure 2 that we can detect oscillations for stars that span about 2 orders of magnitude in luminosity along the cluster sequence.

We used four different pipelines (Hekker et al. 2009a; Huber et al. 2009; Mathur et al. 2009; Mosser & Appourchaux 2009) to extract the average frequency separation between modes of the same degree (the so-called large frequency separation, $\Delta\nu$). We have also obtained the frequency of maximum oscillation power, ν_{\max} , and the oscillation amplitude. The measured values of $\Delta\nu$ are indicated by vertical dotted lines in Figure 2 centered on the highest oscillation peaks near ν_{\max} . While the stars in Figure 2, particularly in the lower panels, show the regular series of peaks expected for solar-like oscillations, the limited length of the time-series data does not allow such structure to be clearly resolved for the most luminous stars in our sample—those with $\nu_{\max} \lesssim 20 \mu\text{Hz}$. We do, however, see humps of excess power in the Fourier spectra (see Figure 2, star nos 2 and 8) with ν_{\max} and amplitude in mutual agreement with oscillations. With longer time series, we expect more firm results for these high-luminosity giants.

4. CLUSTER MEMBERSHIP FROM ASTEROSEISMOLOGY

It is immediately clear from Figure 2 that not all stars follow the expected trend of increasing ν_{\max} with decreasing apparent magnitude, suggesting that some of the stars might be intrinsically brighter or fainter than expected. Since oscillations in a star only depend on the physical properties of the star, we can use asteroseismology to judge whether or not a star is likely to be a cluster member independently of its distance and of

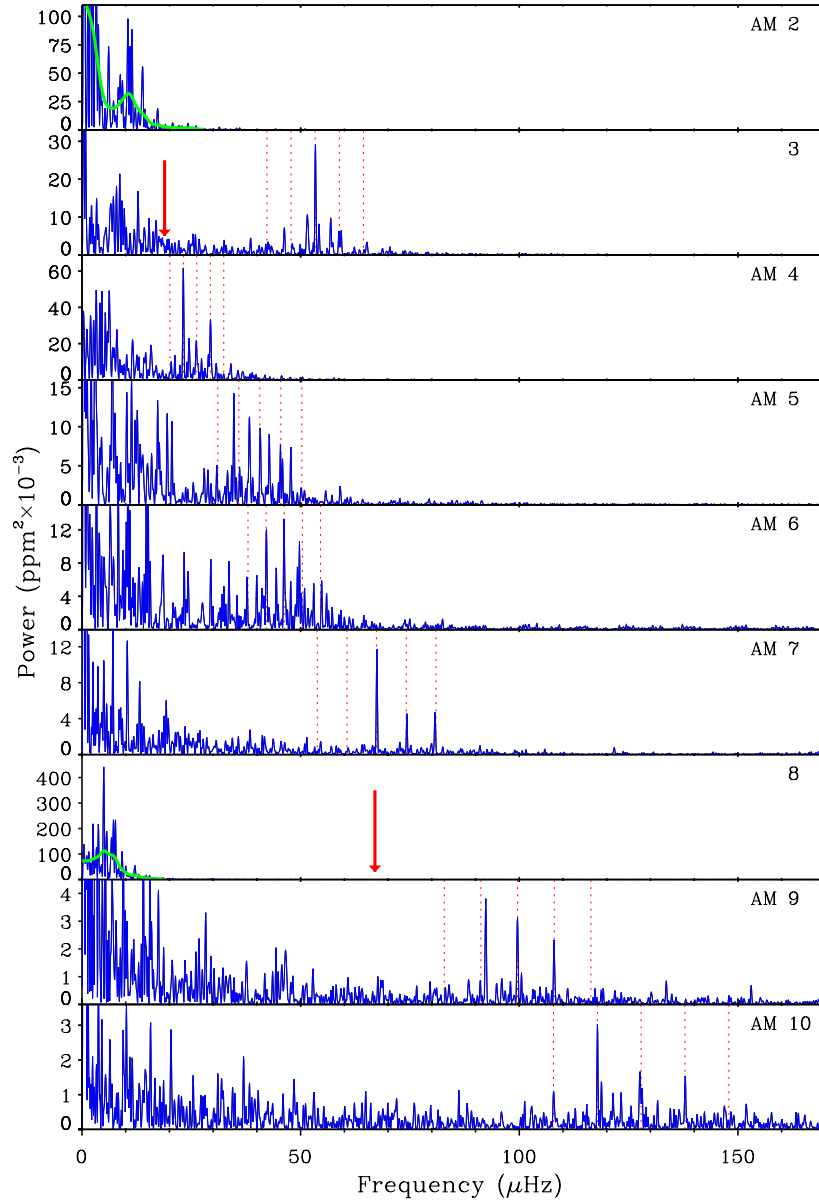


Figure 2. Fourier spectra of a representative set of red giants along the cluster sequence sorted by apparent magnitude. Annotated numbers in each panel refer to the star identification (see Figure 1 and Table 1). “AM” indicates that the star is an asteroseismic member. Red solid curves show the smoothed spectrum for stars with $\nu_{\max} < 20 \mu\text{Hz}$. To guide the eye, we have plotted dotted lines to indicate the measured average large frequency separation. The central dotted line is centered on the highest oscillation peaks near ν_{\max} . Note that since $\Delta\nu$ is generally frequency dependent, only the central dotted line is expected to line up with a peak in the oscillation spectrum. The red arrows indicate the position of the expected ν_{\max} (see Equation (1)) for stars where the observed value does not agree with the expectations for this cluster (see Section 4).

interstellar absorption and reddening. For cool stars, ν_{\max} scales with the acoustic cutoff frequency, and it is well established that we can estimate ν_{\max} by scaling from the solar value (Brown et al. 1991; Kjeldsen & Bedding 1995)

$$\frac{\nu_{\max}}{\nu_{\max,\odot}} = \frac{M/M_{\odot}(T_{\text{eff}}/T_{\text{eff},\odot})^{3.5}}{L/L_{\odot}}, \quad (1)$$

where $\nu_{\max,\odot} = 3100 \mu\text{Hz}$. The accuracy of such estimates is good to within 5% (Stello et al. 2009) assuming we have good estimates of the stellar parameters M , L , and T_{eff} .

In the following, we assume the idealistic scenario where all cluster members follow standard stellar evolution described by the isochrone. Stellar mass along the red-giant branch of the cluster isochrone varies by less than 1%. The variation is less than 5% even if we also consider the asymptotic giant

branch. For simplicity, we therefore adopt a mass of $1.55 M_{\odot}$ for all stars, which is representative for the isochrone from Marigo et al. (2008; Figure 1) and a similar isochrone by Vandenberg et al. (2006). Neglecting binarity (see Table 1), we derive the luminosity of each star in our subset from its V -band apparent magnitude, adopting reddening and distance modulus of $E(B - V) = 0.1$ and $(M - m)_V = 12.3$, respectively (obtained from simple isochrone fitting, see Hole et al. 2009). We used the calibration of Flower (1996) to convert the stellar $(B - V)_0$ color to T_{eff} . Bolometric corrections were also taken from Flower (1996). The derived quantities were then used to estimate ν_{\max} for each star (Equation (1)), and compared with the observed value (see Figure 3).

Figure 3 shows four obvious outliers (nos 1, 3, 8, and 11), three of which are also outliers in the CMD (nos 1, 3, and 11). For the rest of the stars we see good agreement between the

Table 1
Cross Identifications and Membership

ID (This Work)	ID (KIC) ^a	WOCs ID (Hole et al.)	ID (Sanders)	Mem.ship (Hole et al.) ^b	Mem.ship (Sanders) ^c	Mem.ship (This Work)
1	5024272	003003		SM 95%		No
2	5024750	001004	141	SM 93%	83%	Yes
3	5023889	004014	42	SM 95%	90%	No
4	5023732	005014	27	SM 94%	90%	Yes
5	5112950	003005	148	SM 95%	92%	Yes
6	5112387	003007	73	SM 95%	88%	Yes
7	5024512	003001	116	SM 93%	90%	Yes
8	4936335	007021	9	SM 95%	68%	No
9	5024405	004001	100	SM 93%	91%	Yes
10	5112072	009010	39	SM 95%	91%	Yes
11	4937257	009015	144	SM 88%	80%	No

Notes.

^a ID from the *Kepler Input Catalog* (Latham et al. 2005).

^b Classification (SM: single member) and membership probability from radial velocity (Hole et al. 2009).

^c Membership probability from proper motion (Sanders 1972).

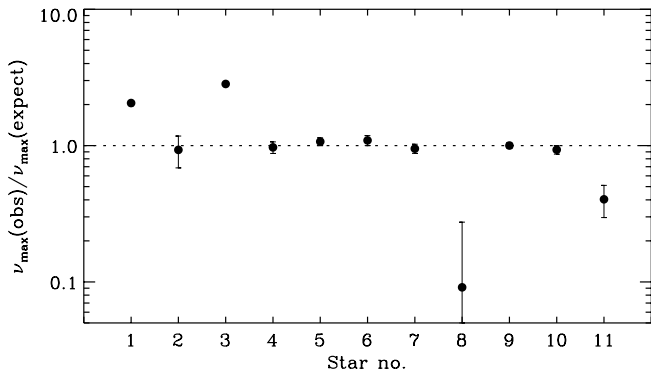


Figure 3. Ratio of observed and expected ν_{\max} . 1σ error bars indicate the uncertainty on $\nu_{\max}(\text{obs})$. Stars clearly above or below the dotted line are either not cluster members or members whose evolution have not followed the standard scenario.

expected and observed value, indicating that the uncertainty on the ν_{\max} estimates are relatively small. Since the variations in mass and effective temperature among the cluster giant stars are small, deviations from the dotted line must be caused by an incorrect estimate of the luminosity. This implies that the luminosities of stars falling significantly above or below the line have been over- or underestimated, respectively. The simplest interpretation is that these outliers are fore- or background stars, and hence not members of the cluster. To explain the differences between the observed and expected value of ν_{\max} would require the deviant stars to have V errors of more than 1 mag, and in some cases $B-V$ errors of about 0.2 mag if they were cluster members. Binarity may explain deviations above the dotted line, but only by up to a factor of 2 in L (and hence, in the ratio of the observed to expected ν_{\max}). The deviation of only one star (no. 1) could potentially be explained this way. However, that would be in disagreement with its single-star classification from multi-epoch radial velocity measurements, assuming it is not a binary viewed pole-on (see Table 1). Hence, under the assumption of a standard stellar evolution, the most likely explanation for all four outliers in Figure 3 is therefore that these stars are not cluster members. This conclusion is, however, in disagreement with their high membership probability from measurements of radial velocity (Hole et al. 2009) and proper motion (Sanders 1972; see Table 1). Another interesting possibility is that the anomalous pulsation properties might be explained by more

exotic stellar evolution scenarios than is generally anticipated for open-cluster stars.

5. ASTEROSEISMIC “COLOR–MAGNITUDE DIAGRAMS”

It is clear from Figure 2 that the amplitudes of the oscillations increase with luminosity for the seismically determined cluster members. Based on calculations by Christensen-Dalsgaard & Frandsen (1983), Kjeldsen & Bedding (1995) have suggested that the photometric oscillation amplitude of p modes scale as $(L/M)^s T_{\text{eff}}^{-2}$, with $s = 1$ (the velocity amplitudes, meanwhile, would scale as $(L/M)^s$). This was revised by Samadi et al. (2007) to $s = 0.7$ based on models of main-sequence stars. Taking advantage of the fewer free parameters within this ensemble of stars, our observations allow us to make some progress toward extrapolating this scaling to red giants and determining the value of s .

In Figure 4, we introduce a new type of diagram that is similar to a CMD, but with magnitude replaced by an asteroseismic parameter—in this case, the measured oscillation amplitude. Amplitudes were estimated for all stars in our sample (except for the four outliers) using methods similar to that of Kjeldsen et al. (2008; see also Michel et al. 2008), which assume that the relative power between radial and non-radial modes is the same as in the Sun. This diagram confirms the relationship between amplitude and luminosity. Despite a large scatter, which is not surprising from this relatively short time series, we see that $s = 0.7$ provides a much better match than $s = 1.0$. Once verified with more data, this relation will allow the use of the measured amplitude as an additional asteroseismic diagnostic for testing cluster membership and for isochrone fitting in general. We note that the other clusters observed by *Kepler* have different metallicities than NGC 6819, which will allow future investigation on the metallicity dependence of the oscillation amplitudes.

We expect to obtain less scatter in the asteroseismic measurements when longer time series become available. That will enable us to expand classical isochrone fitting techniques to include diagrams like this, where amplitude could also be replaced by ν_{\max} or $\Delta\nu$. In particular, we should be able to determine the absolute radii aided by $\Delta\nu$ of the red-giant branch stars, which would be an important calibrator for theoretical

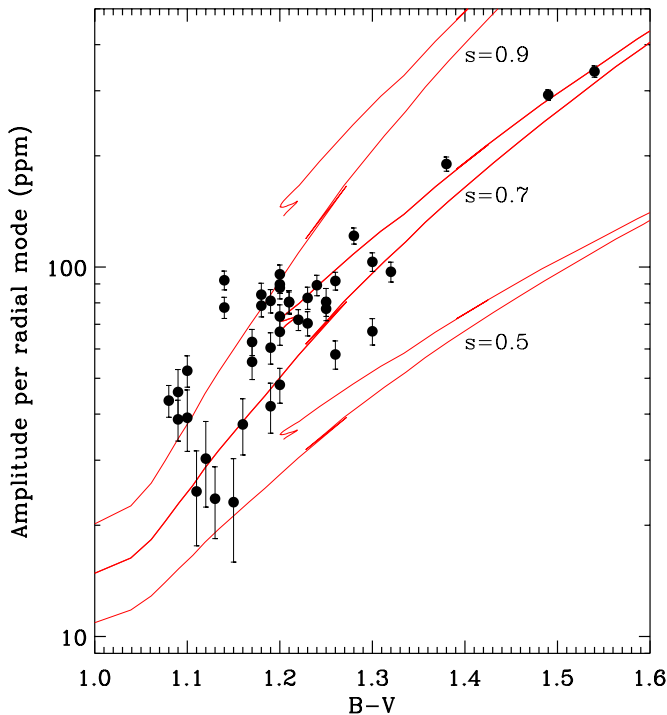


Figure 4. Amplitude color diagram of red giant stars in NGC 6819 with the Marigo et al. (2008) isochrone overlaid with three values of s in the amplitude scaling relation: $(L/M)^s T_{\text{eff}}^{-2}$. The solar value used in this scaling is 4.7 ppm (Kjeldsen & Bedding 1995).

isochrones. Additionally, the distributions of the asteroseismic parameters—such as ν_{max} —can potentially be used to test stellar population synthesis models (Hekker et al. 2009b; Miglio et al. 2009b). Applying this approach to clusters could lead to further progress in understanding of physical processes such as mass loss during the red-giant phase (see, e.g., Miglio et al. 2009a). Note that a few clear outliers are indicative of non-membership or exotic stellar evolution, as a result of factors such as stellar collisions or heavy mass loss, while a general deviation from the theoretical predictions by a large group of stars would suggest that the standard theory may need revision.

Finally, we note that NGC 6819 and another *Kepler* cluster, NGC 6791, contain detached eclipsing binaries (Talamantes & Sandquist 2009; Street et al. 2005; de Marchi et al. 2007; Mochejska et al. 2005). For these stars masses and radii can be determined independently (Grundahl et al. 2008), which will further strengthen results of asteroseismic analyses.

6. DISCUSSION AND CONCLUSIONS

Photometric data of red giants in NGC 6819 obtained by NASA's *Kepler Mission* have enabled us to make the first clear detection of solar-like oscillations in cluster stars. The general properties of the oscillations ($\Delta\nu$, ν_{max} , and amplitudes) agree well with results of field red giants made by *Kepler* (Bedding et al. 2010) and CoRoT (de Ridder et al. 2009; Hekker et al. 2009b). We find that the oscillation amplitudes of the observed stars scale as $(L/M)^{0.7} T_{\text{eff}}^{-2}$, suggesting that previous attempts to detect oscillations in clusters from ground were at the limit of detection.

We find that the oscillation properties provide additional tests for cluster membership, allowing us to identify four stars that are either non-members or exotic stars. All four stars have membership probability higher than 80% from radial velocity

measurements, but three of them appear to be photometric non-members. We further point out that deviations from the theoretical predictions of the asteroseismic parameters among a large sample of cluster stars have the potential of being used as additional constraints in the isochrone fitting process, which can lead to improved stellar models.

Our results, based on limited data of about one month, highlight the unique potential of asteroseismology on the brightest stars in the stellar clusters observed by *Kepler*. With longer series sampled at the spacecraft's short cadence (≈ 1 minute), we expect to detect oscillations in the subgiants and turnoff stars, as well as in the blue stragglers in this cluster.

Funding for this Discovery mission is provided by NASA's Science Mission Directorate. The authors thank the entire *Kepler* team without whom this investigation would not have been possible. The authors also thank all funding councils and agencies that have supported the activities of Working Group 2 of the *Kepler Asteroseismic Science Consortium* (KASC).

Facilities: *Kepler*

REFERENCES

- Bedding, T. R., et al. 2010, *ApJ*, 713, L176
 Borucki, W., et al. 2009, in *IAU Symp.* 253, *Transiting Planets*, ed. F. Pont, D. Sasselov, & M. Holman (Dordrecht: Kluwer), 289
 Brown, T. M., & Gilliland, R. L. 1994, *ARA&A*, 32, 37
 Brown, T. M., Gilliland, R. L., Noyes, R. W., & Ramsey, L. W. 1991, *ApJ*, 368, 599
 Christensen-Dalsgaard, J. 2002, *Rev. Mod. Phys.*, 74, 1073
 Christensen-Dalsgaard, J., & Frandsen, S. 1983, *Sol. Phys.*, 82, 469
 de Marchi, F., et al. 2007, *A&A*, 471, 515
 de Ridder, J., et al. 2009, *Nature*, 459, 398
 Edmonds, P. D., & Gilliland, R. L. 1996, *ApJ*, 464, L157
 Flower, P. J. 1996, *ApJ*, 469, 355
 Frandsen, S., et al. 2007, *A&A*, 475, 991
 Gilliland, R. L., et al. 1993, *AJ*, 106, 2441
 Gough, D. O., & Novotny, E. 1993, in *ASP Conf. Ser.* 42, *GONG 1992: Seismic Investigation of the Sun and Stars*, ed. T. M. Brown (San Francisco, CA: ASP), 355
 Grundahl, F., Clausen, J. V., Hardis, S., & Frandsen, S. 2008, *A&A*, 492, 171
 Hekker, S., et al. 2009a, *MNRAS*, in press (arXiv:0911.2612)
 Hekker, S., et al. 2009b, *A&A*, 506, 465
 Hole, K. T., Geller, A. M., Mathieu, R. D., Platais, I., Meibom, S., & Latham, D. W. 2009, *AJ*, 138, 159
 Huber, D., Stello, D., Bedding, T. R., Chaplin, W. J., Arentoft, T., Quirion, P., & Kjeldsen, H. 2009, *Commun. Asteroseismol.*, 160, 74
 Kjeldsen, H., & Bedding, T. R. 1995, *A&A*, 293, 87
 Kjeldsen, H., et al. 2008, *ApJ*, 682, 1370
 Latham, D. W., Brown, T. M., Monet, D. G., Everett, M., Esquerdo, G. A., & Hergenrother, C. W. 2005, *BAAS*, 37, 1340
 Marigo, P., Girardi, L., Bressan, A., Groenewegen, M. A. T., Silva, L., & Granato, G. L. 2008, *A&A*, 482, 883
 Mathur, S., et al. 2009, *A&A*, in press (arXiv:0912.3367)
 Michel, E., et al. 2008, *Science*, 322, 558
 Miglio, A., Montalbán, J., Eggenberger, P., Hekker, S., & Noels, A. 2009a, in *AIP Conf. Ser.* 1170, *Stellar Pulsation: Challenges for Theory and Observatory*, ed. J. A. Guzik & P. A. Bradley (Melville, NY: AIP), 132
 Miglio, A., et al. 2009b, *A&A*, 503, L21
 Mochejska, B. J., et al. 2005, *AJ*, 129, 2856
 Mosser, B., & Appourchaux, T. 2009, *A&A*, 508, 877
 Samadi, R., Georgobiani, D., Trampedach, R., Goupil, M. J., Stein, R. F., & Nordlund, Å. 2007, *A&A*, 463, 297
 Sanders, W. L. 1972, *A&A*, 19, 155
 Stello, D., Chaplin, W. J., Basu, S., Elsworth, Y., & Bedding, T. R. 2009, *MNRAS*, 400, 80
 Stello, D., & Gilliland, R. L. 2009, *ApJ*, 700, 949
 Stello, D., et al. 2007, *MNRAS*, 377, 584
 Street, R. A., et al. 2005, *MNRAS*, 358, 795
 Talamantes, A., & Sandquist, E. L. 2009, *BAAS*, 41, 320
 VandenBerg, D. A., Bergbusch, P. A., & Dowler, P. D. 2006, *ApJS*, 162, 375

Appendix C

PHOTOSPHERIC AND CHROMOSPHERIC ACTIVITY ON EY DRA

Photospheric and chromospheric activity on EY Dra*

H. Korhonen^{1,**}, K. Brogaard², K. Holhjem^{3,4}, S. Ramstedt⁵, J. Rantala⁶, C.C. Thöne⁷, and K. Vida^{8,9}

¹ Astrophysikalisches Institut Potsdam, An der Sternwarte 16, D-14482 Potsdam, Germany

² Department of Physics and Astronomy, University of Aarhus, DK-8000 Aarhus C, Denmark

³ Nordic Optical Telescope, Apartado 474, E-38700 Santa Cruz de La Palma, Spain

⁴ Argelander-Institut für Astronomie, Auf dem Hügel 71, D-53121 Bonn, Germany

⁵ Stockholm Observatory, AlbaNova University Centre, S-10691 Stockholm, Sweden

⁶ Observatory, PO Box 14, FI-00014 University of Helsinki, Finland

⁷ Dark Cosmology Centre, Niels Bohr Institute, University of Copenhagen, Juliane Maries Vej 30, DK-2100 Copenhagen Ø, Denmark

⁸ Eötvös Loránd University, Department of Astronomy, H-1518 Budapest, PO Box 32, Hungary

⁹ Konkoly Observatory of the Hungarian Academy of Sciences, H-1525 Budapest, Hungary

Received 2007 Mar 20, accepted 2007 May 7

Published online 2007 Oct 18

Key words stars: activity – atmospheres – chromospheres – starspots – stars: individual (EY Dra)

Magnetic activity in the photosphere and chromosphere of the M dwarf EY Dra is studied and possible correlations between the two are investigated using photometric observations in the V and R bands and optical and near infrared spectroscopy. The longitudinal spot configuration in the photosphere is obtained from the V band photometry, and the chromospheric structures are investigated using variations in the $H\alpha$ line profile and observations of the Paschen β line. The shape of the V band light-curve indicates two active regions on the stellar surface, about 0.4 in phase apart. The spectroscopic observations show enhanced $H\alpha$ emission observed close to the phases of the photometrically detected starspots. This could indicate chromospheric plages associated with the photospheric starspots. Some indications of prominence structures are also seen. The chromospheric pressure is limited to $\log m_{\text{TR}} < -4$ based on the non-detection of emission in the Paschen β wavelength region.

© 2007 WILEY-VCH Verlag GmbH & Co. KGaA, Weinheim

1 Introduction

EY Dra (RE 1816+541) is a very active M dwarf that was discovered by the ROSAT extreme ultraviolet (EUV) all sky survey in the early 1990's (Pounds et al. 1993). The optical counterpart of the EUV source RE 1816+541 was first observed by Jeffries et al. (1994) who did a thorough analysis of the object using optical spectroscopy. They observed strong, variable $H\alpha$ emission and molecular lines, and concluded that the source is an M1-2e dwarf, and thereby one of the most active stars in the solar neighbourhood. They also discovered that EY Dra is a very rapid rotator with a $v \sin i \approx 61 \text{ km s}^{-1}$ and a rotation period of about $12 \sin i$ hours. Jeffries et al. (1994) determined the radial velocity of the target to be $-21.9 \pm 1.5 \text{ km s}^{-1}$. A higher spectral and temporal resolution study of EY Dra was carried out by Eibe (1998) who found significant variations in the $H\alpha$ profile, which were interpreted as chromospheric plages and prominence clouds higher up in the atmosphere, but still below the corotation radius.

The first photometric observations of EY Dra were obtained by Schwartz et al. (1995) who established the star's brightness to be 11.83 in the V band and the colours of $(B - V) = 1.45$, $(V - R) = 0.96$ and $(R - I) = 1.05$, also indicating a cool star. The first long-term photometric study of EY Dra was carried out by Robb & Cardinal (1995) who measured the rotation period of $0^{\text{d}}.4589$ and remarked that the light-curve shape indicated two large spots or active regions on the stellar surface. Barnes & Collier Cameron (2001) used Doppler imaging techniques to obtain the first precise surface structure maps of EY Dra. These surface temperature maps showed spots on a very large latitude range ($20^\circ - 80^\circ$), but no polar spot.

In this paper we carry out the first simultaneous photometric and spectroscopic observations of EY Dra to study the photospheric spots and correlate them with the variability seen in the chromosphere. The longitudinal spot configuration is obtained from the photometric observations and the chromosphere is studied with the high resolution $H\alpha$ line observations. In addition, medium resolution near infrared (NIR) observations of the Paschen β line were used to further investigate the chromosphere of EY Dra.

* Based on observations made with the Nordic Optical Telescope, operated on the island of La Palma jointly by Denmark, Finland, Iceland, Norway, and Sweden, in the Spanish Observatorio del Roque de los Muchachos of the Instituto de Astrofísica de Canarias.

** Corresponding author: hkorhonen@aip.de

2 Observations

All the observations presented in this paper were obtained at the Nordic Optical Telescope in early July 2006. The optical data were taken using ALFOSC, which is owned by the Instituto de Astrofísica de Andalucía (IAA) and operated at the Nordic Optical Telescope under agreement between IAA and the NBIfAFG of the Astronomical Observatory of Copenhagen. The NIR spectroscopy was obtained using NOTCam.

All the observations have been phased using the ephemeris, $HJD = 2449927.752 + 0^d.4589 \times E$, from Robb & Cardinal (1995).

2.1 Photometry

Photometric observations of EY Dra in the V and R bands were obtained with ALFOSC. The detector is an E2V Technologies 2k back-illuminated CCD with $13.5\mu m$ pixels, giving a field-of-view (FOV) of $6.5' \times 6.5'$. This FOV made it possible to observe the comparison star (GSC 0390400259) and the check star (GSC 0390400361) in one frame together with the target, and thus do differential photometry of EY Dra. The comparison star and the check star are both from the Hubble Space Telescope Guide Star Catalogue (Jenkner et al. 1990).

The photometric observations of EY Dra were obtained during the nights starting 2006 July 1 and July 3. The exposure time was 1–3 s in the V band and 1 s in the R band. In total observations from 9 rotational phases were obtained. Each observation consisted of 1–7 individual exposures that were first bias and sky flat field corrected, and then averaged after the determination of the differential magnitude (object-comparison star). The error of each phase was determined as the standard deviation of all the points used in the average and divided by the square-root of the number of observations. The data reduction was done and the photometry obtained using Image Reduction and Analysis Facility (IRAF) distributed by KPNO/NOAO. Table 1 gives more details on the photometric observations.

2.2 Optical spectroscopy

Optical spectroscopy of EY Dra around the $H\alpha$ line was obtained using ALFOSC, grism #17, and a $0''.5$ off-set slit during the nights starting 2006 July 1 and July 3. This instrument configuration gives a resolving power ($\lambda/\Delta\lambda$) of 10 000 and a spectral coverage approximately from 6200 Å to 6700 Å. Due to the fringing in the E2V CCD starting around 6400 Å, the observations were done in sets of five 120 second exposures. Between each separate spectrum the object was moved along the slit to be able to remove this fringe pattern from the observations. After every five object exposures, two Halogen flat fields and one Neon arc spectrum were obtained. After basic reduction steps (bias subtraction, image trimming and flat field correction) the five

Table 1 Details of the photometric observations of EY Dra. The Heliocentric Julian Date, rotational phase, instrumental differential magnitude, the error of the magnitude and the number of observations used to obtain the magnitude are given for both the V and R bands. The error for each data point is the standard deviation of the measurements divided by the square root of the number of the measurements.

HJD 2453000+	Phase	Mag.	Error	No.
<i>V</i> band				
918.41440	0.148	−1.197	0.002	4
918.46784	0.265	−1.202	0.010*	1
918.52188	0.382	−1.184	0.004	3
918.61168	0.578	−1.163	0.003	3
920.41944	0.517	−1.173	0.004	5
920.53116	0.761	−1.172	0.003	2
920.58829	0.885	−1.163	0.004	3
920.62317	0.961	−1.149	0.007	2
920.67216	0.068	−1.178	0.003	3
<i>R</i> band				
918.41845	0.157	−1.772	0.003	4
918.46948	0.268	−1.773	0.003	3
918.52399	0.387	−1.757	0.004	3
918.61382	0.583	−1.738	0.003	3
920.42230	0.524	−1.749	0.004	3
920.54907	0.800	−1.718	0.010*	1
920.59153	0.892	−1.732	0.002	7
920.62466	0.965	−1.729	0.004	3
920.67405	0.072	−1.749	0.002	3

*) Only one observation was obtained during this phase, so no standard deviation of the measurements could be obtained to estimate the error of the data point. An error value of 0.010 was adopted.

consecutive observations were combined to obtain 15 better signal-to-noise (S/N) spectra with minimum fringe patterns. A radial velocity standard (HD 103095) and a B star (BD+33 2642) were also observed. The B star spectrum was used for checking contribution from terrestrial lines in this spectral region. The reductions were carried out using the 4A reduction package (Ilyin 2000). More details on the observations are given in Table 2.

2.3 Near IR spectroscopy

The medium resolution NIR observations were obtained in the region around the Paschen β line, using the NOTCam with the high resolution camera, grism #1, and J filter. This instrument configuration gives a resolving power ($\lambda/\Delta\lambda$) of 5700 and a wavelength coverage of 12620–13520 Å. The detector is a Rockwell Science Center “HAWAII” array with $1024 \times 1024 \times 18.5\mu m$ pixels in HgCdTe. Two spectra with 4×450 s exposure time were obtained in the evening of 2006 July 5.

For removing the IR background we used an ABBA dithering pattern along the slit, which gave 4 separate spectra that were combined into one spectrum during the reduc-

Table 2 Optical spectroscopy of EY Dra. Heliocentric Julian Date, rotational phase, radial velocity obtained with IRAF fxcor task and the S/N per pixel are given.

HJD 2453000+	Phase	RV (km s ⁻¹)	S/N
918.44256	0.210	-21.6 ± 2.7	150
918.45631	0.239	-21.3 ± 3.0	162
918.48694	0.306	-17.7 ± 3.6	128
918.49864	0.332	-17.6 ± 3.3	94
918.50970	0.356	-15.6 ± 3.1	93
918.62720	0.612	-28.7 ± 3.3	58
920.39421	0.462	-25.3 ± 2.5	116
920.56335	0.831	-22.7 ± 2.1	139
920.57345	0.853	-15.9 ± 2.3	164
920.64873	0.017	-13.4 ± 2.3	133
920.66079	0.043	-13.5 ± 2.2	114
920.69449	0.117	-31.8 ± 2.6	131
920.70800	0.146	-33.3 ± 2.3	108
920.71966	0.172	-31.9 ± 2.5	124
920.72899	0.192	-33.7 ± 2.0	91

tions. Each spectrum was obtained using non-destructive readouts which were acted upon by a linear regression calculation reducing the Poisson noise of the observation. The whole spectral region shows strong fringing pattern that did not completely disappear even after the flat fielding. For removing the skylines an A0 star (HD 172728) was observed as an atmospheric standard. The data were reduced using IRAF.

3 Radial velocity

The radial velocity of EY Dra was investigated from the lines in the wavelength region 6400–6500 Å using the IRAF fxcor routine. Before the cross-correlation all three radial velocity standard observations were combined to one higher S/N spectrum, after which the resulting spectrum was spun-up to the $v \sin i$ of EY Dra, 61 km s⁻¹ (Jeffries et al. 1994). The measurements for the individual phases are given in Table 2.

The radial velocity for the whole dataset is -22.6 ± 1.9 km s⁻¹. This is in agreement with the values published by (Jeffries et al. 1994) and Eibe (1998). The radial velocities obtained from each night's data set are -20.1 ± 1.9 km s⁻¹ and -24.3 ± 2.9 km s⁻¹, for 2006 July 1 and July 3, respectively. Note that the errors stated assume that the errors are random.

4 Photosphere

The V and R band light-curves of EY Dra together with the errors of the individual points are shown in Fig. 1. The V band light-curve has in general a W shape. The phases 0.76 and 0.88 form the bump seen in the broad light-curve minimum. The two minima in the V band light-curve are located

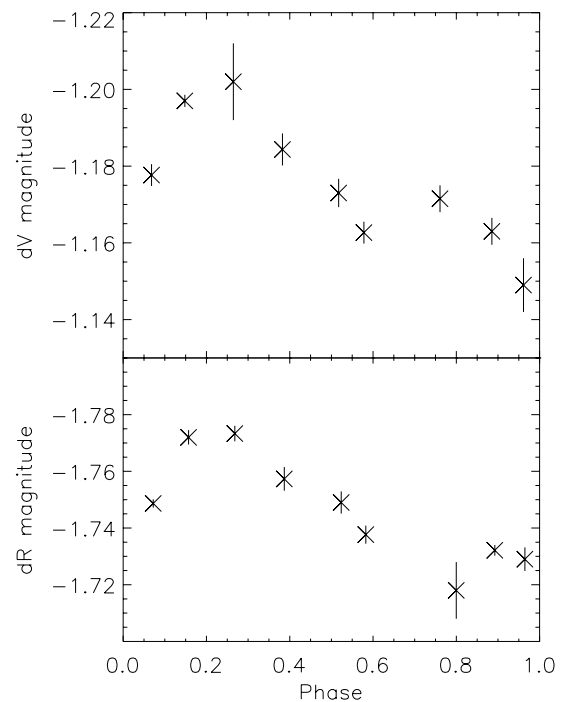


Fig. 1 Differential V and R band photometry of EY Dra with the errors.

around the phases 0.3–0.75 and 0.85–1.15. The main maximum occurs around the phases 0.15–0.3. On the whole, the V band light-curve indicates two active regions separated by about 0.4 in phase on the surface of EY Dra.

In the V band observations of Robb & Cardinal (1995) from 1995 similar W shape was present. Also, the photometry obtained before and after our observations at the Konkoly observatory (Vida & Oláh 2006) exhibits the W shape. This photometry, which will be published later, is shown in Fig. 2 together with our observations. In the plot the plus-signs are data obtained at the Konkoly observatory between 2006 April 21 and May 12, crosses are the NOT observations and the stars are observations from the Konkoly observatory obtained between 2006 July 22 and August 8. The relatively large scatter seen in the latter Konkoly observations is most likely due to the non-optimal observing conditions during this time period.

In the R band observations obtained at NOT the W shape is not really seen. The light-curve shows a broad minimum around the phases 0.8–1.1. The observations at the phase 0.89 show indications of the bump, but unfortunately the phase 0.8, which also would be in the bump, only has one individual observation and as such a large photometric error. The R band observations from the Konkoly observatory show the W shape for the time periods before and after the NOT observations. When the instrumental ($V - R$) colour is calculated, no clear modulation of the colour with the stellar rotation period is seen. But the data point at the phase 0.8 deviates strongly from the others.

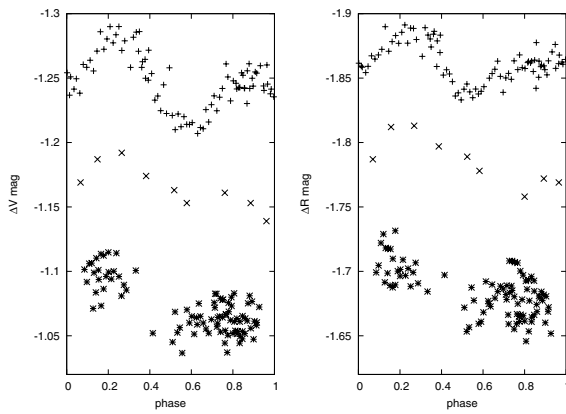


Fig. 2 Differential V (left) and R (right) band observations of EY Dra. The plus-signs are data obtained at the Konkoly observatory on average 62 days before the NOT observations, crosses are the NOT observations and the stars are observations obtained at the Konkoly observatory on average 27 days after the NOT observations. Offsets have been applied to the individual datasets to show the light-curve shapes better.

5 Chromosphere

5.1 $H\alpha$ line

In EY Dra the $H\alpha$ line is a quite broad emission feature. All the profiles from the 15 epochs observed in this study are plotted in Fig. 3a. The radial velocities stated in Table 2 have been removed from the profiles. As can be seen, the strength of the profile varies significantly with time. The thick line in the plot is the mean of all the profiles. The residual variations in the profile after the mean profile has been subtracted are given in Fig. 3b. For both plots in Fig. 3 the data from the night starting 2006 July 1 are presented with dotted lines and the data from the night starting 2006 July 3 are given by dashed lines.

To study the $H\alpha$ behaviour in more detail the profiles showing the difference between the observations and the mean spectrum were investigated more thoroughly. In Fig. 4 a dynamic spectrum constructed from these difference profiles is shown. Brighter colours in the plot correspond to enhanced emission and the darker colours to the emission that is less than the average. The phases of the observations are shown with crosses on the plot. The data for the phases where there are no observations are just interpolations between the closest phases with data.

The relatively low spectral resolution of the data does not allow such a detailed analysis of the chromospheric absorption and emission clouds as was done in Eibe (1998). However, our data also indicates chromospheric structures. The dynamic spectrum clearly shows enhanced emission in the $H\alpha$ around the phases 0.75–1.1, and a small enhancement around the phase 1.5. In the dynamic spectrum the features with increased and decreased $H\alpha$ emission often seem to move from blue to red, and could indicate chromospheric plagues and prominences. Especially the enhanced emission around the phases 0.75–1.1 seems to move from

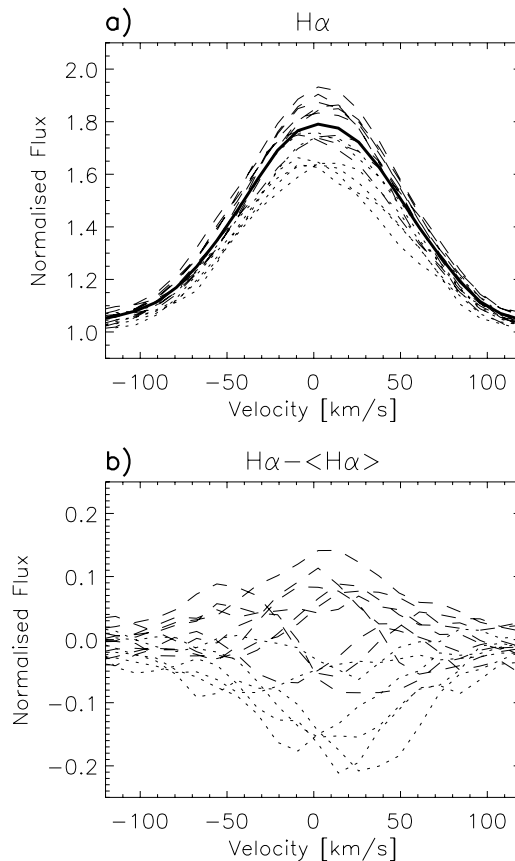


Fig. 3 The $H\alpha$ line variations in EY Dra. a) All the 15 individual $H\alpha$ observations obtained in this study. The line profiles are plotted against the velocity obtained in relation to the rest wavelength of the $H\alpha$. The radial velocity has been removed from all the profiles. The thick line gives the average line profile. b) The residual variations in the $H\alpha$. The mean profile has been subtracted from all the observations. In both of the plots the dotted line gives the observations from the night starting 2006 July 1 and the dashed line observations from the night starting 2006 July 3.

blue to red, and could be associated with a plague. The other enhancement, around the phase 0.5, is, due to the sparse data sampling, only seen in one spectrum. The feature could be associated with a plague, though this cannot be confirmed. The feature of decreased $H\alpha$ emission around the phases 1.25–1.5 is seen to move across the line profile, and could thus be associated with a prominence cloud. It has to be noted though, that the interpolation used to fill the phase gaps in the dynamic spectrum can artificially enhance the perception of moving features.

5.2 Paschen β line

Atmospheric models of M dwarfs calculated by Short & Doyle (1998) show that the Paschen β line profile can be used to determine the chromospheric pressure and thereby the activity level in such stars. This spectral line, which is in the NIR part of the spectrum ($\lambda = 12\,818 \text{ \AA}$), was therefore also observed.

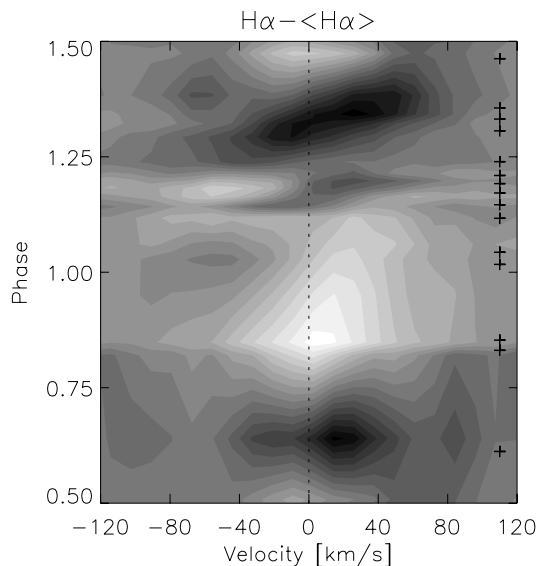


Fig. 4 Dynamic spectrum of the $H\alpha$ line of EY Dra. The image shows the difference profiles after the mean profile has been subtracted from the observations. Bright colour means more emission in the $H\alpha$. The measured radial velocity for each observations has been removed from the profiles. The crosses on the right hand side of the plot give the phases of the observations and the dashed line the 0 velocity.

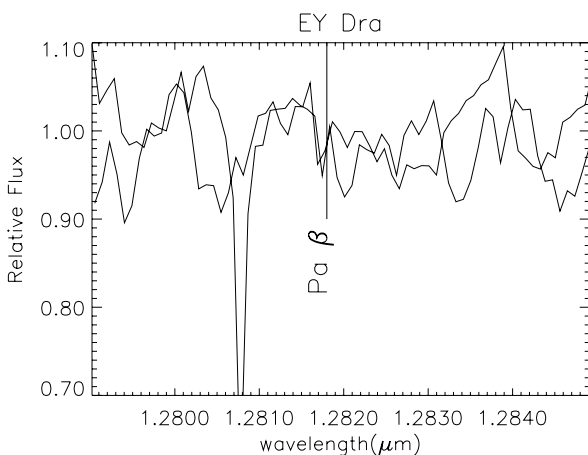


Fig. 5 The final two background subtracted, flat fielded, normalised and radial velocity corrected NIR spectra of EY Dra. The absorption line present in one spectrum and not in the other is a telluric feature. The vertical line is the position where the Paschen β line centre should be if present in the spectra.

Figure 5 shows the two observed NIR spectra of EY Dra around the Paschen β line. The resolution of the spectra is poor and a strong fringing pattern is seen in the spectra even after the flat field correction. Still, it is clear from the observations that no strong emission line is seen around the Paschen β wavelength.

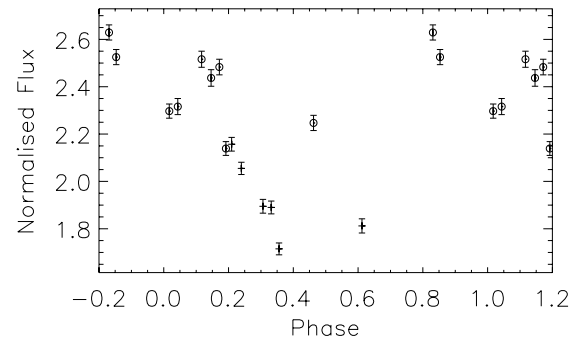


Fig. 6 The variation of the $H\alpha$ flux obtained by integrating over the whole line and plotted against the rotational phase. The observations from the night starting 2006 July 1 are given by crosses and the observations from the night starting July 3 by circles.

6 Discussion

6.1 Night to night variation of $H\alpha$

When looking at Fig. 3 it seems that in general the observations obtained during the night starting 2006 July 1 (dotted line) show less emission than the ones observed during the night starting 2006 July 3 (dashed line). This could be caused by a real difference in the activity level between the two nights, or by the observations from the first night coinciding with the less active rotational phases. In Fig. 6 the integrated $H\alpha$ flux is plotted against the phase. The behaviour seen during the second observing night (circles), can be interpreted as more or less constant $H\alpha$ emission, whereas the behaviour during the first observing night (crosses), shows clearly diminishing activity with increasing phase.

In principal the behaviour seen during the first observing night could be explained by a gradual decline of a chromospheric flare. On the other hand, if the behaviour seen during the first observing night is due to a declining flare, then flux seen in the phases 0.3–0.35 indicates the normal $H\alpha$ flux. This would imply that the observations from the second observing night, that have a higher flux than that, would be from a flaring state. Also, if it indeed is a flare that is seen during the second observing night, then this flare would last the whole night without showing any decline. We also note that the $H\alpha$ flux at the phase 0.192, from the second observing night, is almost identical with the flux at the phase 0.210, obtained during the first observing night (see Fig. 6). All this implies that the difference seen in the activity levels between these two nights is most likely just caused by the observations during the first observing night coinciding with the less active regions on the stellar surface.

6.2 Spot longitudes

For measuring the longitudes of the photospheric spots a spot filling factor map was obtained from the V band light-curve using light-curve inversion methods (see e.g., Lanza

et al. (1998) for the method and Oláh et al. (2006) for the implementation used here). Light-curve inversions were decided to be used for the spot longitude determination, as tests show that the inversions result in more accurate determination of the spot longitudes than just simply determining the light-curve minimum gives (see Savanov & Strassmeier 2007). In some cases, especially when dealing with close-by spots, taking the light-curve minimum results in wrong spot longitude, whereas the inversion gives the correct longitudinal spot configuration.

For the inversion the unspotted surface temperature is set to 4000 K, which is consistent with the observations of the spectral type. Spots are assumed to be 1000 K cooler than the unspotted surface, in line with observations of other active stars. The instrumental differential V band magnitude that corresponds to the unspotted surface is estimated to be -1^m25 , though as the photometric time series of EY Dra is short this parameter is relatively uncertain. However, changing the brightest magnitude will not affect the positions of the spots seen in the filling factor maps, only the filling factor values themselves. The inclination was set to 66° measured by Robb & Cardinal (1995).

One should also note that one-dimensional data, as the light-curve is, do not give information on the latitudinal distribution of the spots. This means that the spot latitude seen in the maps arises from the fact that the inversion process tends to introduce the spots to the location where they have the maximum impact on the light-curve, i.e., at the centre of the visible stellar disk. From photometry it is impossible to discern whether the light-curve minimum is caused by a single large spot or an active region consisting of several spots. For simplicity the structure causing the light-curve minimum, and seen in the spot filling factor map, is called a spot.

The resulting filling factor map of EY Dra for early July 2006 is given in Fig. 7b. It clearly shows two large spots on the surface. These spots are located at phases 0.4–0.6 (centred at the phase 0.53) and 0.8–1.1 (centred at the phase 0.91). This implies two active longitudes separated by 0.4 in phase. A longer time series of photometric observations is needed for confirming whether or not this configuration is the normal case for EY Dra. The earlier photometric observations (Robb & Cardinal 1995; Vida & Oláh 2006) have also shown the W shape, which implies that this kind of active longitude structure is relatively stable on EY Dra. A spot configuration where two spots are located on the stellar surface about 0.5 in phase apart is common for active stars (see e.g., Jetsu et al. 1993; Berdyugina & Tuominen 1998). Recent dynamo calculations can also produce active longitudes that are 0.25–0.5 in phase apart (e.g., Moss 2004; Elstner & Korhonen 2005).

6.3 Correlating activity in the photosphere and chromosphere

In the Sun, photospheric dark spots are often associated with bright plages in the chromosphere. Some active stars also

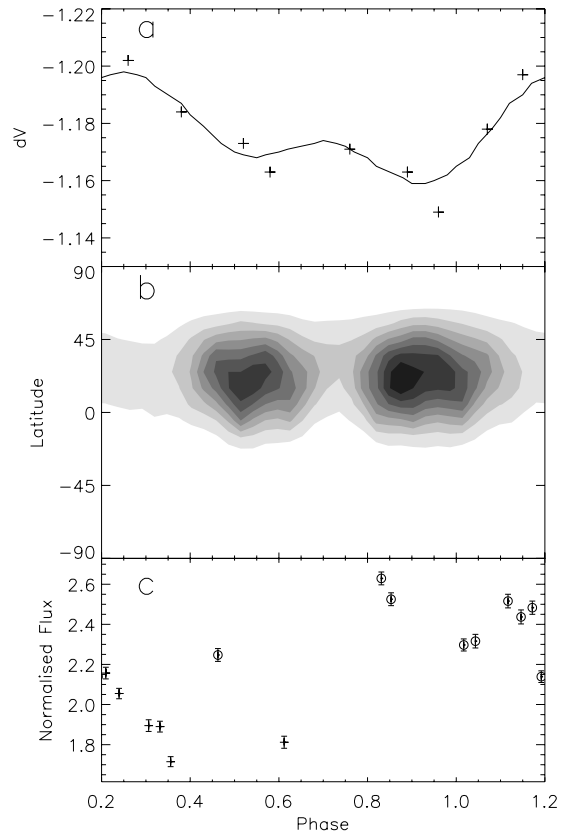


Fig. 7 Correlating photospheric and chromospheric activity. a) The differential V band observations (crosses) with the fit (solid line) obtained from the inversion. b) The spot filling factor map, where the darker colour means larger spot filling factor. c) Variation in the $H\alpha$ flux (symbols as in Fig. 6). In all the plots the phases from 0.2 to 1.2 are plotted to show the active regions better.

show evidence for correlated magnetic activity in the photosphere and chromosphere. Alekseev & Kozlova (2002) investigated quasi-simultaneous photometric observations, photo-polarimetry and high-resolution spectra of a young solar-like star LQ Hya. They found evidence for a connection between plages, magnetic regions and the starspot longitudes. Similar results have been obtained also for an active binary MS Ser (Alekseev & Kozlova 2003).

The possible correlation between the photospheric spots and chromospheric plages on EY Dra was studied using the data presented in this paper. The spot positions determined from the light-curve inversions of the V band data (Fig. 7a,b) show that the photospheric active regions occur at two active longitudes: one centred around the phase 0.53 and the other one centred around the phase 0.91. On the other hand the enhanced $H\alpha$ emission occurs at the phases 0.8–1.1 and another small increase is seen around the phase 0.5 (see Fig. 7c). Unfortunately the extent of this weaker feature cannot be determined, as there is only one observation around this enhancement. In general, the increases in the $H\alpha$ emission occur near the same phases where the

photospheric spots are centred. Thus, the observations of EY Dra obtained at NOT in early July 2006 can be interpreted as bright plagues in the chromosphere associated with the photospheric active region centred at the phase 0.91, and possibly also on the photospheric active region centred at the phase 0.53.

6.4 Chromospheric pressure

The Paschen β line is expected to vary with chromospheric pressure; changing with increasing pressure from a weak absorption line to a stronger absorption line and finally to an emission line (Short & Doyle 1998). The pressure at the top of the chromosphere, or equivalently at the bottom of the transition region, is measured as a column density and given by $\log m_{\text{TR}}$. According to the models by Short & Doyle (1998) the line responds to the increasing chromospheric pressure in the same way as the $\text{H}\alpha$. For low chromospheric pressure it is weakly in absorption with minimal equivalent width W_λ . As the chromospheric pressure increases the line becomes more strongly absorbent, with maximal W_λ occurring at $\log m_{\text{TR}} = -4.2$. Then, as the chromospheric pressure increases further the line makes a rapid transition to emission. With $\log m_{\text{TR}} = -4.0$ the line is either balanced between absorption and emission or is weakly in emission, depending on the exact model. The more precise behaviour can be seen in Sort & Doyle (1998, Fig. 3)

Our NIR spectra of EY Dra do not show any indication of an emission line around the wavelength of Paschen β . According to the models of Short & Doyle (1998) the chromospheric pressure of EY Dra is hence $\log m_{\text{TR}} \leq -4$. The non-detection of the Paschen β line in the EY Dra spectra can be due to the low resolution of the observations, though a strong emission line would be visible even with this relatively low quality data.

Short & Doyle (1998) also present models for the $\text{H}\alpha$ line. According to their calculations the pressure value of $\log m_{\text{TR}} = -4.0$ causes the $\text{H}\alpha$ to be strongly in emission, even though the Paschen β line is not yet in emission. The $\text{H}\alpha$ emission observed in EY Dra supports the idea that the chromospheric pressure of EY Dra is close to $\log m_{\text{TR}} = -4.0$, as with much lower pressures the $\text{H}\alpha$ line would not be in emission either.

7 Conclusions

Based on the photometric and spectroscopic observations of EY Dra the following conclusions can be drawn:

- The light-curve shape indicates two active regions approximately 0.4 in phase apart. Other photometric observations of EY Dra show that this could be the normal spot configuration.

- The $\text{H}\alpha$ shows strong variations during the two nights of observations. Indications for plagues and prominences are seen.
- The main enhancement seen in the $\text{H}\alpha$ emission occurs close to the phases of the photospheric active region that is centred at the phase 0.91. This indicates bright chromospheric plagues associated with the dark photospheric spots, as is often seen in the Sun.
- Chromospheric pressure is limited to $\log m_{\text{TR}} < -4$, based on the non-detection of Paschen β emission.

Acknowledgements. The observations used in this paper were obtained during the 2006 Nordic Baltic Research School at NOT and SST in La Palma, running from June 27 until July 8 2006. This summer school was financed by NordForsk and the main organiser was Dr. J. Sollerman. The authors would also like to thank Dr. A. Djupvik for her extremely valuable help with the NIR observations and reductions and Dr. M.I. Andersen for his help with the photometry. HK acknowledges the support from the German *Deutsche Forschungsgemeinschaft*, DFG project number KO 2310/1-2. KH acknowledges support from a doctoral fellowship awarded by the Research council of Norway, project number 177254/V30. KV acknowledges the financial support of the Hungarian government through OTKA T048961 and T043504. The Dark Cosmology Centre is funded by the Danish National Research Foundation.

References

- Alekseev, I.Yu., Kozlova, O.V.: 2002, A&A 396, 203
 Alekseev, I.Yu., Kozlova, O.V.: 2003, A&A 403, 205
 Barnes, J.R., Collier Cameron, A.: 2001, MNRAS 326, 950
 Berdyugina, S.V., Tuominen, I.: 1998, A&A 336, L25
 Eibe, M.T.: 1998, A&A 337, 757
 Elstner, D., Korhonen, H.: 2005, AN 326, 278
 Ilyin, I.V.: 2000, PhD Thesis
 Jeffries, R.D., James, D.J., Bromage, G.E.: 1994, MNRAS 271, 476
 Jenkner, H., Lasker, B.M., Sturch, C.R., McLean, B.J., Shara, M.M., Russel, J.L.: 1990, AJ, 99, 2082
 Jetsu, L., Pelt, J., Tuominen, I.: 1993, A&A 278, 449
 Lanza, A.F., Catalano, S., Cutispoto, G., Pagano, I., Rodonò, M.: 1998, A&A 332, 541
 Moss, D.: 2004, MNRAS 352, L17
 Oláh, K., Korhonen, H., Kóvári, Zs., Forgács-Dajka, E., Strassmeier, K.G.: 2006, A&A 452, 303
 Pounds, K.A., Allan, D.J., Barber, C., et al.: 1993, MNRAS 260, 77
 Robb, R.M., Cardinal, R.D.: 1995, IBVS, 4270
 Savanov, I.S., Strassmeier, K.G.: 2007, A&A, submitted
 Schwartz, R.D., Dawkins, D., Findley, D., Chen, D.: 1995, PASP 107, 667
 Short, C.I., Doyle, J.G.: 1998, A&A 331, L5
 Vida, K., Oláh, K.: 2006, in: *Solar and Stellar Activity Cycles*, 26th meeting of the IAU, JD08, #56

Appendix D

OSCILLATIONS IN PROCYON A: FIRST RESULTS FROM A MULTI-SITE CAMPAIGN

Oscillations in Procyon A First results from a multi-site campaign

S Hekker¹, T Arentoft², H Kjeldsen², T R Bedding³,
J Christensen-Dalsgaard², S Reffert⁴, H Bruntt³, R P Butler⁵,
L L Kiss³, S J O'Toole³, E Kambe⁶, H Ando⁷, H Izumiura⁶, B Sato⁸,
M Hartmann⁹, A P Hatzes⁹, T Appourchaux¹⁰, C Barban¹¹,
G Berthomieu¹², F Bouchy¹³, R A García¹⁴, J-C Lebrun¹⁵,
M Martić¹⁵, E Michel¹¹, B Mosser¹¹, P A P Nghiem¹⁴, J Provost¹²,
R Samadi¹¹, F Thévenin¹², S Turck-Chièze¹⁴, S A Bonanno¹⁶,
S Benatti¹⁷, R U Claudi¹⁷, R Cosentino¹⁸, S Leccia¹⁹, S Frandsen²,
K Brogaard², F Grundahl², H C Stempels²⁰, M Bazot², T H Dall²¹,
C Karoff², F Carrier²², P Eggenberger²³, D Sosnowska²⁴,
R A Wittenmyer²⁵, M Endl²⁶ and T S Metcalfe²⁷

¹ Leiden Observatory, Leiden University, P.O. Box 9513, 2300 RA Leiden, The Netherlands

² Department of Physics and Astronomy, University of Aarhus, DK-8000 Aarhus C, Denmark

³ School of Physics A28, University of Sydney, NSW 2006, Australia

⁴ ZAH, Landessternwarte Heidelberg, Königstuhl 12, D-69117 Heidelberg, Germany

⁵ Carnegie Institute of Washington, Department of Terrestrial Magnetism, 5241 Broad Branch Road NW, Washington, DC 20015-1305, USA

⁶ Okayama Astrophysical Observatory, National Astronomical Observatory of Japan, Asakuchi, Okayama 719-0232, Japan

⁷ National Astronomical Observatory of Japan, Mitaka, Tokyo 181-8588, Japan

⁸ Tokyo Institute of Technology, 2-12-1-S6-6, Okayama, Meguro-ku, Tokyo 152-8550, Japan

⁹ Thüringer Landessternwarte Tautenburg, Sternwarte 5, 07778 Tautenburg, Germany

¹⁰ Institut d'Astrophysique Spatiale, Université Paris XI-CNRS, Bâtiment 121, 91405 Orsay cedex, France

¹¹ LESIA, CNRS, Université Pierre et Marie Curie, Université Denis Diderot, Observatoire de Paris, 92195 Meudon cedex, France

¹² Laboratoire Cassiopée, UMT CNRS 6202, Observatoire de la Côte d'Azur, BP 4229, 06304 Nice cedex, France

¹³ Institut d'Astrophysique de Paris, CNRS, 98^{bis} BD Arago, 75014 Paris, France

¹⁴ DAPNIA/DSM/Service d'Astrophysique, CEA/Saclay, 91191 Gif-sur Yvette cedex, France

¹⁵ Service d'Aéronomie du CNRS, BP 3, 91371 Verrières le Buisson, France

¹⁶ INAF- Osservatorio Astrofisico di Catania, via S. Sofia 78, 95123 Catania, Italy

¹⁷ INAF- Osservatorio Astronomica di Padova, Vicolo Osservatorio 5 35122 Padova, Italy

¹⁸ INAF-Telescopio Nazionale Galileo, 38700 Santa Cruz de La Palma, TF, Spain

¹⁹ INAF-Astronomical Observatory of Capodimonte, Salita Moiariello 16, I-80131 Napoli, Italy

²⁰ School of Physics and Astronomy, University of St Andrews, North Haugh, St Andrews KY16 9SS, Scotland, UK

²¹ Gemini Observatory, 670 N. A'ohoku Pl., Hilo, HI 96720, USA

²² Instituut voor Sterrenkunde, KU Leuven, Celestijnenlaan 200D, 3001 Leuven, Belgium

²³ Institut d'Astrophysique et de Géophysique de l'Université de Liège, Allée du 6 Août, 4000 Liège, Belgium

²⁴ Observatoire de Genève, Université de Genève, 51 chemin des Maillettes, 1290 Sauverny, Switzerland

²⁵ Astronomy Department, The University of Texas at Austin, Austin, TX 78712, USA

²⁶ McDonald Observatory, The University of Texas at Austin, Austin, TX 78712, USA

²⁷ High Altitude Observatory and Scientific Computing Division, NCAR, PO Box 3000, CO 80307, USA

E-mail: saskia@strw.leidenuniv.nl

Abstract. Procyon A is a bright F5IV star in a binary system. Although the distance, mass and angular diameter of this star are all known with high precision, the exact evolutionary state is still unclear. Evolutionary tracks with different ages and different mass fractions of hydrogen in the core pass, within the errors, through the observed position of Procyon A in the Hertzsprung-Russell diagram. For more than 15 years several different groups have studied the solar-like oscillations in Procyon A to determine its evolutionary state. Although several studies independently detected power excess in the periodogram, there is no agreement on the actual oscillation frequencies yet. This is probably due to either insufficient high-quality data (i.e., aliasing) or due to intrinsic properties of the star (i.e., short mode lifetimes). Now a spectroscopic multi-site campaign using 10 telescopes world-wide (minimizing aliasing effects) with a total time span of nearly 4 weeks (increase the frequency resolution) is performed to identify frequencies in this star and finally determine its properties and evolutionary state.

1. Introduction

The bright F5 subgiant Procyon A is the primary of an astrometric binary system with a white dwarf in a 40 year orbit. Procyon A is the brightest northern-hemisphere asteroseismology candidate with well-determined characteristics, such as distance, mass and angular diameter. Brown *et al* [7] were among the first to observe an excess power between 0.5 and 1.5 mHz in radial velocity observations confirmed by several other radial velocity studies, e.g. [16], [6], [13], [17], [11], [10], [15]. So far these studies have independently revealed detections of power excess, but there is no agreement yet on the actual oscillation frequencies. This may be due to aliases present in the spectral window, short mode lifetimes, shifts from the asymptotic relation due to avoided crossings, or any combination of these factors. Although the frequencies are not yet known in detail, most studies obtain a large frequency spacing of $55 \pm 1 \mu\text{Hz}$.

Table 1. Stellar parameters of Procyon A from [1].

Mass [M_{\odot}]	1.42 ± 0.06
T_{eff} [K]	6512 ± 49
Radius [R_{\odot}]	2.071 ± 0.020
[Fe/H] [dex]	-0.09 ± 0.03
$v_{\text{rot}} \sin i$ [km s^{-1}]	3.16 ± 0.50

Another point of discussion is the fact that [18] did not detect any power excess in their MOST photometry and published Procyon A as a flat liner. Other photometric studies such as WIRE [8] and a reanalysis of the MOST 2004 data [20] claim to detect power excess in the same region as the radial velocity studies. A recent reanalysis of the MOST 2004 data and the analysis of new MOST data taken in 2005 reinforce the null detection of p-modes [12]. This issue is discussed more extensively by [4], who claim that the non-detection of oscillations in Procyon by the MOST satellite is fully consistent with the ground based radial-velocity studies due to a combination of several noise sources and the low photometric amplitude of the oscillations.

Table 2. Observatory, telescope, spectrograph, start of run (beginning of the night, local time), end of run (end of the night, local time), number of observed hours, number of spectra, mean uncertainty on the spectra (σ) in m s^{-1} for all facilities used for this multi-site campaign (ordered according to starting date and length of the run).

Observatory	Telescope	Spectrograph	Start	End	Hours	Spectra	σ [m s^{-1}]
Okayama	1.9 m	HIDES	Dec 28	Jan 17	90	1997	2.0
McDonald	2.7 m		Dec 28	Jan 3	15	1719	4.6
TLS	2.0 m		Dec 29	Jan 18	19	494	2.9
Siding Spring	3.9 m AAT	UCLES	Dec 29	Jan 10	53	2451	1.7
La Palma	2.5 m NOT	FIES	Dec 31	Jan 10	17	1087	5.2
OHP	1.9 m	SOPHIE	Jan 2	Jan 11	57	3924	1.9
La Silla	3.6 m	HARPS	Jan 3	Jan 11	62	5698	0.8
La Palma	3.6 m TNG	SARG	Jan 8	Jan 12	19	693	1.9
Lick	0.6 m CAT	Hamilton	Jan 7	Jan 22	106	1900	2.7
La Silla	1.2 m	CORALIE	Jan 11	Jan 17	34	936	2.0

Procyon A is in a very interesting evolutionary state near the end of its main sequence life. The stellar parameters (see Table 1) are all known to high precision, but several evolutionary tracks with different ages and different hydrogen core mass fractions overlap, within the errors, with its position in the HR-diagram. The exact evolutionary state of a star can be revealed by means of asteroseismology and therefore the oscillation frequencies are needed.

To determine the actual frequencies of Procyon A a ground-based multi-site campaign using 10 telescopes with a total time span of nearly 4 weeks was performed from December 28, 2006 till January 22, 2007. Here we present first results of this campaign. In Section 2 the campaign is described, while Section 3 discusses the way the data of the different telescopes are combined, and a final power spectrum is obtained. Some concluding remarks and future prospects are provided in Section 4.

2. Multi-site campaign

For this multi-site campaign 10 telescopes around the world with high-resolution spectrographs were used, and in total 20899 spectra were obtained during 472 hours. During the central 9 days of this campaign the coverage was 89%.

For most of the facilities the available reduction pipelines were used to compute the radial velocity variations. For the SOPHIE spectrograph mounted on the 1.93 m telescope, Observatoire de Haute Provence, France this was one of the first runs after commissioning. The capabilities of SOPHIE for seismology are shown by [19] and the iodine method used at Okayama is described by [14] both using data from the current multi-site campaign. For the FIES spectrograph mounted on the Nordic Optical Telescope, La Palma the observations of Procyon were part of the commissioning run and the reduction pipeline was optimised using the Procyon data.

In Table 2 we list the time span and the number of hours of observations, the number of spectra collected as well as the mean uncertainty for the data obtained at each telescope.

3. Data combination

The radial velocities from all different telescopes are combined using the method developed by [9] for α Cen A. For each spectrum the measurement uncertainty σ_i is used to assign a weight

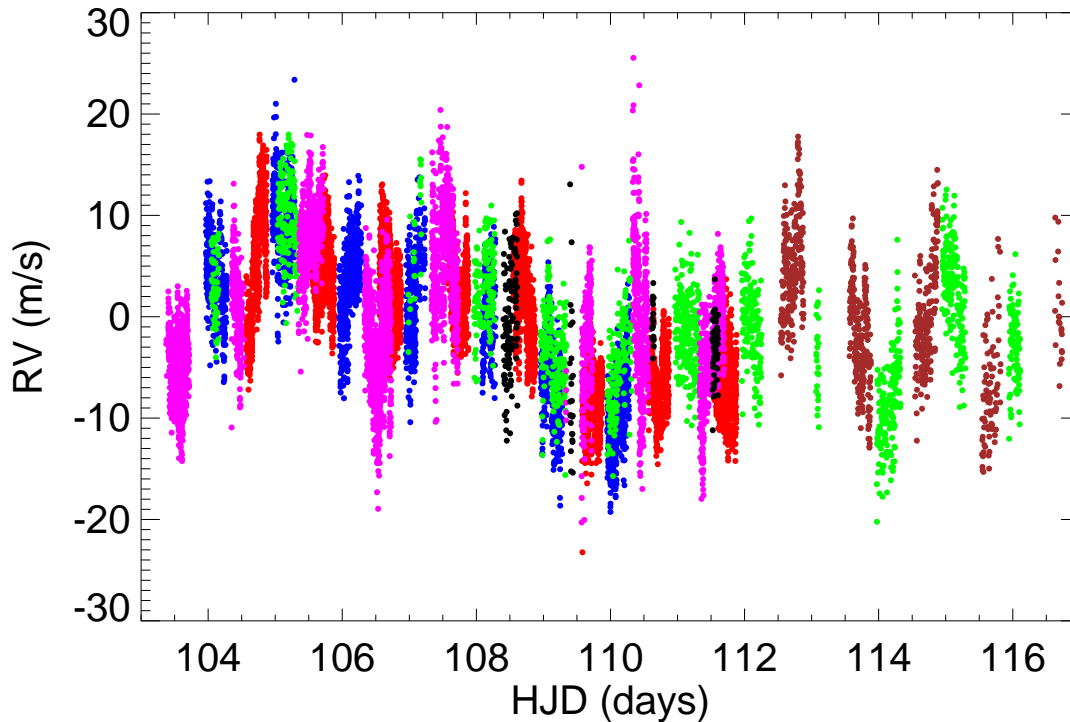


Figure 1. The central part of the radial velocity observations as a function of time. The different colours indicate data obtained with different telescopes.

($w_i = 1/\sigma_i^2$). This weight is re-scaled to match the actual noise per site and for each night, using the following relation:

$$\sigma_{\text{amp}}^2 \sum_{i=1}^N \sigma_i^{-2} = \pi, \quad (1)$$

where the mean variance of the data is set to be equal to the variance deduced from the noise level σ_{amp} in the amplitude spectrum. We then follow a procedure very similar to the one described in [9] to identify poor data points, and adjust the uncertainties of these points to give them lower weights. With this procedure the combined data set is noise-optimised, i.e., the weights have been chosen to minimize the noise.

In Figure 1 the central part of the radial velocity data of the campaign is shown. From this figure it becomes clear that there is variation with a periodicity of the order of 6 days, while the solar-like oscillations are in the range of 10–30 minutes. This slow drift is present in the data of all observatories and is therefore most likely intrinsic to the star and not due to instrumental effects. In Figure 2 all radial velocity variations obtained with the different telescopes is shown, with the slow drift subtracted.

The data obtained at the best sites will get the highest weights in a noise-optimised data set. This enhances the sidelobes in the spectral window function. As is well known, these sidelobes complicate the oscillation spectrum, especially for weaker modes, and could lead to mis-identification. In order to optimise the window function, the weights are adjusted on a night-by-night basis, i.e., we allocate an adjustment factor for each night and telescope. The noise-optimised weights are multiplied by these factors and a new spectral window is calculated.

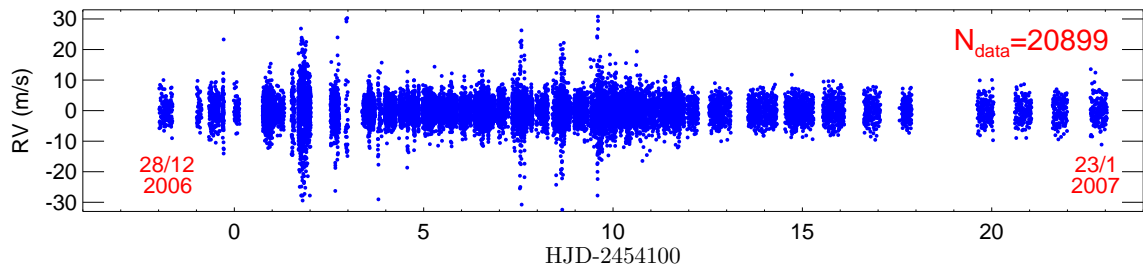


Figure 2. All 20899 radial velocity data points as a function of time. The slow drifts have been subtracted. The errors in the data points are $1\text{--}3\text{ m s}^{-1}$ and the coverage during the central 9 days is 89%.

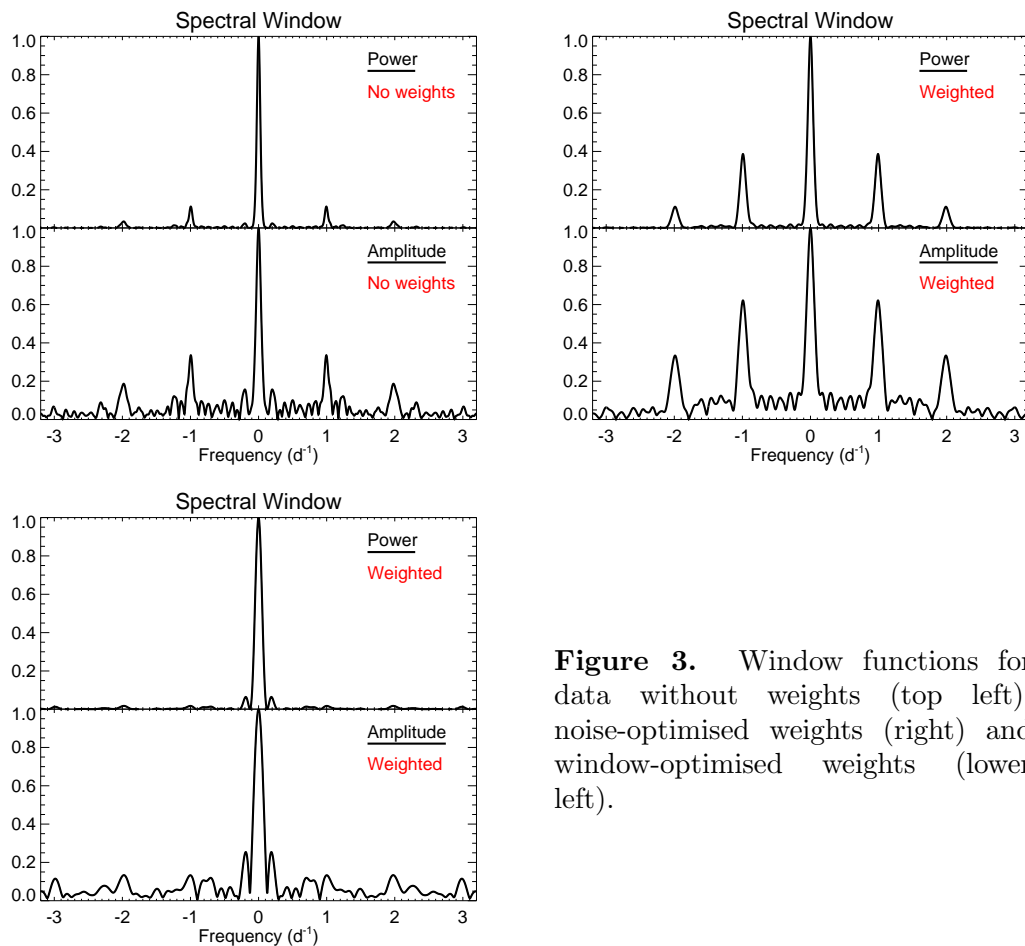


Figure 3. Window functions for data without weights (top left), noise-optimised weights (right) and window-optimised weights (lower left).

This process is iterated to minimize the height of the sidelobes as was also done by [3]. In this way we create a window-optimised data set for which the sidelobes are effectively negligible. In Figure 3, window functions are shown for the data without weights, with noise-optimised weights and with window-optimised weights.

From the combined high-pass filtered data with window-optimised weights the power

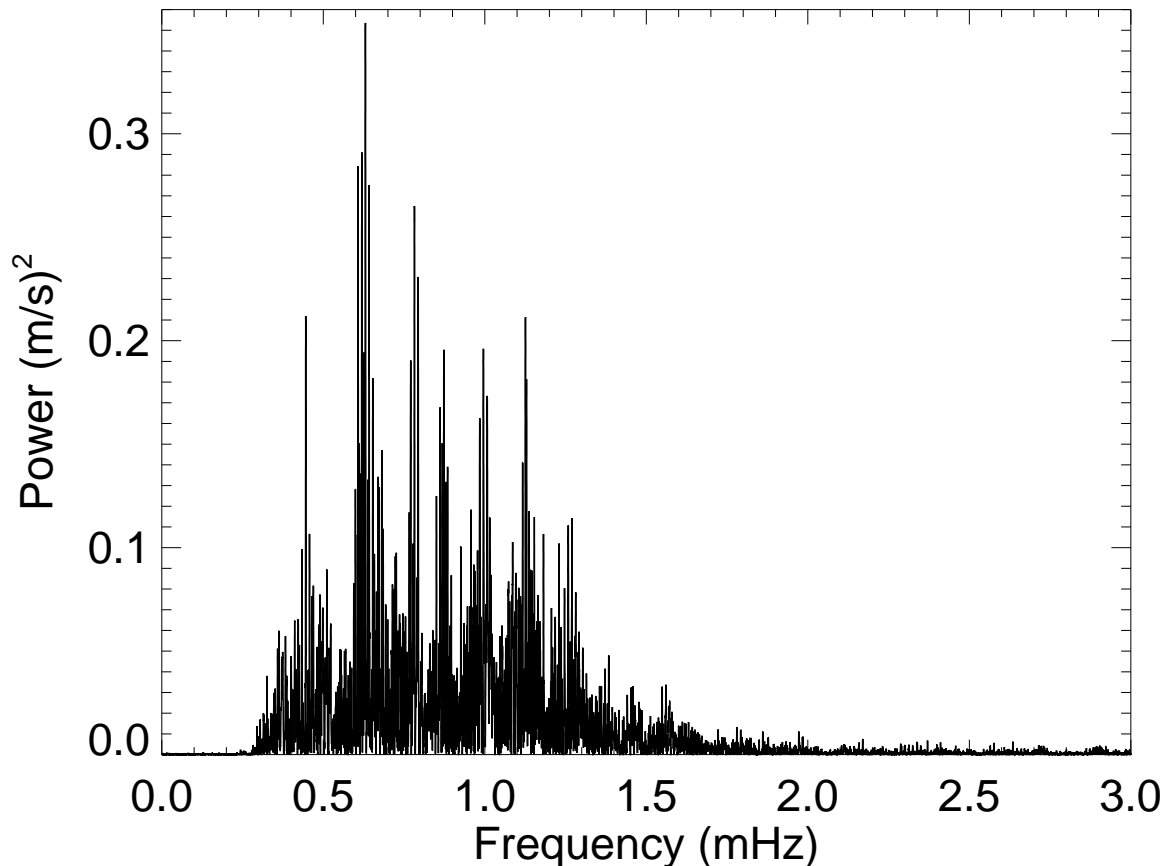


Figure 4. Final power spectrum of Procyon A with window-optimised weights. The data are high-pass filtered to remove low-frequency drifts.

spectrum is calculated and shown in Figure 4. From this power spectrum we can recognise a regular pattern with a large frequency separation of about $55 \mu\text{Hz}$, consistent with earlier determinations.

4. Concluding remarks and future prospects

The Procyon campaign presented here is the largest spectroscopic campaign, so far, aimed at the detection and identification of solar-like oscillations. Using 10 telescopes over a time span of nearly 4 weeks provided us with a unique data set with high time coverage and frequency resolution. The details of the data processing methods will be fully described by [2], while the oscillation frequencies extracted from the full data set acquired during the spectroscopic Procyon campaign will be presented by [5].

References

- [1] Allende Prieto C, Asplund M, López R J G and Lambert D L 2002 *ApJ* **567** 544–65
- [2] Arentoft *et al* 2008 *in preparation*
- [3] Bedding T R, Kjeldsen H, Butler R P, McCarthy C, Marcy G W, O’Toole S J, Tinney C G and Wright J T 2004 *ApJ* **614** 380–5
- [4] Bedding T R, Kjeldsen H, Bouchy F, Bruntt H, Butler R P, Buzasi D L, Christensen-Dalsgaard J, Frandsen S, Lebrun J-C, Martić M and Schou J 2005 *A&A* **432** L43–8

- [5] Bedding *et al* 2008 *in preparation*
- [6] Bouchy F, Schmitt J, Bertaux J-L and Connes P 2002 *ASP Conference Proceedings* **259** 472
- [7] Brown T M, Gilliland R L, Noyes R W and Ramsey L W 1991 *ApJ* **368** 599–609
- [8] Bruntt H, Kjeldsen H, Buzasi D L and Bedding T R 2005 *AJ* **633** 440–6
- [9] Butler R P, Bedding T R, Kjeldsen H, McCarthy C, O’Toole S J, Tinney C G, Marcy G W and Wright J T 2004 *AJ* **600** L75–8
- [10] Claudi R U, Bonanno A, Leccia S, Ventura R, Desidera S, Gratton R, Cosentino R, Paternò L and Endl M 2005 *A&A* **429** L17–20
- [11] Eggenberger P, Carrier F, Bouchy F and Blecha A 2004 *A&A* **422** 247–52
- [12] Guenther D B, Kallinger T, Reegen P, Weiss W W, Matthews J M, Kuschnig R, Moffat A F J, Rucinski S M, Sasselov D and Walker G A H 2007 *Comm. in Asteroseismology* **151**
- [13] Kambe E, Sato B, Takeda Y, Izumiura H, Masuda S and Ando H 2003 *Astrophysics and Space Science* **284** 331–4
- [14] Kambe E *et al* 2007 *PASJ submitted*
- [15] Leccia S, Kjeldsen H, Bonanno A, Claudi R U, Ventura R and Paternò 2007 *A&A* **464** 1059–67
- [16] Martić M, Schmitt J, Lebrun J-C, Barban C, Connes P, Bouchy F, Michel E, Baglin A, Appourchaux T and Bertaux J-L 1999 *A&A* **351** 993–1002
- [17] Martić M, Lebrun J-C, Appourchaux T and Korzennik S G 2004 *A&A* **418** 295–303
- [18] Matthews J M, Kuschnig R, Guenther D B, Walker G A H, Moffat A F J, Rucinski S M, Sasselov D and Weiss W W 2004 *Nature* **430** 51–3
- [19] Mosser B, Bouchy F, Martić M, Appourchaux T, Barban C, Berthomieu G, Catala C, García R A, Lebrun J-C, Michel E, Nghiem P, Provost J, Samadi R, Thévenin F and Turk-Chièze 2007 *A&A submitted*
- [20] Régulo C and Roca Cortés T 2005 *A&A* **444** L5–8

Appendix E

A MULTISITE CAMPAIGN TO MEASURE SOLAR-LIKE OSCILLATIONS IN PROCYON. I. OBSERVATIONS, DATA REDUCTION, AND SLOW VARIATIONS

A MULTISITE CAMPAIGN TO MEASURE SOLAR-LIKE OSCILLATIONS IN PROCYON. I. OBSERVATIONS, DATA REDUCTION, AND SLOW VARIATIONS

TORBEN ARENTOFT,¹ HANS KJELSDEN,¹ TIMOTHY R. BEDDING,² MICHAËL BAZOT,^{1,3} JØRGEN CHRISTENSEN-DALSGAARD,¹ THOMAS H. DALL,⁴
CHRISTOFFER KAROFF,¹ FABIEN CARRIER,⁵ PATRICK EGGENBERGER,⁶ DANUTA SOSNOWSKA,⁷ ROBERT A. WITTENMYER,⁸ MICHAEL ENDL,⁸
TRAVIS S. METCALFE,⁹ SASKIA HEKKER,^{10,11} SABINE REFFERT,¹² R. PAUL BUTLER,¹³ HANS BRUNTT,² LÁSZLÓ L. KISS,²
SIMON J. O'TOOLE,¹⁴ EJI KAMBE,¹⁵ HIROYASU ANDO,¹⁶ HIDEYUKI IZUMIURA,¹⁵ BUN'EI SATO,¹⁷ MICHAEL HARTMANN,¹⁸
ARTIE HATZES,¹⁸ FRANCOIS BOUCHY,¹⁹ BENOIT MOSSER,²⁰ THIERRY APPOURCHAUX,²¹ CAROLINE BARBAN,²⁰
GABRIELLE BERTHOMIEU,²² RAFAEL A. GARCIA,²³ ERIC MICHEL,²⁰ JANINE PROVOST,²²
SYLVAIN TURCK-CHIEZE,²³ MILENA MARTIĆ,²⁴ JEAN-CLAUDE LEBRUN,²⁴ JEROME SCHMITT,²⁵
JEAN-LOUP BERTAUX,²⁴ ALFIO BONANNO,²⁶ SERENA BENATTI,²⁷ RICCARDO U. CLAUDI,²⁷
ROSARIO COSENTINO,²⁶ SILVIO LECCIA,²⁸ SØREN FRANDSEN,¹ KARSTEN BROGAARD,¹
LARS GLOWIENKA,¹ FRANK GRUNDAHL,¹ AND ERIC STEMPELS²⁹

Received 2008 June 5; accepted 2008 July 17

ABSTRACT

We have carried out a multisite campaign to measure oscillations in the F5 star Procyon A. We obtained high-precision velocity observations over more than three weeks with 11 telescopes, with almost continuous coverage for the central 10 days. This represents the most extensive campaign so far organized on any solar-type oscillator. We describe in detail the methods we used for processing and combining the data. These involved calculating weights for the velocity time series from the measurement uncertainties and adjusting them in order to minimize the noise level of the combined data. The time series of velocities for Procyon shows the clear signature of oscillations, with a plateau of excess power that is centered at 0.9 mHz and is broader than has been seen for other stars. The mean amplitude of the radial modes is $38.1 \pm 1.3 \text{ cm s}^{-1}$ (2.0 times solar), which is consistent with previous detections from the ground and by the *WIRE* spacecraft, and also with the upper limit set by the *MOST* spacecraft. The variation of the amplitude during the observing campaign allows us to estimate the mode lifetime to be $1.5_{-0.8}^{+1.9}$ days. We also find a slow variation in the radial velocity of Procyon, with good agreement between different telescopes. These variations are remarkably similar to those seen in the Sun, and we interpret them as being due to rotational modulation from active regions on the stellar surface. The variations appear to have a period of about 10 days, which presumably equals the stellar rotation period or, perhaps, half of it. The amount of power in these slow variations indicates that the fractional area of Procyon covered by active regions is slightly higher than for the Sun.

Subject headings: stars: individual (Procyon A) — stars: oscillations

¹ Danish AsteroSeismology Centre (DASC), Department of Physics and Astronomy, University of Aarhus, DK-8000 Aarhus C, Denmark; toar@phys.au.dk, hans@phys.au.dk, jcd@phys.au.dk, karoff@phys.au.dk, srf@phys.au.dk, kfb@phys.au.dk, f002769@phys.au.dk, fgj@phys.au.dk.

² Institute of Astronomy, School of Physics, University of Sydney, NSW 2006, Australia; bedding@physics.usyd.edu.au, bruntt@physics.usyd.edu.au, laszlo@physics.usyd.edu.au.

³ Centro de Astrofísica da Universidade do Porto, Rua das Estrelas, 4150-762 Porto, Portugal; bazot@astro.up.pt.

⁴ Gemini Observatory, 670 N. A'ohoku Place, Hilo, HI 96720; tdall@gemini.edu.

⁵ Instituut voor Sterrenkunde, Katholieke Universiteit Leuven, Celestijnenlaan 200 B, 3001 Leuven, Belgium; fabien@ster.kuleuven.be.

⁶ Observatoire de Genève, Ch. des Maillettes 51, CH-1290 Sauverny, Switzerland; patrick.eggenberger@obs.unige.ch.

⁷ Laboratoire d'astrophysique, EPFL Observatoire CH-1290 Versoix, Switzerland; danuta.sosnowska@epfl.ch.

⁸ McDonald Observatory, University of Texas at Austin, Austin, TX 78712; robw@astro.as.utexas.edu, mike@astro.as.utexas.edu.

⁹ High Altitude Observatory, National Centre for Atmospheric Research, Boulder, CO 80307-3000; travis@ucar.edu.

¹⁰ Leiden Observatory, Leiden University, 2300 RA Leiden, Netherlands.

¹¹ Royal Observatory of Belgium, 1180 Brussels, Belgium; saskia@oma.be.

¹² ZAH-Landessternwarte, 69117 Heidelberg, Germany; sreffert@lsw.uni-heidelberg.de.

¹³ Carnegie Institution of Washington, Department of Terrestrial Magnetism, 5241 Broad Branch Road NW, Washington, DC 20015-1305; paul@dtm.ciw.edu.

¹⁴ Anglo-Australian Observatory, P.O. Box 296, Epping, NSW 1710, Australia; ootoole@aaoepp.aao.gov.au.

¹⁵ Okayama Astrophysical Observatory, National Astronomical Observatory of Japan, National Institutes of Natural Sciences, 3037-5 Honjyo, Kamogata, Asakuchi, Okayama 719-0232, Japan; kambe@oao.nao.ac.jp, izumiura@oao.nao.ac.jp.

¹⁶ National Astronomical Observatory of Japan, National Institutes of Natural Sciences, 2-21-1 Osawa, Mitaka, Tokyo 181-8588, Japan; ando@optik.mtk.nao.ac.jp.

¹⁷ Global Edge Institute, Tokyo Institute of Technology 2-12-1-S6-6, Ookayama, Meguro-ku, Tokyo 152-8550, Japan; sato.b.aa@m.titech.ac.jp.

¹⁸ Thüringer Landessternwarte Tautenburg, Sternwarte 5, 07778 Tautenburg, Germany; michael@tls-tautenburg.de, artie@tls-tautenburg.de.

¹⁹ Institut d'Astrophysique de Paris, UMR7095, Université Pierre et Marie Curie, 98bis Boulevard Arago, 75014 Paris, France; bouchy@iap.fr.

²⁰ Observatoire de Paris, LESIA, UMR 8109, F-92195 Meudon, France; benoit.mosser@obspm.fr, caroline.barban@obspm.fr, eric.michel@obspm.fr.

²¹ Institut d'Astrophysique Spatiale, Université Paris XI-CNRS, Bâtiment 121, 91405 Orsay cedex, France; thierry.appourchaux@ias.u-psud.fr.

²² Laboratoire Cassiopée, UMR CNRS 6202, Observatoire de la Côte d'Azur, BP 4229, 06304 Nice cedex 4, France; gabrielle.berthomieu@obs-nice.fr, janine.provost@obs-nice.fr.

²³ DAPNIA/DSM/Service d'Astrophysique, CEA/Saclay, 91191 Gif-sur-Yvette Cedex, France; rafael.garcia@cea.fr, sylvaine.turck-chieze@cea.fr.

²⁴ Service d'Aéronomie du CNRS, BP 3, 91371 Verrières le Buisson, France; milena.martić@aerov.jussieu.fr, jean-claude.lebrun@aerov.jussieu.fr, jean-loup.bertraux@aerov.jussieu.fr.

²⁵ Observatoire de Haute Provence, 04870 St Michel l'Observatoire, France; jerome.schmitt@oamp.fr.

²⁶ INAF-Osservatorio Astrofisico di Catania, via S. Sofia 78, 95123 Catania, Italy; abo@oact.inaf.it, rco@ct.astro.it.

²⁷ INAF-Astronomical Observatory of Padua, Vicolo Osservatorio 5, 35122 Padova, Italy; serena.benatti@oapd.inaf.it, riccardo.claudi@oapd.inaf.it.

²⁸ INAF-Astronomical Observatory of Capodimonte, Salita Moiariello 16, 80131 Napoli, Italy; leccia@na.astro.it.

²⁹ School of Physics and Astronomy, University of St. Andrews, North Haugh, St. Andrews KY16 9SS, Scotland; eric.stempels@st-andrews.ac.uk.

TABLE 1
PARTICIPATING TELESCOPES

Identifier	Telescope/Spectrograph	Observatory	Technique	Reference
HARPS.....	3.6 m/HARPS	ESO, La Silla, Chile ¹	ThAr	1
CORALIE.....	1.2 m Euler Telescope/CORALIE	ESO, La Silla, Chile	ThAr	2
McDonald.....	2.7 m Harlan J. Smith Tel./coudé échelle	McDonald Obs., Texas USA	Iodine	3
Lick.....	0.6 m CAT/Hamilton échelle	Lick Obs., California USA	Iodine	4
UCLES.....	3.9 m AAT/UCLES	Siding Spring Obs., Australia	Iodine	4
Okayama.....	1.88 m/HIDES	Okayama Obs., Japan	Iodine	5
Tautenburg.....	2 m/coudé échelle	Karl Schwarzschild Obs., Germany	Iodine	6
SOPHIE.....	1.93 m/SOPHIE	Obs. de Haute-Provence, France	ThAr	7
EMILIE.....	1.52 m/EMILIE+AAA	Obs. de Haute-Provence, France	White light with iodine	8
SARG.....	3.58 m TNG/SARG	ORM, La Palma, Spain	Iodine	9
FIES.....	2.5 m NOT/FIES	ORM, La Palma, Spain	ThAr	10

¹ Based on observations collected at the European Southern Observatory, La Silla, Chile (ESO Program 078.D-0492 [A]).

REFERENCES.—(1) Rupprecht et al. 2004; (2) Bouchy & Carrier 2002; (3) Endl et al. 2005; (4) Butler et al. 1996; (5) Kambe et al. 2008; (6) Hatzes et al. 2003; (7) Mosser et al. 2008b; (8) Bouchy et al. 2002, and J. Schmitt 2008, private communication; (9) Claudi et al. 2005; (10) Frandsen & Lindberg 2000.

1. INTRODUCTION

Measuring solar-like oscillations in main-sequence and sub-giant stars requires high-precision observations—either with spectroscopy or photometry—combined with coverage that is as continuous as possible. Most of the results have come from high-precision Doppler measurements using ground-based spectrographs, while measurements from spacecraft have also been reported (see Bedding & Kjeldsen [2007] and Aerts et al. [2008] for recent summaries).

Procyon has long been a favorite target for oscillation searches. At least eight separate velocity studies have reported an excess in the power spectrum, beginning with that by Brown et al. (1991), which was the first report of a solar-like power excess in another star. For the most recent examples, see Martić et al. (2004), Eggenberger et al. (2004), Bouchy et al. (2004), and Leccia et al. (2007). These studies agreed on the location of the excess power (around 0.5–1.5 mHz), but they disagreed on the individual oscillation frequencies. However, a consensus has emerged that the large separation (the frequency separation between consecutive overtone modes of a given angular degree) is about 55 μ Hz. Evidence for this value was first given by Mosser et al. (1998) and the first clear detection was made by Martić et al. (1999).

Controversy was generated when photometric observations obtained with the *Microvariability and Oscillations of Stars (MOST)* satellite failed to reveal evidence for oscillations (Matthews et al. 2004; Guenther et al. 2007; Baudin et al. 2008). However, Bedding et al. (2005) argued that the *MOST* nondetection was consistent with the ground-based data. Meanwhile, Régulo & Roca Cortés (2005) suggested that the signature of oscillations is indeed present in the *MOST* data at a low level (see also Marchenko 2008). Using space-based photometry with the *Wide Field Infrared Explorer (WIRE)* satellite, Bruntt et al. (2005) extracted parameters for the stellar granulation and found evidence for an excess due to oscillations.

All published velocity observations of Procyon have been made from a single site, with the exception of two-site observations by Martić et al. (2004). Here we describe a multisite campaign on Procyon carried out in 2007 January, which was the most extensive velocity campaign so far organized on any solar-type oscillator. The only other comparable effort to measure oscillations in this type of star was the multisite photometric campaign of the open cluster M67 (Gilliland et al. 1993).

2. VELOCITY OBSERVATIONS

We observed Procyon from 2006 December 28 until 2007 January 23, using a total of 11 telescopes at eight observatories. These are listed in Table 1, ordered westward by longitude. Note that the FIES spectrograph on the Nordic Optical Telescope was still being commissioned during the observations and the velocity precision is therefore somewhat lower than for the other telescopes.

The team members from each telescope were responsible for producing a velocity time series from the observations, together with estimates of uncertainties. In six of the spectrographs, the stellar light was passed through an iodine absorption cell to provide a stable wavelength reference. In four others, wavelength calibration was achieved by recording the spectrum from a thorium-argon emission lamp alongside the stellar spectrum, while with EMILIE, exposures of the stellar spectrum were alternated with those of a white-light source passing through an iodine cell. Details of the methods used with each spectrograph are given in the references listed in Table 1 and details of the observations are given in Table 2.

The velocity time series of Procyon is shown in Figure 1a, using a different color for each telescope. Differences between telescopes in the absolute zero point of velocity are not significant, and so all the curves have been shifted into alignment by subtracting a constant offset. This was done by setting the velocities from each telescope to have zero mean, excepting Lick and SARG, for which better alignment was achieved by setting the means to -6 and -5 m s^{-1} , respectively. Note that EMILIE is not shown in Figure 1a because those data were referenced to a different value on each night and so the night-to-night variations are not measurable (this does not affect their usefulness for oscillations studies, however). FIES is also not shown in Figure 1a because it has much greater scatter than the rest.

In Figure 1a we see variations in the radial velocity of Procyon on timescales of days. The good agreement between the different telescopes indicates that these slow variations have a stellar origin, although the imperfect match in overlapping sections shows that there is also a contribution from instrumental drifts. Figure 1b shows a close-up of the central part of the campaign, during which the coverage was above 90%. The solid curve shows the velocities after smoothing, to better reveal the slow variations, which are discussed in § 4.1 below.

While interesting in their own right, the slow variations in the velocity series significantly affect our ability to detect oscillations,

TABLE 2
SUMMARY OF OBSERVATIONS

Identifier	Nights Allocated	Eff. Obs. Time (hr)	Spectra	Median t_{exp} (s)	Deadtime (s)	f_{Nyq} (mHz)	Noise Level (cm s ⁻¹)	Noise per Minute (m s ⁻¹)
HARPS.....	8	52.0	5698	5	31	13.8	2.0	0.64
CORALIE.....	6	27.0	936	40	85	4.0	9.8	2.2
McDonald.....	6	16.2	1719	17	15	15.6	14.4	2.5
Lick.....	14	95.4	1900	180	54	2.1	10.9	4.7
UCLES.....	12	41.4	2451	16	45	8.2	6.6	1.9
Okayama.....	20	83.4	1997	54	110	3.1	8.0	3.2
Tautenburg.....	21	14.6	494	60	65	4.0	22.8	3.8
SOPHIE.....	9	35.1	3924	23	28	9.7	4.7	1.2
EMILIE.....	4	25.7	1631	47	17	7.8	10.1	2.2
SARG.....	4	15.2	693	19	65	5.9	12.6	2.1
FIES.....	10 × 1/2	12.6	1087	18	45	7.9	21.7	3.4

due to spectral leakage of power from the low-frequency part of the spectrum to the oscillation region at higher frequencies. Before merging the data from the individual telescopes, we therefore removed the low-frequency variations from the velocity series. This was done for each telescope by removing all the power below 280 μHz , a value that was chosen so as to effectively remove the slow variations without affecting the oscillation signal. This filtering was done by subtracting a smoothed version of the time series that contained all the power below that cutoff frequency.

In Figure 1c we show a close-up of a segment during which three spectrographs were observing simultaneously. The stellar oscillations are clearly visible, with typical periods of about 15 minutes, and there is good agreement between the different telescopes. Note that these data have been filtered to remove the slow variations.

3. OPTIMIZING THE WEIGHTS

The procedures for extracting velocities for each telescope also produced estimates of the uncertainties, σ_i . In our analysis, we used these uncertainties to calculate noise-optimized weights in the usual way, namely $w_i = 1/\sigma_i^2$. If weights are not used when calculating the power spectrum, a few bad data points can dominate and increase the noise floor significantly.

We now describe the process we used to adjust these weights, which aims to minimize the noise level in the final power spectrum. The procedure involves identifying and revising those uncertainties that were too optimistic, and at the same time rescaling the uncertainties to be in agreement with the actual noise levels in the data. These methods have already been described in previous papers (Butler et al. 2004; Bedding et al. 2007; Leccia et al. 2007), but the present analysis differs slightly from those descriptions and we will therefore describe them in some detail. One difference is that the analysis had to be tailored to the individual time series because of the large range of Nyquist frequencies (see Table 2).

To illustrate the process, we show in Figures 2 and 3 segments of data at different stages in the process for two telescopes (HARPS and EMILIE). The top panels (Figs. 2a and 3a) show the velocities for a single night, with the slow variations removed. The remaining panels show the uncertainties at different stages in the analysis.

It is important to stress that we are not adjusting the velocities, only the uncertainties. Of course, those adjustments still affect the power spectrum of the velocities (which is, after all, why we are making the adjustments) and so it is important to ensure that they do not distort the oscillation signal and that the final weights reflect as accurately as possible the actual noise properties of the series.

3.1. Scaling the Uncertainties

We have scaled the uncertainties so that they agree with the noise level in the corresponding amplitude spectrum, σ_{amp} , as measured at high frequencies. This was done for each night and each telescope by multiplying the uncertainties, σ_i , by a constant so that they satisfied equation (3) of Butler et al. (2004):

$$\sigma_{\text{amp}}^2 \sum_{i=1}^N \sigma_i^{-2} = \pi. \quad (1)$$

This scaling was repeated after each step in the process described below. Figures 2b and 3b show the uncertainties after scaling, and before any further adjustments.

3.2. Filtering the Uncertainties

It is clear that the uncertainties in some parts of the time series show variations that correlate with the oscillations of Procyon. The clearest example is HARPS, as shown by comparing the top two panels of Figure 2, but the effect is also visible for other telescopes (e.g., Fig. 3). To remove this structure in the uncertainties, we have bandpass-filtered each of the uncertainty time series to remove all power in the frequency range 280–2200 μHz . This removed fluctuations in the weights on the timescale of the stellar oscillations, while retaining information on longer timescales (such as poorer conditions at the beginnings and ends of nights) and on shorter timescales (such as individual bad data points). This process resulted in slightly lower noise levels in the final power spectra for some of the individual telescopes, reflecting the fact that the uncertainties, like any measurement, contain noise that is reduced by bandpass filtering. Figures 2c and 3c show the uncertainties after filtering.

We also noticed a few data points (~ 10) with unrealistically low uncertainties. These points would be given too high a weight in the analysis and the uncertainties were therefore reset to the mean uncertainty for that telescope night.

3.3. Down-weighting Bad Data Points

Down-weighting of bad data points was done following the method described by Butler et al. (2004), with one difference that is discussed below. The first step was to make a high-pass-filtered version of the velocity time series in which both the slow variations and the stellar oscillations were removed. This gave us a series of residual velocities, r_i , in which we could identify data points that needed to be down weighted, without being affected by spectral leakage from the oscillations. The frequency limit of

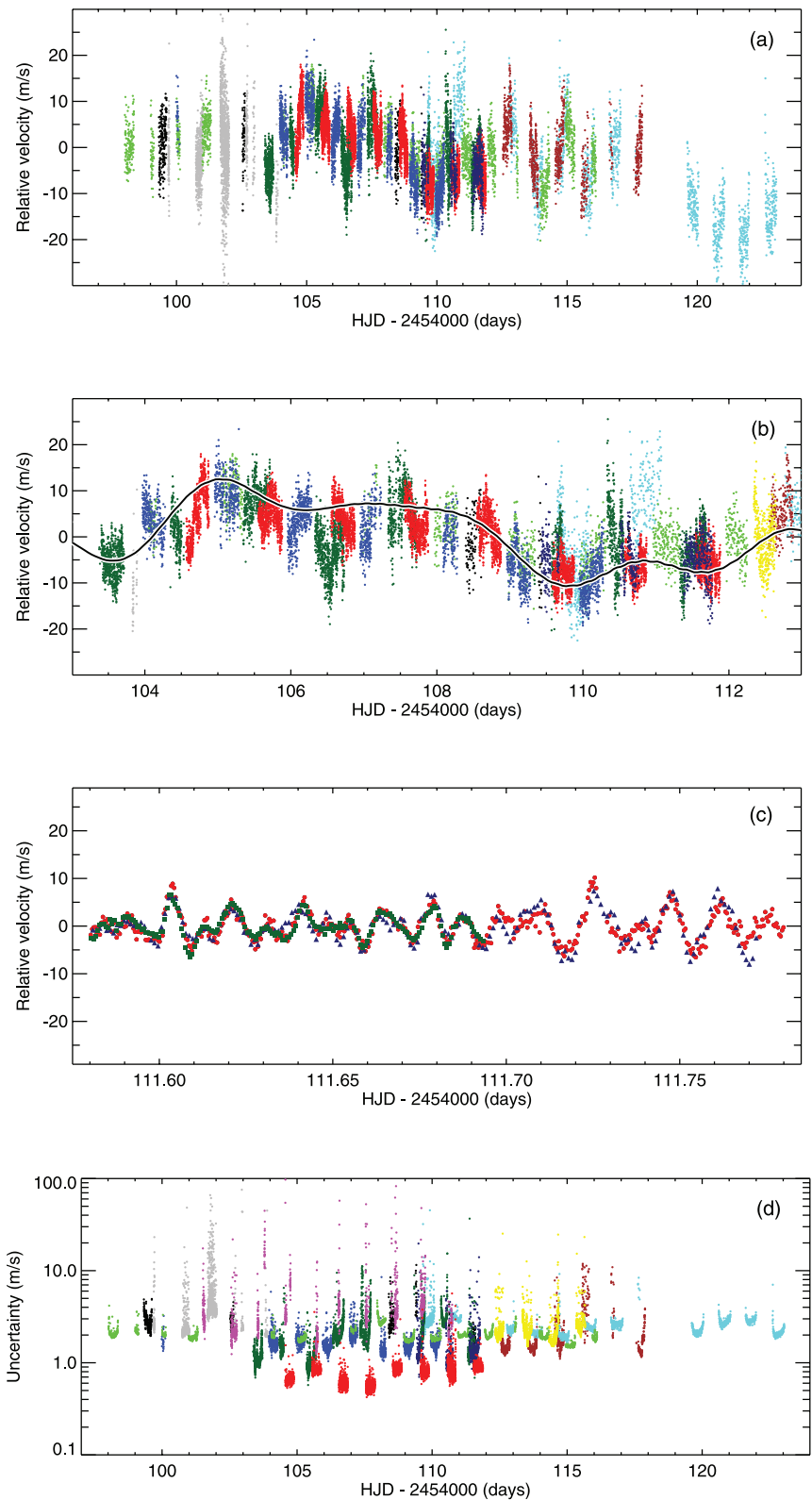


FIG. 1.— Velocity measurements of Procyon, color coded as follows. HARPS: red; CORALIE: brown; McDonald: gray; Lick: cyan; UCLES: blue; Okayama: green; Tautenburg: black; SOPHIE: dark green; SARG: dark blue; FIES: magenta; EMILIE: yellow. (a) Full time series, before any removal of slow trends (EMILIE and FIES are not shown). (b) Close-up of the central 10 days (FIES not shown). (c) Close-up of a 5 hr segment during which three spectrographs observed simultaneously: HARPS (red circles), SOPHIE (dark green squares), and SARG (dark blue triangles). All three series have been high-pass filtered to remove slow trends and the SOPHIE and SARG data have been smoothed slightly (using a boxcar with a width of three data points). (d) Time series of the final noise-optimized uncertainties, showing all 11 telescopes.

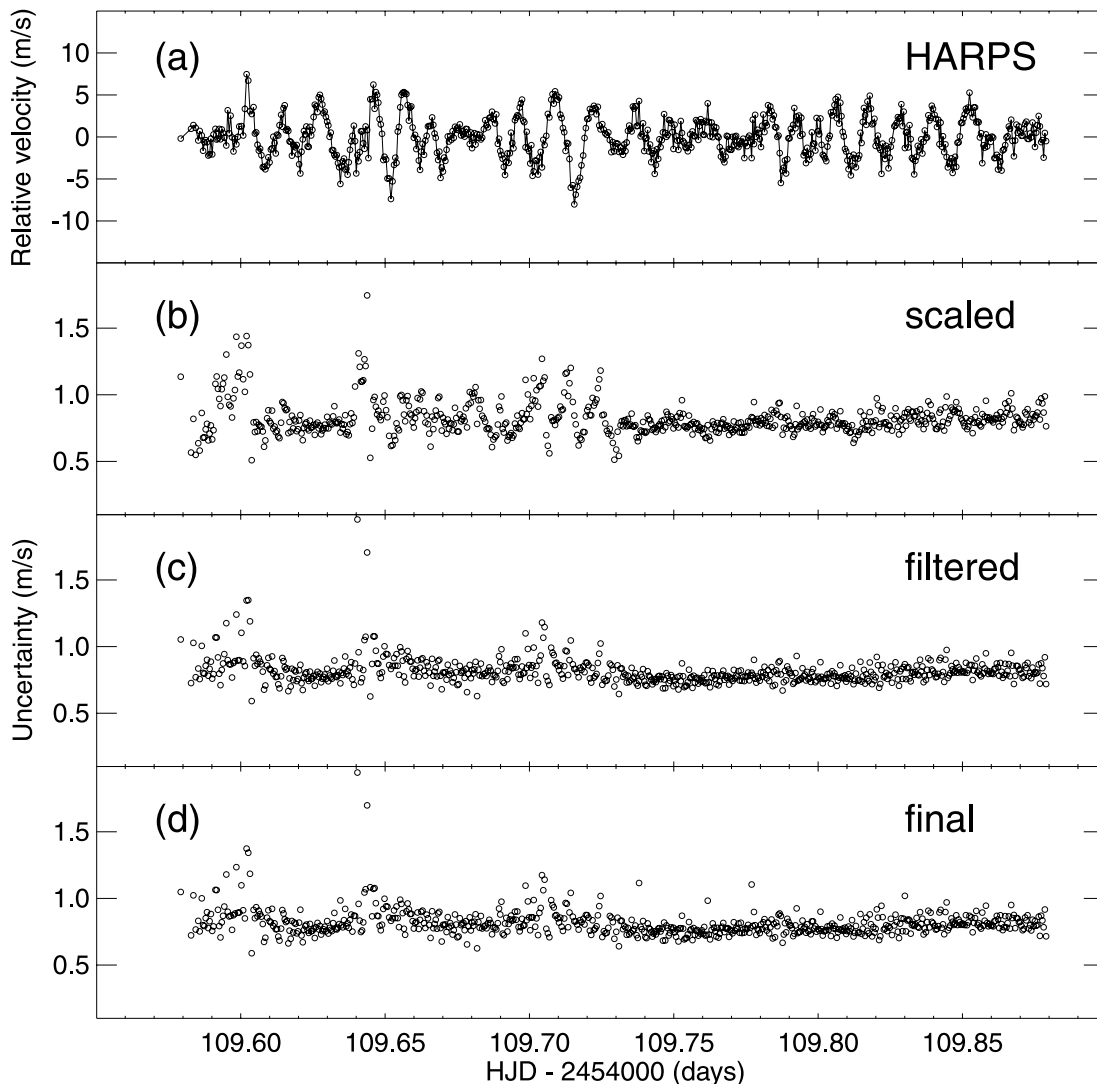


FIG. 2.—Steps in the adjustments of weights, illustrated using HARPS data from a single night. (a) Velocities, with the slow variations removed. (b) Uncertainties, after scaling to satisfy eq. (1) but before any further adjustments. (c) Uncertainties after filtering to remove power on the timescale of the oscillations. (d) Final uncertainties, after adjusting to optimize the noise (see text).

this high-pass filter varied from telescope to telescope, depending on the Nyquist frequency of the data.

We compared the velocity residuals, r_i , with the corresponding uncertainty estimates, σ_i . Bad data points are those for which the ratio $|r_i/\sigma_i|$ is large, i.e., where the residual velocity deviates from zero by more than expected from the uncertainty estimate. Butler et al. (2004), who analyzed data similar to ours, found that the fraction of good data points was essentially unity up to $|r_i/\sigma_i| = 2$ and then dropped off quickly for larger values of $|r_i/\sigma_i|$; see Figure 3 of Butler et al. (2004). They therefore introduced the factor f , which is the fraction of good data points as a function of $|r_i/\sigma_i|$ and which they obtained as the ratio between the distribution of data points in a cumulative histogram of $|r_i/\sigma_i|$ and a best-fit Gaussian distribution.

We used a slightly different approach. With the knowledge that points with large values of $|r_i/\sigma_i|$ are bad, we introduced an analytical function

$$f(x_i) = \frac{1}{1 + (x_i/x_0)^{10}}, \quad x_i = |r_i/\sigma_i|, \quad (2)$$

which has shape very similar to the fraction f as a function of $|r_i/\sigma_i|$ in Butler et al. (2004). The adjustable parameter x_0 controls the amount of down weighting; it sets the value of $|r_i/\sigma_i|$ for which the weights are multiplied by 0.5, and so it determines how bad a data point should be before it is down weighted. The optimum choice for x_0 was found through iteration, as described below. Once this was done, we used $f(x_i)$ to adjust the weights by dividing σ_i by $(f[x_i])^{1/2}$, as in Butler et al. (2004).

The noise level used for optimizing x_0 was measured in a frequency band near 2 mHz in a weighted amplitude spectrum, between the oscillations and the high-frequency part of the spectrum used for determining the $|r_i/\sigma_i|$ values. The exact position of the band was chosen for each spectrograph separately, because of the differences in Nyquist frequencies. For each trial value of x_0 , the noise level was determined from a time series in which all power had been removed at both the low- and high-frequency side of the frequency band, i.e., from a bandpass-filtered time series containing information in the specific frequency band only. This was done because applying the weights changes the spectral window function and thus the amount of spectral leakage into the frequency band where we determine the noise: if we did not filter

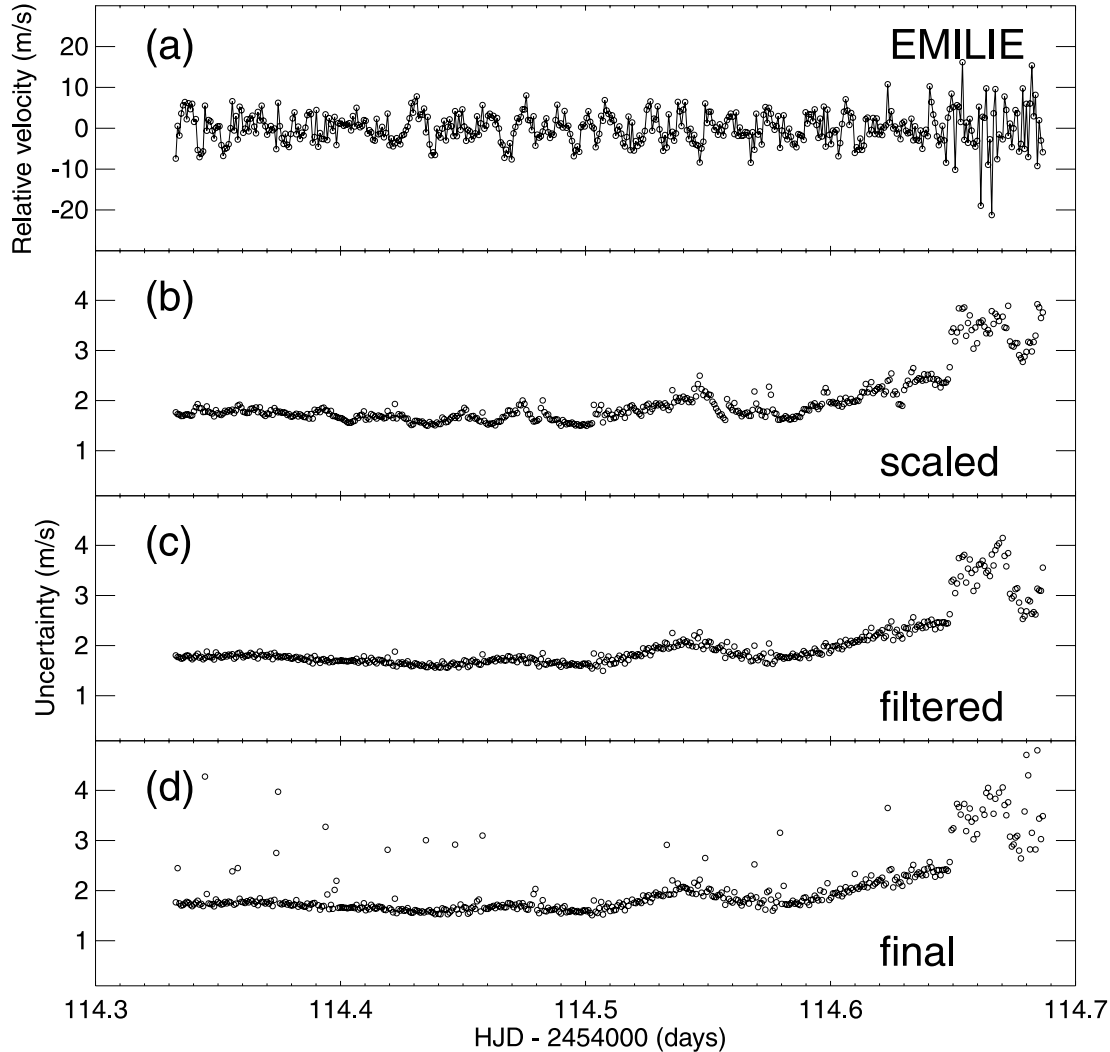


FIG. 3.—Same as Fig. 2, but for a single night from EMILIE.

out the oscillations and the high-frequency part of the spectrum, we would optimize for a combination of low noise *and* minimum amount of spectral leakage (from both the low- and high-frequency side of the passband). In other words, the spectral window function would influence our choice of x_0 , which is not optimal for obtaining the lowest possible noise level.

The procedure described above was repeated for a range of x_0 values and we chose the one that resulted in the lowest noise in the power spectrum. Depending on the telescope, and hence the noise properties of the time series, the optimal values of x_0 ranged from 1.7 to 4.3. Figures 2d and 3d show the final uncertainties for HARPS and EMILIE.

This completes our description of the process used to adjust the uncertainties. The results from calculating weighted power spectra using these uncertainties are presented in § 4.2. First, however, we discuss the slow variations in the velocity of Procyon that are present in our data.

4. RESULTS

4.1. Slow Variations in Stellar Velocity

The slow variations in the radial velocity of Procyon seen in Figure 1 are remarkably similar to those seen in the Sun. This can be seen from Figure 4, which shows a typical time series of solar

velocity measurements made with the GOLF instrument on the *SOHO* spacecraft (Ulrich et al. 2000; García et al. 2005). Longer series of GOLF data show variations with a period of about 13 days arising from active regions crossing the solar disk (Fig. 11 in García et al. 2005; see also B. Tingley et al. 2008, in preparation). This 13 day periodicity in solar velocities was first observed by Claverie et al. (1982), who attributed it to rapid rotation of the core, but it was subsequently shown to be due to surface rotation of active regions (Durrant & Schröter 1983; Andersen & Maltby 1983; Edmunds & Gough 1983). Similarly, we attribute the slow variations in the radial velocity of Procyon to the appearance and disappearance of active regions and their rotation across the stellar disk. This explanation was also invoked by Mosser et al. (2005) to explain much larger velocity variations measured with HARPS for the COROT target HR 2530 (HD 49933; spectral type F5 V).

The slow variations in Procyon appear to have a period of $P_{\text{slow}} = 10.3 \pm 0.5$ days, as measured from the highest peak in the power spectrum. This agrees with an apparent periodicity of about 10 days in two-site observations of Procyon obtained over 20 nights by Kambe et al. (2008; see their Fig. 12). Identifying this as the stellar rotation period and using a radius of $2.05 R_{\odot}$ (Kervella et al. 2004) implies a surface rotational speed at the equator of $v = 10 \pm 0.5 \text{ km s}^{-1}$. The measured value of P_{slow} might also correspond to half the rotation period (Clarke 2003),

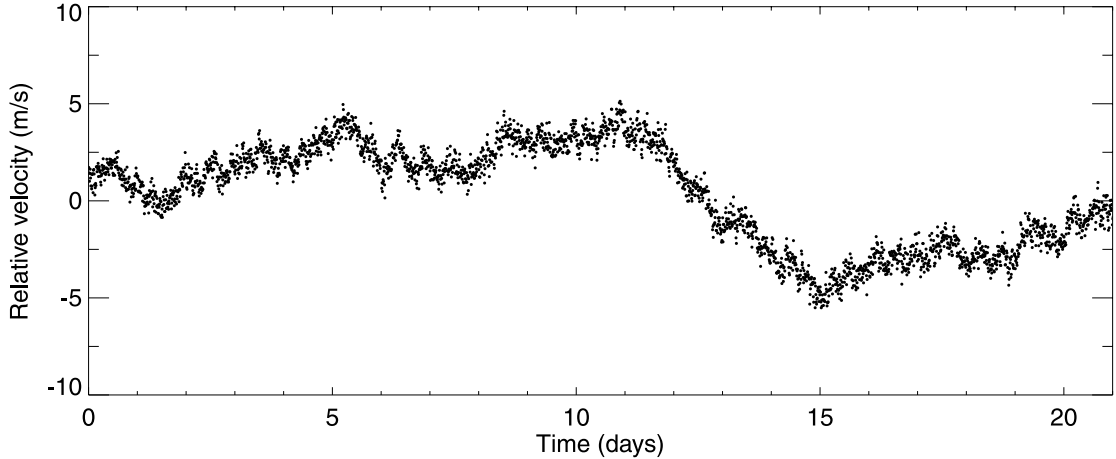


FIG. 4.—Time series of velocity measurements of the Sun obtained over 21 days with the GOLF instrument on the *SOHO* spacecraft.

in which case the rotational speed would be half the value given above. Combining with the spectroscopic value of $v \sin i = 3.16 \pm 0.50 \text{ km s}^{-1}$ (Allende Prieto et al. 2002) gives an inclination angle of $i = 18^\circ \pm 3^\circ$ (if $P_{\text{rot}} = P_{\text{slow}}$) and $i = 39^\circ \pm 7^\circ$ (if $P_{\text{rot}} = 2P_{\text{slow}}$). The inclination of the binary orbit is $31.1^\circ \pm 0.6^\circ$ (Girard et al. 2000) and so, if we require that the rotation axis of Procyon is aligned with the orbital rotation axis, it may be that $P_{\text{rot}} = 2P_{\text{slow}}$.

4.2. Power Spectra and Stellar Activity

The weighted power spectrum for each telescope and for the combined time series, based on the uncertainties discussed in § 3, are shown in Figure 5. The noise levels, as measured at high frequencies in the amplitude spectrum (σ_{amp}), are given in the eighth column of Table 2. The final column of that table gives the mean noise level per minute of observing time, with a spread that reflects a combination of factors, including telescope aperture, observing duty cycle, and spectrograph design, as well as atmospheric conditions such as seeing.

The power spectrum of the combined time series is shown again in Figure 6, both with and without the use of weights. As is well established, using weights reduces the noise level significantly, at the cost of increasing the sidelobes in the spectral window (because the best data segments are given more weight; see insets). When weights are used, the noise level above 3 mHz is 1.9 cm s^{-1} in amplitude, but this does include some degree of spectral leakage from the oscillations. If we high-pass filter the spectrum up to 3 mHz, the noise level drops to 1.5 cm s^{-1} in amplitude. Note that without the use of weights, the noise level is higher by more than a factor of 2.

Looking again at Figure 6, we see that the use of weights appears to have increased the amplitude of the oscillations. In fact, this indicates the finite lifetime of the oscillation modes: in Figure 6b the HARPS data are given the highest weight, and so the effective duration of the observations is decreased (and the sidelobes in the spectral window become much stronger). Our estimate of the mode lifetime is given in § 4.3.

It is also useful to convert to power density, which is independent of the observing window and therefore allows us to compare noise levels. This is done by multiplying the power spectrum by the effective length of the observing run, which we calculate as the reciprocal of the area integrated under the spectral window (in power). The values for the different telescopes are given in the third column of Table 2. In Figure 7 we show the power density spectrum on a logarithmic scale for the HARPS data, which has

the lowest noise per minute of observing time. We see three components: (1) the oscillations (about 300–1100 μHz); (2) white noise at high frequencies; and (3) a sloping background of power at low frequencies (stellar granulation and activity, and presumably also some instrumental drift). Figure 8 compares the power density spectra for the different telescopes. They show a similar oscillation signal and similar background from stellar noise at lower frequencies (below about 250 μHz), with different levels of white noise at higher frequencies (above about 2000 μHz), reflecting the different levels of photon noise.

In Figure 7, the lower two dashed lines indicate the background level in the Sun, as measured from the GOLF data during solar minimum and maximum, respectively. The upper dashed line is the solar maximum line shifted to match the power density of Procyon, which required multiplying by a factor of 40. We can use this scaling factor to estimate the fraction of Procyon’s surface that is covered by active regions, relative to the Sun, as follows. The low-frequency part of the velocity power-density spectrum from the Sun falls off as frequency squared (Harvey 1985; Pallé et al. 1999), and we see the same behavior for Procyon. Hence, in both cases we have

$$\text{PD}(\nu) \propto \nu^{-2}. \quad (3)$$

Let T be the typical time for an active region to be visible on the surface (which may depend on both rotation and the typical lifetime of active regions). The amplitude of the velocity signal at frequency $\nu_0 = 1/T$ will be proportional to the fractional area covered by active regions, da/a , and to the projected rotational velocity, $v \sin i$. The power density at ν_0 is therefore

$$\text{PD}(\nu_0) = (da/a)^2 (v \sin i)^2. \quad (4)$$

Combining these gives

$$\text{PD}(\nu) = \left(\frac{da}{a}\right)^2 \left(\frac{v \sin i}{T}\right)^2 \nu^{-2}. \quad (5)$$

We will assume that T is proportional to the rotation period, which we take to be 10.3 days (or twice that value) for Procyon and 25.4 days for the Sun. The measured values for $v \sin i$ are 3.2 km s^{-1} for Procyon (Allende Prieto et al. 2002) and 2.0 km s^{-1} for the Sun. Combining these values with our measurement of the power densities indicates that the area covered by active regions on Procyon is about 1.6 times the solar maximum value (or twice

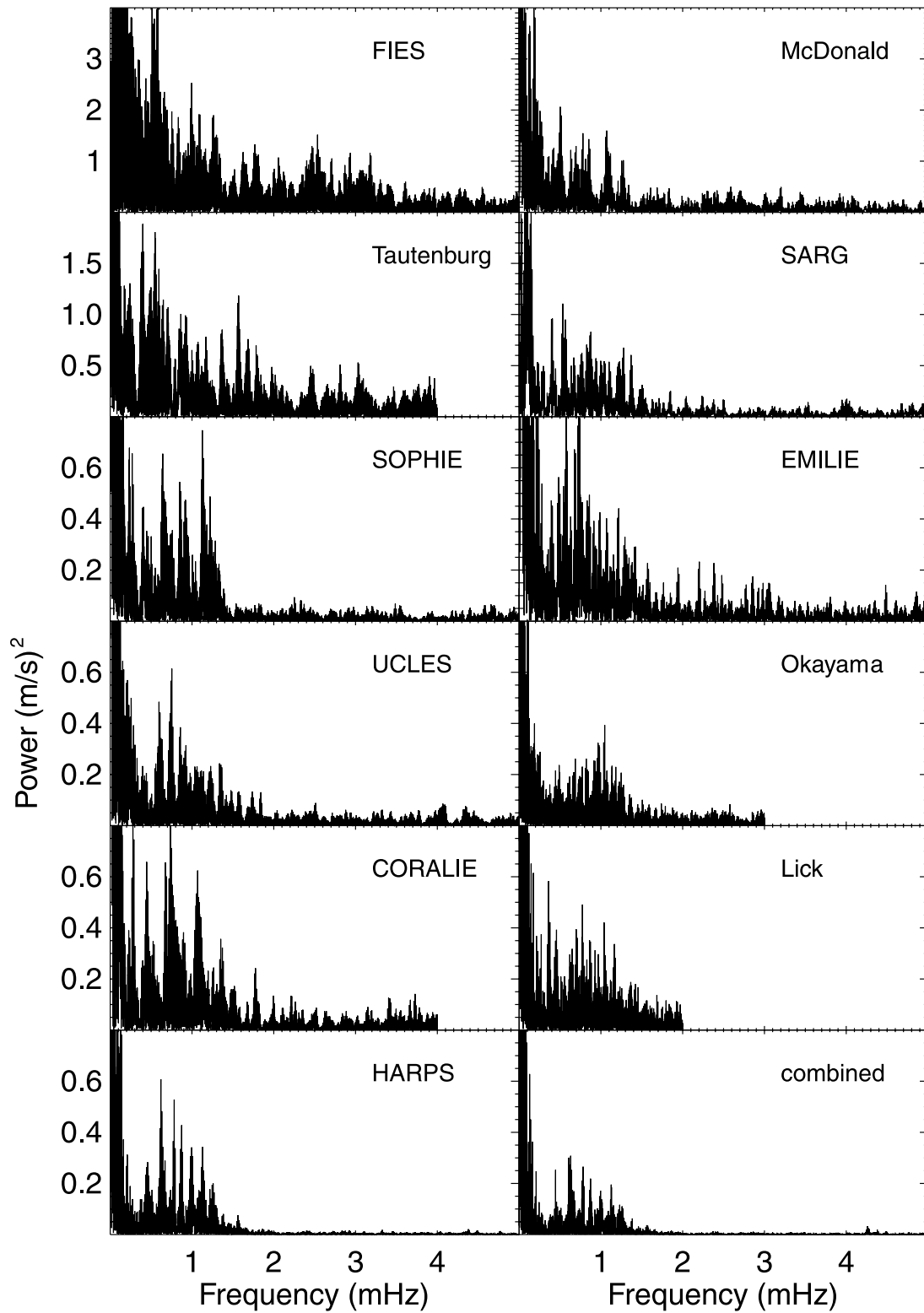


FIG. 5.—Power spectra for all 11 telescopes, together with that of the combined series. Note that the vertical scale is not the same for all panels.

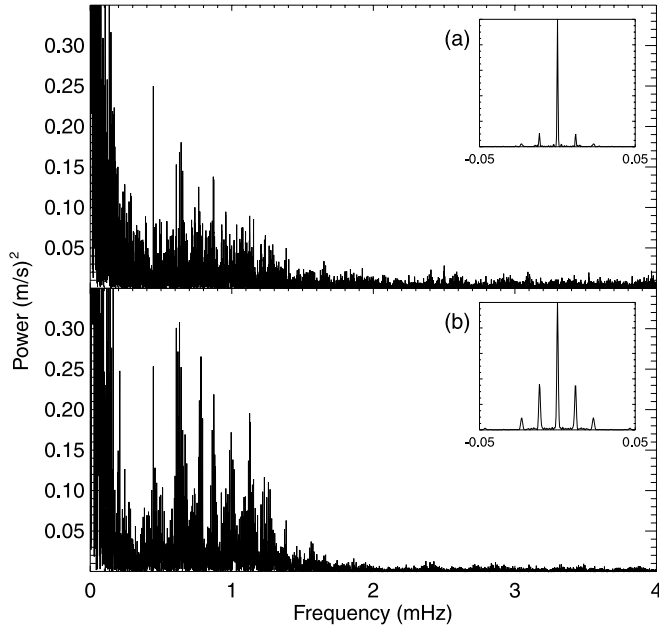


FIG. 6.—Final power spectrum based on the noise-optimized weights (*bottom*), and also without applying the weights (*top*). The inset shows the spectral window.

that value). No detection of a magnetic field in Procyon has been reported, and published upper limits imply that the average field cannot be more than a few times solar (see Table 3 in Kim et al. 2007), which appears to be consistent with our results.

4.3. Oscillation Amplitude and Mode Lifetime

To measure the amplitude of oscillations in Procyon, we have used the method described by Kjeldsen et al. (2008). In brief, this involves the following steps: (1) heavily smoothing the power spectrum (by convolving with a Gaussian having a full width at half-maximum of $4\Delta\nu$, where $\Delta\nu$ is the large frequency separation), to produce a single hump of excess power that is insensitive to the fact that the oscillation spectrum has discrete peaks; (2) converting to power density (see § 4.2); (3) fitting and subtracting the background noise; and (4) multiplying by $\Delta\nu/4.09$ and taking the square root, in order to convert to amplitude per radial oscillation mode. Note that 4.09 is the effective number of modes per order for full-disk velocities observations, normalized to the amplitudes of radial ($l = 0$) modes; see Kjeldsen et al. (2008) for details.

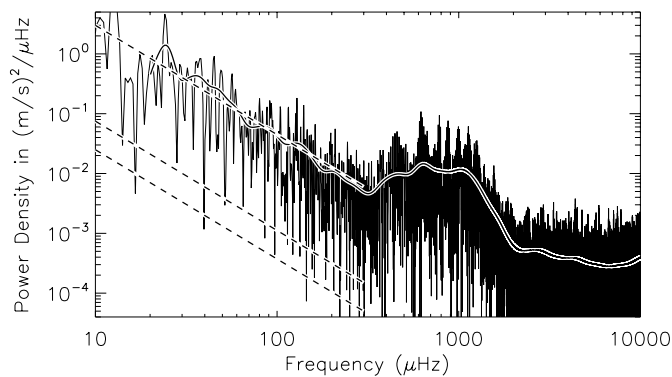


FIG. 7.—Power density spectrum of Procyon from the HARPS data, and the same after smoothing. The lower two dashed lines show the solar activity level at minimum and maximum, and the upper line is the solar maximum activity shifted upwards by a factor of 40.

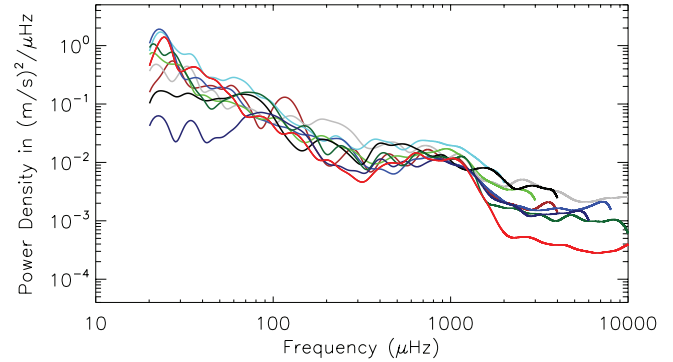


FIG. 8.—Smoothed power density spectra (see Fig. 7) for the nine telescopes shown in Fig. 1*a*, showing a similar background from stellar noise at low frequencies and different levels of white noise at high frequencies. The color coding is the same as in Fig. 1.

We applied this method to each of the telescopes separately, and the result is shown in Figure 9. There are significant differences between the different curves, which we attribute to intrinsic variations in the star arising from the stochastic nature of the excitation and damping. To investigate this further, we also applied the method to the combined time series, after first subdividing it into 10 2 day subsets. Figure 10 shows these amplitude curves and their average.

The amplitude curve of Procyon has a broad plateau, rather than the single peak that has been seen for other stars. Figure 11 shows the smoothed amplitude curve for Procyon compared to the Sun and other stars. It is an updated version of Figure 8 of Kjeldsen et al. (2008), where the following stars have been added: μ Ara (Bouchy et al. 2005), HD 49933 (Mosser et al. 2005), μ Her (Bonanno et al. 2008), γ Pav (Mosser et al. 2008a), and τ Cet (Teixeira et al. 2008).

The plateau for Procyon is centered at $900 \mu\text{Hz}$ and is about $500 \mu\text{Hz}$ wide, with a mean amplitude across that range of $38.1 \pm 1.3 \text{ cm s}^{-1}$. This is our estimate for the amplitude of the radial ($l = 0$) modes in Procyon. Comparing with the corresponding measurement for the Sun ($18.7 \pm 0.7 \text{ cm s}^{-1}$; Kjeldsen et al. 2008) implies that the velocity oscillations in Procyon are 2.04 ± 0.10 times solar. In both Procyon and the Sun, the modes with $l = 1$ are higher by a factor of 1.35 (see Table 1 of Kjeldsen et al. 2008).

The corresponding intensity amplitude, after accounting for the higher effective temperature of Procyon (see eq. [5] in Kjeldsen & Bedding 1995), is 1.60 times solar. This implies an amplitude at 500 nm of 6.8 ppm for $l = 0$ and 8.5 ppm for $l = 1$ (see Table 1

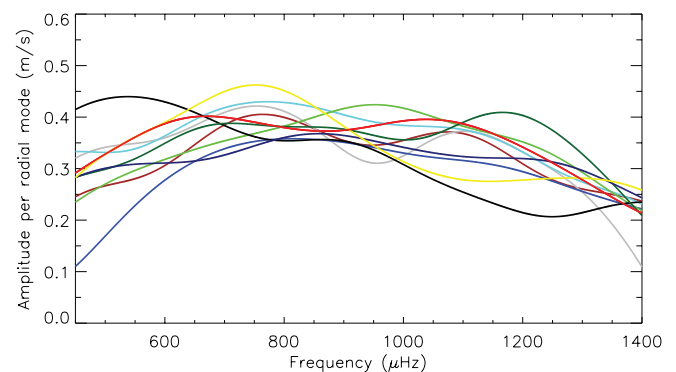


FIG. 9.—Smoothed amplitude curves for Procyon for 10 telescopes, using the same color coding as Fig. 1.

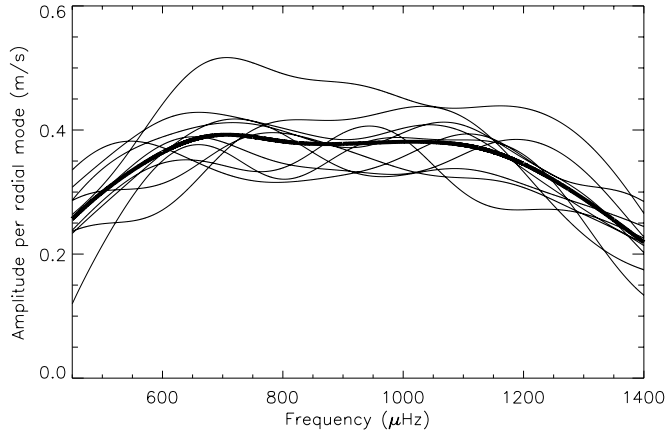


FIG. 10.—Smoothed amplitude curves for Procyon from 10 2 day segments of the combined time series (*thin lines*), together with their mean (*thick line*).

of Kjeldsen et al. 2008). These amplitudes are completely consistent with the detection of oscillations in Procyon by *WIRE* (Bruntt et al. 2005) and with the upper limit set by *MOST* (Matthews et al. 2004; Bedding et al. 2005).

The standard deviation of the 10 segments in Figure 10 is $\sigma_A/A = 10.4\% \pm 2.3\%$, which reflects the finite lifetime of the modes. We can use equation (3) from Kjeldsen et al. (2008) to estimate the mode lifetime, but we must account for the much greater width of the oscillation envelope in Procyon. Note that this equation was established empirically and we have confirmed it analytically using the work of Toutain & Appourchaux (1994). We estimate the mode lifetime to be $\tau = 1.5^{+1.9}_{-0.8}$ days. This equals, within rather large uncertainties, the solar value of 2.9 days (e.g., Chaplin et al. 1997).

5. CONCLUSIONS

We have presented multisite velocity observations of Procyon that we obtained with 11 telescopes over more than 3 weeks. Combining data that spans a range of precisions and sampling rates presents a significant challenge. When calculating the power spectrum, it is important to use weights that are based on the measurement uncertainties, otherwise the result is dominated by the noisiest data. We have described in detail our methods for adjusting the weights in order to minimize the noise level in the final power spectrum.

Our velocity measurements show the clear signature of oscillations. The power spectrum shows an excess in a plateau that is centered at 0.9 mHz and is broader than has been seen for other solar-type stars. The mean amplitude of the radial modes is $38.1 \pm 1.3 \text{ cm s}^{-1}$ (2.04 ± 0.10 times solar), which is consistent

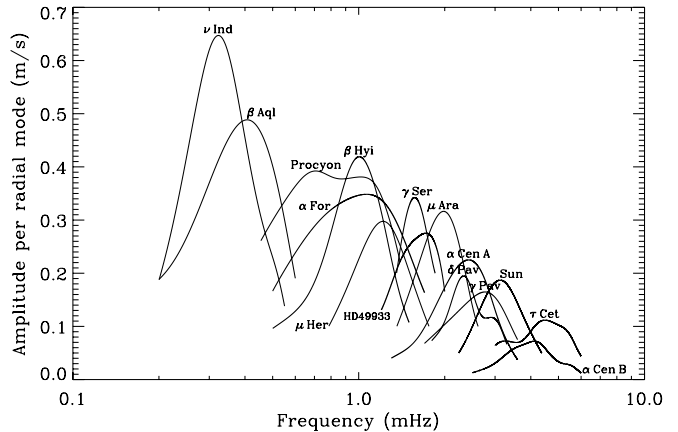


FIG. 11.—Smoothed amplitude curves for oscillations in Procyon and other stars.

with previous detections from the ground and by the *WIRE* spacecraft, and also with the upper limit set by the *MOST* spacecraft. The variation of the amplitude during the observing campaign allowed us to estimate the mode lifetime to be $1.5^{+1.9}_{-0.8}$ days.

We also found a slow variation in the radial velocity of Procyon, with good agreement between different telescopes. These variations are remarkably similar to those seen in the Sun, and we interpret them as being due to rotational modulation from active regions on the stellar surface. The variations appear to have a period of about 10 days, which presumably equals the stellar rotation period or, perhaps, half of it. The amount of power in these slow variations indicates that the fractional area of Procyon that is covered by active regions is slightly higher than for the Sun.

The excellent coverage of the observations and the high signal-to-noise ratio should allow us to produce a good set of oscillation frequencies for Procyon. This analysis will be presented in subsequent papers.

This work was supported financially by the Danish Natural Science Research Council, the Australian Research Council, the Swiss National Science Foundation, NSF grant AST-9988087 (R. P. B.), and by SUN Microsystems. We thank Hugh Jones, Chris Tinney, and the other members of the Anglo-Australian Planet Search for agreeing to a time swap that allowed our AAT observations to be scheduled. M. M. is grateful to N. Kameswara Rao, G. Pandey, and S. Sriram for their participation in campaign with VBT Echelle Spectrometer, which was used for the first time for Doppler spectroscopy observations.

REFERENCES

- Aerts, C., Christensen-Dalsgaard, J., Cunha, M., & Kurtz, D. W. 2008, *Sol. Phys.*, 251, 3
- Allende Prieto, C., Asplund, M., López, R. J. G., & Lambert, D. L. 2002, *ApJ*, 567, 544
- Andersen, B. N., & Maltby, P. 1983, *Nature*, 302, 808
- Baudin, F., Appourchaux, T., Boumier, P., Kuschnig, R., Leibacher, J. W., & Matthews, J. M. 2008, *A&A*, 478, 461
- Bedding, T. R., & Kjeldsen, H. 2007, in *AIP Conf. Proc.* 948, *Unsolved Problems in Stellar Physics: A Conference in Honour of Douglas Gough*, ed. R. J. Stancliff et al. (Melville: AIP), 117
- Bedding, T. R., et al. 2005, *A&A*, 432, L43
- . 2007, *ApJ*, 663, 1315
- Bonanno, A., Benatti, S., Claudi, R., Desidera, S., Gratton, R., Leccia, S., & Paternò, L. 2008, *ApJ*, 676, 1248
- Bouchy, F., Bazot, M., Santos, N. C., Vauclair, S., & Sosnowska, D. 2005, *A&A*, 440, 609
- Bouchy, F., & Carrier, F. 2002, *A&A*, 390, 205
- Bouchy, F., Maeder, A., Mayor, M., Mégevand, D., Pepe, F., & Sosnowska, D. 2004, *Nature*, 432, 7015
- Bouchy, F., Schmitt, J., Bertaux, J.-L., & Connes, P. 2002, in *ASP Conf. Ser.* 259, *Radial and Nonradial Pulsations as Probes of Stellar Physics*, ed. C. Aerts, T. R. Bedding, & J. Christensen-Dalsgaard (San Francisco: ASP), 472
- Brown, T. M., Gilliland, R. L., Noyes, R. W., & Ramsey, L. W. 1991, *ApJ*, 368, 599
- Bruntt, H., Kjeldsen, H., Buzasi, D. L., & Bedding, T. R. 2005, *ApJ*, 633, 440
- Butler, R. P., Marcy, G. W., Williams, E., McCarthy, C., Dosanji, P., & Vogt, S. S. 1996, *PASP*, 108, 500
- Butler, R. P., et al. 2004, *ApJ*, 600, L75
- Chaplin, W. J., Elsworth, Y., Isaak, G. R., McLeod, C. P., Miller, B. A., & New, R. 1997, *MNRAS*, 288, 623
- Clarke, D. 2003, *A&A*, 407, 1029
- Claudi, R. U., et al. 2005, *A&A*, 429, L17

- Claverie, A., Isaak, G. R., McLeod, C. P., van der Raay, H. B., Palle, P. L., & Roca Cortes, T. 1982, *Nature*, 299, 704
- Durrant, C. J., & Schröter, E. H. 1983, *Nature*, 301, 589
- Edmunds, M. G., & Gough, D. O. 1983, *Nature*, 302, 810
- Eggenberger, P., Carrier, F., Bouchy, F., & Blecha, A. 2004, *A&A*, 422, 247
- Endl, M., Cochran, W. D., Hatzes, A. P., & Wittenmyer, R. A. 2005, *Rev. Mex. AA*, 23, 64
- Frandsen, S., & Lindberg, B. 2000, in *The Third MONS Workshop: Science Preparation and Target Selection*, ed. T. Teixeira, & T. R. Bedding (Aarhus: Aarhus Univ.), 163
- García, R. A., et al. 2005, *A&A*, 442, 385
- Gilliland, R. L., et al. 1993, *AJ*, 106, 2441
- Girard, T. M., et al. 2000, *AJ*, 119, 2428
- Guenther, D. B., et al. 2007, *Commun. Asteroseis.*, 151, 5
- Harvey, J. 1985, in *Future Missions in Solar, Heliospheric & Space Plasma Physics*, ed. E. Rolfe, & B. Battrick (ESA SP-235; Noordwijk: ESA), 199
- Hatzes, A. P., Guenther, E., Kürster, M., & McArthur, B. 2003, in *Earths: DARWIN/TPF and the Search for Extrasolar Terrestrial Planets*, ed. M. Fridlund, T. Henning, & H. Lacoste (ESA SP-539; Noordwijk: ESA), 441
- Kambe, E., 2008, *PASJ*, 60, 45
- Kervella, P., Thévenin, F., Morel, P., Berthomieu, G., Bordé, P., & Provost, J. 2004, *A&A*, 413, 251
- Kim, K.-M., et al. 2007, *PASP*, 119, 1052
- Kjeldsen, H., & Bedding, T. R. 1995, *A&A*, 293, 87
- Kjeldsen, H., et al. 2008, *ApJ*, 682, 1370
- Leccia, S., Kjeldsen, H., Bonanno, A., Claudi, R. U., Ventura, R., & Paternò, L. 2007, *A&A*, 464, 1059
- Marchenko, S. V. 2008, *A&A*, 479, 845
- Martić, M., Lebrun, J.-C., Appourchaux, T., & Korzennik, S. G. 2004, *A&A*, 418, 295
- Martić, M., et al. 1999, *A&A*, 351, 993
- Matthews, J. M., Kuschnig, R., Guenther, D. B., et al. 2004, *Nature*, 430, 51 (erratum 430, 921)
- Mosser, B., Deheuvels, S., Michel, E., Thevenin, F., Dupret, M. A., Samadi, R., Barban, C., & Goupil, M. J. 2008a, *A&A*, in press (arXiv:0804.3119)
- Mosser, B., Maillard, J. P., Mékarnia, D., & Gay, J. 1998, *A&A*, 340, 457
- Mosser, B., et al. 2005, *A&A*, 431, L13
- . 2008b, *A&A*, 478, 197
- Pallé, P. L., Roca Cortés, T., Jiménez, A., Golf, & VIRGO Teams. 1999, in *ASP Conf. Ser. 173, Workshop on Stellar Structure Theory and Tests of Convective Energy Transport*, ed. A. Giménez, E. F. Guinan, & G. Montesinos (San Francisco: ASP), 297
- Régulo, C., & Roca Cortés, T. 2005, *A&A*, 444, L5
- Rupprecht, G., et al. 2004, *Proc. SPIE*, 5492, 148
- Teixeira, T., et al. 2008, *A&A*, submitted
- Toutain, T., & Appourchaux, T. 1994, *A&A*, 289, 649
- Ulrich, R. K., et al. 2000, *A&A*, 364, 799

Appendix F

A MULTI-SITE CAMPAIGN TO MEASURE SOLAR-LIKE OSCILLATIONS IN PROCYON. II. MODE FREQUENCIES

A MULTI-SITE CAMPAIGN TO MEASURE SOLAR-LIKE OSCILLATIONS IN PROCYON. II. MODE FREQUENCIES

TIMOTHY R. BEDDING¹, HANS KJELDSSEN², TIAGO L. CAMPANTE^{2,3}, THIERRY APPOURCHAUX⁴, ALFIO BONANNO⁵,
WILLIAM J. CHAPLIN⁶, RAFAEL A. GARCIA⁷, MILENA MARTIĆ⁸, BENOIT MOSSER⁹, R. PAUL BUTLER¹⁰, HANS BRUNTT^{1,11},
LÁSZLÓ L. KISS^{1,12}, SIMON J. O'TOOLE¹³, EJI KAMBE¹⁴, HIROYASU ANDO¹⁵, HIDEYUKI IZUMIURA¹⁴, BUN'EI SATO¹⁶,
MICHAEL HARTMANN¹⁷, ARTIE HATZES¹⁷, CAROLINE BARBAN¹¹, GABRIELLE BERTHOMIEU¹⁸, ERIC MICHEL¹¹, JANINE PROVOST¹⁸,
SYLVAINE TURCK-CHIÈZE⁷, JEAN-CLAUDE LEBRUN⁸, JEROME SCHMITT¹⁹, JEAN-LOUP BERTAUX⁸, SERENA BENATTI²⁰,
RICCARDO U. CLAUDI²¹, ROSARIO COSENTINO⁵, SILVIO LECCIA²², SØREN FRANDSEN², KARSTEN BROGAARD², LARS GLOWIENKA²,
FRANK GRUNDAHL², ERIC STEMPELS²³, TORBEN ARENTOFT², MICHAËL BAZOT², JØRGEN CHRISTENSEN-DALSGAARD²,
THOMAS H. DALL²⁴, CHRISTOFFER KAROFF², JENS LUNDGREEN-NIELSEN², FABIEN CARRIER²⁵, PATRICK EGGENBERGER²⁶,
DANUTA SOSNOWSKA²⁷, ROBERT A. WITTENMYER^{28,29}, MICHAEL ENDL²⁸, TRAVIS S. METCALFE³⁰, SASKIA HEKKER^{6,31},

AND SABINE REFFERT³²

¹ Sydney Institute for Astronomy (SIFA), School of Physics, University of Sydney, NSW 2006, Australia; bedding@physics.usyd.edu.au

² Danish AsteroSeismology Centre (DASC), Department of Physics and Astronomy, Aarhus University, DK-8000 Aarhus C, Denmark

³ Centro de Astrofísica da Universidade do Porto, Rua das Estrelas, 4150-762 Porto, Portugal

⁴ Institut d'Astrophysique Spatiale, Université Paris XI-CNRS, Bâtiment 121, 91405 Orsay Cedex, France

⁵ INAF—Osservatorio Astrofisico di Catania, via S. Sofia 78, 95123 Catania, Italy

⁶ School of Physics and Astronomy, University of Birmingham, Edgbaston, Birmingham B15 2TT, UK

⁷ DAPNIA/DSM/Service d'Astrophysique, CEA/Saclay, 91191 Gif-sur-Yvette Cedex, France

⁸ LATMOS, University of Versailles St Quentin, CNRS, BP 3, 91371 Verrières le Buisson Cedex, France

⁹ LESIA, CNRS, Université Pierre et Marie Curie, Université Denis Diderot, Observatoire de Paris, 92195 Meudon Cedex, France

¹⁰ Carnegie Institution of Washington, Department of Terrestrial Magnetism, 5241 Broad Branch Road NW, Washington, DC 20015-1305, USA

¹¹ Laboratoire AIM, CEA/DSM—CNRS—Université Paris Diderot—IRFU/Sap, 91191 Gif-sur-Yvette Cedex, France

¹² Konkoly Observatory of the Hungarian Academy of Sciences, H-1525 Budapest, P.O. Box 67, Hungary

¹³ Anglo-Australian Observatory, P.O. Box 296, Epping, NSW 1710, Australia

¹⁴ Okayama Astrophysical Observatory, National Astronomical Observatory of Japan, National Institutes of Natural Sciences, 3037-5 Honjyo, Kamogata, Asakuchi, Okayama 719-0232, Japan

¹⁵ National Astronomical Observatory of Japan, National Institutes of Natural Sciences, 2-21-1 Osawa, Mitaka, Tokyo 181-8588, Japan

¹⁶ Global Edge Institute, Tokyo Institute of Technology 2-12-1-S6-6, Ookayama, Meguro-ku, Tokyo 152-8550, Japan

¹⁷ Thüringer Landessternwarte Tautenburg, Sternwarte 5, 07778 Tautenburg, Germany

¹⁸ Université de Nice Sophia-Antipolis, CNRS UMR 6202, Laboratoire Cassiopée, Observatoire de la Côte d'Azur, BP 4229, 06304 Nice Cedex, France

¹⁹ Observatoire de Haute Provence, 04870 St Michel l'Observatoire, France

²⁰ CISAS—University of Padova, Via Venezia 5, 35131, Padova, Italy

²¹ INAF—Astronomical Observatory of Padua, Vicolo Osservatorio 5, 35122 Padua, Italy

²² INAF—Osservatorio Astronomico di Capodimonte, Salita Moiariello 16, 80131 Napoli, Italy

²³ Department of Physics and Astronomy, P.O. Box 516, SE-751 20 Uppsala, Sweden

²⁴ European Southern Observatory, D-85748 Garching, Germany

²⁵ Instituut voor Sterrenkunde, Katholieke Universiteit Leuven, Celestijnenlaan 200 B, 3001 Leuven, Belgium

²⁶ Observatoire de Genève, Université de Genève, Ch. des Maillettes 51, CH-1290 Sauverny, Switzerland

²⁷ Laboratoire d'astrophysique, EPFL Observatoire CH-1290 Versoix, Switzerland

²⁸ McDonald Observatory, University of Texas at Austin, Austin, TX 78712, USA

²⁹ School of Physics, University of New South Wales, NSW 2052, Australia

³⁰ High Altitude Observatory, National Centre for Atmospheric Research, Boulder, CO 80307-3000, USA

³¹ Leiden Observatory, Leiden University, 2300 RA Leiden, The Netherlands

³² ZAH-Landessternwarte, 69117 Heidelberg, Germany

Received 2010 January 19; accepted 2010 February 26; published 2010 March 29

ABSTRACT

We have analyzed data from a multi-site campaign to observe oscillations in the F5 star Procyon. The data consist of high-precision velocities that we obtained over more than three weeks with 11 telescopes. A new method for adjusting the data weights allows us to suppress the sidelobes in the power spectrum. Stacking the power spectrum in a so-called échelle diagram reveals two clear ridges, which we identify with even and odd values of the angular degree ($l = 0$ and 2 , and $l = 1$ and 3 , respectively). We interpret a strong, narrow peak at $446 \mu\text{Hz}$ that lies close to the $l = 1$ ridge as a mode with mixed character. We show that the frequencies of the ridge centroids and their separations are useful diagnostics for asteroseismology. In particular, variations in the large separation appear to indicate a glitch in the sound-speed profile at an acoustic depth of ~ 1000 s. We list frequencies for 55 modes extracted from the data spanning 20 radial orders, a range comparable to the best solar data, which will provide valuable constraints for theoretical models. A preliminary comparison with published models shows that the offset between observed and calculated frequencies for the radial modes is very different for Procyon than for the Sun and other cool stars. We find the mean lifetime of the modes in Procyon to be $1.29^{+0.55}_{-0.49}$ days, which is significantly shorter than the 2–4 days seen in the Sun.

Key words: stars: individual (Procyon A) – stars: oscillations

1. INTRODUCTION

The success of helioseismology and the promise of asteroseismology have motivated numerous efforts to measure oscillations in solar-type stars. These began with ground-based observations (for recent reviews see Bedding & Kjeldsen 2007; Aerts et al. 2008) and now extend to space-based photometry, particularly with the *CoRoT* and *Kepler* Missions (e.g., Michel et al. 2008; Gilliland et al. 2010).

We have carried out a multi-site spectroscopic campaign to measure oscillations in the F5 star Procyon A (HR 2943; HD 61421; HIP 37279). We obtained high-precision velocity observations over more than three weeks with 11 telescopes, with almost continuous coverage for the central 10 days. In Arentoft et al. (2008, hereafter Paper I) we described the details of the observations and data reduction, measured the mean oscillation amplitudes, gave a crude estimate for the mode lifetime and discussed slow variations in the velocity curve that we attributed to rotational modulation of active regions. In this paper, we describe the procedure used to extract the mode parameters, provide a list of oscillation frequencies, and give an improved estimate of the mode lifetimes.

2. PROPERTIES OF SOLAR-LIKE OSCILLATIONS

We begin with a brief summary of the relevant properties of solar-like oscillations (for reviews see, for example, Brown & Gilliland 1994; Bedding & Kjeldsen 2003; Christensen-Dalsgaard 2004).

To a good approximation, in main-sequence stars the cyclic frequencies of low-degree p -mode oscillations are regularly spaced, following the asymptotic relation (Tassoul 1980; Gough 1986):

$$\nu_{n,l} \approx \Delta\nu(n + \frac{1}{2}l + \epsilon) - l(l+1)D_0. \quad (1)$$

Here, n (the radial order) and l (the angular degree) are integers, $\Delta\nu$ (the large separation) depends on the sound travel time across the whole star, D_0 is sensitive to the sound speed near the core and ϵ is sensitive to the reflection properties of the surface layers. It is conventional to define three so-called small frequency separations that are sensitive to the sound speed in the core: $\delta\nu_{02}$ is the spacing between adjacent modes with $l = 0$ and $l = 2$ (for which n will differ by 1); $\delta\nu_{13}$ is the spacing between adjacent modes with $l = 1$ and $l = 3$ (ditto); and $\delta\nu_{01}$ is the amount by which $l = 1$ modes are offset from the midpoint of the $l = 0$ modes on either side.³³ To be explicit, for a given radial order, n , these separations are defined as follows:

$$\delta\nu_{02} = \nu_{n,0} - \nu_{n-1,2}, \quad (2)$$

$$\delta\nu_{01} = \frac{1}{2}(\nu_{n,0} + \nu_{n+1,0}) - \nu_{n,1}, \quad (3)$$

$$\delta\nu_{13} = \nu_{n,1} - \nu_{n-1,3}. \quad (4)$$

If the asymptotic relation (Equation (1)) were to hold exactly, it would follow that all of these separations would be independent of n and that $\delta\nu_{02} = 6D_0$, $\delta\nu_{13} = 10D_0$, and $\delta\nu_{01} = 2D_0$. In practice, Equation (1) is only an approximation. In the Sun and other stars, theoretical models and observations show that

$\Delta\nu$, D_0 , and ϵ vary somewhat with frequency, and also with l . Consequently, the small separations also vary with frequency.

The mode amplitudes are determined by the excitation and damping, which are stochastic processes involving near-surface convection. We typically observe modes over a range of frequencies, which in Procyon is especially broad (about 400–1400 μHz ; see Paper I). The observed amplitudes also depend on l via various projection factors (see Table 1 of Kjeldsen et al. 2008a). Note, in particular, that velocity measurements are much more sensitive to modes with $l = 3$ than are intensity measurements. The mean mode amplitudes are modified for a given observing run by the stochastic nature of the excitation, resulting in considerable scatter of the peak heights about the envelope.

Oscillations in the Sun are long-lived compared to their periods, which allows their frequencies to be measured very precisely. However, the lifetime is not infinite and the damping results in each mode in the power spectrum being split into multiple peaks under a Lorentzian profile. The FWHM of this Lorentzian, which is referred to as the linewidth Γ , is inversely proportional to the mode lifetime: $\Gamma = 1/(\pi\tau)$. We follow the usual definition that τ is the time for the mode amplitude to decay by a factor of e . The solar value of τ for the strongest modes ranges from 2 to 4 days, as a decreasing function of frequency (e.g., Chaplin et al. 1997).

Procyon is an evolved star, with theoretical models showing that it is close to, or just past, the end of the main sequence (e.g., Guenther & Demarque 1993; Barban et al. 1999; Chaboyer et al. 1999; Di Mauro & Christensen-Dalsgaard 2001; Kervella et al. 2004; Eggenberger et al. 2005; Provost et al. 2006; Bonanno et al. 2007; Guenther et al. 2008). As such, its oscillation spectrum may show deviations from the regular comb-like structure described by Equation (1), especially at low frequencies. This is because some modes, particularly those with $l = 1$, are shifted by avoided crossings with gravity modes in the stellar core (also called “mode bumping”; see Osaki 1975; Aizenman et al. 1977). These so-called “mixed modes” have p -mode character near the surface but g -mode character in the deep interior. Some of the theoretical models of Procyon cited above indeed predict these mixed modes, depending on the evolutionary state of the star, and we must keep this in mind when attempting to identify oscillation modes in the power spectrum. The mixed modes are rich in information because they probe the stellar core and are very sensitive to age, but they complicate the task of mode identification.

We should also keep in mind that mixed modes are expected to have lower amplitudes and longer lifetimes (smaller linewidths) than regular p -modes because they have larger mode inertias (e.g., Christensen-Dalsgaard 2004). Hence, for a data series that is many times longer than the lifetime of the pure p -modes, a mixed mode may appear in the power spectrum as a narrow peak that is higher than the others, even though its power (amplitude squared) is not especially large.

Another potential complication is that stellar rotation causes modes with $l \geq 1$ to split into multiplets. The peaks of these multiplets are characterized by the azimuthal degree m , which takes on values of $m = 0, \pm 1, \dots, \pm l$, with a separation that directly measures the rotation rate averaged over the region of the star that is sampled by the mode. The measurements are particularly difficult because a long time series is needed to resolve the rotational splittings. We argue in Appendix A that the low value of $v \sin i$ observed in Procyon implies that rotational splitting of frequencies is not measurable in our observations.

³³ One can also define an equivalent quantity, $\delta\nu_{10}$, as the offset of $l = 0$ modes from the midpoint between the surrounding $l = 1$ modes, so that $\delta\nu_{10} = \nu_{n,0} - \frac{1}{2}(\nu_{n-1,1} + \nu_{n,1})$.

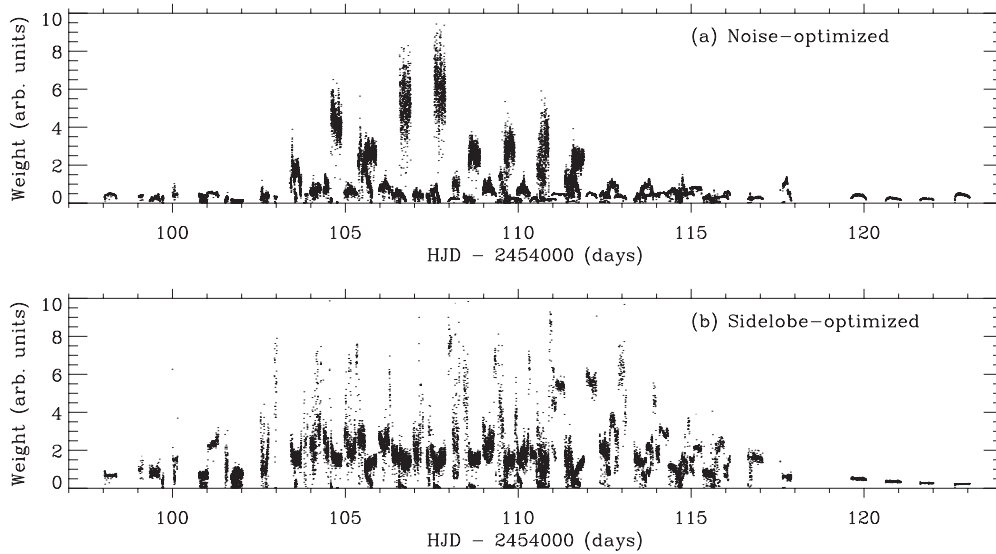


Figure 1. Weights for time series of velocity observations of Procyon, optimized to minimize: (a) the noise level and (b) the height of the sidelobes.

3. WEIGHTING THE TIME SERIES

The time series of velocity observations was obtained over 25 days using 11 telescopes at eight observatories and contains just over 22,500 data points. As discussed in Paper I, the velocity curve shows slow variations that we attribute to a combination of instrumental drifts and rotational modulation of stellar active regions. We have removed these slow variations by subtracting all the power below $280 \mu\text{Hz}$, to prevent spectral leakage into higher frequencies that would degrade the oscillation spectrum. We take this high-pass-filtered time series of velocities, together with their associated measurement uncertainties, as the starting point in our analysis.

3.1. Noise-optimized Weights

Using weights when analyzing ground-based observations of stellar oscillations (e.g., Gilliland et al. 1993; Frandsen et al. 1995) allows one to take into account the significant variations in data quality during a typical observing campaign, especially when two or more telescopes are used. The usual practice, which we followed in Paper I, is to calculate the weights for a time series from the measurement uncertainties, σ_i , according to $w_i = 1/\sigma_i^2$.

These “raw” weights can then be adjusted to minimize the noise level in the final power spectrum by identifying and revising those uncertainties that are too optimistic, and at the same time rescaling the uncertainties to be in agreement with the actual noise levels in the data. This procedure is described in Paper I and references therein. The time series of these noise-optimized weights is shown in Figure 1(a). These are the same as those shown in Figure 1(d) of Paper I, but this time as weights rather than uncertainties.

The power spectrum of Procyon based on these noise-optimized weights is shown in Figure 2(a). This is the same as shown in Paper I (lower panel of Figure 6), except that the power at low frequencies, which arises from the slow variations, has been removed. As described in Paper I, the noise level above 3 mHz in this noise-optimized spectrum is 1.9 cm s^{-1} in amplitude. This includes some degree of spectral leakage from the oscillations and if we high-pass filter the spectrum up to 3 mHz to remove the oscillation signal, the noise level drops to 1.5 cm s^{-1} in amplitude.

The task of extracting oscillation frequencies from the power spectrum is complicated by the presence of structure in the spectral window, which are caused by gaps or otherwise uneven coverage in the time series. The spectral window using the noise-optimized weights is shown in Figure 3(a). Prominent sidelobes at $\pm 11.57 \mu\text{Hz}$ correspond to aliasing at one cycle per day. Indeed, the prospect of reducing these sidelobes is the main reason for acquiring multi-site observations. However, even with good coverage the velocity precision varies greatly, both for a given telescope during the run and from one telescope to another (see Figure 1(a)). As pointed out in Paper I, using these measurement uncertainties as weights has the effect of increasing the sidelobes in the spectral window. We now discuss a technique for addressing this issue.

3.2. Sidelobe-optimized Weights

Adjusting the weights allows one to suppress the sidelobe structure; the trade-off is an increase in the noise level. This technique is routinely used in radio astronomy when synthesizing images from interferometers (e.g., Högbom & Brouw 1974). An extreme case is to set all weights to be equal, which is the same as not using weights at all. This is certainly not optimal because it produces a power spectrum with greatly increased noise (by a factor of 2.3) but still having significant sidelobes, as can be seen in Figure 6(a) of Paper I. Adjusting the weights on a night-by-night basis in order to minimize the sidelobes was used in the analysis of dual-site observations of α Cen A (Bedding et al. 2004), α Cen B (Kjeldsen et al. 2005), and β Hyi (Bedding et al. 2007). For our multi-site Procyon data, this is impractical because of the large number of (partly overlapping) telescope nights. We have developed a more general algorithm for adjusting weights to minimize the sidelobes (H. Kjeldsen et al. 2010, in preparation). The new method, which is superior because it does not assume the oscillations are coherent over the whole observing run, is based on the principle that equal weight is given to all segments of the time series. The method produces the cleanest possible spectral window in terms of suppressing the sidelobes, and we have tested it with good results using published data for α Cen A and B and β Hyi (Arentoft et al. 2010).

The new method operates with two timescales, T_1 and T_2 . All data segments of length T_1 ($=2 \text{ hr}$, in this case) are required to

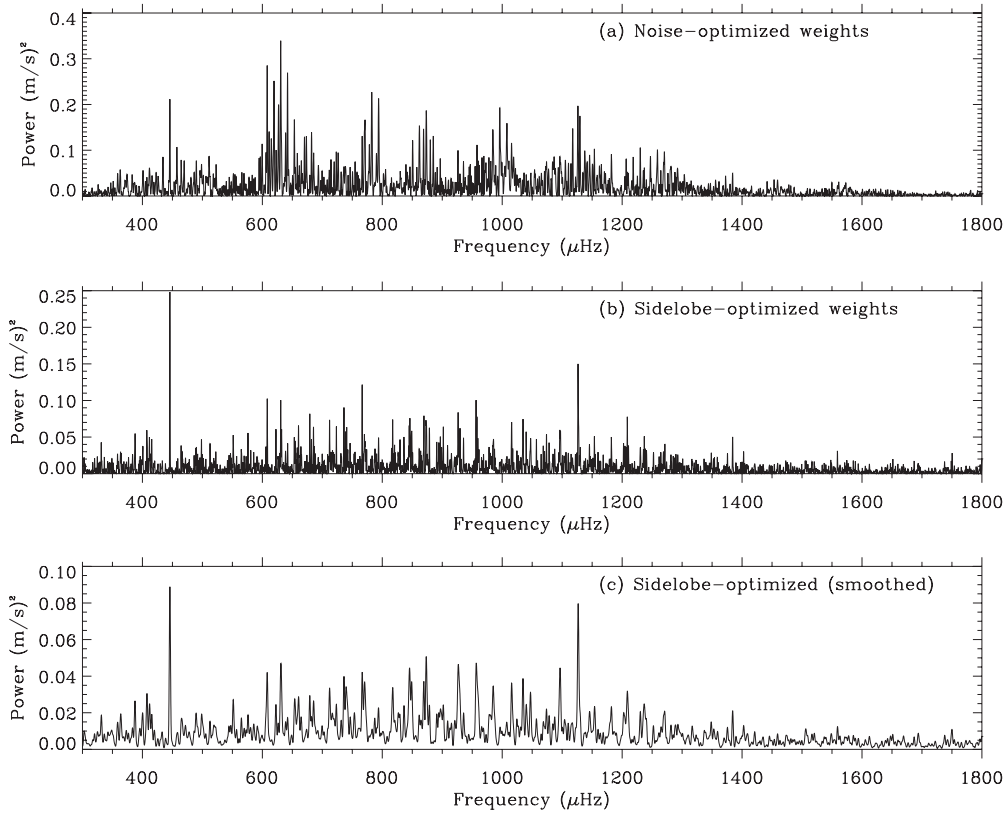


Figure 2. Power spectrum of oscillations in Procyon: (a) using the noise-optimized weights; (b) using the sidelobe-optimized weights; (c) using the sidelobe-optimized weights and smoothing by convolution with a Gaussian with FWHM $2 \mu\text{Hz}$.

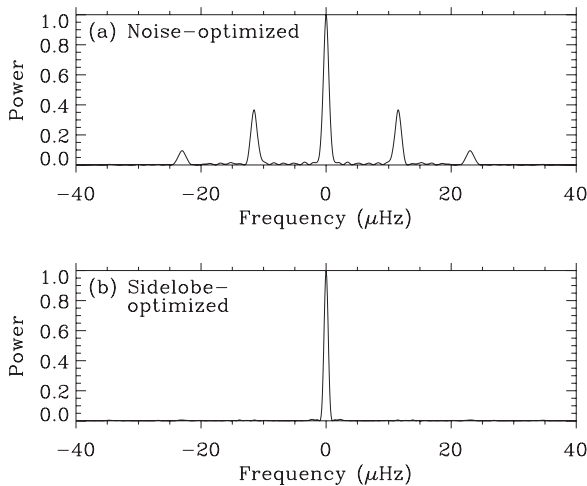


Figure 3. Spectral window for the Procyon observations using (a) noise-optimized weights and (b) sidelobe-optimized weights.

have the same total weight throughout the time series, with the relaxing condition that variations on timescales longer than T_2 ($=12$ hr) are retained. To be explicit, the algorithm works as follows. We adjust the weights so that all segments of length T_1 have the same total weight. That is, for each point w_i in the time series of weights, define $\{S_i\}$ to be the set of weights in a segment of width T_1 centered at that time stamp, and divide each w_i by the sum of the weights in $\{S_i\}$. However, this adjustment suffers from edge effects, since it gives undue weight to points adjacent to a gap. To compensate, we also divide by an asymmetry factor

$$R = 1 + \left| \frac{\Sigma_{\text{left}} - \Sigma_{\text{right}}}{\Sigma_{\text{left}} + \Sigma_{\text{right}}} \right|. \quad (5)$$

Here, Σ_{left} is the sum of the weights in the segment $\{S_i\}$ that have time stamps less than t_i , and Σ_{right} is the sum of the weights in the segment $\{S_i\}$ that have time stamps greater than t_i . Note that R ranges from 1, for points that are symmetrically placed in their T bin, up to 2 for points at one edge of a gap.

Once the above procedure is done for T_1 , which is the shortest timescale on which we wish to adjust the weights, we do it again with T_2 , which is the longest timescale for adjusting the weights. Finally, we divide the first set of adjusted weights by the second set, and this gives the weights that we adopt (Figure 1(b)).

3.3. The Sidelobe-optimized Power Spectrum

Figure 2(b) shows the power spectrum of Procyon based on the sidelobe-optimized weights. The spectral window has improved tremendously (Figure 3(b)), while the noise level at high frequencies (above 3 mHz) has increased by a factor of 2.0.

The power spectrum now clearly shows a regular series of peaks, which are even more obvious after smoothing (Figure 2(c)). We see that the large separation of the star is about $55 \mu\text{Hz}$, confirming the value indicated by several previous studies (Mosser et al. 1998; Martić et al. 1999, 2004; Eggenberger et al. 2004; Régulo & Roca Cortés 2005; Leccia et al. 2007; Guenther et al. 2008). The very strong peak at $446 \mu\text{Hz}$ appears to be a candidate for a mixed mode, especially given its narrowness (see Section 2).

Plotting the power spectrum in échelle format using a large separation of $56 \mu\text{Hz}$ (Figure 4) clearly shows two ridges, as

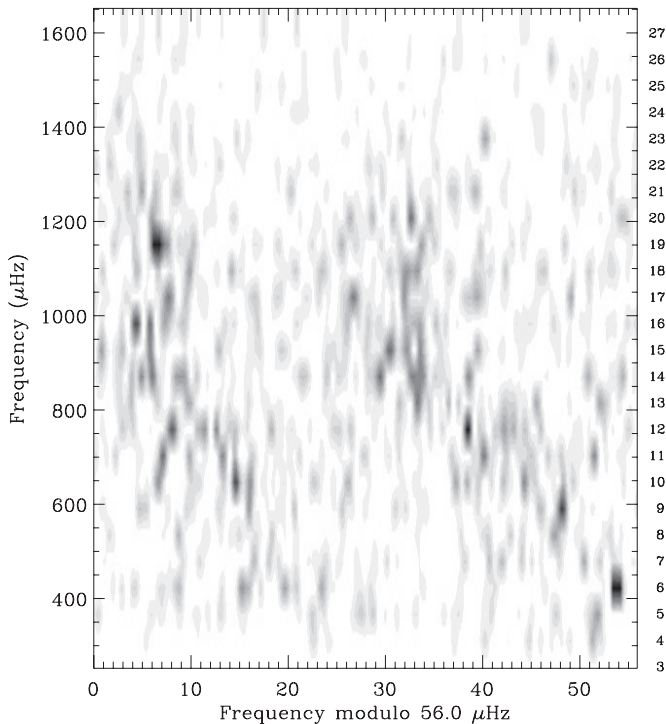


Figure 4. Power spectrum of Procyon in échelle format using a large separation of $56 \mu\text{Hz}$, based on the sidelobe-optimized weights. Two ridges are clearly visible. The upper parts are vertical but the lower parts are tilted, indicating a change in the large separation as a function of frequency. The orders are numbered sequentially on the right-hand side.

expected.³⁴ The upper parts are vertical but the lower parts are tilted, indicating a change in the large separation as a function of frequency. This large amount of curvature in the échelle diagram goes a long way toward explaining the lack of agreement between previous studies on the mode frequencies of Procyon (see the list of references given in the previous paragraph).

The advantage of using the sidelobe-optimized weights is demonstrated by Figure 5. This is the same as Figure 4 but for the noise-optimized weights and the ridges are no longer clearly defined.

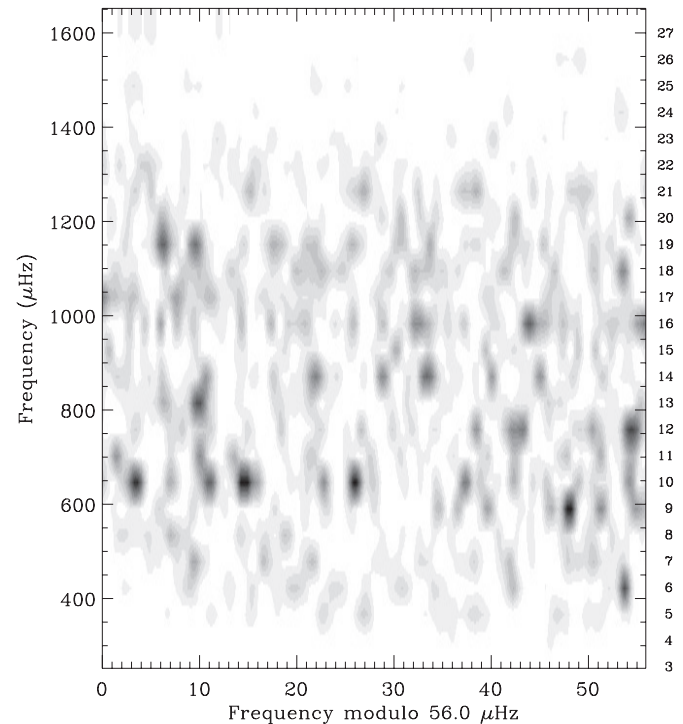


Figure 5. Same as Figure 4, but for the noise-optimized weights. The sidelobes from daily aliasing mean that the ridges can no longer be clearly distinguished.

4. IDENTIFICATION OF THE RIDGES

We know from asymptotic theory (see Equation (1)) that one of the ridges in the échelle diagram (Figure 4) corresponds to modes with even degree ($l = 0$ and 2) and the other to modes with odd degree ($l = 1$ and 3). However, it is not immediately obvious which is which. We also need to keep in mind that the asymptotic relation in evolved stars does not hold exactly. We designate the two possibilities Scenario A, in which the left-hand ridge in Figure 4 corresponds to modes with odd degree, and Scenario B, in which the same ridge corresponds to modes with even degree. Figure 6 shows the Procyon power spectrum collapsed along several orders. We now see double peaks that suggest the identifications shown, which corresponds to Scenario B.

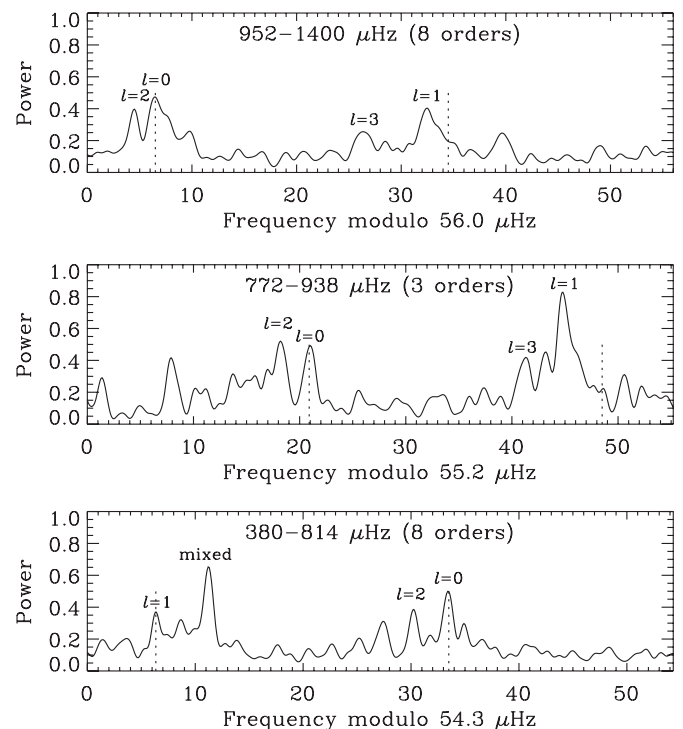


Figure 6. Power spectrum of Procyon collapsed along several orders. Note that the power spectrum was first smoothed slightly by convolving with a Gaussian with FWHM $0.5 \mu\text{Hz}$. The dotted lines are separated by exactly $\Delta\nu/2$, to guide the eye in assessing the 0–1 small separation.

³⁴ When making an échelle diagram, it is common to plot ν versus $(\nu \bmod \Delta\nu)$, in which case each order slopes slightly upward. However, for gray-scale images, it is preferable to keep the orders horizontal, as was done in the original presentation of the diagram (Grec et al. 1983). We have followed that approach in this paper, and the value given on the vertical axis indicates the frequency at the middle of each order.

We can check that the small separation $\delta\nu_{01}$ has the expected sign. According to asymptotic theory (Equation (1)), each $l = 1$ mode should be at a slightly lower frequency than the midpoint of the adjacent $l = 0$ modes. This is indeed the case for the identifications given in Figure 6, but would not be if the even

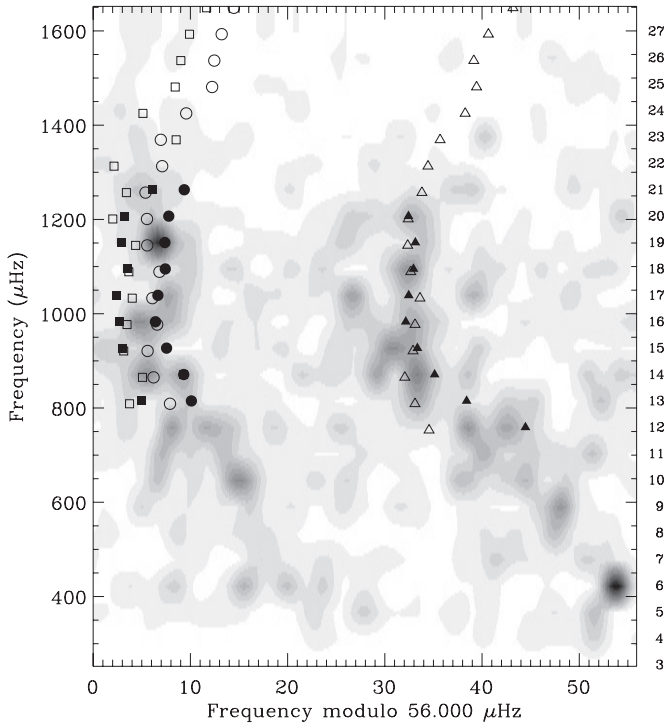


Figure 7. Échelle diagram for Procyon smoothed to $2 \mu\text{Hz}$ (grayscale) overlaid with scaled frequencies for two stars observed by *CoRoT*. The filled symbols are oscillation frequencies for HD 49385 reported by Deheuvels et al. (2010), after multiplying by 0.993. Open symbols are oscillation frequencies for HD 49933 from the revised identification by Benomar et al. (2009b, Scenario B) after multiplying by 0.6565. Symbol shapes indicate mode degree: $l = 0$ (circles), $l = 1$ (triangles), and $l = 2$ (squares).

and odd degrees were reversed. We should be careful, however, since $\delta\nu_{01}$ has been observed to have the opposite sign in red giant stars (Carrier et al. 2010; Bedding et al. 2010).

The problem of ridge identification in F stars was first encountered by Appourchaux et al. (2008) when analyzing *CoRoT* observations of HD 49933 and has been followed up by numerous authors (Benomar et al. 2009a, 2009b; Gruberbauer et al. 2009; Mosser & Appourchaux 2009; Roxburgh 2009; Kallinger et al. 2010). Two other F stars observed by *CoRoT* have presented the same problem, namely HD 181906 (García et al. 2009) and HD 181420 (Barban et al. 2009). A discussion of the issue was recently given by Bedding & Kjeldsen (2010), who proposed a solution to the problem that involves comparing two (or more) stars on a single échelle diagram after first scaling their frequencies.

Figure 7 shows the échelle diagram for Procyon overlaid with scaled frequencies for two stars observed by *CoRoT*, using the method described by Bedding & Kjeldsen (2010). The filled symbols are scaled oscillation frequencies for the G0 star HD 49385 observed by *CoRoT* (Deheuvels et al. 2010). The scaling involved multiplying all frequencies by a factor of 0.993 before plotting them, with this factor being chosen to align the symbols as closely as possible with the Procyon ridges. For this star, the *CoRoT* data gave an unambiguous mode identification, which is indicated by the symbol shapes. This confirms that the left-hand ridge of Procyon corresponds to modes with even l (Scenario B).

The open symbols in Figure 7 are oscillation frequencies for HD 49933 from the revised identification by Benomar et al. (2009b, Scenario B), after multiplying by a scaling factor of

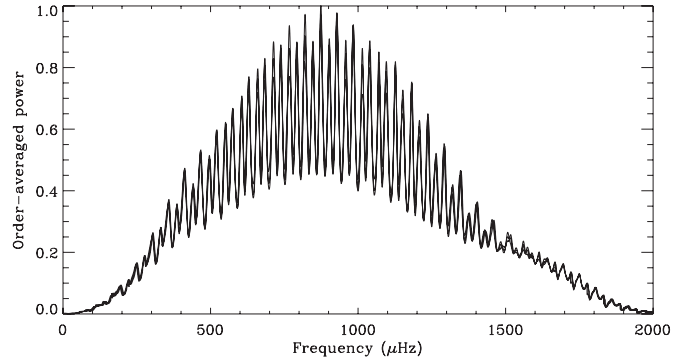


Figure 8. Order-averaged power spectrum (OAPS), where smoothing was done with a FWHM of 4.0 orders (see the text). The OAPS is plotted for three values of the large separations (54, 55, and $56 \mu\text{Hz}$), and we see that the positions of the maxima are not very sensitive to the value of $\Delta\nu$.

0.6565. The alignment with HD 49385 was already demonstrated by Bedding & Kjeldsen (2010). We show HD 49933 here for comparison and to draw attention to the different amounts of bending at the bottom of the right-hand ($l = 1$) ridge for the three stars. The *CoRoT* target that is most similar to Procyon is HD 170987 but unfortunately the signal-to-noise ratio (S/N) is too low to provide a clear identification of the ridges (Mathur et al. 2010).

The above considerations give us confidence that Scenario B in Procyon is the correct identification, and we now proceed on that basis.

5. FREQUENCIES OF THE RIDGE CENTROIDS

Our next step in the analysis was to measure the centroids of the two ridges in the échelle diagram. We first removed the strong peak at $446 \mu\text{Hz}$ (it was replaced by the mean noise level). We believe this to be a mixed mode and its extreme power means that it would significantly distort the result. We then smoothed the power spectrum to a resolution of $10 \mu\text{Hz}$ (FWHM). To further improve the visibility of the ridges, we also averaged across several orders, which corresponds to smoothing in the vertical direction in the échelle diagram (Bedding et al. 2004; Kjeldsen et al. 2005; Karoff 2007). That is, for a given value of $\Delta\nu$, we define the “order-averaged” power spectrum to be

$$\text{OAPS}(\nu, \Delta\nu) = \sum_{j=-4}^4 c_j \text{PS}(\nu + j\Delta\nu). \quad (6)$$

The coefficients c_j are chosen to give a smoothing with a FWHM of $k\Delta\nu$:

$$c_j = c_{-j} = \frac{1}{1 + (2j/k)^2}. \quad (7)$$

We show in Figure 8 the OAPS based on smoothing over 4 orders ($k = 4.0$), and so we used $(c_0, \dots, c_4) = (1, 0.8, 0.5, 0.31, 0.2)$. The OAPS is plotted for three values of the large separations (54, 55, and $56 \mu\text{Hz}$), and they are superimposed. The three curves are hardly distinguishable, and we see that the positions of the maxima are not sensitive to the value of $\Delta\nu$.

We next calculated a modified version of the OAPS in which the value at each frequency is the maximum value of the OAPS over a range of large separations ($53\text{--}57 \mu\text{Hz}$). This is basically the same as the comb response, as used previously by several authors (Kjeldsen et al. 1995; Mosser et al. 1998; Martić et al. 1999; Leccia et al. 2007). The maxima of this function define the centroids of the two ridges, which are shown in Figure 9.

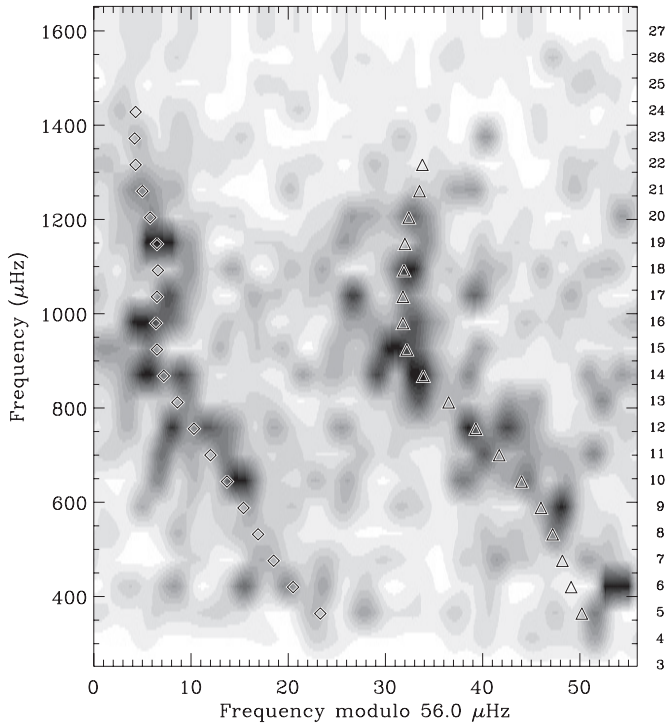


Figure 9. Centroids of the two ridges, as measured from the comb response. The grayscale shows the sidelobe-optimized power spectrum from which the peaks were calculated.

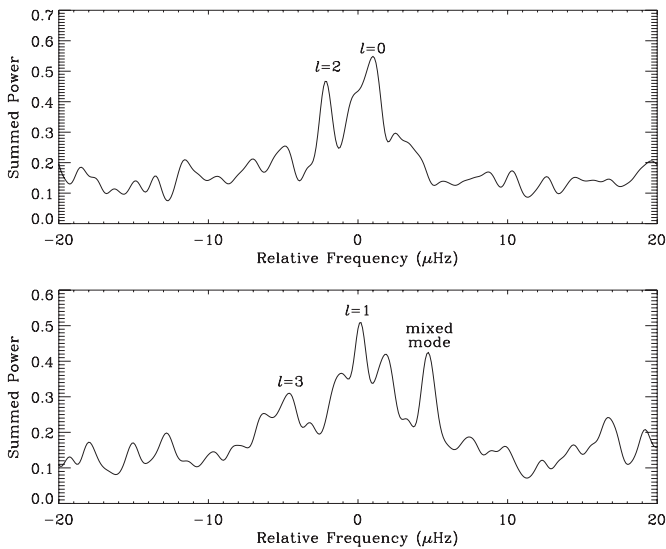


Figure 10. Power spectrum of Procyon collapsed along the ridges, over the full range of oscillations (18 orders). The upper panel shows the left-hand ridge, which we identify with modes having even degree, and the lower panel shows the right-hand ridge (odd degree). Note that the power spectrum was first smoothed slightly by convolving with a Gaussian with FWHM $0.6 \mu\text{Hz}$.

In Figure 10, we show the full power spectrum of Procyon (using sidelobe-optimized weights) collapsed along the ridges. This is similar to Figure 6 except that each order was shifted before the summation, so as to align the ridge peaks (symbols in Figure 9) and hence remove the curvature. This was done separately for both the even- and odd-degree ridges, as shown in the two panels of Figure 10. The collapsed spectrum clearly shows the power corresponding to $l = 0-3$, as well as the extra power from the mixed modes (for this figure, the peak at $446 \mu\text{Hz}$ has not been removed).

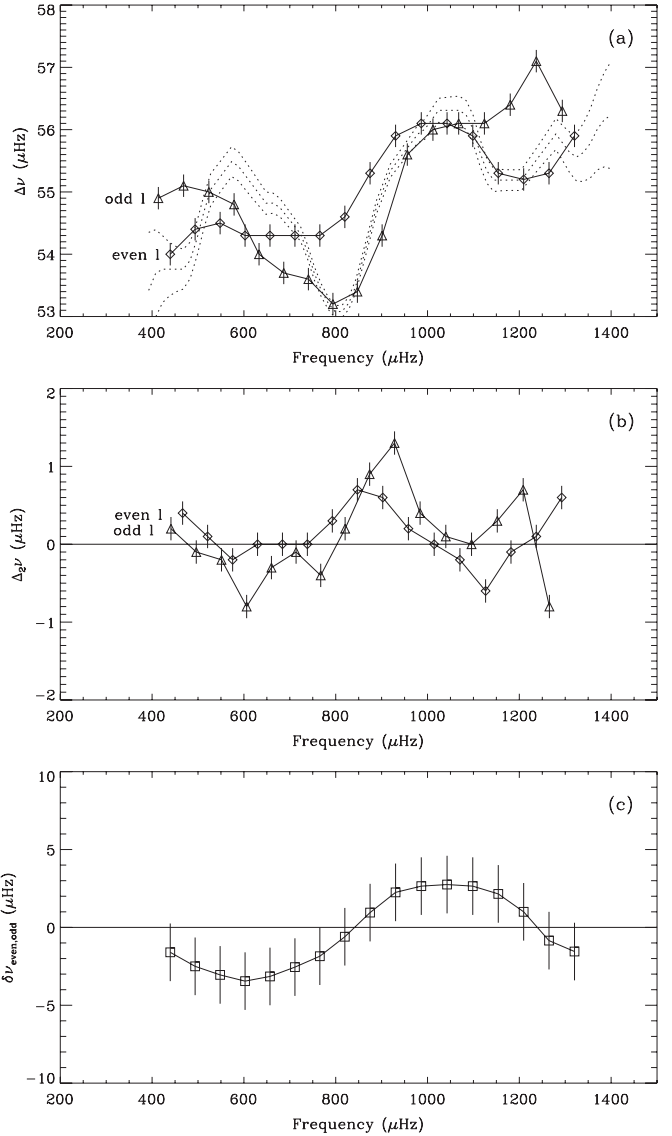


Figure 11. Symbols show the frequency separations in Procyon as a function of frequency, as measured from the ridge centroids: (a) large frequency separation, (b) second differences, and (c) small frequency separation. The dotted lines in panel *a* show the variation in $\Delta\nu$ (with $\pm 1\sigma$ range) calculated from the autocorrelation of the time series—see the text.

In Section 6 below, we use the ridges to guide our identification of the individual modes. First, however, we show that some asteroseismological inferences can be made solely from the ridges themselves. This is explained in more detail in Appendix B.

5.1. Large Separation of the Ridges

Figure 11(a) shows the variation with frequency of the large separation for each of the two ridges (diamonds and triangles). The smoothing across orders (Equation (6)) means that the ridge frequencies are correlated from one order to the next and so we used simulations to estimate uncertainties for the ridge centroids.

The oscillatory behavior of $\Delta\nu$ as a function of frequency seen in Figure 11(a) is presumably a signature of the helium ionization zone (e.g., Gough 1990). The oscillation is also seen in Figure 11(b), which shows the second differences for the two ridges, defined as follows (see Gough 1990; Ballot et al. 2004;

Houdek & Gough 2007):

$$\Delta_2 \nu_{n,\text{even}} = \nu_{n-1,\text{even}} - 2\nu_{n,\text{even}} + \nu_{n+1,\text{even}}, \quad (8)$$

$$\Delta_2 \nu_{n,\text{odd}} = \nu_{n-1,\text{odd}} - 2\nu_{n,\text{odd}} + \nu_{n+1,\text{odd}}. \quad (9)$$

The period of the oscillation is $\sim 500 \mu\text{Hz}$, which implies a glitch at an acoustic depth that is approximately twice the inverse of this value (Gough 1990; Houdek & Gough 2007), namely ~ 1000 s. To determine this more precisely, we calculated the power spectrum of the second differences for both the odd and even ridges, and measured the highest peak. We found the period of the oscillation in the second differences to be $508 \pm 18 \mu\text{Hz}$. Comparing this result with theoretical models will be the subject of a future paper.

The dotted lines in Figure 11(a) show the variation of $\Delta\nu$ with frequency calculated from the autocorrelation of the time series using the method of Mosser & Appourchaux (2009; see also Roxburgh & Vorontsov 2006). The mixed mode at $446 \mu\text{Hz}$ was first removed and the smoothing filter had FWHM equal to 3 times the mean large separation. We see general agreement with the values calculated from the ridge separations. Some of the differences presumably arise because the autocorrelation analysis of the time series averages the large separation over all degrees.

5.2. Small Separation of the Ridges

Using only the centroids of the ridges, we can measure a small separation that is useful for asteroseismology. By analogy with $\delta\nu_{01}$ (see Equation (3)), we define it as the amount by which the odd ridge is offset from the midpoint of the two adjacent even ridges, with a positive value corresponding to a leftward shift (as observed in the Sun). That is,

$$\delta\nu_{\text{even,odd}} = \frac{\nu_{n,\text{even}} + \nu_{n+1,\text{even}}}{2} - \nu_{n,\text{odd}}. \quad (10)$$

Figure 11(c) shows our measurements of this small separation.³⁵ It is related in a simple way to the conventional small separations $\delta\nu_{01}$, $\delta\nu_{02}$, and $\delta\nu_{13}$ (see Appendix B for details) and so, like them, it gives information about the sound speed in the core. Our measurements of this small separation can be compared with theoretical models using the equations in Appendix B (e.g., see Christensen-Dalsgaard & Houdek 2009).

6. FREQUENCIES OF INDIVIDUAL MODES

We have extracted oscillation frequencies from the time series using the standard procedure of iterative sine-wave fitting. Each step of the iteration involves finding the strongest peak in the sidelobe-optimized power spectrum and subtracting the corresponding sinusoid from the time series. Figure 12 shows the result. The two ridges are clearly visible but the finite mode lifetime causes many modes to be split into two or more peaks. We might also be tempted to propose that some of the multiple peaks are due to rotational splitting but, as shown in Appendix A, this is unlikely to be the case.

Deciding on a final list of mode frequencies with correct l identifications is somewhat subjective. To guide this process, we used the ridge centroids shown in Figure 9 as well as

³⁵ We could also define a small separation $\delta\nu_{\text{odd,even}}$ to be the amount by which the centroid of the even ridge is offset rightward from the midpoint of the adjacent odd ridges. This gives similar results.

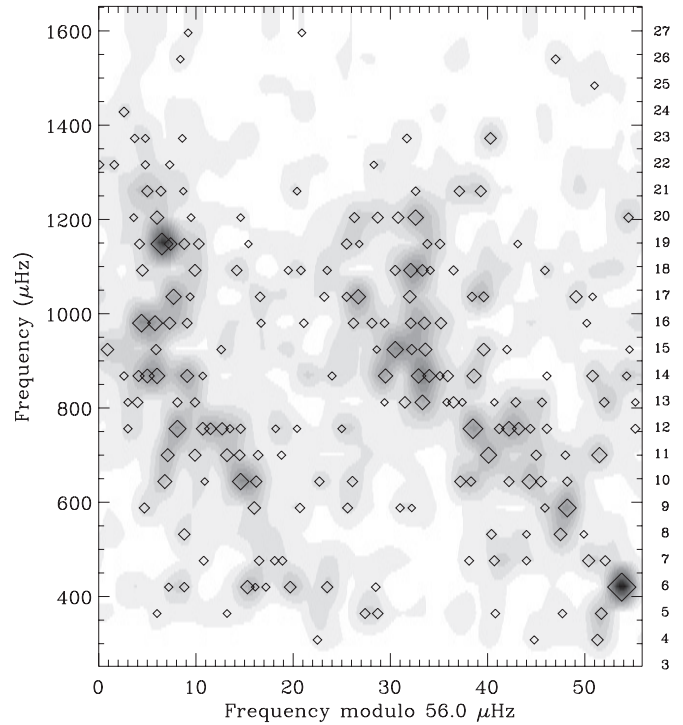


Figure 12. Peaks extracted from sidelobe-optimized power spectrum using iterative sine-wave fitting. Symbol size is proportional to amplitude (after the background noise has been subtracted). The grayscale shows the sidelobe-optimized power spectrum on which the fitting was performed, to guide the eye.

the small separations $\delta\nu_{02}$ and $\delta\nu_{13}$ from the collapsed power spectrum (see Figures 6 and 10). Each frequency extracted using iterative sine-wave fitting that lay close to a ridge was assigned an l value and multiple peaks from the same mode were averaged. The final mode frequencies are listed in Table 1, while peaks with $S/N \geq 3.5$ that we have not identified are listed in Table 2. Figures 13 and 14 show these peaks overlaid on the sidelobe-optimized power spectrum. Figure 15 shows the three small separations (Equations (2)–(4)) as calculated from the frequencies listed in Table 1. The uncertainties in the mode frequencies are shown in parentheses in Table 1. These depend on the S/N of the peak and were calibrated using simulations (e.g., see Bedding et al. 2007).

The entries in Table 2 are mostly false peaks due to noise and to residuals from the iterative sine-wave fitting, but may include some genuine modes. To check whether some of them may be daily aliases of each other or of genuine modes, we calculated the differences of all combinations of frequencies in Tables 1 and 2. The histogram of these pairwise differences was flat in the vicinity of $11.6 \mu\text{Hz}$ and showed no excess, confirming that daily aliases do not contribute significantly to the list of frequencies in the tables.

We also checked whether the number peaks in Table 2 agrees with expectations. We did this by analyzing a simulated time series that matched the observations in terms of oscillation properties (frequencies, amplitudes, and mode lifetimes), noise level, window function, and distribution of weights. We extracted peaks from the simulated power spectrum using iterative sine-wave fitting, as before, and found the number of “extra” peaks (not coinciding with the oscillation ridges) to be similar to that seen in Figure 12. Finally, we remark that the peak at $408 \mu\text{Hz}$ is a candidate for a mixed mode with $l = 1$, given that

Table 1
Oscillation Frequencies in Procyon (in μHz)

Order	$l = 0$	$l = 1$	$l = 2$	$l = 3$
4	...	331.3 (0.8)
5	...	387.7 (0.7)
6	415.5 (0.8)	445.8 (0.3)	411.7 (0.7)	...
7	466.5 (1.0)	498.6 (0.7)	464.5 (0.9)	488.7 (0.9)
8	...	551.5 (0.7)	...	544.4 (0.9)
9	576.0 (0.7)	608.2 (0.5)
10	630.7 (0.6)	660.6 (0.7)	627.0 (1.1)	653.6 (0.8)
11	685.6 (0.7)	712.1 (0.5)	681.9 (0.7)	...
12	739.2 (0.7)	766.5 (0.5)	736.2 (0.5)	...
13	793.7 (0.9)	817.2 (0.6)	792.3 (0.9)	...
14	849.1 (0.7)	873.5 (0.6)	845.4 (0.6)	869.5 (0.6)
15	901.9 (0.8)	929.2 (0.7)	...	926.6 (0.6)
16	957.8 (0.6)	985.3 (0.7)	956.4 (0.5)	980.4 (0.9)
17	1015.8 (0.6)	1040.0 (0.7)	...	1034.5 (0.7)
18	1073.9 (0.7)	1096.5 (0.7)	1068.5 (0.7)	...
19	1126.7 (0.5)	1154.6 (0.9)	1124.3 (0.9)	...
20	1182.0 (0.7)	1208.5 (0.6)	1179.9 (1.0)	...
21	1238.3 (0.9)	1264.6 (1.0)	1237.0 (0.8)	...
22	1295.2 (1.0)	...	1292.8 (1.0)	...
23	1352.6 (1.1)	1375.7 (1.0)	1348.2 (1.0)	...

it lies in the same order as the previously identified mixed mode at 446 μHz (note that we expect one extra $l = 1$ mode to occur at an avoided crossing).

The modes listed in Table 1 span 20 radial orders and more than a factor of 4 in frequency. This range is similar to that obtained from long-term studies of the Sun (e.g., Broomhall et al. 2009) and is unprecedented in asteroseismology. It was made possible by the unusually broad range of excited modes in Procyon and the high S/N of our data. Since the stellar background at low frequencies in intensity measurements is expected to be much higher than for velocity measurements, it seems unlikely that even the best data from the *Kepler* Mission will return such a wide range of frequencies in a single target.

7. MODE LIFETIMES

As discussed in Section 2, if the time series is sufficiently long then damping causes each mode in the power spectrum to be split into a series of peaks under a Lorentzian envelope having FWHM $\Gamma = 1/(\pi\tau)$, where τ is the mode lifetime. Our observations of Procyon are not long enough to resolve the modes into clear Lorentzians, and instead we see each mode as a small number of peaks (sometimes one). Furthermore, the centroid of these peaks may be offset from the position of the true mode, as illustrated in Figure 1 of Anderson et al. (1990). This last feature allows one to use the scatter of the extracted frequencies about smooth ridges in the échelle diagram, calibrated using simulations, to estimate the mode lifetime (Kjeldsen et al. 2005; Bedding et al. 2007). That method cannot be applied to Procyon because the $l = 0$ and $l = 2$ ridges are not well resolved and the $l = 1$ ridge is affected by mixed modes.

Rather than looking at frequency shifts, we have estimated the mode lifetime from the variations in mode amplitudes (again calibrated using simulations). This method is less precise but has the advantage of being independent of the mode identifications (e.g., Leccia et al. 2007; Carrier et al. 2007; Bedding et al. 2007). In Paper I, we calculated the smoothed amplitude curve for Procyon in 10 two-day segments and used the fluctuations about the mean to make a rough estimate of the mode lifetime:

Table 2
Unidentified Peaks with S/N ≥ 3.5

ν (μHz)	S/N
407.6 (0.8)	3.5
512.8 (0.8)	3.6
622.8 (0.6)	4.3
679.1 (0.7)	4.0
723.5 (0.6)	4.7
770.5 (0.7)	4.1
878.5 (0.6)	4.4
890.8 (0.7)	3.6
935.6 (0.7)	3.9
1057.2 (0.7)	3.7
1384.3 (0.7)	3.6

$\tau = 1.5^{+1.9}_{-0.8}$ days. We have attempted to improve on that estimate by considering the amplitude fluctuations of individual modes, as has been done for the Sun (e.g., Toutain & Fröhlich 1992; Baudin et al. 1996; Chang & Gough 1998), but were not able to produce well-calibrated results for Procyon.

Instead, we have measured the “peakiness” of the power spectrum (see Bedding et al. 2007) by calculating the ratio between the square of the mean amplitude of the 15 highest peaks in the range 500–1300 μHz (found by iterative sine-wave fitting) and the mean power in the same frequency range. The value for this ratio from our observations of Procyon is 6.9. We made a large number of simulations (3600) having a range of mode lifetimes and with the observed frequency spectrum, noise level, window function, and weights. Comparing the simulations with the observations led to a mode lifetime for Procyon of $1.29^{+0.55}_{-0.49}$ days.

This agrees with the value found in Paper I but is more precise, confirming that modes in Procyon are significantly more short-lived than those of the Sun. As discussed in Section 2, the dominant modes in the Sun have lifetimes of 2–4 days (e.g., Chaplin et al. 1997). The tendency for hotter stars to have shorter mode lifetimes has recently been discussed by Chaplin et al. (2009).

8. FITTING TO THE POWER SPECTRUM

Extracting mode parameters by fitting directly to the power spectrum is widely used in helioseismology, where the time series extends continuously for months or even years, and so the individual modes are well resolved (e.g., Anderson et al. 1990). Mode fitting has not been applied to ground-based observations of solar-type oscillations because these data typically have shorter durations and significant gaps. Global fitting has been carried out on spacecraft data, beginning with the 50-day time series of α Cen A taken with the *WIRE* spacecraft (Fletcher et al. 2006) and the 60-day light curve of HD 49933 from *CoRoT* (Appourchaux et al. 2008). Our observations of Procyon are much shorter than either of these cases but, given the quality of the data and the spectral window, we considered it worthwhile to attempt a fit.

Global fits to the Procyon power spectrum were made by several of us. Here, we present results from a fit using a Bayesian approach (e.g., Gregory 2005), which allowed us to include in a straightforward way our prior knowledge of the oscillation properties. The parameters to be extracted were the frequencies, heights, and linewidths of the modes. To obtain the marginal probability distributions of these parameters

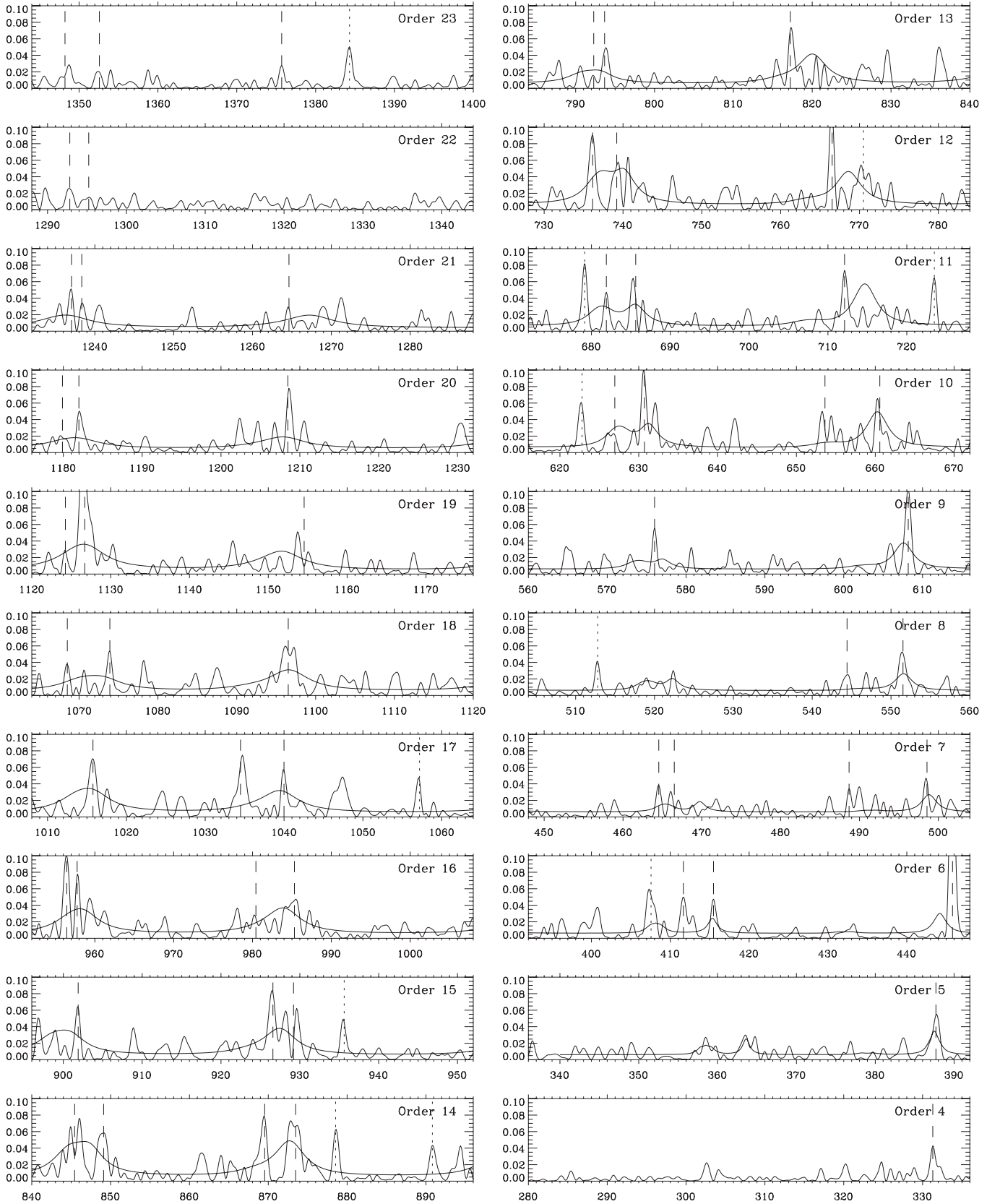


Figure 13. Power spectrum of Procyon at full resolution, with the orders in each column arranged from top to bottom, for easy comparison with the échelle diagrams. Vertical dashed lines show the mode frequencies listed in Table 1 and dotted lines show the peaks that have not been identified, as listed in Table 2. The smooth curve shows the global fit to the power spectrum for Scenario B (see Section 8).

and their associated uncertainties, we employed an Automated Parallel Tempering Markov Chain Monte Carlo (APT MCMC)

algorithm. It implements the Metropolis–Hastings sampler by performing a random walk in parameter space while drawing

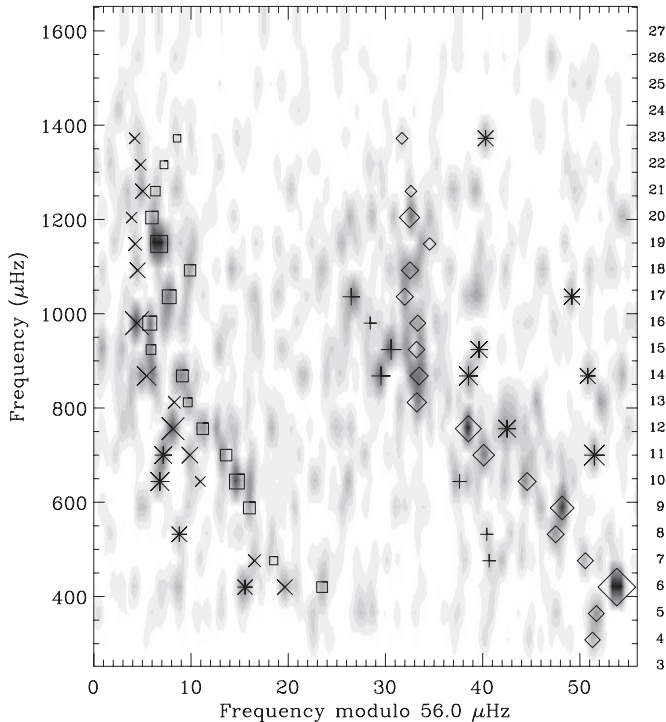


Figure 14. Power spectrum of Procyon overlaid with mode frequencies listed in Table 1. Symbols indicate angular degree (squares: $l = 0$; diamonds: $l = 1$; crosses: $l = 2$; pluses: $l = 3$). Asterisks show the peaks that have not been identified, as listed in Table 2.

samples from the posterior distribution (Gregory 2005). Further details of our implementation of the algorithm will be given elsewhere (T. L. Campante et al. 2010, in preparation).

The details of the fitting are as follows.

1. The fitting was performed over 17 orders (5–21) using the sidelobe-optimized power spectrum. In each order, we fitted modes with $l = 0, 1$, and 2, with each individual profile being described by a symmetric Lorentzian with FWHM Γ and height H . The mode frequencies were constrained to lie close to the ridges and to have only small jumps from one order to the next (a Gaussian prior with $\sigma = 3 \mu\text{Hz}$). The S/Ns of modes with $l = 3$ were too low to permit a fit. In order to take their power into account, we included them in the model with their frequencies fixed by the asymptotic relation (Equation (1)).
2. The data are not good enough to provide a useful estimate of the linewidth of every mode, or even of every order. Therefore, the linewidth was parameterized as a linear function of frequency, defined by two parameters Γ_{600} and Γ_{1200} , which are the values at 600 and 1200 μHz . These parameters were determined by the fit, in which both were assigned a uniform prior in the range 0–10 μHz .
3. The height of each mode is related to the linewidth and amplitude according to (Chaplin et al. 2005):

$$H = \frac{2A^2}{\pi\Gamma}. \quad (11)$$

The amplitudes A of the modes were determined as follows. For the radial modes ($l = 0$), we used the smoothed amplitude curve measured from our observations, as shown in Figure 10 of Paper I. The amplitudes of the non-radial modes ($l = 1$ –3) were then calculated from the radial

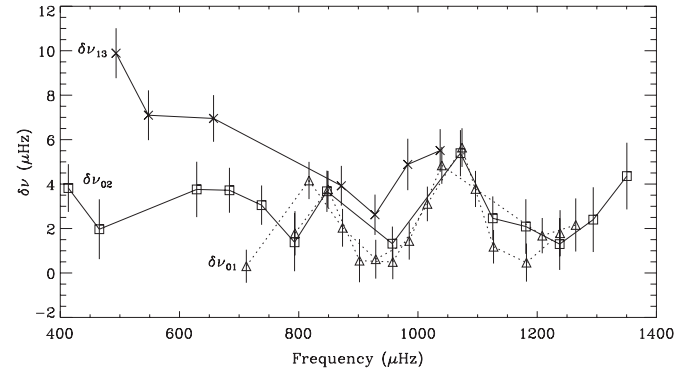


Figure 15. Small frequency separations in Procyon, as measured from the mode frequencies listed in Table 1.

Table 3
Frequencies from Global Fit Using Scenario B (in μHz , with $-/+$ Uncertainties)

Order	$l = 0$	$l = 1$	$l = 2$
5	363.6 (0.8/0.9)	387.5 (0.6/0.6)	358.5 (1.3/1.2)
6	415.3 (3.3/1.0)	...	408.1 (1.0/3.7)
7	469.7 (1.6/2.1)	498.8 (0.7/0.8)	465.3 (1.1/1.3)
8	522.3 (1.4/1.4)	551.6 (0.8/0.7)	519.0 (1.5/1.6)
9	577.0 (1.6/2.5)	607.6 (0.6/0.7)	573.9 (2.2/2.8)
10	631.3 (0.8/0.8)	660.3 (1.0/1.3)	627.4 (2.1/2.8)
11	685.6 (1.2/1.6)	714.7 (1.4/1.2)	681.2 (2.3/1.9)
12	740.1 (1.6/1.7)	768.6 (0.9/1.0)	737.0 (1.5/1.7)
13	793.2 (1.3/1.7)	820.0 (1.7/1.2)	790.9 (2.0/1.9)
14	847.3 (1.2/1.4)	872.7 (1.1/0.9)	844.7 (1.7/1.5)
15	901.0 (1.8/1.7)	927.5 (0.8/0.8)	898.6 (2.1/2.1)
16	958.7 (1.4/1.1)	983.9 (1.0/1.3)	957.2 (1.0/1.3)
17	1015.9 (1.5/1.8)	1039.5 (1.6/1.7)	1014.0 (1.8/2.4)
18	1073.2 (1.5/2.2)	1096.6 (1.1/1.0)	1070.3 (2.2/2.3)
19	1127.2 (1.0/1.3)	1151.8 (1.4/1.4)	1125.9 (1.3/1.4)
20	1182.3 (1.5/1.4)	1207.9 (1.4/1.1)	1180.5 (1.6/1.6)
21	1236.9 (1.7/1.6)	1267.4 (1.7/1.5)	1235.5 (2.0/1.7)

modes using the ratios given in Table 1 of Kjeldsen et al. (2008a), namely, $S_0 : S_1 : S_2 : S_3 = 1.00 : 1.35 : 1.02 : 0.47$.

4. The background was fitted as a flat function.
5. We calculated the rotationally split profiles of the non-radial modes using the description given by Gizon & Solanki (2003). The inclination angle of the rotation axis was fixed at 31° , which is the inclination of the binary orbit (Girard et al. 2000) and, as discussed in Paper I (Section 4.1), is consistent with the rotational modulation of the velocity curve. The rotational splitting was fixed at $0.7 \mu\text{Hz}$, which was chosen to match the observed value of $v \sin i = 3.16 \text{ km s}^{-1}$ (Allende Prieto et al. 2002), given the known radius of the star. As discussed in Appendix A, choosing different values for the inclination (and hence the splitting) does not affect the mode profile, assuming reasonable values of the linewidth.

We carried out the global fit using both scenarios discussed in Section 4. The fit for Scenario B is shown as the smooth curve in Figure 13 and the fitted frequencies are given in Table 3. Note that the mixed mode at 446 μHz was not properly fitted because it lies too far from the ridge (see point 1 above). To check the agreement with the results discussed in Section 6, we examined the differences between the frequencies in Tables 1 and 3. We found a reduced χ^2 of 0.74, which indicates good agreement. A

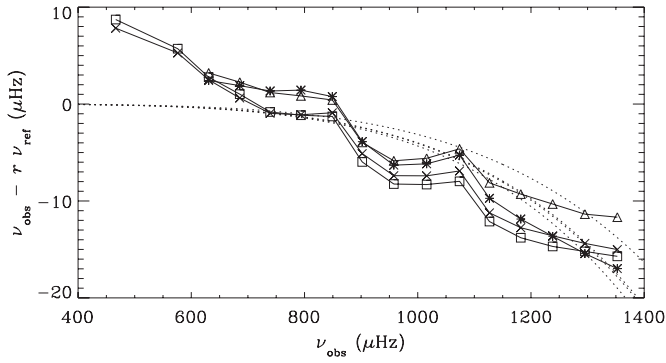


Figure 16. Difference between observed frequencies of radial modes in Procyon and those of scaled models. The symbols indicate different models, as follows: squares from Chaboyer et al. (1999, Table 2), crosses from Di Mauro & Christensen-Dalsgaard (2001), asterisks from Kervella et al. (2004, Table 4), and triangles from Eggenberger et al. (2005, model M1a). In each case, the dotted curve shows the correction calculated using Equation (4) of Kjeldsen et al. (2008b).

value less than 1 is not surprising given that both methods were constrained to find modes close to the ridges.

The fitted linewidths (assumed to be a linear function of frequency, as described above) gave mode lifetimes of 1.5 ± 0.4 days at $600 \mu\text{Hz}$ and 0.6 ± 0.3 days at $1200 \mu\text{Hz}$. These agree with the single value of $1.29^{+0.55}_{-0.49}$ days found above (Section 7), and indicate that the lifetime increases toward lower frequencies, as is the case for the Sun and for the F-type *CoRoT* targets HD 49933 (Benomar et al. 2009b) and HD 181420 (Barban et al. 2009).

We also carried out the global fit using Scenario A. We found through Bayesian model selection that Scenario A was statistically favored over Scenario B by a factor of 10:1. This factor classifies as “significant” on the scale of Jeffreys (1961; see Table 1 of Liddle 2009). On the same scale, posterior odds of at least $\sim 13:1$ are required for a classification of “strong to very strong,” and “decisive” requires at least $\sim 150:1$. In our Bayesian fit to Procyon, the odds ratio in favor of Scenario A did not exceed 13:1, even when different sets of priors were imposed.

In light of the strong arguments given in Section 4 in favor of Scenario B, we do not consider the result from Bayesian model selection to be sufficiently compelling to cause us to reverse our identification. Of course, it is possible that Scenario A is correct and, for completeness, we show these fitted frequencies in Table 4. The fit using Scenario A gave mode lifetimes of 0.9 ± 0.2 days at $600 \mu\text{Hz}$ and 1.0 ± 0.3 days at $1200 \mu\text{Hz}$.

9. PRELIMINARY COMPARISON WITH MODELS

A detailed comparison of the observed frequencies of Procyon with theoretical models is beyond the scope of this paper, but we will make some preliminary comments on the systematic offset between the two. It is well established that incorrect modeling of the surface layers of the Sun is responsible for discrepancies between the observed and calculated oscillation frequencies (Christensen-Dalsgaard et al. 1988; Dziembowski et al. 1988; Rosenthal et al. 1999; Li et al. 2002).

To address this problem for other stars, Kjeldsen et al. (2008b) proposed an empirical correction to be applied to model frequencies that takes advantage of the fact that the offset between observations and models is independent of l and goes to zero with decreasing frequency. They measured the offset for the Sun to be a power law with exponent $b = 4.9$ and applied

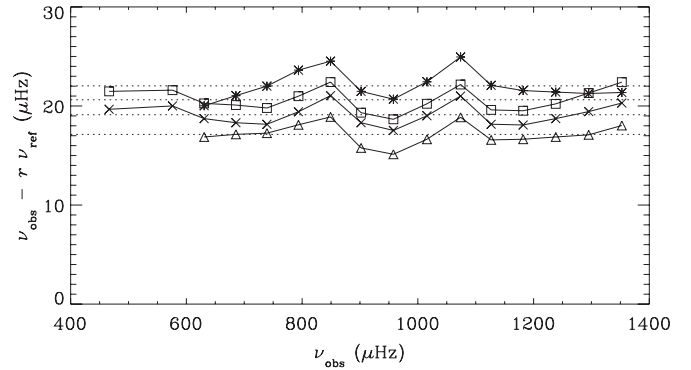


Figure 17. Same as Figure 16, but with a constant near-surface correction ($b = 0$).

Table 4
Frequencies from Global Fit Using Scenario A (in μHz , with $-/+$ Uncertainties)

Order	$l = 0$	$l = 1$	$l = 2$
5	387.7 (1.9/1.8)	361.9 (1.8/2.0)	385.1 (1.9/2.6)
6	...	412.5 (1.7/2.3)	439.3 (2.6/2.6)
7	498.7 (1.1/1.6)	467.6 (1.4/1.3)	493.2 (2.6/2.0)
8	552.2 (1.5/1.5)	520.7 (1.2/1.3)	549.3 (2.2/2.0)
9	607.8 (1.0/0.9)	576.2 (1.1/1.4)	605.4 (2.2/2.3)
10	661.3 (1.3/1.5)	631.1 (0.7/0.8)	657.1 (1.7/1.6)
11	716.8 (1.3/1.7)	684.7 (1.2/1.2)	712.6 (1.2/1.2)
12	769.9 (1.2/1.3)	739.1 (1.1/1.2)	766.6 (1.4/1.4)
13	822.7 (1.9/2.7)	792.9 (1.3/1.3)	817.8 (1.3/1.4)
14	874.5 (1.3/1.3)	846.4 (0.9/0.8)	869.9 (1.6/1.3)
15	928.8 (1.2/1.2)	900.0 (1.3/1.4)	925.9 (1.3/1.1)
16	985.1 (1.0/1.1)	958.2 (0.8/0.8)	980.9 (1.9/1.6)
17	1043.4 (2.8/2.8)	1015.7 (1.0/0.9)	1035.2 (1.0/0.8)
18	1097.6 (1.5/0.9)	1072.5 (1.1/1.2)	1091.8 (3.7/4.2)
19	1153.7 (0.9/0.8)	1126.9 (0.5/0.6)	1146.8 (1.3/1.0)
20	1209.1 (0.8/0.9)	1181.8 (1.0/0.9)	1204.8 (1.3/1.4)
21	1269.2 (1.0/1.1)	1237.1 (0.9/0.9)	1264.8 (1.5/1.5)

this correction to the radial modes of other stars, finding very good results that allowed them to estimate mean stellar densities very accurately (better than 0.5%).

We have applied this method to Procyon, comparing our observed frequencies for the radial modes with various published models to determine the scaling factor r and the offset (see Kjeldsen et al. 2008b for details of the method). The results are shown in Figure 16. Interestingly, the offset between the observations and scaled models does not go to zero with decreasing frequency. This contrasts with the G- and K-type stars investigated by Kjeldsen et al. (2008b), namely, the Sun, α Cen A and B, and β Hyi.

The method of Kjeldsen et al. (2008b) assumes the correction to be applied to the models to have the same form as in the Sun, namely, a power law with an exponent of $b = 4.9$. The fit in Figure 16 is poor and is not improved by modest adjustments to b . Instead, the results seem to imply an offset that is constant. Setting $b = 0$ and repeating the calculations produce the results shown in Figure 17, where we indeed see a roughly constant offset between the models and the observations of about $20 \mu\text{Hz}$.

As a check, we can consider the density implied for Procyon. The stellar radius can be calculated from the interferometric radius and the parallax. The angular diameter of 5.404 ± 0.031 mas (Aufdenberg et al. 2005, their Table 7) and the revised *Hipparcos* parallax of 285.93 ± 0.88 mas (van Leeuwen 2007) gives a radius of $2.041 \pm 0.015 R_{\odot}$.

Procyon is in a binary system (the secondary is a white dwarf), allowing the mass to be determined from astrometry. Girard et al. (2000) found a value of $1.497 \pm 0.037 M_{\odot}$, while Gatewood & Han (2006) found $1.431 \pm 0.034 M_{\odot}$ (see Guenther et al. 2008 for further discussion).

The density obtained using the fits shown in Figure 16 is in the range $0.255\text{--}0.258 \text{ g cm}^{-3}$. Combining with the radius implies a mass in the range $1.54\text{--}1.56 M_{\odot}$. The density obtained using the fits shown in Figure 17 is in the range $0.242\text{--}0.244 \text{ g cm}^{-3}$, implying a mass of $1.46\text{--}1.48 M_{\odot}$. The latter case seems to be in much better agreement with the astrometrically determined mass, lending some support to the idea that the offset is constant.

We can also consider the possibility that our mode identification is wrong and that Scenario A is the correct one (see Sections 4 and 8). With this reversed identification, the radial modes in Procyon are those in Table 1 listed as having $l = 1$. Assuming these to be radial modes, the offset between them and the model frequencies is again constant, as we would expect, but this time with a mean value close to zero. The implied density for Procyon is again consistent with the observed mass and radius.

The preceding discussion makes it clear that the correction that needs to be applied to models of Procyon is very different from that for the Sun and other cool stars, regardless of whether Scenario B or A is correct. In particular, the substantial nearly constant offset implied by Figure 16 would indicate errors in the modeling extending well beyond the near-surface layers. We also note that in terms of the asymptotic expression (Equation (1)) a constant offset would imply an error in the calculation of ϵ .

10. CONCLUSION

We have analyzed results from a multi-site campaign on Procyon that obtained high-precision velocity observations over more than three weeks (Paper I). We developed a new method for adjusting the weights in the time series that allowed us to minimize the sidelobes in the power spectrum that arise from diurnal gaps and so to construct an échelle diagram that shows two clear ridges of power. To identify the odd and even ridges, we summed the power across several orders. We found structures characteristic of $l = 0$ and 2 in one ridge and $l = 1$ and 3 in the other. This identification was confirmed by comparing our Procyon data in a scaled échelle diagram (Bedding & Kjeldsen 2010) with other stars for which the ridge identification is known. We showed that the frequencies of the ridge centroids and their large and small separations are easily measured and are useful diagnostics for asteroseismology. In particular, an oscillation in the large separation appears to indicate a glitch in the sound-speed profile at an acoustic depth of ~ 1000 s.

We identify a strong narrow peak at $446 \mu\text{Hz}$, which falls slightly away from the $l = 1$ ridge, as a mixed mode. In Table 1, we give frequencies, extracted using iterative sine-wave fitting, for 55 modes with angular degrees l of 0–3. These cover 20 radial orders and a factor of more than 4 in frequency, which reflects the broad range of excited modes in Procyon and the high S/N of our data, especially at low frequencies. Intensity measurements will suffer from a much higher stellar background at low frequencies, making it unlikely that even the best data from the *Kepler* Mission will yield the wide range of frequencies found here. This is a strong argument in favor of continuing efforts toward ground-based Doppler studies, such as the Stellar Observations Network Group (SONG; Grundahl et al. 2008), which is currently under

construction, and the proposed Antarctic instrument Seismic Interferometer to Measure Oscillations in the Interior of Stars (SIAMOIS; Mosser et al. 2008).

We estimated the mean lifetime of the modes by comparing the “peakiness” of the power spectrum with simulations and found a value of $1.29^{+0.55}_{-0.49}$ days, significantly below that of the Sun. A global fit to the power spectrum using Bayesian methods confirmed this result and provided evidence that the lifetime increases toward lower frequencies. It also casts some doubt on the mode identifications. We still favor the identification discussed above, but leave open the possibility that this may need to be reversed. Finally, comparing the observed frequencies of radial modes in Procyon with published theoretical models showed an offset that appears to be constant with frequency, making it very different from that seen in the Sun and other cool stars. Detailed comparisons of our results with theoretical models will be carried out in future papers.

We would be happy to make the data presented in this paper available on request.

This work was supported financially by the Australian Research Council, the Danish Natural Science Research Council, the Swiss National Science Foundation, NSF grant AST-9988087 (R.P.B.), and by SUN Microsystems. We gratefully acknowledge support from the European Helio- and Asteroseismology Network (HELAS), a major international collaboration funded by the European Commission’s Sixth Framework Programme.

APPENDIX A

ROTATIONAL SPLITTING

We expect non-radial modes to be split due to the rotation of the star. The rotation period of Procyon is not known, although slow variations in our velocity observations (Paper I) indicated a value of either 10.3 days or twice that value. The projected rotational velocity has been measured spectroscopically. Allende Prieto et al. (2002) determined a value of $v \sin i = 3.16 \pm 0.50 \text{ km s}^{-1}$, although they note that the actual value may be lower by about 0.5 km s^{-1} .

Gizon & Solanki (2003) have studied the effect of rotation on the profiles of solar-like oscillations as a function of inclination and mode lifetime (see also Ballot et al. 2006). We have repeated their calculations for our observations of Procyon (with sidelobe-optimized weights). The results are shown in Figure 18, which shows the effects of rotational splitting, inclination angle, and mode lifetime on the theoretical profile of the modes.³⁶ Note that the calculations do not include the stochastic nature of the excitation and so the function shown here should properly be called the expectation value of the power spectrum, also known as the *limit spectrum*. Figure 18 is similar to Figure 2 of Gizon & Solanki (2003) except that instead of fixing the rotation period, we have fixed $v \sin i$ to be the measured value. For $l = 0$, the profile does not depend on the inclination angle, while for $l = 1, 2,$ and 3 the solid and dashed lines show calculations for $i = 30^\circ$ ($P_{\text{rot}} = 16.4$ days) and $i = 80^\circ$ ($P_{\text{rot}} = 32.3$ days), respectively. In each panel, results are shown for three values of the mode lifetime: 1.5 days (top curve), 3 days (middle curve), and infinite (bottom curve). For each mode lifetime, the curves for different i and l are all normalized to have the same area.

³⁶ Note that we have made the quite reasonable assumption that the internal rotation has a similar period to the surface rotation.

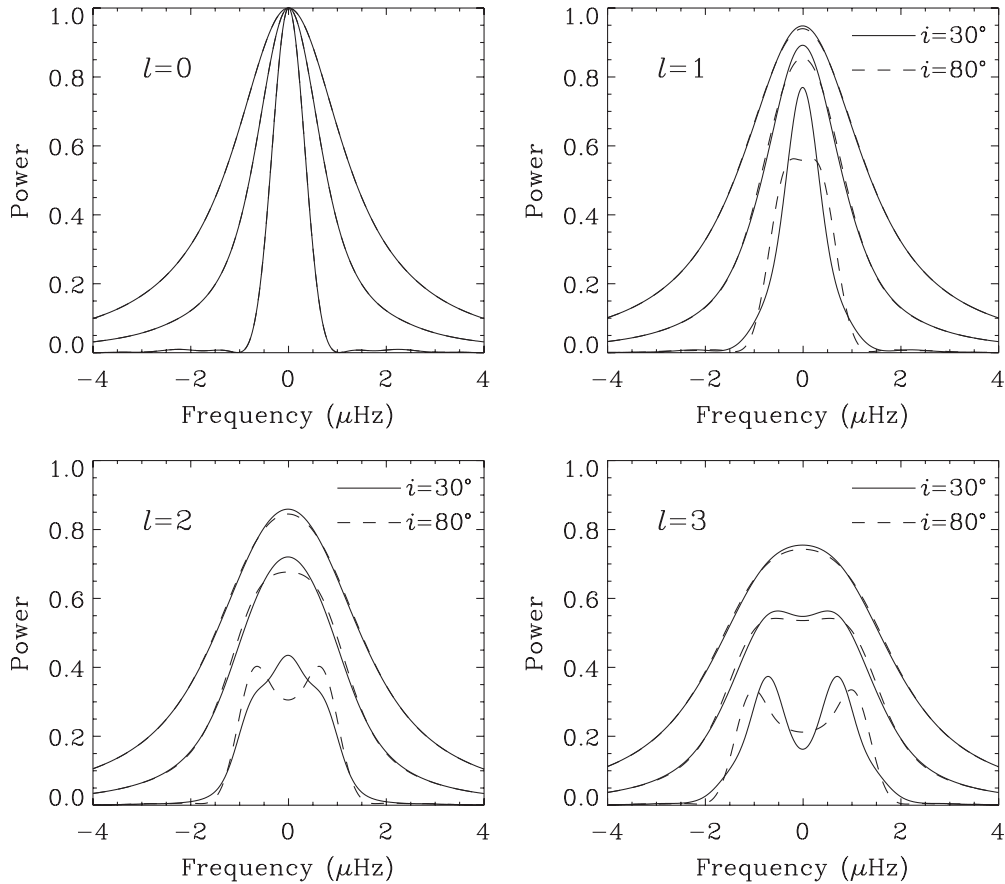


Figure 18. Theoretical line profiles showing rotational splitting for different mode degrees, similar to Figure 2 of Gizon & Solanki (2003) but here using a fixed value of $v \sin i$, namely 3.16 km s^{-1} , as measured for Procyon (Allende Prieto et al. 2002). For $l = 0$, the profile does not depend on the inclination angle, while for $l = 1, 2,$ and 3 the solid and dashed lines show calculations for $i = 30^\circ$ ($P_{\text{rot}} = 16.4$ days) and $i = 80^\circ$ ($P_{\text{rot}} = 32.3$ days), respectively. In each panel, results are shown for three values of the mode lifetime: 1.5 days (top curve), 3 days (middle curve), and infinite (bottom curve). For each mode lifetime, the curves for different i and l are all normalized to have the same area.

We see from Figure 18 that for a fixed $v \sin i$, the width of the profile stays roughly constant as a function of inclination. If the rotation axis of the star happens to be in the plane of the sky ($i = 90^\circ$), then the rotation period is too low to produce a measurable splitting. At the other extreme, if the inclination is small (so that the rotation is close to pole-on), then the rotational splitting will be large but most of the power will be in the central peak ($m = 0$). Either way, once the profile has been broadened by the mode lifetime, the splitting will be unobservable.

We conclude that for realistic values of the mode lifetime, our observations are not long enough to detect rotational splitting in Procyon. The line profiles are broadened by rotation, but it is not possible to disentangle the rotation rate from the inclination angle. Rotational splitting is not measurable in Procyon, except perhaps with an extremely long data set. The detection of rotational splitting requires choosing a star with a larger $v \sin i$ or a longer mode lifetime, or both.

APPENDIX B

RELATING RIDGE CENTROIDS TO MODE FREQUENCIES

As discussed in Section 5, the frequencies of the ridge centroids are useful for asteroseismology in cases where it is difficult to resolve the ridges into their component modes. In this appendix, we relate the frequencies of the ridge centroids to those of the underlying modes, which allows us to express the small separation of the ridges (Equation (10)) in terms of

the conventional small separations ($\delta\nu_{01}$, $\delta\nu_{02}$, and $\delta\nu_{13}$). These relationships will allow the observations to be compared with theoretical models.

The ridge centroids depend on the relative contributions of modes with $l = 0, 1, 2,$ and 3 . The power in the even ridge is approximately equally divided between $l = 0$ and $l = 2$, while the odd ridge is dominated by $l = 1$ but with some contribution from $l = 3$. The exact ratios depend on the observing method, as discussed by Kjeldsen et al. (2008a). For velocity measurements, such as those presented in this paper for Procyon, the amplitude ratios given by Kjeldsen et al. (2008a, their Table 1) yield the following expressions for the centroids in power:

$$\nu_{n,\text{even}}^{\text{vel}} = 0.49\nu_{n,0} + 0.51\nu_{n-1,2}, \quad (\text{B1})$$

$$\nu_{n,\text{odd}}^{\text{vel}} = 0.89\nu_{n,1} + 0.11\nu_{n-1,3}, \quad (\text{B2})$$

where the superscript indicates these apply to velocity measurements.

For photometric measurements, such as those currently being obtained with the *CoRoT* and *Kepler* Missions, the relative contributions from the various l values are different. Table 1 of Kjeldsen et al. (2008a) gives response factors for intensity measurements in the three VIRGO passbands, namely, 402, 500, and 862 nm. For *CoRoT* and *Kepler*, it is appropriate to use a central wavelength of 650 nm. Using the same method as Kjeldsen et al. (2008a), we find the ratios (in amplitude) for this case to be $S_0 : S_1 : S_2 : S_3 = 1.00 : 1.23 : 0.71 : 0.14$. The

ridge centroids measured from such data would then be

$$\nu_{n,\text{even}}^{650} = 0.66\nu_{n,0} + 0.34\nu_{n-1,2}, \quad (\text{B3})$$

$$\nu_{n,\text{odd}}^{650} = 0.99\nu_{n,1} + 0.01\nu_{n-1,3}. \quad (\text{B4})$$

We can express the new small separation of the ridge centroids (Equation (10)) in terms of the conventional ones. For velocity, we have

$$\delta\nu_{\text{even,odd}}^{\text{vel}} = \delta\nu_{01} - 0.51\delta\nu_{02} + 0.11\delta\nu_{13}; \quad (\text{B5})$$

and for photometry, we have

$$\delta\nu_{\text{even,odd}}^{650} = \delta\nu_{01} - 0.34\delta\nu_{02} + 0.01\delta\nu_{13}. \quad (\text{B6})$$

Finally, we can express these in terms of D_0 under the assumption that the asymptotic relation (Equation (1)) holds exactly, although in fact this is not likely to be the case:

$$\delta\nu_{\text{even,odd}}^{\text{vel}} = 0.04D_0 \quad (\text{B7})$$

and

$$\delta\nu_{\text{even,odd}}^{650} = 0.06D_0. \quad (\text{B8})$$

REFERENCES

- Aerts, C., Christensen-Dalsgaard, J., Cunha, M., & Kurtz, D. W. 2008, *Sol. Phys.*, **251**, 3
- Aizenman, M., Smeyers, P., & Weigert, A. 1977, *A&A*, **58**, 41
- Allende Prieto, C., Asplund, M., López, R. J. G., & Lambert, D. L. 2002, *ApJ*, **567**, 544
- Anderson, E. R., Duvall, T. L., & Jefferies, S. M. 1990, *ApJ*, **364**, 699
- Appourchaux, T., et al. 2008, *A&A*, **488**, 705
- Arentoft, T., Kjeldsen, H., & Bedding, T. R. 2010, in ASP Conf. Ser. 416, GONG 2008/SOHO XXI Meeting on Solar-Stellar Dynamos as Revealed by Helio- and Asteroseismology, ed. M. Dikpati et al. (San Francisco, CA: ASP), in press (arXiv:0901.3632)
- Arentoft, T., et al. 2008, *ApJ*, **687**, 1180 (Paper I)
- Aufdenberg, J. P., Ludwig, H.-G., & Kervella, P. 2005, *ApJ*, **633**, 424
- Ballot, J., García, R. A., & Lambert, P. 2006, *MNRAS*, **369**, 1281
- Ballot, J., Turck-Chièze, S., & García, R. A. 2004, *A&A*, **423**, 1051
- Barban, C., Michel, E., Martić, M., Schmitt, J., Lebrun, J. C., Baglin, A., & Bertaux, J. L. 1999, *A&A*, **350**, 617
- Barban, C., et al. 2009, *A&A*, **506**, 51
- Baudin, F., Gabriel, A., Gibert, D., Pallé, P. L., & Régulo, C. 1996, *A&A*, **311**, 1024
- Bedding, T. R., & Kjeldsen, H. 2003, *PASA*, **20**, 203
- Bedding, T. R., & Kjeldsen, H. 2007, in AIP Conf. Proc. 948, Unsolved Problems in Stellar Physics: A Conference in Honour of Douglas Gough, ed. R. J. Stanciliffe et al. (Melville, NY: AIP), **117**
- Bedding, T. R., & Kjeldsen, H. 2010, *Commun. Asteroseismol.*, **161**, 3
- Bedding, T. R., Kjeldsen, H., Butler, R. P., McCarthy, C., Marcy, G. W., O'Toole, S. J., Tinney, C. G., & Wright, J. T. 2004, *ApJ*, **614**, 380
- Bedding, T. R., et al. 2007, *ApJ*, **663**, 1315
- Bedding, T. R., et al. 2010, *ApJ*, in press (arXiv:1001.0229)
- Benomar, O., Appourchaux, T., & Baudin, F. 2009a, *A&A*, **506**, 15
- Benomar, O., et al. 2009b, *A&A*, **507**, L13
- Bonanno, A., Küker, M., & Paternò, L. 2007, *A&A*, **462**, 1031
- Broomhall, A.-M., Chaplin, W. J., Davies, G. R., Elsworth, Y., Fletcher, S. T., Hale, S. J., Miller, B., & New, R. 2009, *MNRAS*, **396**, L100
- Brown, T. M., & Gilliland, R. L. 1994, *ARA&A*, **32**, 37
- Carrier, F., et al. 2007, *A&A*, **470**, 1059
- Carrier, F., et al. 2010, *A&A*, **55**, A73
- Chaboyer, B., Demarque, P., & Guenther, D. B. 1999, *ApJ*, **525**, L41
- Chang, H.-Y., & Gough, D. O. 1998, *Sol. Phys.*, **181**, 251
- Chaplin, W. J., Elsworth, Y., Isaak, G. R., McLeod, C. P., Miller, B. A., & New, R. 1997, *MNRAS*, **288**, 623
- Chaplin, W. J., Houdek, G., Elsworth, Y., Gough, D. O., Isaak, G. R., & New, R. 2005, *MNRAS*, **360**, 859
- Chaplin, W. J., Houdek, G., Karoff, C., Elsworth, Y., & New, R. 2009, *A&A*, **500**, L21
- Christensen-Dalsgaard, J. 2004, *Sol. Phys.*, **220**, 137
- Christensen-Dalsgaard, J., Däppen, W., & Lebreton, Y. 1988, *Nature*, **336**, 634
- Christensen-Dalsgaard, J., & Houdek, G. 2009, *Ap&SS*, in press (arXiv:0911.4629)
- Deheuvels, S., et al. 2010, *A&A*, submitted
- Di Mauro, M. P., & Christensen-Dalsgaard, J. 2001, in IAU Symp. 203, Recent Insights into the Physics of the Sun and Heliosphere: Highlights from SOHO and Other Space Missions, ed. P. Brekke, B. Fleck, & J. B. Gurman (San Francisco, CA: ASP), **94**
- Dziembowski, W. A., Paternò, L., & Ventura, R. 1988, *A&A*, **200**, 213
- Eggenberger, P., Carrier, F., & Bouchy, F. 2005, *New Astron.*, **10**, 195
- Eggenberger, P., Carrier, F., Bouchy, F., & Blecha, A. 2004, *A&A*, **422**, 247
- Fletcher, S. T., Chaplin, W. J., Elsworth, Y., Schou, J., & Buzasi, D. 2006, *MNRAS*, **371**, 935
- Frandsen, S., Jones, A., Kjeldsen, H., Viskum, M., Hjorth, J., Andersen, N. H., & Thomsen, B. 1995, *A&A*, **301**, 123
- García, R. A., et al. 2009, *A&A*, **506**, 41
- Gatewood, G., & Han, I. 2006, *AJ*, **131**, 1015
- Gilliland, R. L., et al. 1993, *AJ*, **106**, 2441
- Gilliland, R. L., et al. 2010, *PASP*, **122**, 131
- Girard, T. M., et al. 2000, *AJ*, **119**, 2428
- Gizon, L., & Solanki, S. K. 2003, *ApJ*, **589**, 1009
- Gough, D. O. 1986, in Hydrodynamic and Magnetodynamic Problems in the Sun and Stars, ed. Y. Osaki (Tokyo: Univ. Tokyo Press), **117**
- Gough, D. O. 1990, in Lecture Notes in Physics, Vol. 367, Progress of Seismology of the Sun and Stars, ed. Y. Osaki & H. Shibahashi (Berlin: Springer), **283**
- Grec, G., Fossat, E., & Pomerantz, M. A. 1983, *Sol. Phys.*, **82**, 55
- Gregory, P. C. 2005, Bayesian Logical Data Analysis for the Physical Sciences (Cambridge: Cambridge Univ. Press)
- Gruberbauer, M., Kallinger, T., Weiss, W. W., & Guenther, D. B. 2009, *A&A*, **506**, 1043
- Grundahl, F., Christensen-Dalsgaard, J., Arentoft, T., Frandsen, S., Kjeldsen, H., Jørgensen, U. G., & Kjaergaard, P. 2008, *Commun. Asteroseismol.*, **157**, 273
- Guenther, D. B., & Demarque, P. 1993, *ApJ*, **405**, 298
- Guenther, D. B., et al. 2008, *ApJ*, **687**, 1448
- Högbom, J. A., & Brouw, W. N. 1974, *A&A*, **33**, 289
- Houdek, G., & Gough, D. O. 2007, *MNRAS*, **375**, 861
- Jeffreys, H. 1961, Theory of Probability (3rd ed.; New York: Oxford Univ. Press)
- Kallinger, T., Gruberbauer, M., Guenther, D. B., Fossati, L., & Weiss, W. W. 2010, *A&A*, **510**, A106
- Karoff, C. 2007, *MNRAS*, **381**, 1001
- Kervella, P., Thévenin, F., Morel, P., Berthomieu, G., Bordé, P., & Provost, J. 2004, *A&A*, **413**, 251
- Kjeldsen, H., Bedding, T. R., & Christensen-Dalsgaard, J. 2008b, *ApJ*, **683**, L175
- Kjeldsen, H., Bedding, T. R., Viskum, M., & Frandsen, S. 1995, *AJ*, **109**, 1313
- Kjeldsen, H., et al. 2005, *ApJ*, **635**, 1281
- Kjeldsen, H., et al. 2008a, *ApJ*, **682**, 1370
- Leccia, S., Kjeldsen, H., Bonanno, A., Claudi, R. U., Ventura, R., & Paternò, L. 2007, *A&A*, **464**, 1059
- Li, L. H., Robinson, F. J., Demarque, P., Sofia, S., & Guenther, D. B. 2002, *ApJ*, **567**, 1192
- Liddle, A. R. 2009, *Annu. Rev. Nucl. Part. Sci.*, **59**, 95
- Martić, M., Lebrun, J.-C., Appourchaux, T., & Korzennik, S. G. 2004, *A&A*, **418**, 295
- Martić, M., et al. 1999, *A&A*, **351**, 993
- Mathur, S., et al. 2010, *A&A*, submitted
- Michel, E., et al. 2008, *Science*, **322**, 558
- Mosser, B., & Appourchaux, T. 2009, *A&A*, **508**, 877
- Mosser, B., Appourchaux, T., Catala, C., Buey, J., & SIAMOIS team 2008, *J. Phys. Conf. Ser.*, **118**, 012042
- Mosser, B., Maillard, J. P., Mékarnia, D., & Gay, J. 1998, *A&A*, **340**, 457
- Osaki, J. 1975, *PASJ*, **27**, 237
- Provost, J., Berthomieu, G., Martić, M., & Morel, P. 2006, *A&A*, **460**, 759
- Régulo, C., & Roca Cortés, T. 2005, *A&A*, **444**, L5
- Rosenthal, C. S., Christensen-Dalsgaard, J., Nordlund, Å., Stein, R. F., & Trampedach, R. 1999, *A&A*, **351**, 689
- Roxburgh, I. W. 2009, *A&A*, **506**, 435
- Roxburgh, I. W., & Vorontsov, S. V. 2006, *MNRAS*, **369**, 1491
- Tassoul, M. 1980, *ApJS*, **43**, 469
- Toutain, T., & Fröhlich, C. 1992, *A&A*, **257**, 287
- van Leeuwen, F. 2007, Hipparchos, the New Reduction of the Raw Data (Dordrecht: Springer)